The Higgs sector of the complex minimal supersymmetric standard model

Williams, Karina E.

The Higgs Sector of the Complex Minimal Supersymmetric Standard Model

A thesis presented for the degree of

Doctor of Philosophy

by

Karina E. Williams

September 2008

Institute of Particle Physics Phenomenology

Abstract

Complete one-loop results for the decay widths of neutral Higgs bosons (h_a) into lighter neutral Higgs bosons (h_b, h_c) are presented for the MSSM with complex parameters. The results are obtained in the Feynman-diagrammatic approach, taking into account the full dependence on the spectrum of supersymmetric particles and all complex phases of the supersymmetric parameters. The genuine triple-Higgs vertex contributions are supplemented with two-loop propagator-type corrections, yielding the currently most precise prediction for this class of processes. The genuine vertex corrections turn out to be very important, yielding a large increase of the decay width compared to a prediction based on the tree-level vertex. One-loop propagator-type mixing between neutral Higgs bosons and Goldstone and Z bosons is also consistently taken into account. Complete one-loop results for the decay of a neutral Higgs boson into fermions are also presented, which include the full dependence on complex phases. The new results are used to analyse the impact of the experimental limits from the LEP Higgs searches on the parameter space with a very light MSSM Higgs boson. It is found that a significant part of the parameter space of the CPX benchmark scenario exists where channels involving the decay $h_2 \to h_1 h_1$ have the highest search sensitivity, and the existence of an unexcluded region with $M_{h_1} \approx 45$ GeV is confirmed. The public code *HiggsBounds* is also presented, which can be used in conjunction with models with an arbitrary number of neutral Higgs bosons to determine whether parameter points have been excluded at the 95% CL by the LEP and Tevatron Higgs searches.

Declaration

I declare that this thesis has not been submitted for another degree at this or any other university.

This thesis is based on the work in the following publications:

- T. Hahn, S. Heinemeyer, W. Hollik, H. Rzehak, G. Weiglein, K.E. Williams, *CP-violating Loop Effects in the Higgs Sector of the MSSM*, IPPP-07-84, DCPT-07-168, LCWS-2007-HIG19, Nov 2007, arXiv:0711.2020 [hep-ph]

- K.E. Williams, G. Weiglein, *Higgs boson decays in the Complex MSSM*, IPPP-07-76, DCPT-07-152, Oct 2007, arXiv:0710.5331 [hep-ph]

- K.E. Williams, G. Weiglein, *Precise predictions for $h_a \to h_b h_c$ decays in the complex MSSM*, Phys.Lett.B660:217-227,2008, DCPT-07-150, IPPP-07-75, Oct 2007, arXiv:0710.5320 [hep-ph]

- T. Hahn, S. Heinemeyer, W. Hollik, H. Rzehak, G. Weiglein, K.E. Williams, *Higher-Order Corrected Higgs Bosons in FeynHiggs 2.5*, Pramana 69:861-870,2007,MPP-2006-100, Nov 2006, hep-ph/0611373

- E. Accomando et al., *Workshop on CP Studies and Non-Standard Higgs Physics*, CERN-2006-009, Jul 2006, hep-ph/0608079

 The work presented here was funded by an STFC studentship.

Preface

Today marked the beginning of a new era in particle physics. At 09.28 BST, amid a veritable media frenzy[1], the first proton beam was fired the entire way round the 27km underground tunnel at CERN, Geneva. This milestone was celebrated across the world as the 'switching on' of the next great particle physics experiment, the Large Hadron Collider.

The LHC will allow the exploration of a very high energy regime, which humans have so far been unable to investigate in controlled conditions. Most scientists believe this regime to be populated with particles holding the clues to crucial questions about the nature of the universe at a fundamental level. One of the key tasks of the LHC experiment will be to attempt to track down the 'Higgs boson', a hypothetical particle which forms a cornerstone of almost all our current theories. If its existence is confirmed, the Higgs boson will provide the answer to one of the biggest questions in particle physics: how elementary particles get their mass.

Against such a backdrop, it may seem strange to be submitting a thesis that focusses particularly on the unsuccessful Higgs searches carried out by the previous occupier of the tunnel at CERN, the Large Electron-Postiron collider (LEP). However, the very fact that a Higgs boson was not discovered by LEP plays a vital role in narrowing down its possible characteristics. In particular, the LEP results give us a lower limit on the mass of the Higgs boson, which varies depending on which of the many particle physics models you believe in. This lower limit was particularly low for the Complex Minimal Supersymmetric Standard Model, since Higgs bosons described by this theory can be trickier to produce in colliders. In this thesis, we focus on the behaviour of these types of Higgs bosons and, in particular, how they would interact with eachother, and we investigate how our predictions affect the interpretation of the results from LEP. We hope to shed further light on which types of Higgs bosons have already been ruled out by past experiments - thus contributing to the effort to provide a clear path forward for the Higgs searches at the LHC and its successors.

K.W., 10th September 2008, Durham, UK.

[1]Depending on who you listen to, the LHC is either "the greatest scientific endeavour since the Apollo moon landings" or a "Doomsday machine" capable of producing Earth-destroying black holes.

Contents

Chapter 1

Introduction

1.1 The Standard Model and Electroweak Symmetry Breaking

The Standard Model (SM) of particle physics has been hugely successful at describing experimental results collected at particle colliders during the last thirty years.

The model is a combination of some of the greatest achievements in theoretical physics in the last half century. Firstly, it uses Glashow-Weinberg-Salam electroweak theory, which was developed in the 1960s to describe electromagnetic and weak interactions between quarks and leptons [1–3]. Secondly, it includes Quantum Chromodynamics (QCD), which emerged in the 1970s to describe strong interactions between quarks [4–9]. Spontaneous electroweak symmetry breaking is required to preserve local gauge invariance and generate particle masses. This is achieved by including a scalar doublet field with non-zero vacuum expectation value [10–14]. As a result, the theory predicts the existence of an additional scalar particle, called the Higgs boson.

Almost all facets of the Standard Model have been thoroughly investigated at collider experiments [15, 16]. However, we are yet to find any direct evidence of the existence of a Higgs particle. The LEP experiment was able to put a lower limit on the mass of a Standard Model-like Higgs boson of 114.4 GeV at the 95% confidence level [17]. Higgs searches are currently being carried out at the Tevatron [18]. If a Standard Model-like Higgs boson exist, it will be seen at the Large Hadron Collider [19], which is about to commence operation.

1.2 Supersymmetry

Although the Standard Model has been very successful at explaining phenomena at current collider experiments, there is a prevalent belief throughout the particle physics community that the SM is a low energy effective theory. There is huge speculation about the prospect of a more fundamental theory. In particular, it is hoped that we will one day have a 'Theory of Everything' (TOE) which will describe all four forces of nature - electromagnetic, weak, strong and gravity.

In addition, Cosmologists have amassed a lot of evidence (such as the shape of galaxy rotation curves and results from weak lensing) which could indicate that most of the mass in the universe is composed of non-relativistic, weakly interacting particles (see [20] for a review). The Standard Model does not contain a candidate for this particle.

The Standard Model also suffers from what is known as the hierarchy problem. When the 1-loop fermion corrections to the Higgs particle are calculated in the Standard Model, the result contains a quadratic divergence. This can be renormalised away, but it is still necessary to do a great deal of fine-tuning to get the 1-loop contributions to the mass to approximately cancel, leaving a Higgs mass at the weak scale, rather than the unification scale (GUT scale).

Supersymmetry (SUSY) is a very popular and widely researched extension to the Standard Model (for a general introduction, see [21, 22]). Although it is only one step along the road to a TOE, supersymmetry emerges naturally in superstring theory, which is an attempt to incorporate gravity in to a quantum field theory. It is the only non-trivial extension of the Poincaré group [23].

Supersymmetry is a symmetry between fermions and bosons. It provides a neat solution to the problem of quadratic divergences because it predicts that every known particle has a partner which we have not yet observed. Loops involving these particles cancel the quadratic divergences from the Standard Model particles.

However, if supersymmetry was an exact symmetry of Nature, particles and their 'superpartners' would have the same mass, and therefore the superpartners should have been observed in collider experiments. Therefore, if SUSY applies to Nature, it must exist as a broken symmetry. Fortunately, it is possible to break SUSY such that the quadratic divergences still cancel (SUSY is broken 'softly').

Realistic softly broken supersymmetric theories (such as the Minimal Supersymmetric Standard Model (MSSM), which will be used in this thesis) have the desirable effect of unifying the gauge couplings at high energies, which is required for unified theories. This does not occur in the Standard Model.

Most realistic theories also impose R-parity, in order to prevent rapid decay of the proton. As a result, sparticles are prevented from decaying into purely Standard Model particles. Therefore the lightest supersymmetric particle is stable, providing an excellent dark matter candidate.

Of course, a fundamentally important prediction of supersymmetric theories is the existence of superpartners for each known Standard Model particle. One of the main aims of the Large Hadron Collider will be to search for these superparticles. In addition, supersymmetric theories also require the existence of more than one Higgs boson, which leads to a wide range of interesting phenomenological consequences.

One example is the ability of the MSSM to evade the LEP restrictions on a Standard Model-like Higgs mass in scenarios containing significant CP violation. In particular, LEP was unable to exclude the possibility that a neutral Higgs boson exists with a mass of ~ 40 GeV [24].

The CP transformation is a combination of charge conjugation C and parity P. In the Standard Model, C and P are conserved separately in strong and electroweak interactions, whereas weak interactions violate C and P separately. Apart from in rare cases, the combination CP is conserved in weak interactions. CP violation was first observed in the neutral kaon system in 1964 [25]. It has also been observed in neutral B meson decays with the BABAR [26] and Belle [27] detectors and can occur in the neutrino mass matrix.

The existence of CP violation is one of the three Sakharov conditions for baryosynthesis, and is therefore required to explain the fact that the observable universe appears to be composed of vastly more matter than antimatter (as discussed in [28]). However, the Standard Model on its own does not contain enough CP violation to explain the matter-antimatter asymmetry we observe, making extensions to the Standard Model which incorporate new sources of CP violation very attractive.

This thesis will cover a range of topics which are useful for carrying out a more detailed investigation into the region of the CP-violating MSSM parameter space that can not be excluded by current Higgs search results. Although this is the unifying theme

of the thesis, many of the topics will have much wider applications. In particular, we will calculate full 1-loop vertex corrections to the Higgs cascade decay in the CP-violating MSSM and combine these with propagator corrections, to obtain the currently most precise prediction for this class of processes. Investigating this decay at future colliders will give us access to the triple Higgs vertex, which is an important line of enquiry if we are to confirm our description of electroweak symmetry breaking. We will then examine the LEP Higgs exclusion regions in the CP-violating MSSM in the context of the new Higgs sector results.

1.3 Thesis Outline

We will begin by a detailed description of the various elements of the MSSM with complex parameters (which can cause CP violation) which will be most relevant to this thesis and thereby fix the notation.

Chapter 3 will discuss the renormalisation of the complex MSSM and derive any counter-terms we require which are not available in the literature. We will also discuss differences between parameters as defined in different renormalisation schemes.

In the following chapter, we will outline the method used in this thesis to calculate the neutral Higgs masses. We will also introduce a pictorial representation of the Higgs sector mixing and discuss the way that propagator corrections can be incorporated in calculations involving an external Higgs boson.

In Chapter 5, we provide a brief introduction to some of the features of Standard Model and SUSY QCD which we will require when calculating the Higgs to b-quark decay width, which we have extended to apply to the complex MSSM.

Chapter 6 will discuss the Higgs cascade decay width. We calculate full 1-loop genuine vertex corrections with full phase dependence and combine these with propagator corrections.

We calculate the full electroweak 1-loop genuine vertex corrections to Higgs to b-quark decay in Chapter 7, again with full phase dependence. These are combined with propagator, QED, SM and SUSY QCD corrections. Similarly, we calculate the genuine vertex corrections to the Higgs to tau-lepton decay width and combine this with QED and propagator corrections.

The numerical effect of these new decay widths on the neutral Higgs branching ratio will be investigated in Chapter 8.

In Chapter 9, we review the results of the LEP Higgs searches for the CP-violating MSSM benchmark scenario, the CPX scenario. We investigate the effect of our new Higgs branching ratios on the LEP exclusions in the CPX scenario. In addition, we examine the effect of new advances in the calculation of the Higgs self-energies which have been made since the original LEP Higgs Working Group analysis.

In order to facilitate the use of LEP results in conjunction with new Higgs sector results, we have created a new fortran program, *HiggsBounds* [29], which we discuss in Chapter 10. In particular, we outline the new features which were added in order to extend this program to use results from the Tevatron Higgs searches.

In Chapter 11 we conclude.

Chapter 2

The Complex MSSM

2.1 Introduction

The Minimal Supersymmetric Standard Model (MSSM) is the simplest realistic supersymmetric extension of the Standard Model. It makes no assumption about the soft SUSY breaking mechanism and introduces the minimum number of new particles. It requires two Higgs doublets, with opposite hypercharge. R-parity is imposed, which means that the Lightest Supersymmetric Particle (LSP) is stable and a viable Dark Matter candidate. Since the model was first proposed, it has been discovered that it features the unification of coupling constants at high energies [30].

Table 2.1 shows the superfields and the particle content of the MSSM. Many of these particles are not physical eigenstates in themselves, but will mix to form physical eigenstates, as given in Table 2.1.

The general structure of the MSSM Lagrangian is

$$\mathcal{L}_{\text{MSSM}} = \mathcal{L}_{\text{superpot.}} + \mathcal{L}_{\text{kin.}} + \mathcal{L}_{\text{soft}} + \mathcal{L}_{\text{gauge fix}} + \mathcal{L}_{\text{ghost}}. \tag{2.1}$$

The term $\mathcal{L}_{\text{superpot.}}$ involves the superpotential. It contains mass terms and interaction terms, including the Yukawa couplings. $\mathcal{L}_{\text{kin.}}$ contain kinetic terms. $\mathcal{L}_{\text{soft}}$ contains the SUSY breaking terms, including scalar mass terms, trilinear scalar interactions and gaugino mass terms, with a total of over 100 free parameters. $\mathcal{L}_{\text{gauge fix}}$ contains the gauge fixing terms and $\mathcal{L}_{\text{ghost}}$ involves the Fadeev-Popov ghosts. Unless otherwise stated, all calculations will be done in the Feynman gauge ($\xi_A = \xi_W = \xi_Z = \xi_G = 1$).

superfield	$(SU(3), SU(2), U(1))$	2HDM particle		SUSY partner	
$\hat{Q}$	$(3, 2, \frac{1}{3})$	$\begin{pmatrix} u_L \\ d_L \end{pmatrix}$	quarks	$\begin{pmatrix} \tilde{u}_L \\ \tilde{d}_L \end{pmatrix}$	squarks
$\hat{U}$	$(3^*, 1, -\frac{4}{3})$	u_R^C		$\tilde{u}_R^\dagger$	
$\hat{D}$	$(3^*, 1, \frac{2}{3})$	d_R^C		$\tilde{d}_R^\dagger$	
$\hat{L}$	$(1, 2, -1)$	$\begin{pmatrix} \nu_L \\ e_L \end{pmatrix}$	leptons	$\begin{pmatrix} \tilde{\nu}_L \\ \tilde{e}_L \end{pmatrix}$	sleptons
$\hat{E}$	$(1, 1, 2)$	e_R^C		$\tilde{e}_R^\dagger$	
$\hat{H}_1$	$(1, 2, -1)$	$\begin{pmatrix} H_{11} \\ H_{12} \end{pmatrix}$	Higgs bosons	$\begin{pmatrix} \tilde{H}_{11} \\ \tilde{H}_{12} \end{pmatrix}$	Higgsinos
$\hat{H}_2$	$(1, 2, 1)$	$\begin{pmatrix} H_{21} \\ H_{22} \end{pmatrix}$		$\begin{pmatrix} \tilde{H}_{21} \\ \tilde{H}_{22} \end{pmatrix}$	
$\hat{W}$	$(1, 3, 0)$	W_μ^i	W_μ^i-boson	$\tilde{W}^i$	winos
$\hat{B}$	$(1, 1, 0)$	B_μ	B_μ-boson	$\tilde{B}^0$	binos
$\hat{G}_a$	$(8, 1, 0)$	g_a	gluons	$\tilde{g}_a$	gluinos

Table 2.1: MSSM superfields and particle content

Physical Particles		arising from
SM-like fermions	f_L, f_R^C	-
gluons	g_a	-
gluinos	$\tilde{g}_a$	-
neutral gauge bosons	Z_μ, A_μ	$W_\mu^3, B_\mu, H_{11}, H_{22}$
charged gauge bosons	$W_\mu^\pm$	$W_\mu^1, W_\mu^2, H_{12}, H_{21}$
neutral Higgs bosons	h, H, A	H_{11}, H_{22}
charged Higgs bosons	$H^\pm$	H_{12}, H_{21}
sfermions	$\tilde{f}_1, \tilde{f}_2$	$\tilde{f}_L, \tilde{f}_R^\dagger$
neutralinos	$\chi_1^0, \chi_2^0, \chi_3^0, \chi_4^0$	$\tilde{W}^3, \tilde{B}^0, \tilde{H}_{11}, \tilde{H}_{22}$
charginos	$\chi_1^\pm, \chi_2^\pm$	$\tilde{W}^1, \tilde{W}^2, \tilde{H}_{12}, \tilde{H}_{21}$

Table 2.2: Physical particles in the MSSM, some of which are created from mixes of particles shown in Table 2.1

In the following sections, we will look at parts of the Lagrangian in more detail, in order to fix the notation and derive the tree level masses and couplings which will be

particularly important in the later chapters. The notation will closely follow that used in [31]. We also discuss some of the important phenomenological aspects of the theory and introduce a commonly used scenario in the complex MSSM – the CPX scenario.

2.2 The Neutral Higgs Sector

In the MSSM, the Higgs potential is

$$\mathcal{L}^{V_H} = -V_H \tag{2.2}$$
$$= \mathcal{L}_F^{V_H} + \mathcal{L}_D^{V_H} + \mathcal{L}_{\text{soft}}^{V_H}. \tag{2.3}$$

$\mathcal{L}_F^{V_H}$ and $\mathcal{L}_D^{V_H}$ are found by substituting for the auxiliary F and D fields in $\mathcal{L}_{\text{superpot.}}$ and $\mathcal{L}_{\text{kin.}}$. $\mathcal{L}_{\text{soft}}^{V_H}$ contains the soft SUSY-breaking terms

$$\mathcal{L}_{\text{soft}}^{V_H} = -\tilde{m}_1^2 H_{1i}^* H_{1i} - \tilde{m}_2^2 H_{2i}^* H_{2i} + \epsilon^{ij}\left(m_{12}^2 H_{1i} H_{2j} + m_{12}^{2*} H_{1i}^* H_{2j}^*\right). \tag{2.4}$$

Therefore,

$$V_H = m_1^2 H_{1i}^* H_{1i} + m_2^2 H_{2i}^* H_{2i} - \epsilon^{ij}(m_{12}^2 H_{1i} H_{2j} + {m_{12}^2}^* H_{1i}^* H_{2j}^*)$$
$$+ \tfrac{1}{8}(g_1^2 + g_2^2)(H_{1i}^* H_{1i} - H_{2i}^* H_{2i})^2 + \tfrac{1}{2} g_2^2 |H_{1i}^* H_{2i}|^2, \tag{2.5}$$

where $m_1^2 = \tilde{m}_1^2 + |\mu|^2, m_2^2 = \tilde{m}_2^2 + |\mu|^2$, thus depending on soft SUSY breaking parameters and the higgsino mass parameter μ. m_{12}^2 is also a soft SUSY breaking parameter, $g_1 = e/c_W$ and $g_2 = e/s_W$ are the U(1) and SU(2) coupling constants and $\epsilon^{12} = 1$. $c_w = \cos\theta_W$ and $s_w = \sin\theta_W$, where θ_W is the weak mixing angle. The Higgs doublets are of the form

$$\mathcal{H}_1 = \begin{pmatrix} H_{11} \\ H_{12} \end{pmatrix} = \begin{pmatrix} v_1 + \frac{1}{\sqrt{2}}(\varphi_1 - i\chi_1) \\ -\phi_1^- \end{pmatrix},$$
$$\mathcal{H}_2 = \begin{pmatrix} H_{21} \\ H_{22} \end{pmatrix} = \begin{pmatrix} \phi_2^+ \\ v_2 + \frac{1}{\sqrt{2}}(\phi_2 + i\chi_2) \end{pmatrix}, \tag{2.6}$$

where v_1 and v_2 are the vacuum expectation values. We define $\tan\beta = v_2/v_1$.

There is no CP violation in the Higgs sector at lowest order since any phase dependence can be rotated away, as discussed in [31]. In addition, the doublet $\mathcal{H}_2$ may also

have a complex phase dependence, which can also be rotated away and thus we do not include it explicitly in equation (2.6). The tree level neutral mass eigenstates h, H, A, G are related to the tree level neutral fields $\phi_1, \phi_2, \chi_1, \chi_2$ through a unitary matrix.

$$\begin{pmatrix} h \\ H \\ A \\ G \end{pmatrix} = \begin{pmatrix} -\sin\alpha & \cos\alpha & 0 & 0 \\ \cos\alpha & \sin\alpha & 0 & 0 \\ 0 & 0 & -\sin\beta_n & \cos\beta_n \\ 0 & 0 & \cos\beta_n & \sin\beta_n \end{pmatrix} \cdot \begin{pmatrix} \varphi_1 \\ \varphi_2 \\ \chi_1 \\ \chi_2 \end{pmatrix}. \tag{2.7}$$

where we can see that the CP-even eigenstates ϕ_1, ϕ_2 do not mix with the CP-odd eigenstates χ_1, χ_2. Unless otherwise stated, h, H, A, G will always represent tree level neutral fields throughout this thesis.

Expanding equation (2.5) gives the mass terms explicitly, as given in [31]. At tree level, the off-diagonal mass terms must vanish, leading to the condition $\beta_n = \beta$. (However, note that, in the scheme we are using, $\beta = \arctan(v_2/v_1)$ is renormalised but β_n is not. Therefore, it is necessary to distinguish between β and β_n when performing the renormalisation). This leads to the expressions for the tree level neutral Higgs masses,

$$m^2_{h,H} = \frac{1}{2}\left(m^2_A + M^2_Z \mp \sqrt{(m^2_A + M^2_Z)^2 - 4m^2_A M^2_Z \cos^2 2\beta}\right), \tag{2.8}$$

$$m^2_A = m^2_{H^\pm} - M^2_W. \tag{2.9}$$

or, equivalently,

$$m^2_h = -M^2_Z \cos 2\beta \frac{\sin(\alpha+\beta)}{\sin(\beta-\alpha)}, \tag{2.10}$$

$$m^2_H = M^2_Z \cos 2\beta \frac{\cos(\alpha+\beta)}{\cos(\beta-\alpha)}, \tag{2.11}$$

$$m^2_A = -M^2_Z \frac{\sin 2(\alpha+\beta)}{\sin 2(\beta-\alpha)}. \tag{2.12}$$

This also leads to an expression for the tree level mixing angle α,

$$\tan 2\alpha = \tan 2\beta \frac{m^2_A + M^2_Z}{m^2_A - M^2_Z}, \tag{2.13}$$

with $-\frac{\pi}{2} < \alpha < 0$.

To specify the Higgs sector, it is necessary to give the values of two parameters - often $\tan\beta$ and one of the Higgs masses. In the real MSSM, CP is conserved and it is usual to take m_A as one of the input parameters. However, in the complex MSSM, A mixes with the states h, H at 1-loop and above. Therefore, it is usual to take $m_{H^\pm}$ as the input parameter in the complex MSSM.

Expanding equation (2.5) also leads to the triple neutral Higgs couplings $h_i h_j h_k$ (where $h_i h_j h_k$ is some combination of h, H, A). These are given in Table 3.2.

2.3 Quark Sector

We require expressions for the quark masses and quark-Higgs interactions. In this section, we are following the procedure and conventions used in [32]. These are obtained from a term in the superpotential

$$\mathcal{L}_{\text{superpot.}} \in \left[\epsilon^{ij}\left(-\lambda_u \hat{H}_{2i}\hat{Q}_j\hat{U} + \lambda_d \hat{H}_{1i}\hat{Q}_j\hat{D}\right)\right]_{\theta\theta} + h.c., \tag{2.14}$$

where $\epsilon^{12} = 1$ and θ^α are Grassmann variables with $\theta\theta = \theta^\alpha\theta_\alpha$. Discarding the parts of the superfields which do not contribute to the quark masses and quark-Higgs interactions leaves

$$\begin{aligned}\mathcal{L}^{q\bar{q},h_i q\bar{q}} &= -\left[\left(\theta^\beta\theta_\beta\right)\left(\lambda_d H_{11}\left(d_L\right)^\alpha\left(d_R^C\right)_\alpha + \lambda_u H_{22}\left(u_L\right)^\alpha\left(u_R^C\right)_\alpha\right)\right]_{\theta\theta} + h.c. \\ &= -\lambda_d H_{11}\left(d_L\right)^\alpha\left(d_R^C\right)_\alpha - \lambda_u H_{22}\left(u_L\right)^\alpha\left(u_R^C\right)_\alpha + h.c.,\end{aligned} \tag{2.15}$$

where $\left(u_L\right)_\alpha, \left(d_L\right)_\alpha, \left(u_R^C\right)_\alpha, \left(d_R^C\right)_\alpha$ are Weyl spinors. These are related to the Dirac spinors u, d by

$$\begin{aligned} u &= \begin{pmatrix}\left(u_L\right)_\alpha \\ \overline{\left(u_R^C\right)^{\dot{\alpha}}}\end{pmatrix}, \qquad d = \begin{pmatrix}\left(d_L\right)_\alpha \\ \overline{\left(d_R^C\right)^{\dot{\alpha}}}\end{pmatrix}, \\ \overline{u} &= \begin{pmatrix}\left(u_R^C\right)^\alpha & \overline{\left(u_L\right)_{\dot{\alpha}}}\end{pmatrix}, \qquad \overline{d} = \begin{pmatrix}\left(d_R^C\right)^\alpha & \overline{\left(d_L\right)_{\dot{\alpha}}}\end{pmatrix}. \end{aligned} \tag{2.16}$$

Therefore, we can rewrite $\mathcal{L}^{q\bar{q},h_i q\bar{q}}$ as

$$\mathcal{L}^{q\bar{q},h_i q\bar{q}} = -\lambda_d H_{11}\bar{d}d - \lambda_u H_{22}\bar{u}u. \tag{2.17}$$

Substituting for H_{11}, H_{22} gives the quark masses $m_u = \lambda_u v_2$ and $m_d = \lambda_d v_1$ and the couplings of the Higgs to the quarks as given in Table 3.3 and Table 3.4. Recall that, at tree level, $\beta = \beta_n$. However, we kept the β_n dependence in these couplings since this information is needed during the renormalisation procedure.

We can also define left-handed and right-handed Dirac spinors, using the projection operators $\omega_\pm = \frac{1}{2}(1 \pm \gamma_5)$,

$$q_L = w_- q, \qquad q_R = w_+ q, \tag{2.18}$$

$$\bar{q}_L = \bar{q} w_+, \qquad \bar{q}_R = \bar{q} w_-. \tag{2.19}$$

We can therefore rewrite $\mathcal{L}^{q\bar{q},h_i q\bar{q}}$ as

$$\mathcal{L}^{q\bar{q},h_i q\bar{q}} \equiv -\lambda_d H_{11}(\bar{d}_R d_L + \bar{d}_L d_R) - \lambda_u H_{22}(\bar{u}_R u_L + \bar{u}_L u_R). \tag{2.20}$$

2.4 Squark Sector

Again, in this section, we are following the procedure and conventions used by [32]. Eliminating the auxiliary fields from $\mathcal{L}_{\text{superpot.}}$, $\mathcal{L}_{\text{kin.}}$, collecting the squark mass terms and adding the soft-breaking terms

$$\mathcal{L}^{\tilde{q}\text{mass}}_{\text{soft}} \equiv -M_L^2\left(\tilde{u}_L^\dagger \tilde{u}_L + \tilde{d}_L^\dagger \tilde{d}_L\right) - M_{\tilde{u}_R}^2 \tilde{u}_L^\dagger \tilde{u}_L - M_{\tilde{d}_R}^2 \tilde{d}_L^\dagger \tilde{d}_L \tag{2.21}$$

$$- \left(\lambda_u A_u v_2 \tilde{u}_L \tilde{u}_L^\dagger + \lambda_d A_d v_1 \tilde{d}_L \tilde{d}_L^\dagger + h.c.\right) \tag{2.22}$$

leads to the squark mass matrix

$$M_{\tilde{q}} = \begin{pmatrix} M_L^2 + m_q^2 + M_Z^2 \cos 2\beta (I_3^q - Q_q s_w^2) & m_q X_q^* \\ m_q X_q & M_{\tilde{q}_R}^2 + m_q^2 + M_Z^2 \cos 2\beta Q_q s_w^2 \end{pmatrix}, \tag{2.23}$$

where

$$\mathcal{L}^{\tilde{q}\text{mass}} = -\begin{pmatrix} \tilde{q}_L^\dagger & \tilde{q}_R^\dagger \end{pmatrix} . M_{\tilde{q}} . \begin{pmatrix} \tilde{q}_L \\ \tilde{q}_R \end{pmatrix}, \tag{2.24}$$

$$X_q = A_q - \mu^* \{\cot\beta, \tan\beta\}. \tag{2.25}$$

and $\cot\beta$ or $\tan\beta$ applies to u-type or d-type quarks respectively. The eigenvalues of equation (2.25) are

$$m^2_{\tilde{q}_{1,2}} = m_q^2 + \frac{1}{2}\Big[M_L^2 + M^2_{\tilde{q}_R} + I_3^q M_Z^2 \cos 2\beta \tag{2.26}$$

$$\mp \sqrt{[M_L^2 - M^2_{\tilde{q}_R} + M_Z^2 \cos 2\beta (I_3^q - 2Q_q s_{\rm w}^2)]^2 + 4m_q^2 |X_q|^2}\ \Big]. \tag{2.27}$$

In the complex MSSM, the trilinear coupling A_q and the higgsino mass parameter μ can have non-zero complex phases. The mass matrix $M_{\tilde{q}}$ can be diagonalised by the matrix $\mathbf{U}_{\tilde{q}}$, where

$$\begin{pmatrix} \tilde{q}_1 \\ \tilde{q}_2 \end{pmatrix} = \mathbf{U}_{\tilde{q}} \begin{pmatrix} \tilde{q}_L \\ \tilde{q}_R \end{pmatrix}, \quad \text{where} \quad \mathbf{U}_{\tilde{q}} = \begin{pmatrix} c_{\tilde{q}} & s_{\tilde{q}} \\ -s^*_{\tilde{q}} & c_{\tilde{q}} \end{pmatrix}, \tag{2.28}$$

and $c_{\tilde{q}}$ is real, $s_{\tilde{q}}$ is complex and $c^2_{\tilde{q}} + |s_{\tilde{q}}|^2 = 1$. They are given by

$$c_{\tilde{q}} = \frac{\sqrt{M_L^2 + m_q^2 + M_Z^2 \cos 2\beta (I_3^q - Q_q s_{\rm w}^2) - m^2_{\tilde{q}_2}}}{\sqrt{m^2_{\tilde{q}_1} - m^2_{\tilde{q}_2}}}, \tag{2.29}$$

$$s_{\tilde{q}} = \frac{m_q X_q^*}{\sqrt{M_L^2 + M_Z^2 \cos 2\beta (I_3^q - Q_q s_{\rm w}^2) + m_q^2 - m^2_{\tilde{q}_2}}\sqrt{m^2_{\tilde{q}_1} - m^2_{\tilde{q}_2}}}. \tag{2.30}$$

The relation $\left(m^2_{\tilde{q}_1} - m^2_{\tilde{q}_2}\right) c_{\tilde{q}} s_{\tilde{q}} = m_q X_q^*$ is often useful when simplifying amplitudes.

2.5 Higgs kinetic terms in the Lagrangian

Expanding $\mathcal{L}_{\rm kin}$ gives a term

$$\mathcal{L}_{\rm kin} \ \in \ (D_\mu \mathcal{H}_1)^\dagger (D^\mu \mathcal{H}_1) + (D_\mu \mathcal{H}_2)^\dagger (D^\mu \mathcal{H}_2), \tag{2.31}$$

where

$$D^\mu = \partial^\mu \mathbb{1} + i\frac{e}{2s_W}\begin{pmatrix} W_3^\mu & W_+^\mu \\ W_-^\mu & -W_3^\mu \end{pmatrix} + i\frac{e}{2c_W} Y B^\mu \mathbb{1}, \tag{2.32}$$

$$W_\pm^\mu = \frac{1}{\sqrt{2}}(W_1^\mu \mp i W_2^\mu). \tag{2.33}$$

$$W_3^\mu = c_W Z^\mu + s_W A^\mu, \tag{2.34}$$

$$B^\mu = -s_W Z^\mu + c_W A^\mu, \tag{2.35}$$

and the hypercharge Y is -1 for the Higgs doublet $\mathcal{H}_1$ and 1 for the Higgs doublet $\mathcal{H}_2$ as in Table 2.1. (Note that in the Standard Model, often the sine of the weak mixing angle, s_W, by convention, has the opposite sign).

This leads to the expressions for the Z and W boson masses as used in [31],

$$M_Z^2 = \frac{e^2}{2}\left(\frac{1}{c_W^2} + \frac{1}{s_W^2}\right)(v_1^2 + v_2^2), \tag{2.36}$$

$$M_W^2 = \frac{1}{2}\frac{e^2}{s_W^2}(v_1^2 + v_2^2). \tag{2.37}$$

2.6 Gluino sector

In this section we follow the method and conventions given in [32]. The coefficient of the gluino mass term in the Lagrangian M_3, is, in general, complex with

$$M_3 = |M_3| e^{i\phi_{M_3}}. \tag{2.38}$$

However, the phase ϕ_{M_3} can be absorbed into the gluino fields, such that mass of the gluino becomes $m_{\tilde{g}} = |M_3|$ [33]. This has implications for the gluino couplings. We will particularly be interested in the quark-squark-gluino coupling, which is found from

$$\mathcal{L}_{q\tilde{q}\tilde{q}} = \bar{\tilde{g}}^a \left(-\sqrt{2} g_s T^a_{jk} (U_{\tilde{q}})_{n1} e^{-i\frac{\phi_{M_3}}{2}} \omega_- + \sqrt{2} g_s T^a_{jk} (U_{\tilde{q}})_{n2} e^{i\frac{\phi_{M_3}}{2}} \omega_+\right) q^k \tilde{q}_n^{j*} \tag{2.39}$$

$$+ \bar{q}^k \left(\sqrt{2} g_s T^a_{kj} (U^*_{\tilde{q}})_{n2} e^{-i\frac{\phi_{M_3}}{2}} \omega_- - \sqrt{2} g_s T^a_{kj} (U^*_{\tilde{q}})_{n1} e^{i\frac{\phi_{M_3}}{2}} \omega_+\right) \tilde{g}^a \tilde{q}_n^j, \tag{2.40}$$

where $n = 1, 2$ are sfermion indices, g_s is the strong coupling constant and T^a are generators of $SU(3)$.

2.7 Chargino and Neutralino sectors

We mention these sectors very briefly in order to fix the notation and we follow the conventions used in [31]. We will use the chargino mass matrix

$$\mathbf{M}_{\text{chargino}} = \begin{pmatrix} M_2 & \sqrt{2}\sin\beta\, M_W \\ \sqrt{2}\cos\beta\, M_W & \mu \end{pmatrix}, \tag{2.41}$$

which includes the soft SUSY-breaking term M_2, which can be complex in the CP-violating MSSM.

We will use the neutralino mass matrix

$$\mathbf{M}_{\text{neutralino}} = \begin{pmatrix} M_1 & 0 & -M_Z\, s_w \cos\beta & M_Z\, s_w \sin\beta \\ 0 & M_2 & M_Z\, c_w \cos\beta & M_Z\, c_w \sin\beta \\ -M_Z\, s_w \cos\beta & M_Z\, c_w \cos\beta & 0 & -\mu \\ M_Z\, s_w \sin\beta & M_Z\, c_w \sin\beta & -\mu & 0 \end{pmatrix}, \tag{2.42}$$

which includes the soft SUSY-breaking term M_1, which can be complex in the CP-violating MSSM.

2.8 Phenomenology and the CPX scenario

CP violation in the MSSM has a number of important phenomenological consequences. As we will see, CP phases in the loop corrections to the Higgs particles will have a large effect on their masses [31, 34, 35] and cause them to have a mixed CP state. This will also affect the coupling of the Higgs particles to fermions, Z bosons and W bosons [36]. One important consequence is a reduction in the coupling of the lightest neutral Higgs to two Z bosons, which makes this scenario more difficult to detect at LEP [37].

Throughout this thesis, we will frequently perform calculations in the CPX scenario, which, for our purposes, we define as

The CPX scenario

- $m_t = 172.6$ GeV

- $M_{\rm SUSY} = 500$ GeV$(= M_L = M_{\tilde{q}_R})$
- $\mu = 2000$ GeV
- $|M_3| = 1000$ GeV
- $M_2 = 200$ GeV
- $|A_{t,b}^{\rm on-shell}| = 900$ GeV
- $\phi_{A_{t,b}} = \phi_{M_3} = \frac{\pi}{2}$
- $M_{H^+} \leq 1000$ GeV

We also use the GUT relation $M_1 = \frac{5}{3}\frac{s_W^2}{c_W^2} M_2$, as described in [38].

Using this particular scenario as an example has some significant advantages. Firstly, the trilinear couplings and M_3 are entirely complex, thus inducing a large amount of CP violation. This scenario is therefore useful as a generic example of a CP-violating scenario.

The second advantage is that this scenario is phenomenologically extremely interesting. It was originally proposed by [39] (although their definition differs slightly from that described above) in order to provide a framework for discussing the significant effect that CP violation has on the interpretation of direct searches for Higgs bosons, such as those at LEP.

Although a Higgs boson was not discovered at LEP, it did produce significant restrictions on the allowed MSSM parameter space. The results from the four LEP collaborations - ALEPH, DELPHI L3 and OPAL - were combined and applied to a number of MSSM benchmark scenarios [24] by the LEP Higgs Working Group. In the CPX scenario, their results show an unexcluded region at 30 GeV $\lesssim M_{h_1} \lesssim$ 50 GeV and $3 \lesssim \tan\beta \lesssim 10$. We will be examining this unexcluded region in more detail in future chapters and therefore it is convenient to use the CPX scenario as an example in earlier chapters in order to get an idea of its characteristics.

It should be noted that our scenario differs from that used in [24] in two main ways. Firstly, we use the top mass as reported in [40], whereas the original analysis mainly used the then current value of 174.3 GeV. Secondly, we use an on-shell definition of the trilinear coupling A, which is the natural choice for a Feynman-diagrammatic calculation. The original analysis defined the trilinear coupling according to the $\overline{\rm DR}$ renormalisation scheme and used a value of $|A_{t,b}^{\overline{\rm DR}}| = 1000$ GeV. We will describe these schemes in

Chapter 3.3.1 and discuss a way to convert between the different parameter definitions in Chapter 3.4.

We note that there are constraints on the CP phases in the complex MSSM from experimental measured upper limits, such as those on the electron and neutron electric dipole moments (EDMs). These provide particularly significant constraints on the CP phases in the first two generations. However, these can be avoided if the masses of the first two generation of squarks are above the TeV scale or if cancellations are arranged between various EDM loop corrections. The EDM limits also constrain the third generation, although, once again, cancellation between different contributions can be arranged (see [37] and references therein for a more detailed discussion).

2.9 Summary

In its general form, the Minimal Supersymmetric Model allows some parameters to be complex. As we have discussed, this includes the trilinear couplings A_f, the Higgsino mass parameter μ, the gluino mass parameter M_3 and the soft SUSY breaking parameters M_1 and M_2 from the neutralino/chargino sector and we note that some phases can be rotated away and thus are not physical. All the tree level couplings of the MSSM are implemented in model files distributed with the program *FeynArts* [41–43], which we have used frequently when producing the results described in this thesis. However, we use a different definition for the quark-squark-gluino coupling, and thus alter the *FeynArts* model file accordingly. We have discussed some of the phenomenological implications of the CP violation and defined the CPX scenario, which we will use frequently in later chapters.

Chapter 3

Renormalisation of the MSSM

3.1 Scalar Integrals

The tensor integrals which appear in loop calculations can be decomposed into scalar integrals, as discussed fully in [44]. These scalar integrals contain pieces which are linearly, logarithmically and quadratically divergent. It is possible to analytically continue the integrals to $D = 4 - \epsilon$ dimensions in order to perform the integration ('dimensional regularisation'), and then afterwards regain expressions with the original divergence in the limit $D \to 4$. Thus we do the substitution

$$\int \frac{d^4q}{(2\pi)^4} \;\to\; \mu_{\rm ren}^{4-D} \int \frac{d^Dq}{(2\pi)^D} \tag{3.1}$$

in the scalar integrals, where $\mu_{\rm ren}$ is an arbitrary reference mass, which has been introduced to keep the couplings dimensionless.

In general, we will use the program *LoopTools* [45] to evaluate these scalar loop integrals. However, in order to calculate leading loop contributions, we will need scalar integrals in the limit of zero external momentum. These can all be decomposed into combinations of 1-point scalar integrals A_0, which are given by

$$\begin{aligned} A_0(m^2) &= \frac{(2\pi\mu_{\rm ren})^{4-D}}{i\pi^2} \int d^Dq \frac{1}{q^2 - m^2 + i\epsilon} \\ &= m^2 \left(\Delta - \log\left(\frac{m^2}{\mu_{\rm ren}^2}\right) + 1 \right) + \mathcal{O}(D-4), \qquad (3.2) \\ \Delta &= \frac{2}{4-D} - \gamma_E + \log(4\pi), \qquad (3.3) \end{aligned}$$

where Δ contains the divergence at $D = 4$ and $\gamma_E = 0.57721...$ is the Euler-Mascheroni constant. The solution to A_0 has been arrived at using the procedure outlined in detail in [46]. Note the dependence on the mass scale $\mu_{\rm ren}$.

3.2 Dimensional Regularisation and Dimensional Reduction

Dimensional regularisation involves extending the momenta and the Dirac algebra into $D = 4-\epsilon$ dimensions. This is valuable for the Standard Model as it respects Lorentz and gauge invariance. However, dimensional regularisation breaks supersymmetry. Therefore, we will use dimensional reduction, in which the momentum integrals are evaluated in $D = 4 - \epsilon$ dimensions but the Dirac algebra is performed in four dimensions (see [22] and references therein). This is the common choice for supersymmetric calculations.

3.3 Renormalisation

3.3.1 Introduction

The divergences in the loop integrals are cancelled during the procedure of renormalisation. We denote the parameters appearing in the Lagrangian as 'bare' parameters. These bare parameters are divergent and unphysical. We replace them with a finite physical 'renormalised' parameter plus a divergent 'counter-term', denoted by δp, where,

$$p_{\rm bare} = p_{\rm ren} + \delta p. \tag{3.4}$$

Similarly, the bare fields in the Lagrangian are also replaced with renormalised fields plus counter-terms, where,

$$\phi_{\rm bare} = \phi_{\rm ren}(1 + \delta Z_\phi) \tag{3.5}$$

The renormalised parameters and fields are fixed by the renormalisation scheme.

In the Minimal Subtraction Scheme (MS), dimensional regularisation is used and the counter-terms simply cancel out the divergences in the loop integrals, whilst leaving the

finite pieces alone. As we saw, the divergent pieces appear in the combination $\Delta = \frac{2}{4-D} - \gamma_E + \log(4\pi)$. The Modified Minimal Subtraction Scheme ($\overline{\text{MS}}$) uses dimensional regularisation and involves counter-terms which simply cancel each occurrence of Δ.

The Modified Dimensional Reduction scheme ($\overline{\text{DR}}$) is similar to the $\overline{\text{MS}}$ scheme in that the counter-terms cancel each term proportional to Δ. However, dimensional reduction is used instead of dimensional regularisation.

A fourth renormalisation scheme is known as the on-shell scheme. In this scheme, the renormalised masses correspond directly to physical masses (by 'physical' mass, we mean that obtained from the real part of the pole of the propagator). The electric charge equals that measured in the limit of low energy Compton scattering of on-shell particles. The on-shell scheme also requires that the residues of the propagator are 1, so that, close to its pole, each propagator has its tree level form except with the bare mass replaced by the renormalised quantity (see [47] and references therein). Therefore, in the on-shell scheme, renormalised parameters correspond directly to actual experimentally measurable quantities.

Unless explicitly stated, this section discusses renormalisation at 1-loop level only. As discussed previously, we frequently use the program *FeynArts* [41–43] to perform Feynman-diagrammatic calculations. This program includes a full list of counter-terms for couplings in the Standard Model. However, in the MSSM, it provides the couplings at tree level. Therefore, in this section, we derive all the counter-terms we will require and edit the *FeynArts* model files to include them.

3.3.2 Renormalisation of Gauge and Higgs boson sectors

Renormalisation transformations

For the W-boson and Z-boson masses, we use the renormalisation transformations

$$M_Z^2 \rightarrow M_Z^2 + \delta M_Z^2, \tag{3.6}$$

$$M_W^2 \rightarrow M_W^2 + \delta M_W^2, \tag{3.7}$$

which lead to (recalling that $c_W = M_W/M_Z$)

$$\frac{\delta s_W}{s_W} = \frac{c_W^2}{2 s_W}\left(\frac{\delta M_Z^2}{M_Z^2} - \frac{\delta M_W^2}{M_W^2}\right). \tag{3.8}$$

For the fields, we use the transformations

$$W^{\pm} \rightarrow (1+\frac{1}{2}\delta Z_{WW})W^{\pm}, \tag{3.9}$$

$$\begin{pmatrix} Z \\ \gamma \end{pmatrix} \rightarrow \begin{pmatrix} 1+\frac{1}{2}\delta Z_{ZZ} & \frac{1}{2}\delta Z_{Z\gamma} \\ \frac{1}{2}\delta Z_{\gamma Z} & 1+\frac{1}{2}\delta Z_{\gamma\gamma} \end{pmatrix} \cdot \begin{pmatrix} Z \\ \gamma \end{pmatrix}. \tag{3.10}$$

In the Higgs sector, we choose to use one renormalisation constant for each Higgs doublet, such that

$$\mathcal{H}_1 \rightarrow (1+\frac{1}{2}\delta Z_{\mathcal{H}_1})\mathcal{H}_1, \tag{3.11}$$

$$\mathcal{H}_2 \rightarrow (1+\frac{1}{2}\delta Z_{\mathcal{H}_2})\mathcal{H}_2. \tag{3.12}$$

This leads to the renormalisation transformation for $\tan\beta$,

$$\tan\beta \rightarrow \tan\beta\,(1+\delta\tan\beta) = \tan\beta\,(1+\frac{1}{2}(\mathcal{H}_2-\mathcal{H}_1)). \tag{3.13}$$

Note that, at this point in the calculation, we still distinguish between $\beta = \arctan(v_2/v_1)$ and the angle of rotation β_n (and also the angle of rotation in the charged Higgs sector). The renormalisation only applies to β.

It will later be convenient to introduce a renormalisation condition for the Higgs tadpoles T_h, T_H and T_A, so we make the transformation

$$T_{h_i} \rightarrow T_{h_i} + \delta T_{h_i}. \tag{3.14}$$

We define a set of counter-terms $\delta Z_{h_ih_j}$, δZ_{h_iG}, δZ_{GG} by

$$\begin{pmatrix} h \\ H \\ A \\ G \end{pmatrix} \rightarrow \begin{pmatrix} 1+\frac{1}{2}\delta Z_{hh} & \frac{1}{2}\delta Z_{hH} & \frac{1}{2}\delta Z_{hA} & \frac{1}{2}\delta Z_{hG} \\ \frac{1}{2}\delta Z_{hH} & 1+\frac{1}{2}\delta Z_{HH} & \frac{1}{2}\delta Z_{HA} & \frac{1}{2}\delta Z_{HG} \\ \frac{1}{2}\delta Z_{hA} & \frac{1}{2}\delta Z_{HA} & 1+\frac{1}{2}\delta Z_{AA} & \frac{1}{2}\delta Z_{AG} \\ \frac{1}{2}\delta Z_{hG} & \frac{1}{2}\delta Z_{HG} & \frac{1}{2}\delta Z_{AG} & 1+\frac{1}{2}\delta Z_{GG} \end{pmatrix} \cdot \begin{pmatrix} h \\ H \\ A \\ G \end{pmatrix}, \tag{3.15}$$

which leads to expressions for $\delta Z_{h_ih_j}$, δZ_{h_iG}, δZ_{GG} in terms of $\delta Z_{\mathcal{H}_1}, \delta Z_{\mathcal{H}_2}$. The explicit expressions are given in [31]. In particular, note that $Z_{hA} = Z_{HA} = Z_{hG} = Z_{HG} = 0$, due to the fact that the Higgs sector is CP-conserving at tree level. Making the above

substitutions in the Lagrangian and defining a set of neutral and charged mass counter-terms

$$\begin{aligned} \mathbf{M}_{h,H,A,G} &\rightarrow \mathbf{M}_{h,H,A,G} + \delta\mathbf{M}_{h,H,A,G}, \\ \text{where} \qquad \delta\mathbf{M}_{h,H,A,G} &= \begin{pmatrix} \delta m_{hh} & \delta m_{hH} & \delta m_{hA} & \delta m_{hG} \\ \delta m_{hH} & \delta m_{HH} & \delta m_{HA} & \delta m_{HG} \\ \delta m_{hA} & \delta m_{HA} & \delta m_{AA} & \delta m_{AG} \\ \delta m_{hG} & \delta m_{HG} & \delta m_{AG} & \delta m_{GG} \end{pmatrix} \end{aligned} \tag{3.16}$$

and

$$\mathbf{M}_{H^\pm,G^\pm} \rightarrow \mathbf{M}_{H^\pm,G^\pm} + \delta\mathbf{M}_{H^\pm,G^\pm}, \quad \text{where} \quad \mathbf{M}_{H^\pm,G^\pm} = \begin{pmatrix} \delta m_{H^-H^-} & \delta m_{H^-G^+} \\ \delta m_{G^-H^+} & \delta m_{G^-G^+} \end{pmatrix} \tag{3.17}$$

leads to the mass counter-terms given in Table 3.1. The counter-terms $\delta m_{h_ih_j}$, δm_{h_iG}, δm_{GG}, $\delta m_{H^-G^-}$, $\delta m_{G^-H^-}$, $\delta m_{G^-G^+}$ are also given by [31].

Renormalised Self Energies

We use the relations

$$\Sigma^{\mu\nu}_{VV'}(\mathbf{p}) = \Sigma^T(p^2)\left(-g^{\mu\nu} + \frac{p^\mu p^\nu}{p^2}\right) - \frac{p^\mu p^\nu}{p^2}\Sigma^L(p^2), \tag{3.18}$$

$$\Sigma^{\mu}_{SV}(\mathbf{p}) = p^\mu \Sigma_{SV}(p^2) \tag{3.19}$$

to express the gauge boson self-energies in terms of the transverse and longitudinal components (where $\mathbf{p}$ is the momentum of the incoming scalar or vector particle) and to isolate the p^μ dependence in the Higgs to gauge boson mixing self-energies. The

renormalised self-energies are given by

$$\hat{\Sigma}_{h_ih_j}(p^2) = \Sigma_{h_ih_j}(p^2) + \delta Z_{h_ih_j}(p^2 - \tfrac{1}{2}(m^2_{h_i} + m^2_{h_j})) - \delta m^2_{h_ih_j}, \tag{3.20a}$$

$$\hat{\Sigma}_{h_iG}(p^2) = \Sigma_{h_iG}(p^2) + \delta Z_{h_iG}(p^2 - \frac{1}{2}m^2_{h_i}) - \delta m^2_{h_iG}, \tag{3.20b}$$

$$\hat{\Sigma}_{h_iZ}(p^2) = \Sigma_{h_iZ}(p^2) - \delta m^2_{h_iZ}, \tag{3.20c}$$

$$\hat{\Sigma}_{GG}(p^2) = \Sigma_{GG}(p^2) + \delta Z_{GG}p^2 - \delta m^2_{GG}, \tag{3.20d}$$

$$\hat{\Sigma}_{GZ}(p^2) = \Sigma_{GZ}(p^2) - \delta m^2_{GZ}, \tag{3.20e}$$

$$\hat{\Sigma}_{H^-H^+}(p^2) = \Sigma_{H^-H^+}(p^2) + \delta Z_{H^-H^+}(p^2 - m^2_{H^\pm}) - \delta m^2_{H^\pm}, \tag{3.20f}$$

$$\hat{\Sigma}_{H^-G^+}(p^2) = \Sigma_{H^-G^+}(p^2) + \delta Z_{H^-G^+}(p^2 - \tfrac{1}{2}m^2_{H^\pm}) - \delta m^2_{H^-G^+}, \tag{3.20g}$$

$$\hat{\Sigma}_{H^-W^+}(p^2) = \Sigma_{H^-W^+}(p^2) - \delta m^2_{H^-W^+}, \tag{3.20h}$$

$$\hat{\Sigma}_{G^-H^+}(p^2) = \hat{\Sigma}^*_{H^-G^+}(p^2), \tag{3.20i}$$

$$\hat{\Sigma}_{G^-G^+}(p^2) = \Sigma_{G^-G^+}(p^2) + \delta Z_{G^-G^+}p^2 - \delta m^2_{G^\pm}, \tag{3.20j}$$

$$\hat{\Sigma}_{G^-W^+}(p^2) = \Sigma_{G^-W^+}(p^2) - \delta m^2_{G^-W^+}, \tag{3.20k}$$

$$\hat{\Sigma}_{\gamma h_i}(p^2) = 0, \tag{3.20l}$$

$$\hat{\Sigma}_{\gamma G}(p^2) = \Sigma_{\gamma G}(p^2) - \delta m^2_{\gamma G}, \tag{3.20m}$$

$$\hat{\Sigma}^T_{\gamma Z}(p^2) = \Sigma^T_{\gamma Z}(p^2) + p^2\frac{\delta Z_{\gamma Z}}{2} + (p^2 - M_Z^2)\frac{\delta Z_{Z\gamma}}{2}, \tag{3.20n}$$

$$\hat{\Sigma}^L_{\gamma Z}(p^2) = \Sigma^L_{\gamma Z}(p^2) - \frac{M_Z^2\delta Z_{Z\gamma}}{2}, \tag{3.20o}$$

$$\hat{\Sigma}^T_{ZZ}(p^2) = \Sigma^T_{ZZ}(p^2) + (p^2 - M_Z^2)\delta Z_{ZZ} - \delta M_Z^2, \tag{3.20p}$$

$$\hat{\Sigma}^L_{ZZ}(p^2) = \Sigma^L_{ZZ}(p^2) - M_Z^2\delta Z_{ZZ} - \delta M_Z^2, \tag{3.20q}$$

$$\hat{\Sigma}^T_{W^-W^+}(p^2) = \Sigma^T_{W^-W^+}(p^2) + (p^2 - M_W^2)\delta Z_{WW} - \delta M_W^2, \tag{3.20r}$$

$$\hat{\Sigma}^L_{W^-W^+}(p^2) = \Sigma^L_{W^-W^+}(p^2) - M_W^2\delta Z_{WW} - \delta M_W^2. \tag{3.20s}$$

Renormalisation Conditions

We now fix the counter-terms by setting the renormalisation conditions. We renormalise the Z-boson, W-boson and charged Higgs masses on-shell. We would like the renormalised mass parameters to be equivalent to the physical masses, which is equivalent to setting the renormalised mass parameter squared to be the pole of the propagator. Thus, the Z-boson, W-boson and charged Higgs renormalised transverse self-energies in

equation (3.20) must vanish at $q^2 = m^2_{\text{ren}}$, leading to the mass counter-terms

$$\delta M_Z^2 = \widetilde{\text{Re}}\Sigma^T_{ZZ}(M_Z^2). \tag{3.21}$$

$$\delta M_W^2 = \widetilde{\text{Re}}\Sigma^T_{WW}(M_W^2). \tag{3.22}$$

$$\delta M_{H^\pm}^2 = \widetilde{\text{Re}}\Sigma_{H^\pm}(M_{H^\pm}^2). \tag{3.23}$$

where the prefix $\widetilde{\text{Re}}$ means that the imaginary parts of the loop integrals are discarded.

We fix the tadpole counter-term by requiring that the renormalised tadpoles vanish, such that

$$\delta T_{h_i} = -T_{h_i}, \tag{3.24}$$

This is convenient as it means that diagrams involving renormalised tadpoles will not need to be considered in calculations.

We renormalise the gauge boson fields on-shell, such that the renormalised self-energy and renormalised self-energy differentiated with respect to p^2 (which we denote Σ') vanish. This leads to the conditions

$$\delta Z_{VV} = -\widetilde{\text{Re}}\Sigma'_{VV}, \tag{3.25}$$

$$\delta Z_{\gamma Z} = -2\frac{\widetilde{\text{Re}}\Sigma^T_{\gamma Z}(M_Z^2)}{M_Z^2}, \tag{3.26}$$

$$\delta Z_{Z\gamma} = 2\frac{\Sigma^T_{\gamma Z}(0)}{M_Z^2}. \tag{3.27}$$

However, for the renormalisation of the Higgs fields, we choose to follow [31] and use the $\overline{\text{DR}}$ scheme, such that

$$\delta Z_{\mathcal{H}_1} = -\left[\widetilde{\text{Re}}\Sigma'_{\phi_1\phi_1}\right]^{\text{div}}, \tag{3.28}$$

$$\delta Z_{\mathcal{H}_2} = -\left[\widetilde{\text{Re}}\Sigma'_{\phi_2\phi_2}\right]^{\text{div}}, \tag{3.29}$$

where 'div' indicates that we have just kept the terms proportional to Δ, as defined in equation (3.3). This choice has been shown to yield numerically stable results in [48–50]. We also need to fix the renormalisation scale for $\delta Z_{\mathcal{H}_1}, \delta Z_{\mathcal{H}_2}$, which we choose to be $\mu_{\text{ren}} = m_t$, as in [31].

XY	δm^2_{XY}
AA	$\delta m^2_{H^\pm} - \delta M^2_W$
hh	$\delta m^2_{H^\pm} c^2_{\alpha-\beta} - \delta M^2_W c^2_{\alpha-\beta} + \delta M^2_Z s^2_{\alpha+\beta}$
	$+\delta\tan\beta\, s_\beta c_\beta (m^2_A 2 s_{\alpha-\beta} c_{\alpha-\beta} + 2M^2_Z s_{\alpha+\beta} c_{\alpha+\beta})$
	$+\frac{e}{2M_Z s_w c_w}(\delta T_H c_{\alpha-\beta} s^2_{\alpha-\beta} + \delta T_h s_{\alpha-\beta}(1 + c^2_{\alpha-\beta}))$
hH	$\delta m^2_{H^\pm} s_{\alpha-\beta} c_{\alpha-\beta} - \delta M^2_W s_{\alpha-\beta} c_{\alpha-\beta} - \delta M^2_Z s_{\alpha+\beta} c_{\alpha+\beta}$
	$+\frac{e}{2M_Z s_w c_w}(\delta T_H s^3_{\alpha-\beta} - \delta T_h c^3_{\alpha-\beta})$
	$-\delta\tan\beta\, s_\beta c_\beta (m^2_A (c^2_{\alpha-\beta} - s^2_{\alpha-\beta}) + M^2_Z (c^2_{\alpha+\beta} - s^2_{\alpha+\beta}))$
HH	$\delta m^2_{H^\pm} s^2_{\alpha-\beta} - \delta M^2_W s^2_{\alpha-\beta} + \delta M^2_Z c^2_{\alpha+\beta}$
	$-\delta\tan\beta\, s_\beta c_\beta (m^2_A 2 s_{\alpha-\beta} c_{\alpha-\beta} + 2M^2_Z s_{\alpha+\beta} c_{\alpha+\beta})$
	$-\frac{e}{2M_Z s_w c_w}(\delta T_H c_{\alpha-\beta}(1 + s^2_{\alpha-\beta}) + \delta T_h s_{\alpha-\beta} c^2_{\alpha-\beta})$
hA	$+\frac{e}{2M_Z s_w c_w}\delta T_A s_{\alpha-\beta}$
HA	$-\frac{e}{2M_Z s_w c_w}\delta T_A c_{\alpha-\beta}$
hG	$-\delta m^2_{HA}$
HG	$+\delta m^2_{hA}$
AG	$\frac{e}{2M_Z s_w c_w}(-\delta T_H s_{\alpha-\beta} - \delta T_h c_{\alpha-\beta}) - m^2_A s_\beta c_\beta \delta\tan\beta$
hZ	0
HZ	0
AZ	$-2iM_Z c_\beta s_\beta \delta\tan\beta$
GG	$\frac{e}{2M_Z s_w c_w}(-\delta T_H c_{\alpha-\beta} + \delta T_h s_{\alpha-\beta})$
GZ	$-\frac{iM_Z}{2}\left(\frac{\delta M^2_Z}{M^2_Z} + \delta Z_{ZZ} + \delta Z_{GG}\right)$
H^-G^+	$\frac{e}{2M_Z s_w c_w}(-\delta T_H s_{\alpha-\beta} - \delta T_h c_{\alpha-\beta} - i\delta t_A) - \delta m^2_{H^\pm} s_\beta c_\beta \delta\tan\beta$
H^-W^+	$-2M_W s_\beta c_\beta \delta\tan\beta$
G^-H^+	$\left(\delta m^2_{H^-G^+}\right)^*$
G^-G^+	$\frac{e}{2M_Z s_w c_w}(-\delta T_H c_{\alpha-\beta} + \delta T_h s_{\alpha-\beta})$
G^-W^+	$-\frac{M_W}{2}\left(\frac{\delta M^2_W}{M^2_W} + \delta Z_{WW} + \delta Z_{G^-G^+}\right)$
γG	$\frac{iM_Z \delta Z_{Z\gamma}}{2}$

Table 3.1: Mass counter-terms for Higgs bosons and mixing between Higgs bosons and gauge bosons in the complex MSSM

3.3.3 Charge Renormalisation

Charge Renormalisation in the full MSSM

We obtain a renormalisation condition for the electric charge by requiring the electric charge to be equal to the full $ee\gamma$ vertex for on-shell external particles in the Thompson limit (i.e. vanishing photon momentum). using the transformation

$$e^{\text{bare}} \to e(0)\left(1+\delta Z_e^{(0)}\right). \tag{3.30}$$

The renormalisation constant is adjusted such that the loop corrections to the $ee\gamma$ vertex vanish in this limit. By considering the component free from γ_5 and proportional to γ_5 separately and using a Ward identity to relate the renormalised vertex with the electron and $Z\gamma$ wave function renormalisation constants (as described in [51]), we arrive at the condition

$$\delta Z_e^{(0)} = -\frac{1}{2}\delta Z_{\gamma\gamma} + \frac{s_W}{2c_W}\delta Z_{Z\gamma} \tag{3.31}$$

$$= \frac{1}{2}\frac{\partial}{\partial q^2}\Sigma_{\gamma\gamma}(q^2)\big|_{q^2=0} + \frac{s_w}{c_w}\frac{\Sigma^{\mathrm{T}}_{\gamma Z}(0)}{M_Z^2}, \tag{3.32}$$

where we have used the expressions for the gauge boson field renormalisation constant from equation (3.27). We can thus identify the renormalised charge with the physical charge $e(0) = \sqrt{4\pi\alpha(0)}$ where $\alpha(0)$ is the fine structure constant. as defined in the Thompson limit.

However, calculating $\delta Z_{\gamma\gamma}$ directly poses problems because it involves large contributions proportional to $\alpha \log\left(\frac{m^2_{\text{light } f}}{s}\right)$, arising from the running of α from $q^2 = 0$ to a higher energy scale. which is a problem because the masses of the light quarks are not well defined.

Instead, we can use the relation

$$\frac{\partial}{\partial q^2}\Sigma_{\gamma\gamma}^{\text{light } f\text{in loops}}(q^2)\big|_{q^2=0} = \Delta\alpha + \frac{1}{M_Z^2}\mathrm{Re}\Sigma_{\gamma\gamma}^{\text{light } f\text{in loops}}(M_Z^2), \tag{3.33}$$

where $\Delta\alpha$ is a finite quantity. It can be split in to the contribution from the e, μ, τ leptons and the contribution from the light quarks (i.e. all quarks except t), $\Delta\alpha = \Delta\alpha_{\text{lept}} + \Delta\alpha^{(5)}_{\text{had}}$.

$\Delta\alpha_{\rm lept}$ has been calculated to 3-loop order [52] as

$$\Delta\alpha_{\rm lept} = 0.031497687. \tag{3.34}$$

while $\Delta\alpha^{(5)}_{\rm had}$ has been measured experimentally via a dispersion relation [53] as

$$\Delta\alpha^{(5)}_{\rm had} = 0.02755 \pm 0.0023. \tag{3.35}$$

Therefore, the charge counter-term can be calculated using

$$\begin{aligned}\delta Z_e^{(0)} &= \frac{1}{2}\frac{\partial}{\partial q^2}\,\Sigma_{\gamma\gamma}^{\text{nolight } f\text{ in loops}}(q^2)\Big|_{q^2=0} \\ &+ \frac{1}{2}\Delta\alpha + \frac{1}{2M_Z^2}\mathrm{Re}\Sigma_{\gamma\gamma}^{\text{light } f\text{ in loops}}(M_Z^2) + \frac{s_{\rm w}}{c_{\rm w}}\frac{\Sigma_{\gamma Z}^{\rm T}(0)}{M_Z^2},\end{aligned} \tag{3.36}$$

where every self-energy involved in this expression has been calculated individually before being combined in this equation.

Alternatively, we could have calculated $\delta Z_{\gamma\gamma} = \frac{\partial}{\partial q^2}\,\Sigma_{\gamma\gamma}(q^2)|_{q^2=0}$ directly, but using 'effective' values for the light quark masses which have been specially adjusted to ensure that the explicitly calculated value of $\frac{\partial}{\partial q^2}\,\Sigma_{\gamma\gamma}^{\text{light } f\text{ in loops}}(q^2)\big|_{q^2=0} - \frac{1}{M_Z^2}\mathrm{Re}\Sigma_{\gamma\gamma}^{\text{light } f\text{ in loops}}(M_Z^2)$ is similar to the current experimental value of $\Delta\alpha$. The disadvantage of this choice is that whenever the value for $\Delta\alpha$ or m_b changes, the values used for the other light fermion masses would need to be adjusted accordingly.

A third way to perform the calculation is to use

$$\begin{aligned}\delta Z_e^{(0)} &= \frac{1}{2}\frac{\partial}{\partial q^2}\,\Sigma_{\gamma\gamma}^{\text{all loops}}(q^2)\Big|_{q^2=0} - \frac{1}{2}\frac{\partial}{\partial q^2}\,\Sigma_{\gamma\gamma}^{\text{light } f\text{ in loops}}(q^2)\Big|_{q^2=0} \\ &+ \frac{1}{2}\Delta\alpha + \frac{1}{2M_Z^2}\mathrm{Re}\Sigma_{\gamma\gamma}^{\text{light } f\text{ in loops}}(M_Z^2) + \frac{s_{\rm w}}{c_{\rm w}}\frac{\Sigma_{\gamma Z}^{\rm T}(0)}{M_Z^2},\end{aligned} \tag{3.37}$$

where, again, every self-energy involved in this expression has been calculated individually before being inserted in to this equation. This should give exactly the same result as equation (3.36), as we have only included some extra diagrams to the first term, which we then cancel by including the second term. However, equation (3.37) is easier to implement, since $\frac{\partial}{\partial q^2}\,\Sigma_{\gamma\gamma}^{\text{light } f\text{ in loops}}(q^2)\Big|_{q^2=0} + \frac{1}{M_Z^2}\mathrm{Re}\Sigma_{\gamma\gamma}^{\text{light } f\text{ in loops}}(M_Z^2)$ is given by a fairly compact expression. We edit one of the model files provided with the program *FeynArts* [41–43] to include this correction.

The above discussion refers to results which are parametrised in terms of $\alpha(0)$ (i.e. we use equation (3.30), which means that the coupling used in tree level vertices is $\alpha(0)$). However, in our calculations, we choose to parametrise the result in terms of $\alpha(M_Z^2)$ where $\alpha(M_Z^2) = \alpha(0)/(1-\Delta\alpha)$. Thus we are absorbing the $\Delta\alpha$ correction into the coupling used in tree level vertices and the renormalisation becomes

$$\begin{aligned} e^{\text{bare}} \to e(0)\left(1+\delta Z_e^{(0)}\right) &= e(0)(1+\frac{1}{2}\Delta\alpha - \frac{1}{2}\Delta\alpha)\left(1+\delta Z_e^{(0)}\right) \\ &= e(M_Z^2)\left(1+\delta Z_e^{e(M_Z^2)}\right) + \text{h.o.t.}, \end{aligned} \tag{3.38}$$

where 'h.o.t.' denotes 'higher order terms', and the charge counter-term becomes

$$\delta Z_e^{e(M_Z^2)} = \delta Z_e^{(0)} - \frac{\Delta\alpha}{2} \tag{3.39}$$

$$\begin{aligned} &= \frac{1}{2}\frac{\partial}{\partial q^2}\Sigma_{\gamma\gamma}^{\text{all loops}}(q^2)\big|_{q^2=0} - \frac{1}{2}\frac{\partial}{\partial q^2}\Sigma_{\gamma\gamma}^{\text{light } f \text{ in loops}}(q^2)\big|_{q^2=0} \\ &+ \frac{1}{2M_Z^2}\text{Re}\Sigma_{\gamma\gamma}^{\text{light } f \text{ in loops}}(M_Z^2) + \frac{s_w}{c_w}\frac{\Sigma_{\gamma Z}^{\text{T}}(0)}{M_Z^2}, \end{aligned} \tag{3.40}$$

where, again, every self-energy written here is calculated explicitly before being combined to give an expression for the charge counter-term.

Charge Renormalisation for diagrams involving Standard Model fermions and their superpartners only

For calculations which only involve Standard Model fermions and their superpartners in loops, we choose to parametrise the electric charge in terms of the Fermi constant G_F (as used, for example, in [54]). The Fermi constant is defined as being proportional to the coupling constant in the muon decay $\mu \to \nu_\mu + e^- + \bar{\nu}_e$, where the process is modelled as just having one vertex $(\mu\nu_\mu e^-\bar{\nu}_e)$, such that, at lowest order,

$$G_F = \frac{e^2(0)}{4\sqrt{2}M_W^2 s_W^2}. \tag{3.41}$$

Higher orders are incorporated through the correction Δr such that

$$G_F = \frac{\alpha(0)\pi}{\sqrt{2}M_W^2 s_W^2}(1+\Delta r). \tag{3.42}$$

For calculations involving SM fermions and their superpartners only, vertex and box corrections do not contribute and the loop corrections are due to the W-boson self-energy on the internal W-boson propagator. Including counter-terms leads to

$$\begin{aligned} G_F &= \frac{\alpha(0)\pi}{\sqrt{2}M_{\mathrm{W}}^2 s_{\mathrm{W}}^2}\left(1+\Delta r^{f\tilde{f}}\right) \\ &= \frac{\alpha(0)\pi}{\sqrt{2}M_{\mathrm{W}}^2 s_{\mathrm{W}}^2}\left(1+2\frac{\delta e}{e}-\frac{\delta s_{\mathrm{W}}^2}{s_{\mathrm{W}}^2}-\frac{\delta M_{\mathrm{W}}^2}{M_{\mathrm{W}}^2}+\frac{\Sigma_{\mathrm{W}\mathrm{W}}^{\mathrm{T}}(0)}{M_{\mathrm{W}}^2}\right). \end{aligned} \tag{3.43}$$

We parametrise our result, in this case, in terms of α_{G_F}, which we define as $\alpha_{G_F} = \frac{1}{\pi}\sqrt{2}G_F M_{\mathrm{W}}^2 s_{\mathrm{W}}^2$ and use the experimental result of G_F as the input.

α_{G_F} is related to $\alpha(0)$ through

$$\alpha_{G_F} = \alpha(0)(1+\Delta r^{f\tilde{f}}). \tag{3.44}$$

Inserting this into the charge renormalisation transformation gives

$$e^{\mathrm{bare}} \rightarrow e(0)(1+\delta Z_e^0) = e(0)(1+\frac{1}{2}\Delta r^{f\tilde{f}}-\frac{1}{2}\Delta r^{f\tilde{f}})(1+\delta Z_e^0) = e_{G_F}(1+\delta Z_e^{G_F}), \tag{3.45}$$

yielding the charge renormalisation counter-term

$$\begin{aligned} \delta Z_e^{G_F} &= \delta Z_e^{(0)} - \frac{1}{2}\Delta r^{f\tilde{f}} \\ &= \frac{\delta s_W}{s_W} - \frac{1}{2M_W^2}\left(\Sigma_{WW}^{\mathrm{T}}(0) - \delta M_W^2\right), \end{aligned} \tag{3.46}$$

where δs_W is given by equation (3.8).

3.3.4 Renormalisation of the quark sector

In this section, we extend the process of applying renormalisation in the Standard Model to the case of the complex MSSM, although we neglect quark mixing. We will closely follow the notation of [47], in which the quark 2-point function and self-energy are described as

$$\Gamma(p) = \not{p}\omega_-\Gamma^L(p^2) + \not{p}\omega_+\Gamma^R(p^2) + \omega_-\Gamma^l(p^2) + \omega_+\Gamma^r(p^2), \tag{3.47}$$

$$\Sigma(p) = \not{p}\omega_-\Sigma^L(p^2) + \not{p}\omega_+\Sigma^R(p^2) + \omega_-\Sigma^l(p^2) + \omega_+\Sigma^r(p^2), \tag{3.48}$$

with $\Gamma(p)^{\rm tree} = i(\not{p} - m)$.

Inserting the renormalisation transformations

$$q_L \rightarrow (1 + \frac{1}{2}\delta Z^L) q_L. \tag{3.49}$$

$$q_R \rightarrow (1 + \frac{1}{2}\delta Z^R) q_R. \tag{3.50}$$

$$m \rightarrow m + \delta m \tag{3.51}$$

into the quark sector of the Lagrangian leads to

$$-i\Gamma^L(p^2) = 1 + \Sigma^L(p^2) + \frac{1}{2}\left(\delta Z^L + \delta Z^{L*}\right), \tag{3.52}$$

$$-i\Gamma^R(p^2) = 1 + \Sigma^R(p^2) + \frac{1}{2}\left(\delta Z^R + \delta Z^{R*}\right), \tag{3.53}$$

$$-i\Gamma^l(p^2) = -m + \Sigma^l(p^2) - \frac{m}{2}\left(\delta Z^L + \delta Z^{R*}\right) - \delta m. \tag{3.54}$$

$$-i\Gamma^r(p^2) = -m + \Sigma^r(p^2) - \frac{m}{2}\left(\delta Z^R + \delta Z^{L*}\right) - \delta m. \tag{3.55}$$

We note that the hermiticity of the Lagrangian implies (neglecting absorptive parts, which are not involved in the renormalisation) that

$$\Sigma^L(p^2) = \Sigma^L(p^2)^*, \tag{3.56}$$

$$\Sigma^R(p^2) = \Sigma^R(p^2)^*, \tag{3.57}$$

$$\Sigma^l(p^2) = \Sigma^r(p^2)^*. \tag{3.58}$$

We renormalise the quarks on-shell. The renormalisation conditions for quarks are therefore

$$\widetilde{\rm Re}\,\Gamma(p)u(p)|_{p^2=m^2} = 0, \tag{3.59}$$

$$\lim_{p^2\rightarrow m^2} \frac{\not{p} + m}{p^2 - m^2} \widetilde{\rm Re}\Gamma(p)u(p) = iu(p). \tag{3.60}$$

Inserting the 2-point function into these equations leads to

$$\begin{aligned}
\delta m &= \frac{1}{2}\widetilde{\mathrm{Re}}\left[m\left(\Sigma^L(m^2)+\Sigma^R(m^2)\right)+\Sigma^l(m^2)+\Sigma^r(m^2)\right], \\
\mathrm{Re}\,\delta Z^L &= \widetilde{\mathrm{Re}}\left[-\Sigma^L(m^2)-m^2\left(\Sigma^{L'}(m^2)+\Sigma^{R'}(m^2)\right)-m\left(\Sigma^{l'}(m^2)+\Sigma^{r'}(m^2)\right)\right], \\
\mathrm{Re}\,\delta Z^R &= \widetilde{\mathrm{Re}}\left[-\Sigma^R(m^2)-m^2\left(\Sigma^{L'}(m^2)+\Sigma^{R'}(m^2)\right)-m\left(\Sigma^{l'}(m^2)+\Sigma^{r'}(m^2)\right)\right].
\end{aligned} \tag{3.61}$$

in direct analogy to the Standard Model. However, whereas in the Standard Model, δZ^L and δZ^R are both real, in the complex MSSM, we make use of the fourth condition,

$$m\left(\mathrm{Im}\delta Z^L - \mathrm{Im}\delta Z^R\right) = 2\mathrm{Im}\Sigma^l(p^2), \tag{3.62}$$

and choose $\mathrm{Im}\delta Z^L = -\mathrm{Im}\delta Z^R$, since it leads to a particularly compact form of the counter-terms. Therefore our quark field renormalisation constants are given by

$$\begin{aligned}
\delta Z^L &= \widetilde{\mathrm{Re}}\left[-\Sigma^L(m^2)+\frac{1}{2m}\left(\Sigma^l(m^2)-\Sigma^r(m^2)\right)\right. \\
&\quad \left.-m^2\left(\Sigma^{L'}(m^2)+\Sigma^{R'}(m^2)\right)-m\left(\Sigma^{l'}(m^2)+\Sigma^{r'}(m^2)\right)\right], \qquad (3.63) \\
\delta Z^R &= \widetilde{\mathrm{Re}}\left[-\Sigma^R(m^2)+\frac{1}{2m}\left(\Sigma^r(m^2)-\Sigma^l(m^2)\right)\right. \\
&\quad \left.-m^2\left(\Sigma^{L'}(m^2)+\Sigma^{R'}(m^2)\right)-m\left(\Sigma^{l'}(m^2)+\Sigma^{r'}(m^2)\right)\right]. \qquad (3.64)
\end{aligned}$$

3.3.5 Renormalisation of the stop sector

Although we will not perform any calculations which explicitly require the renormalisation of the stop sector, we will use the 2-loop corrections to the Higgs self-energies [55], which have been incorporated into the program *FeynHiggs* [31, 56–58]. Therefore, it is useful to know the renormalisation conditions which were used in this calculation.

The stop masses were put on-shell, such that

$$\left(\mathbf{U}_{\tilde{\mathbf{t}}}\delta\mathbf{M}_{\tilde{\mathbf{t}}}\mathbf{U}_{\tilde{\mathbf{t}}}^{\dagger}\right)_{\mathbf{11}} = \delta m^2_{\tilde{t}_1} = \widetilde{\mathrm{Re}}\Sigma_{\tilde{t}_{11}}(m^2_{\tilde{t}_1}), \tag{3.65}$$

$$\left(\mathbf{U}_{\tilde{\mathbf{t}}}\delta\mathbf{M}_{\tilde{\mathbf{t}}}\mathbf{U}_{\tilde{\mathbf{t}}}^{\dagger}\right)_{\mathbf{22}} = \delta m^2_{\tilde{t}_2} = \widetilde{\mathrm{Re}}\Sigma_{\tilde{t}_{22}}(m^2_{\tilde{t}_2}), \tag{3.66}$$

and additional constraints were imposed on the diagonal elements of the stop mass matrix, such that

$$\left(\mathbf{U}_{\tilde{\mathbf{t}}}\delta\mathbf{M}_{\tilde{\mathbf{t}}}\mathbf{U}_{\tilde{\mathbf{t}}}^{\dagger}\right)_{\mathbf{12}} = \delta Y_{\tilde{t}} = \frac{1}{2}\left(\widetilde{\mathrm{Re}}\Sigma_{\tilde{t}_{12}}(m^2_{\tilde{t}_1}) + \widetilde{\mathrm{Re}}\Sigma_{\tilde{t}_{12}}(m^2_{\tilde{t}_2})\right). \tag{3.67}$$

$$\left(\mathbf{U}_{\tilde{\mathbf{t}}}\delta\mathbf{M}_{\tilde{\mathbf{t}}}\mathbf{U}_{\tilde{\mathbf{t}}}^{\dagger}\right)_{\mathbf{21}} = \delta Y_{\tilde{t}}^{*} = \frac{1}{2}\left(\widetilde{\mathrm{Re}}\Sigma_{\tilde{t}_{21}}(m^2_{\tilde{t}_1}) + \widetilde{\mathrm{Re}}\Sigma_{\tilde{t}_{21}}(m^2_{\tilde{t}_2})\right). \tag{3.68}$$

The soft SUSY breaking terms M_L, $M_{\tilde{q}_R}$, the absolute value and phase of the trilinear coupling A_t were chosen as the input parameters. Therefore the counter-terms used were

$$\delta M_L^2 = -2m_t\delta m_t + U_{11}^{*}U_{11}\delta m^2_{\tilde{t}_1} + U_{21}^{*}U_{21}\delta m^2_{\tilde{t}_2} + U_{11}^{*}U_{21}\delta Y_{\tilde{t}} + U_{21}^{*}U_{11}\delta Y_{\tilde{t}}^{*}, \tag{3.69}$$

$$\delta M_{\tilde{q}_R}^2 = -2m_t\delta m_t + U_{12}^{*}U_{12}\delta m^2_{\tilde{t}_1} + U_{22}^{*}U_{22}\delta m^2_{\tilde{t}_2} + U_{12}^{*}U_{22}\delta Y_{\tilde{t}} + U_{22}^{*}U_{12}\delta Y_{\tilde{t}}^{*} \tag{3.70}$$

and

$$\delta A_t^{*} = e^{-i\phi_{A_t}}\left(\delta|A_t| - i|A_t|\,\delta\phi_{A_t}\right), \tag{3.71}$$

$$\delta|A_t| = \frac{1}{m_t}\mathrm{Re}\left[e^{i\phi_{A_t}}\delta K_t\right], \tag{3.72}$$

$$\delta\varphi_{A_t} = -\frac{1}{m_t|A_t|}\mathrm{Im}\left[e^{i\phi_{A_t}}\delta K_t\right], \tag{3.73}$$

$$\delta K_t = -\left(A_t^{*} - \mu\cot\beta\right)\delta m_t + U_{11}^{*}U_{12}\delta m^2_{\tilde{t}_1} + U_{21}^{*}U_{22}\delta m^2_{\tilde{t}_2} + U_{11}^{*}U_{22}\delta Y_{\tilde{t}} + U_{21}^{*}U_{12}\delta Y_{\tilde{t}}^{*}. \tag{3.74}$$

3.4 Comparing calculations which have used different renormalisation schemes

Calculations in different renormalisation schemes use different definitions for parameters. Therefore, to compare between these results it is necessary to perform a parameter conversion. This is needed if one wishes, for example, to compare between the two main public codes for calculating the complex MSSM Higgs sector, *FeynHiggs* [31,56–58] and *CPsuperH* [59]. *FeynHiggs* is based on the Feynman-diagrammatic approach and on-shell mass renormalisation while *CPsuperH* is based on a renormalisation group improved effective potential calculation and $\overline{\mathrm{DR}}$ renormalisation (we will discuss the status of Higgs mass calculations in the complex MSSM in more detail in Section 4.1). Both codes contain corrections at $\mathcal{O}(\alpha_t\alpha_s)$. Therefore, since the top/stop sector enters the

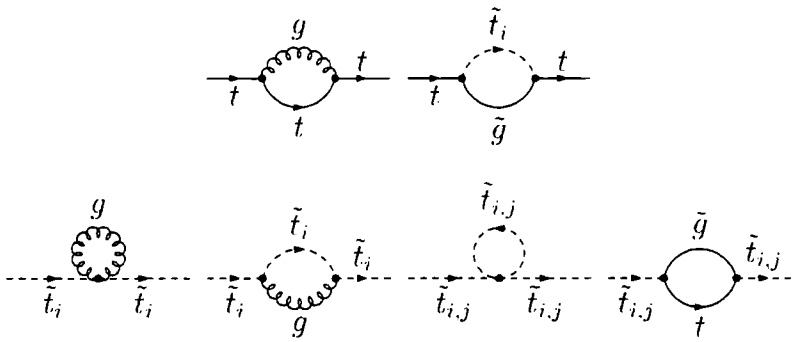

Figure 3.1: Diagrams used to calculate the shifts shown in equation (3.77) - (3.82), which convert between $\overline{\text{DR}}$ and on-shell parameters. ($i = 1, 2.$ $j = 1, 2$)

Higgs mass calculation at the 1-loop level, we need to consider differences in the top/stop sector parameter definitions at $\mathcal{O}(\alpha_s)$. We consider loops involving gluons, gluinos, stops and tops as shown in Figure 3.1.

We label the difference between the parameters p in the different renormalisation schemes by Δp, where

$$p^{\overline{\text{DR}}} = p^{\text{on-shell}} + \Delta p. \tag{3.75}$$

This is related to the counter-terms by

$$\Delta p = \delta p^{\text{on-shell}} - \delta p^{\overline{\text{DR}}}. \tag{3.76}$$

Recall that $\delta p^{\overline{\text{DR}}} = \left[\delta p^{\text{on-shell}}\right]^{\text{div}}$, where the 'div' denotes that only terms proportional to $\frac{2}{4-D} - \gamma_E + \log(4\pi)$ are kept. Therefore this means that $\Delta p = \left[\delta p^{\text{on-shell}}\right]^{\text{fin}}$, where the 'fin' denotes the finite pieces remaining once terms proportional to $\frac{2}{4-D} - \gamma_E + \log(4\pi)$ have been subtracted out.

For a comparison of the Feynman-diagrammatic result with the effective potential result for the particular case where all the MSSM parameters are real, see [60].

For the stop sector, we can directly adapt equation (3.69) - (3.74) to get the shifts

$$\begin{aligned}
\Delta M_L^2 &= -2m_t\Delta m_t \\
&+ U_{11}^* U_{11}\Delta m_{\tilde{t}_1}^2 + U_{21}^* U_{21}\Delta m_{\tilde{t}_2}^2 + U_{11}^* U_{21}\Delta Y_{\tilde{t}} + U_{21}^* U_{11}\Delta Y_{\tilde{t}}^*. && (3.77)\\
\Delta M_{\tilde{t}_R}^2 &= -2m_t\Delta m_t \\
&+ U_{12}^* U_{12}\Delta m_{\tilde{t}_1}^2 + U_{22}^* U_{22}\Delta m_{\tilde{t}_2}^2 + U_{12}^* U_{22}\Delta Y_{\tilde{t}} + U_{22}^* U_{12}\Delta Y_{\tilde{t}}^*. && (3.78)\\
\Delta A_t^* &= e^{-i\phi_{A_t}}\left(\Delta|A_t| - i|A_t|\Delta\varphi_{A_t}\right), && (3.79)\\
\Delta K_t &= -\left(A_t^* - \mu\cot\beta\right)\Delta m_t \\
&+ U_{11}^* U_{12}\Delta m_{\tilde{t}_1}^2 + U_{21}^* U_{22}\Delta m_{\tilde{t}_2}^2 + U_{11}^* U_{22}\Delta Y_{\tilde{t}} + U_{21}^* U_{12}\Delta Y_{\tilde{t}}^*, && (3.80)\\
\Delta|A_t| &= \frac{1}{m_t}\mathrm{Re}\left[e^{i\phi_{A_t}}\Delta K_t\right], && (3.81)\\
\Delta\varphi_{A_t} &= -\frac{1}{m_t|A_t|}\mathrm{Im}\left[e^{i\phi_{A_t}}\Delta K_t\right]. && (3.82)
\end{aligned}$$

The $\overline{\mathrm{DR}}$ parameters are defined at a certain scale μ_{ren}. We use this scale in the loop integrals in the parameter shifts. We will use $\mu_{\mathrm{ren}}^2 = M_{\mathrm{SUSY}}^2 + m_t^2 =: M_S^2$, in analogy to [60]. We calculate the strong coupling constant at the scale of the top mass, $\alpha_s(m_t^2)$. We neglect the D-terms in the stop mass matrix given in equation (2.23) (the terms proportional to M_Z^2) and we only keep those term in the shifts of $\mathcal{O}(\alpha_s)$, again, in analogy to the calculation in [60].

We will convert the parameters used as input to *CPsuperH* to parameters which we can use as input to *FeynHiggs*. Therefore, we will need to convert $A_t^{\overline{\mathrm{DR}}}(M_S^2)$, $M_L^{\overline{\mathrm{DR}}}(M_S^2)$ and $M_{\tilde{t}_R}^{\overline{\mathrm{DR}}}(M_S^2)$ to $A_t^{\mathrm{on-shell}}$, $M_L^{\mathrm{on-shell}}$ and $M_{\tilde{t}_R}^{\mathrm{on-shell}}$. *CPsuperH* requires the on-shell top mass as input, which is then converted internally in the program. Therefore, although the shifts in A_t, M_L and $M_{\tilde{t}_R}$ will depend on Δm_t, we will be able to use the same value of m_t as input in both programs.

We will calculate the shifts as functions of parameters of type $p^{\overline{\mathrm{DR}}}$ i.e. as a function of $m_t^{\overline{\mathrm{DR}}}(M_S^2)$, $A_t^{\overline{\mathrm{DR}}}(M_S^2)$, $M_L^{\overline{\mathrm{DR}}}(M_S^2)$ and $M_{\tilde{t}_R}^{\overline{\mathrm{DR}}}(M_S^2)$. This means that we must first use the shift Δm_t to calculate $m_t^{\overline{\mathrm{DR}}}(M_S^2)$ [1]. The difference between using $p^{\overline{\mathrm{DR}}}$ and $p^{\mathrm{on-shell}}$ in the shifts is formally a higher order effect.

In order to give an example of the size of these shifts, we use $m_t^{\mathrm{on-shell}} = 172.6$ GeV, $A_t^{\overline{\mathrm{DR}}}(M_S^2) = 1000i$ GeV, $M_{\mathrm{SUSY}}^{\overline{\mathrm{DR}}}(M_S^2) = M_L^{\overline{\mathrm{DR}}}(M_S^2) = M_{\tilde{t}_R}^{\overline{\mathrm{DR}}}(M_S^2) = 500$ GeV, $\mu =$

[1] Therefore, Δm_t, in this case, is a function of $m_t^{\mathrm{on-shell}}$, $A_t^{\overline{\mathrm{DR}}}(M_S^2)$, $M_L^{\overline{\mathrm{DR}}}(M_S^2)$ and $M_{\tilde{t}_R}^{\overline{\mathrm{DR}}}(M_S^2)$

2000 GeV. $M_3 = 1000i$ GeV and $M_2 = 200$ GeV. (This is a variation of the CPX scenario, which we defined in Section 2.8.)

The resulting on-shell parameters $\mathrm{Re}A_t^{\text{on-shell}}$, $\mathrm{Im}A_t^{\text{on-shell}}$, $M_L^{\text{on-shell}}$ and $M_{\tilde{t}_R}^{\text{on-shell}}$, are shown in Figure 3.2 (labelled '$p^{\overline{\text{DR}}}$ in shifts'). In this example, the shift in $\mathrm{Re}A_t$ is less than 2.1% of $|A_t^{\overline{\text{DR}}}(M_S^2)|$ and the shift in $\mathrm{Im}A_t$ is ~ 4.2 % of $|A_t^{\overline{\text{DR}}}(M_S^2)|$. Although these shifts appear small, they can have a big impact on the Higgs sector, which, as we will see in Chapter 6, is extremely sensitive to variations in A_t. The shifts in M_L and $M_{\tilde{t}_R}$ are less than 0.64% of $M_{\text{SUSY}}^{\overline{\text{DR}}}(M_S^2)$, which is numerically insignificant in comparison.

Figure 3.2 shows the effect of using $p^{\text{on-shell}}$ in all the parameter shifts (labelled '$p^{\text{on-shell}}$ in shifts'). We achieve this by first calculating the shift as functions of $m_t^{\overline{\text{DR}}}(M_S^2)$, $A_t^{\overline{\text{DR}}}(M_S^2)$, $M_L^{\overline{\text{DR}}}(M_S^2)$ and $M_{\tilde{t}_R}^{\overline{\text{DR}}}(M_S^2)$, as previously. We then use these shifts to obtain the $\mathrm{Re}A_t^{\text{on-shell}}$, $\mathrm{Im}A_t^{\text{on-shell}}$, $M_L^{\text{on-shell}}$ and $M_{\tilde{t}_R}^{\text{on-shell}}$ shown in Figure 3.2 (labelled '$p^{\overline{\text{DR}}}$ in shifts'). These values (together with the original $m_t^{\text{on-shell}}$) are then used to calculate a new set of shifts, which are displayed in Figure 3.2 (labelled '$p^{\text{on-shell}}$ in shifts'). This rather convoluted approach is useful for obtaining an idea of the uncertainty in the parameter conversion. In particular, we can see that the value of $\mathrm{Im}A_t^{\text{on-shell}}$ changes by $\sim 9\%$. Although this is less than 1% of $|A_t^{\overline{\text{DR}}}(M_S^2)|$, this does have a noticeable effect in Higgs mass calculations.

In order to understand the effect of these parameter shifts, it is useful to find a simple approximation which includes the significant features. As we have discussed, the shifts in M_L and $M_{\tilde{t}_R}$ are less numerically significant than the shifts in A_t and therefore, for the purposes of this approximation, can be neglected. Since we have neglected the D-terms in the stop mass matrix and use $M_{\text{SUSY}}^{\overline{\text{DR}}}(M_S^2) = M_L^{\overline{\text{DR}}}(M_S^2) = M_{\tilde{t}_R}^{\overline{\text{DR}}}(M_S^2)$, the stop mixing matrix has the simple form

$$\mathbf{U}_{\tilde{q}} = \frac{1}{\sqrt{2}} \begin{pmatrix} 1 & -e^{-i\phi_{X_t}} \\ e^{i\phi_{X_t}} & 1 \end{pmatrix}. \tag{3.83}$$

Therefore, the relation between $|X_t^{\text{on-shell}}|$ and $|X_t^{\overline{\text{DR}}}(M_S^2)|$ simplifies to

$$|X_t^{\text{on-shell}}| = |X_t^{\overline{\text{DR}}}| \left(1 + \frac{\Delta m_t}{m_t}\right) - \frac{1}{2m_t}\left(\Delta m_{\tilde{t}_2}^2 - \Delta m_{\tilde{t}_1}^2\right), \tag{3.84}$$

where

$$\Delta m_t = \frac{\alpha_s}{6\pi m_t}\left[g_1^t + g_2^t + m_t^2\left(6\log\frac{m_t^2}{\mu_{\rm ren}^2} - 10\right) + 2m_{\tilde{g}}^2\left(\log\frac{m_{\tilde{g}}^2}{\mu_{\rm ren}^2} - 1\right)\right]. \quad (3.85)$$

$$\Delta m_{\tilde{t}_1}^2 - \Delta m_{\tilde{t}_2}^2 = \frac{2\alpha_s}{3\pi}\left(g_1^{\tilde{t}} - g_2^{\tilde{t}}\right), \quad (3.86)$$

$$g_i^t = -m_{\tilde{t}_i}^2\left(\log\frac{m_{\tilde{t}_i}^2}{\mu_{\rm ren}^2} - 1\right) + f_i \mathrm{Re}\left[\mathcal{B}_0[m_t^2, m_{\tilde{g}}^2, m_{\tilde{t}_i}^2]\right], \quad (3.87)$$

$$g_i^{\tilde{t}} = 2m_{\tilde{t}_i}^2\left(\log\frac{m_{\tilde{t}_i}^2}{\mu_{\rm ren}^2} - 2\right) - f_i \mathrm{Re}\left[\mathcal{B}_0[m_{\tilde{t}_i}^2, m_{\tilde{g}}^2, m_t^2]\right], \quad (3.88)$$

$$f_i = m_{\tilde{g}}^2 + m_t^2 - m_{\tilde{t}_i}^2 - (-1)^i 2m_{\tilde{g}} m_t \cos(\phi_{M_3} - \phi_{X_t}), \quad (3.89)$$

and $\mathcal{B}_0 = [B_0]^{\rm fin}$. where the scalar integral B_0 is defined in Appendix A. We have been following a procedure similar to that used in [60] to find an approximation in the real MSSM[2].

Numerical results for $\mathrm{Re}A_t^{\rm on-shell}$ and $\mathrm{Im}A_t^{\rm on-shell}$ in this approximation are shown in Figure 3.2 (labelled 'approximation'). We can see that the shifts in $\mathrm{Re}A_t$ and $\mathrm{Im}A_t$ in this approximation vary by less that 1.6 GeV i.e. less than 0.16% of $|A_t^{\overline{\rm DR}}|$, so this approximation is very effective in this scenario. Therefore, examining the structure of equation (3.85)–(3.89) will allow us to understand characteristics of the full result. In particular, we can see that the shifts depend on the phase $(\phi_{M_3} - \phi_{X_t})$ and that the gluino mass $m_{\tilde{g}}$ features prominently in the shifts.

[2]However, in [60], the comparison is performed for $m_{\tilde{g}} = M_{\rm SUSY}$. It is then further simplified by assuming $m_t/M_S << 1$ and $m_t X_t/M_S^2 << 1$.

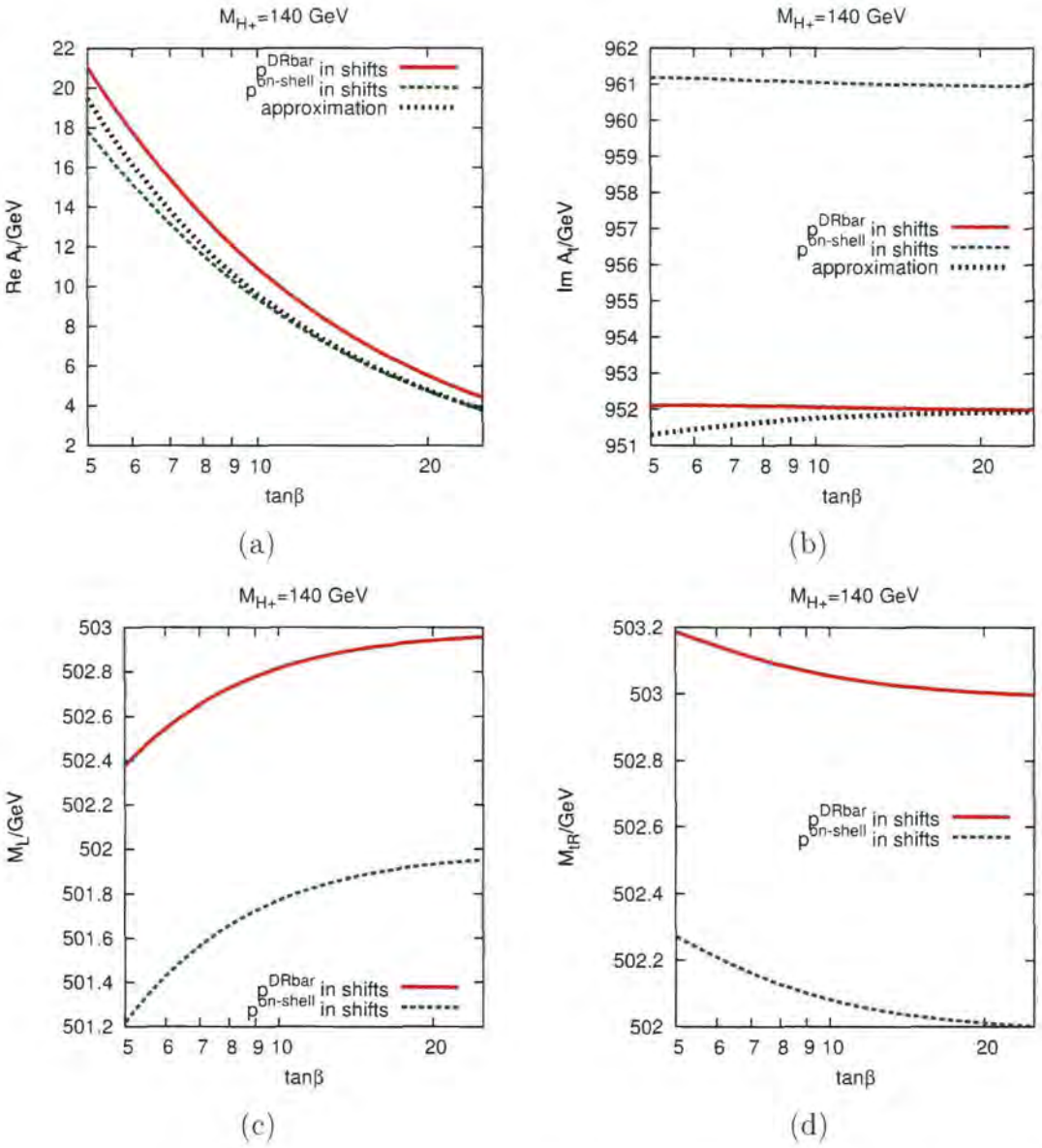

Figure 3.2: The on-shell parameters $\mathrm{Re}A_t^{\text{on-shell}}$, $\mathrm{Im}A_t^{\text{on-shell}}$, $M_L^{\text{on-shell}}$ and $M_{\tilde{t}_R}^{\text{on-shell}}$ which are calculated by applying shifts to the $\overline{\text{DR}}$ parameters $m_t^{\overline{\text{DR}}}(M_S^2)$, $A_t^{\overline{\text{DR}}}(M_S^2)$, $M_L^{\overline{\text{DR}}}(M_S^2)$ and $M_{\tilde{t}_R}^{\overline{\text{DR}}}(M_S^2)$, as in equation (3.75). A variation of the CPX scenario is used (see text). '$p^{\overline{\text{DR}}}$ in shifts' indicates that the shifts are calculated using equation (3.77) to equation (3.82) as functions of $m_t^{\overline{\text{DR}}}(M_S^2)$, $A_t^{\overline{\text{DR}}}(M_S^2)$, $M_L^{\overline{\text{DR}}}(M_S^2)$ and $M_{\tilde{t}_R}^{\overline{\text{DR}}}(M_S^2)$ (default method). '$p^{\text{on-shell}}$ in shifts' indicates that the shifts are calculated using equation (3.77) to equation (3.82) as functions of $\mathrm{Re}A_t^{\text{on-shell}}$, $\mathrm{Im}A_t^{\text{on-shell}}$, $M_L^{\text{on-shell}}$ and $M_{\tilde{t}_R}^{\text{on-shell}}$ (see text for further explanation). 'approximation' indicates that the expressions given in equation (3.85)–(3.89) have been used.

ijk	$\Gamma^{\text{tree}}_{ijk}$	$\delta^{1-\text{loop}}\Gamma_{ijk}$
hhh	$-3c_{2\alpha}s_{\alpha+\beta}\frac{ieM_W}{2c_W^2 s_W}$	$\Gamma^{\text{tree}}_{hhh}(\frac{3}{2}\delta Z_{hh}+\frac{3}{2}\delta Z_{hH}\frac{\Gamma^{\text{tree}}_{hhH}}{\Gamma^{\text{tree}}_{hhh}}$ $+\delta s_W\frac{s_W^2-c_W^2}{s_W c_W^2}+\frac{\delta M_Z^2}{2M_Z^2}+\frac{\delta e}{e}+s_\beta c_\beta\frac{\Gamma^{\text{tree}}_{HHH}}{\Gamma^{\text{tree}}_{hhh}}\delta t_\beta)$
HHH	$-3c_{2\alpha}c_{\alpha+\beta}\frac{ieM_W}{2c_W^2 s_W}$	$\Gamma^{\text{tree}}_{HHH}(\frac{3}{2}\delta Z_{HH}+\frac{3}{2}\delta Z_{hH}\frac{\Gamma^{\text{tree}}_{hHH}}{\Gamma^{\text{tree}}_{HHH}}$ $+\delta s_W\frac{s_W^2-c_W^2}{s_W c_W^2}+\frac{\delta M_Z^2}{2M_Z^2}+\frac{\delta e}{e}-s_\beta c_\beta\frac{\Gamma^{\text{tree}}_{hhh}}{\Gamma^{\text{tree}}_{HHH}}\delta t_\beta)$
AAA	0	0
hhH	$(c_{2\alpha}c_{\alpha+\beta}-2s_{2\alpha}s_{\alpha+\beta})\frac{ieM_W}{2c_W^2 s_W}$	$\Gamma^{\text{tree}}_{hhH}(\delta Z_{hh}+\frac{1}{2}\delta Z_{HH}+\frac{1}{2}\delta Z_{hH}\frac{\Gamma^{\text{tree}}_{hhh}}{\Gamma^{\text{tree}}_{hhH}}+\delta Z_{hH}\frac{\Gamma^{\text{tree}}_{hHH}}{\Gamma^{\text{tree}}_{hhH}}$ $+\delta s_W\frac{s_W^2-c_W^2}{s_W c_W^2}+\frac{\delta M_Z^2}{2M_Z^2}+\frac{\delta e}{e}-s_\beta c_\beta\frac{\Gamma^{\text{tree}}_{hHH}}{\Gamma^{\text{tree}}_{hhH}}\delta t_\beta)$
hhA	0	0
HHA	0	0
hHH	$(c_{2\alpha}s_{\alpha+\beta}+2s_{2\alpha}c_{\alpha+\beta})\frac{ieM_W}{2c_W^2 s_W}$	$\Gamma^{\text{tree}}_{hHH}(\delta Z_{HH}+\frac{1}{2}\delta Z_{hh}+\frac{1}{2}\delta Z_{hH}\frac{\Gamma^{\text{tree}}_{HHH}}{\Gamma^{\text{tree}}_{hHH}}+\delta Z_{hH}\frac{\Gamma^{\text{tree}}_{hhH}}{\Gamma^{\text{tree}}_{hHH}}$ $+\delta s_W\frac{s_W^2-c_W^2}{s_W c_W^2}+\frac{\delta M_Z^2}{2M_Z^2}+\frac{\delta e}{e}+s_\beta c_\beta\frac{\Gamma^{\text{tree}}_{hhH}}{\Gamma^{\text{tree}}_{hHH}}\delta t_\beta)$
hAA	$-c_{2\beta}s_{\alpha+\beta}\frac{ieM_W}{2c_W^2 s_W}$	$\Gamma^{\text{tree}}_{hAA}(\delta Z_{AA}+\frac{1}{2}\delta Z_{hh}+\frac{1}{2}\delta Z_{hH}\frac{\Gamma^{\text{tree}}_{HAA}}{\Gamma^{\text{tree}}_{hAA}}+\delta Z_{AG}\frac{\Gamma^{\text{tree}}_{hAG}}{\Gamma^{\text{tree}}_{hAA}})$ $+\delta s_W\frac{s_W^2-c_W^2}{s_W c_W^2}+\frac{\delta M_Z^2}{2M_Z^2}+\frac{\delta e}{e}-s_\beta c_\beta\frac{\Gamma^{\text{tree}}_{HAA}}{\Gamma^{\text{tree}}_{hAA}}\delta t_\beta)$
HAA	$c_{2\beta}c_{\alpha+\beta}\frac{ieM_W}{2c_W^2 s_W}$	$\Gamma^{\text{tree}}_{HAA}(\frac{1}{2}\delta Z_{HH}+\delta Z_{AA}+\frac{1}{2}\delta Z_{hH}\frac{\Gamma^{\text{tree}}_{hAA}}{\Gamma^{\text{tree}}_{HAA}}+\delta Z_{AG}\frac{\Gamma^{\text{tree}}_{HAG}}{\Gamma^{\text{tree}}_{HAA}}$ $+\delta s_W\frac{s_W^2-c_W^2}{s_W c_W^2}+\frac{\delta M_Z^2}{2M_Z^2}+\frac{\delta e}{e}+s_\beta c_\beta\frac{\Gamma^{\text{tree}}_{hAA}}{\Gamma^{\text{tree}}_{HAA}}\delta t_\beta)$
HHA	0	0

Table 3.2: Triple Higgs tree level coupling (h,H,A basis) and counter terms in the complex MSSM.

h_i	$g^{\text{tree}}_{h_i f_d f_d}$	$\delta^{1-\text{loop}}\Gamma_{h_i f_d \bar{f}_d}$
h	$\frac{e}{2M_W s_W}\frac{m_{f_d}}{c_\beta}(is_\alpha)$	$C^- = g^{\text{tree}}_{h f_d \bar{f}_d}\left(\frac{\delta e}{e}+\frac{1}{2}\delta Z_{hh}+\frac{1}{2}\delta Z_{hH}\frac{g^{\text{tree}}_{Hf_df_d}}{g^{\text{tree}}_{hf_d\bar{f}_d}}-\frac{\delta M_W^2}{2M_W^2}-\frac{\delta s_W}{s_W}+s_\beta^2\delta\tan\beta+\frac{\delta m_{f_d}}{m_{f_d}}+\frac{1}{2}\left[\delta Z^L_{f_d}+\delta Z^{R\dagger}_{f_d}\right]\right)$
		$C^+ = g^{\text{tree}}_{h f_d \bar{f}_d}\left(\frac{\delta e}{e}+\frac{1}{2}\delta Z_{hh}+\frac{1}{2}\delta Z_{hH}\frac{g^{\text{tree}}_{Hf_df_d}}{g^{\text{tree}}_{hf_df_d}}-\frac{\delta M_W^2}{2M_W^2}-\frac{\delta s_W}{s_W}+s_\beta^2\delta\tan\beta+\frac{\delta m_{f_d}}{m_{f_d}}+\frac{1}{2}\left[\delta Z^R_{f_d}+\delta Z^{L\dagger}_{f_d}\right]\right)$
H	$\frac{e}{2M_W s_W}\frac{m_{f_d}}{c_\beta}(-ic_\alpha)$	$C^- = g^{\text{tree}}_{H f_d \bar{f}_d}\left(\frac{\delta e}{e}+\frac{1}{2}\delta Z_{HH}+\frac{1}{2}\delta Z_{hH}\frac{g^{\text{tree}}_{hf_d\bar{f}_d}}{g^{\text{tree}}_{Hf_d\bar{f}_d}}-\frac{\delta M_W^2}{2M_W^2}-\frac{\delta s_W}{s_W}+s_\beta^2\delta\tan\beta+\frac{\delta m_{f_d}}{m_{f_d}}+\frac{1}{2}\left[\delta Z^L_{f_d}+\delta Z^{R\dagger}_{f_d}\right]\right)$
		$C^+ = g^{\text{tree}}_{H f_d \bar{f}_d}\left(\frac{\delta e}{e}+\frac{1}{2}\delta Z_{HH}+\frac{1}{2}\delta Z_{hH}\frac{g^{\text{tree}}_{hf_df_d}}{g^{\text{tree}}_{Hf_d\bar{f}_d}}-\frac{\delta M_W^2}{2M_W^2}-\frac{\delta s_W}{s_W}+s_\beta^2\delta\tan\beta+\frac{\delta m_{f_d}}{m_{f_d}}+\frac{1}{2}\left[\delta Z^R_{f_d}+\delta Z^{L\dagger}_{f_d}\right]\right)$
A	$\frac{e}{2M_W s_W}\frac{m_{f_d}}{c_\beta}(s_{\beta_n})$	$C^- = g^{\text{tree}}_{A f_d \bar{f}_d}\left(\frac{\delta e}{e}+\frac{1}{2}\delta Z_{AA}+\frac{1}{2}\delta Z_{AG}\frac{g^{\text{tree}}_{Gf_df_d}}{g^{\text{tree}}_{Af_d\bar{f}_d}}-\frac{\delta M_W^2}{2M_W^2}-\frac{\delta s_W}{s_W}+s_\beta^2\delta\tan\beta+\frac{\delta m_{f_d}}{m_{f_d}}+\frac{1}{2}\left[\delta Z^L_{f_d}+\delta Z^{R\dagger}_{f_d}\right]\right)$
		$C^+ = -g^{\text{tree}}_{A f_d \bar{f}_d}\left(\frac{\delta e}{e}+\frac{1}{2}\delta Z_{AA}+\frac{1}{2}\delta Z_{AG}\frac{g^{\text{tree}}_{Gf_df_d}}{g^{\text{tree}}_{Af_d\bar{f}_d}}-\frac{\delta M_W^2}{2M_W^2}-\frac{\delta s_W}{s_W}+s_\beta^2\delta\tan\beta+\frac{\delta m_{f_d}}{m_{f_d}}+\frac{1}{2}\left[\delta Z^R_{f_d}+\delta Z^{L\dagger}_{f_d}\right]\right)$

Table 3.3: Higgs to d-type fermions tree level couplings and counter-terms in the h, H, A basis. C^- and C^+ are the coefficients of ω_- and ω_+ respectively. For h or H, the tree coupling is $g^{\text{tree}}_{hf\bar{f},Hf\bar{f}}(\omega_- + \omega_+)$, whilst for A, the tree coupling is $g^{\text{tree}}_{Af\bar{f}}(\omega_- - \omega_+)$ (d can also be replaced with e, μ, τ to get the Higgs couplings to leptons).

h_i	$g^{\text{tree}}_{h_i f_u \bar{f}_u}$	$\delta^{1-\text{loop}} g_{h_i f_u \bar{f}_u}$
h	$\frac{e}{2M_W s_W}\frac{m_{f_u}}{s_\beta}(-ic_\alpha)$	$C^- = g^{\text{tree}}_{hf_uf_u}\left(\frac{\delta e}{e}+\frac{1}{2}\delta Z_{hh}+\frac{1}{2}\delta Z_{hH}\frac{g^{\text{tree}}_{Hf_uf_u}}{g^{\text{tree}}_{hf_uf_u}}-\frac{\delta M_W^2}{2M_W^2}-\frac{\delta s_W}{s_W}+c_\beta^2\delta\tan\beta\right.$ $\left.+\frac{\delta m_{f_u}}{m_{f_u}}+\frac{1}{2}\left[\delta Z^L_{f_u}+\delta Z^{R\dagger}_{f_u}\right]\right)$
		$C^+ = g^{\text{tree}}_{hf_uf_u}\left(\frac{\delta e}{e}+\frac{1}{2}\delta Z_{hh}+\frac{1}{2}\delta Z_{hH}\frac{g^{\text{tree}}_{Hf_uf_u}}{g^{\text{tree}}_{hf_uf_u}}-\frac{\delta M_W^2}{2M_W^2}-\frac{\delta s_W}{s_W}+c_\beta^2\delta\tan\beta\right.$ $\left.+\frac{\delta m_{f_u}}{m_{f_u}}+\frac{1}{2}\left[\delta Z^R_{f_u}+\delta Z^{L\dagger}_{f_u}\right]\right)$
H	$\frac{e}{2M_W s_W}\frac{m_{f_u}}{s_\beta}(-is_\alpha)$	$C^- = g^{\text{tree}}_{Hf_u\bar{f}_u}\left(\frac{\delta e}{e}+\frac{1}{2}\delta Z_{HH}+\frac{1}{2}\delta Z_{hH}\frac{g^{\text{tree}}_{hf_uf_u}}{g^{\text{tree}}_{Hf_uf_u}}-\frac{\delta M_W^2}{2M_W^2}-\frac{\delta s_W}{s_W}+c_\beta^2\delta\tan\beta\right.$ $\left.+\frac{\delta m_{f_u}}{m_{f_u}}+\frac{1}{2}\left[\delta Z^L_{f_u}+\delta Z^{R\dagger}_{f_u}\right]\right)$
		$C^+ = g^{\text{tree}}_{Hf_uf_u}\left(\frac{\delta e}{e}+\frac{1}{2}\delta Z_{HH}+\frac{1}{2}\delta Z_{hH}\frac{g^{\text{tree}}_{hf_uf_u}}{g^{\text{tree}}_{Hf_uf_u}}-\frac{\delta M_W^2}{2M_W^2}-\frac{\delta s_W}{s_W}+c_\beta^2\delta\tan\beta\right.$ $\left.+\frac{\delta m_{f_u}}{m_{f_u}}+\frac{1}{2}\left[\delta Z^R_{f_u}+\delta Z^{L\dagger}_{f_u}\right]\right)$
A	$\frac{e}{2M_W s_W}\frac{m_{f_u}}{s_\beta}(c_{\beta_n})$	$C^- = g^{\text{tree}}_{Af_u\bar{f}_u}\left(\frac{\delta e}{e}+\frac{1}{2}\delta Z_{AA}+\frac{1}{2}\delta Z_{AG}\frac{g^{\text{tree}}_{Gf_uf_u}}{g^{\text{tree}}_{Af_uf_u}}-\frac{\delta M_W^2}{2M_W^2}-\frac{\delta s_W}{s_W}+c_\beta^2\delta\tan\beta\right.$ $\left.+\frac{\delta m_{f_u}}{m_{f_u}}+\frac{1}{2}\left[\delta Z^L_{f_u}+\delta Z^{R\dagger}_{f_u}\right]\right)$
		$C^+ = -g^{\text{tree}}_{Af_u\bar{f}_u}\left(\frac{\delta e}{e}+\frac{1}{2}\delta Z_{AA}+\frac{1}{2}\delta Z_{AG}\frac{g^{\text{tree}}_{Gf_uf_u}}{g^{\text{tree}}_{Af_uf_u}}-\frac{\delta M_W^2}{2M_W^2}-\frac{\delta s_W}{s_W}+c_\beta^2\delta\tan\beta\right.$ $\left.+\frac{\delta m_{f_u}}{m_{f_u}}+\frac{1}{2}\left[\delta Z^R_{f_u}+\delta Z^{L\dagger}_{f_u}\right]\right)$

Table 3.4: Higgs to u-type fermions tree level couplings and counter-terms in the h, H, A basis. C^- and C^+ are the coefficients of ω_- and ω_+ respectively. For h or H, the tree coupling is $g^{\text{tree}}_{hf\bar{f},Hf\bar{f}}(\omega_- + \omega_+)$, whilst for A, the tree coupling is $g^{\text{tree}}_{Af\bar{f}}(\omega_- - \omega_+)$.

Chapter 4

Loop corrections to Higgs masses and mixing

4.1 Introduction

Knowing the Higgs masses and mixing properties of the Higgs particles accurately is vital for an investigation of the phenomenology of the Higgs sector of the MSSM. These calculations have been the subject of much work over the last decade. We will briefly summarise the results here (for a review, see [61]).

In the real MSSM, the full 1-loop result is known. At 2-loop level, the $\mathcal{O}(\alpha_s\alpha_t)$, the $\mathcal{O}(\alpha_t^2)$, $\mathcal{O}(\alpha_s\alpha_b)$, $\mathcal{O}(\alpha_t\alpha_b)$ and $\mathcal{O}(\alpha_b^2)$ have been calculated. Resummation of the term $\mathcal{O}(\alpha_b(\alpha_s\tan\beta)^n)$ has been performed. As a result of these corrections, it is estimated that the remaining theoretical error on the lightest CP-even Higgs mass is $\lesssim 3$ GeV. A full 2-loop effective potential calculation has also been published. (For details on the real MSSM corrections, see [31] and references therein)

In the complex MSSM, 1-loop corrections from the fermion/sfermion sector and some leading logarithmic corrections from the gaugino sector and the dominant 2-loop results have been calculated in the effective potential approach and renormalisation group improved effective potential method [34, 36, 37, 62–67]. In the Feynman-diagrammatic approach, the full 1-loop result has been calculated [31, 35, 68]. At 2-loop, the $\mathcal{O}(\alpha_s\alpha_t)$ corrections are available [55].

Most of these results have been incorporated either into the public code *FeynHiggs* [31, 56–58], [49, 69, 70][1], which uses the Feynman-diagrammatic approach or the public code *CPsuperH* [59][2], which uses the renormalisation group improved effective potential approach.

In this chapter, we will outline the method used in this thesis to calculate the neutral Higgs masses, which will use self-energies obtained with the program *FeynHiggs*, and discuss the behaviour of the main corrections with the aid of numerical examples. We will also introduce a pictorial representation of the Higgs sector mixing. We will discuss the way that loop-corrected propagator corrections can be incorporated in calculations involving an external Higgs boson. We will conclude with a description of a method which allows the inclusion of Higgs mixing with Goldstone bosons and Z bosons into processes involving an external Higgs bosons, without introducing gauge parameter dependence at the 1-loop level.

4.2 Definition of neutral Higgs masses

In general, the neutral Higgs masses are obtained from the real parts of the poles of the propagator matrix. In this section, we will neglect mixing with the Goldstone and Z bosons as these are sub-leading 2-loop contributions to the Higgs masses. We therefore use a 3×3 propagator matrix $\mathbf{\Delta}(p^2)$ in the (h, H, A) basis.

In order to find the neutral Higgs masses we must find the three solutions to

$$\frac{1}{|\mathbf{\Delta}(p^2)|} = 0, \tag{4.1}$$

which, in the case with non-zero mixing between all three neutral Higgs bosons, is equivalent to solving

$$\frac{1}{\Delta_{ii}(p^2)} = 0, \tag{4.2}$$

[1] Unless explicitly stated otherwise, '*FeynHiggs*' will refer to *FeynHiggs* version 2.6.4 throughout this thesis.

[2] There is also an extension, *CPsuperH2.0*, which includes the calculation of electric dipole moments and some B meson observables [71].

where $i = h, H$ or A. The propagator matrix is related to the 3×3 matrix of the irreducible 2-point vertex-functions $\hat{\mathbf{\Gamma}}_2(p^2)$ through the equation

$$\left[-\mathbf{\Delta}(p^2)\right]^{-1} = \hat{\mathbf{\Gamma}}_2(p^2) = i\left[p^2\mathbb{1} - \mathbf{M}(p^2)\right]. \tag{4.3}$$

where

$$\mathbf{M}(p^2) = \begin{pmatrix} m_h^2 - \hat{\Sigma}_{hh}(p^2) & -\hat{\Sigma}_{hH}(p^2) & -\hat{\Sigma}_{hA}(p^2) \\ -\hat{\Sigma}_{hH}(p^2) & m_H^2 - \hat{\Sigma}_{HH}(p^2) & -\hat{\Sigma}_{HA}(p^2) \\ -\hat{\Sigma}_{hA}(p^2) & -\hat{\Sigma}_{HA}(p^2) & m_A^2 - \hat{\Sigma}_{AA}(p^2) \end{pmatrix}. \tag{4.4}$$

As before, m_h,m_H,m_A refer to the tree level masses given in equation (2.9). $\hat{\Sigma}_{ij}(p^2)$ are renormalised Higgs self-energies. These self-energies are given at 1-loop by equation (3.20a). In the main numerical analysis, we will use renormalised self-energies which also contain the leading 2-loop pieces. If there is CP conservation, $\hat{\Sigma}_{hA}(p^2) = \hat{\Sigma}_{HA}(p^2) = 0$ and the CP-even Higgs bosons h, H do not mix with the CP-odd Higgs boson A.

In general, the renormalised Higgs self-energies can be complex, due to absorptive parts. Therefore, the three poles of the propagator matrix $\mathcal{M}_a^2$ can be written as

$$\mathcal{M}_{h_a}^2 = M_{h_a}^2 - iM_{h_a}W_{h_a}, \tag{4.5}$$

where M_{h_a} is real and is interpreted as the loop-corrected (i.e. physical) mass, W_{h_a} is the width parameter and $a = 1, 2, 3$.

In the CP-violating MSSM, the loop-corrected masses are labelled in size order such that

$$M_{h_1} \leq M_{h_2} \leq M_{h_3}. \tag{4.6}$$

In the CP-conserving MSSM, the masses are labelled such that the CP-even loop-corrected Higgs bosons have masses M_h and M_H with $M_h \leq M_H$ and the CP-odd loop-corrected Higgs boson has mass M_A.

4.3 Calculating the renormalised neutral Higgs self-energies

Although our main numerical analysis is based on complete 1-loop self-energies which include leading 2-loop corrections, we will first outline various approximations which can be used when calculating the renormalised neutral Higgs self-energies $\hat{\Sigma}_{ij}(p^2)$. All 1-loop examples will use the programs *FeynArts* [41-43] and *FormCalc* [43, 45] to draw and calculate the Feynman diagrams and the program *LoopTools* [45] to evaluate the loop integrals (apart from some special cases - see Appendix A for more details).

4.3.1 Yukawa Approximation

The leading corrections (at low/moderate $\tan\beta$) can be found by considering 1-loop corrections involving the top quark and the stop quarks and selecting only those terms proportional to m_t^2/M_W^2 ('Yukawa terms'). The resulting corrections will be finite and proportional to m_t^4. They are obtained by a calculation at zero incoming momentum i.e. $\hat{\Sigma}_{ij}(p^2 = 0)$.

In this approximation, the renormalisation constants δt_β, δM_W^2, δM_Z^2 and δZ_{ij}, which appear in equation (3.20a), are all zero.

For consistency, the stop masses $m_{\tilde{t}_1}$ and $m_{\tilde{t}_2}$ must also be calculated in the Yukawa approximation, i.e.

$$m^2_{\tilde{q}_{1,2}} = m_q^2 + \frac{1}{2}\Big[M_L^2 + M_{\tilde{q}_R}^2 \mp \sqrt{[M_L^2 - M_{\tilde{q}_R}^2]^2 + 4m_q^2|X_q|^2}\,\Big], \tag{4.7}$$

rather than using the full expression given in equation (2.27). In the CP-conserving MSSM, this gives

$$\begin{aligned}
\hat{\Sigma}_{\phi_1\phi_1} &= +\frac{3e^2m_t^4}{16\pi^2 M_W^2 s_W^2 s_\beta^2}\frac{\mu^2 X_t^2}{m_{\tilde{t}_1}^2 - m_{\tilde{t}_2}^2} C_{112-122}, \\
\hat{\Sigma}_{\phi_1\phi_2} &= -\frac{3e^2m_t^4}{16\pi^2 M_W^2 s_W^2 s_\beta^2}\frac{\mu X_t}{m_{\tilde{t}_1}^2 - m_{\tilde{t}_2}^2}\left[-2\log\left(\frac{m_{\tilde{t}_1}}{m_{\tilde{t}_2}}\right) + A_t X_t C_{112-122}\right], \\
\hat{\Sigma}_{\phi_2\phi_2} &= -\frac{3e^2m_t^4}{8\pi^2 M_W^2 s_W^2 s_\beta^2}\left[\log\left(\frac{m_{\tilde{t}_1}m_{\tilde{t}_2}}{m_t^2}\right) + \frac{A_t X_t}{m_{\tilde{t}_1}^2 - m_{\tilde{t}_2}^2}\left(2\log\left(\frac{m_{\tilde{t}_1}}{m_{\tilde{t}_2}}\right) - \frac{A_t X_t}{2} C_{112-122}\right)\right], \\
\hat{\Sigma}_{\phi_1 A} &= 0,\ \hat{\Sigma}_{\phi_2 A} = 0,\ \hat{\Sigma}_{AA} = 0,
\end{aligned}$$

where

$$\begin{aligned} C_{112-122} &= C_0\left(0,0,0,m_{\tilde{t}_1}^2,m_{\tilde{t}_1}^2,m_{\tilde{t}_2}^2\right) - C_0\left(0,0,0,m_{\tilde{t}_1}^2,m_{\tilde{t}_2}^2,m_{\tilde{t}_2}^2\right) \\ &= -2\left(\frac{1}{m_{\tilde{t}_1}^2 - m_{\tilde{t}_2}^2} - \frac{\left(m_{\tilde{t}_1}^2 + m_{\tilde{t}_2}^2\right)}{\left(m_{\tilde{t}_1}^2 - m_{\tilde{t}_2}^2\right)^2}\log\left(\frac{m_{\tilde{t}_1}}{m_{\tilde{t}_2}}\right)\right). \end{aligned} \tag{4.8}$$

and the C_0 integrals are defined in Appendix A. Note that the C_0 integrals do not appear automatically, as no 3-point functions are calculated. However, substituting C_0 integrals for combinations of the A_0 and B_0 integrals which appear naturally in the calculation (all at zero momentum) does make the self-energy expressions more compact.

As discussed previously, $\hat{\Sigma}_{\phi_1 A} = 0, \hat{\Sigma}_{\phi_2 A} = 0, \hat{\Sigma}_{AA} = 0$ ensures that the CP-even Higgs bosons do not mix with the CP-odd Higgs bosons.

These calculations were done with pen and paper, using the Feynman rules in [72] and using the programs *FeynArts* [41–43] and *FormCalc* [43,45], and the results agreed. We have confirmed these expressions through discussion with the authors of [57]. Note that these self-energies simplify considerably for the no-mixing case ($X_t = 0$).

In the CP-violating MSSM, the expressions for the neutral Higgs self-energies in the Yukawa approximation involve the charged Higgs self-energy (since $M_{H^\pm}$ is the input parameter rather than M_A), which is also taken at zero incoming momentum, such that

$$\delta M_{H^\pm}^2 = \Sigma_{H^-H^+}(0). \tag{4.9}$$

These diagrams will involve the $b, \tilde{b}$ sector in addition to the $t, \tilde{t}$ sector, and they are related through the parameter M_L^2 in equation (2.25). Therefore, some of the renormalised self-energies contain a dependence on $M_{\tilde{b}_R}^2$, which, in this approximation, is related to stop sector parameters through the equation,

$$M_{\tilde{b}_R}^{2,m_t^4} = -m_t^2 + m_{\tilde{t}_1}^2 - \left(m_{\tilde{t}_1}^2 - m_{\tilde{t}_2}^2\right) s_{\tilde{t}} s_{\tilde{t}}^*, \tag{4.10}$$

where $s_{\tilde{t}}$ was defined in equation (2.28).

The expression for the renormalised neutral Higgs energies are then given by

$$\hat{\Sigma}_{\phi_1\phi_1} = \frac{3e^2m_t^4}{16\pi^2M_W^2 s_W^2 s_\beta^2}\left(\frac{\mathrm{Re}^2[\mu X_t]}{m_{\tilde{t}_1}^2 - m_{\tilde{t}_2}^2}\mathcal{C}_{112-122} + \mu\mu^*\frac{\mathcal{C}_{12R}}{2}\right). \tag{4.11}$$

$$\hat{\Sigma}_{\phi_1\phi_2} = -\frac{3e^2m_t^4}{16\pi^2M_W^2 s_W^2 s_\beta^2}\left(\frac{\mu\mu^*}{t_\beta}\frac{\mathcal{C}_{12R}}{2} + \frac{\mathrm{Re}\,[\mu X_t]}{m_{\tilde{t}_1}^2 - m_{\tilde{t}_2}^2}\left(\mathrm{Re}\,[A_t^* X_t]\mathcal{C}_{112-122} - 2\log\left(\frac{m_{\tilde{t}_1}}{m_{\tilde{t}_2}}\right)\right)\right), \tag{4.12}$$

$$\hat{\Sigma}_{\phi_2\phi_2} = -\frac{3e^2m_t^4}{16\pi^2M_W^2 s_W^2 s_\beta^2}\left(2\log\left(\frac{m_{\tilde{t}_1}m_{\tilde{t}_2}}{m_t^2}\right) - \frac{\mu\mu^*}{t_\beta^2}\frac{\mathcal{C}_{12R}}{2} + \frac{\mathrm{Re}\,[A_t^* X_t]}{m_{\tilde{t}_1}^2 - m_{\tilde{t}_2}^2}\left(4\log\left(\frac{m_{\tilde{t}_1}}{m_{\tilde{t}_2}}\right) - \mathrm{Re}\,[A_t^* X_t]\mathcal{C}_{112-122}\right)\right), \tag{4.13}$$

$$\hat{\Sigma}_{\phi_1 A} = -\frac{3e^2m_t^4}{32\pi^2M_W^2 s_W^2 s_\beta^3}\frac{\mathrm{Im}\,[\mu^2 X_t^2]}{m_{\tilde{t}_1}^2 - m_{\tilde{t}_2}^2}\mathcal{C}_{112-122}, \tag{4.14}$$

$$\hat{\Sigma}_{\phi_2 A} = \frac{3e^2m_t^4}{16\pi^2M_W^2 s_W^2 s_\beta^3}\frac{\mathrm{Im}\,[\mu X_t]}{\left(m_{\tilde{t}_1}^2 - m_{\tilde{t}_2}^2\right)}\left(\mathrm{Re}\,[A_t^* X_t]\mathcal{C}_{112-122} - 2\log\left(\frac{m_{\tilde{t}_1}}{m_{\tilde{t}_2}}\right)\right), \tag{4.15}$$

$$\hat{\Sigma}_{AA} = \frac{3e^2m_t^4}{16\pi^2M_W^2 s_W^2 s_\beta^4}\left(\frac{\mathrm{Im}^2[\mu X_t]}{m_{\tilde{t}_1}^2 - m_{\tilde{t}_2}^2}\mathcal{C}_{112-122} + \mu\mu^*\frac{\mathcal{C}_{12R}}{2}\right), \tag{4.16}$$

where

$$\mathcal{C}_{12R} = \mathrm{C}_0\left(0, 0, 0, m_{\tilde{t}_1}^2, m_{\tilde{t}_2}^2, M_{\tilde{b}_R}^{2,m_t^4}\right). \tag{4.17}$$

Note that $\hat{\Sigma}_{\phi_1 A}$ and $\hat{\Sigma}_{\phi_2 A}$ are now non-zero, driving CP-violation in the Higgs sector. It is also interesting to see that although the $\hat{\Sigma}$ involve complex parameters, they are themselves entirely real. This means that the poles of the propagator matrix will also be real in this approximation. Equations for the Yukawa contribution to the renormalised neutral Higgs self-energies $\hat{\Sigma}$ in CP-violating MSSM are also available in [73].

4.3.2 $p^2 = 0$ approximation

Another approximation that is sometimes useful involves setting the incoming momentum p^2 in the renormalised neutral Higgs self-energies $\hat{\Sigma}_{ij}$ to zero, such that

$$\hat{\Sigma}_{kk}(p^2) \rightarrow \hat{\Sigma}_{kk}(0), \tag{4.18}$$

$$\hat{\Sigma}_{jk}(p^2) \rightarrow \hat{\Sigma}_{jk}(0). \tag{4.19}$$

All counter terms are calculated in full (see Section 3.3.2). This approximation includes all the Yukawa terms. Once again, $\hat{\Sigma}_{ij}$ are real, leading to real poles of the propagator matrix.

4.3.3 real p^2 on-shell approximation

In this approximation, the incoming momentum is set to a combination of the tree level masses,

$$\hat{\Sigma}_{kk}(p^2) \rightarrow \mathrm{Re}\left[\hat{\Sigma}_{kk}(m_k^2)\right], \tag{4.20}$$

$$\hat{\Sigma}_{jk}(p^2) \rightarrow \mathrm{Re}\left[\hat{\Sigma}_{jk}(\frac{1}{2}(m_j^2 + m_k^2))\right]. \tag{4.21}$$

4.3.4 complex p^2 on-shell approximation

This approximation is similar to the real p^2 on-shell approximation but does not discard the complex parts of the self-energies,

$$\hat{\Sigma}_{kk}(p^2) \rightarrow \hat{\Sigma}_{kk}(m_k^2), \tag{4.22}$$

$$\hat{\Sigma}_{jk}(p^2) \rightarrow \hat{\Sigma}_{jk}(\frac{1}{2}(m_j^2 + m_k^2)). \tag{4.23}$$

This approximation allows complex solutions to equation (4.1), which, as we will see, makes it useful as a starting point for a fully momentum dependent calculation.

4.3.5 Full momentum dependence at 1-loop

The Yukawa, $p^2 = 0$, real p^2 on-shell and complex p^2 on-shell approximation all involve approximations to the incoming momenta. The full momentum dependence is more complicated to calculate as it involves an iterative procedure in order to calculate $\mathbf{M}(p^2)$ at $p^2 = \mathcal{M}^2_{h_a}$.

As discussed previously, in general the solutions to equation (4.1) are complex. The program *LoopTools* [45] calculates loop integrals at real momenta only. Therefore, the unrenormalised self-energies were calculated using an expansion about the real part of the pole, $M^2_{h_a}$, such that

$$\hat{\Sigma}_{jk}(\mathcal{M}^2_{h_a}) \simeq \hat{\Sigma}_{jk}(M^2_{h_a}) + i\mathrm{Im}\left[\mathcal{M}^2_{h_a}\right]\hat{\Sigma}'_{jk}(M^2_{h_a}), \tag{4.24}$$

with $j = h, H, A$ and $k = h, H, A$.

For each h_a, the initial value of $\mathcal{M}^2_{h_a}$ was the result from the 'complex p^2 on-shell approximation'. This solution was then refined using

$$\mathcal{M}^{2,[n+1]}_{h_a} = a\text{th eigenvalue of } \mathbf{M}(\mathcal{M}^{2,[n]}_{h_a}), \tag{4.25}$$

where the eigenvalues have been sorted into ascending value, according to their real parts. Once $\mathcal{M}^{2,[n+1]}_{h_a}$ and $\mathcal{M}^{2,[n]}_{h_a}$ are very similar, a final iteration is done using the expansion

$$\begin{aligned}\hat{\Sigma}_{jk}(\mathcal{M}^2_{h_a}) &\simeq \hat{\Sigma}_{jk}(M^2_{h_a}) + i\mathrm{Im}\left[\mathcal{M}^2_{h_a}\right]\hat{\Sigma}'_{jk}(M^2_{h_a}) \\ &+ \frac{1}{2}\left(i\mathrm{Im}\left[\mathcal{M}^2_{h_a}\right]\hat{\Sigma}''_{jk}(M^2_{h_a})\right)^2,\end{aligned} \tag{4.26}$$

in order to check that the inclusion of the second order terms does not significantly change the masses.

4.3.6 2-loop contribution to Higgs self-energies

The program *FeynHiggs* [31,56–58] contains $\hat{\Sigma}_{jk}(M^2_{h_a})$ and $\hat{\Sigma}'_{jk}(M^2_{h_a})$, which have the full 1-loop and some 2-loop terms. These can be obtained using the the function `FHGetSelf`, which has the incoming momentum (real) as an argument. We used these $\hat{\Sigma}_{jk}(M^2_{h_a})$ and $\hat{\Sigma}'_{jk}(M^2_{h_a})$ to calculate the Higgs masses using the procedure described above.

FeynHiggs allows the user to select the type of 2-loop corrections to be used. This is an important choice in the complex MSSM because *FeynHiggs* only contains the full phase dependence for contributions at $\mathcal{O}(\alpha_t\alpha_s)$ [55]. However, there is the option of including sub-leading 2-loop corrections which have been calculated without phase dependence. The user can use the flag `tlCplxApprox`=1,2 or 3 to specify how the types of 2-loop corrections are combined. All of these options include the 2-loop corrections at $\mathcal{O}(\alpha_t\alpha_s)$. `tlCplxApprox`=1 uses no other 2-loop contributions. `tlCplxApprox`=2 also includes the sub-leading 2-loop corrections where parameters which were assumed to be real during the derivation are now taken to be the real parts of any complex parameters [74–78]. `tlCplxApprox`=3 calculates the sub-leading contributions at phase of π and $-\pi$ for each complex parameter and interpolates between these results.

Figure 4.1 compares the results for the lightest Higgs mass M_{h_1}, which have been calculated using various *FeynHiggs* options in the CPX scenario with $M_{H^+} = 140$ GeV. It can be seen that the 'recommended' setting of `tlCplxApprox`=3 is inappropriate for this scenario. This is because the CPX scenario is on the border of stable parameter space and thus one of the combinations of real parameters crosses the border into unstable parameter space, skewing the interpolation in favour of the unstable values. We therefore choose `tlCplxApprox`=1 throughout the rest of this thesis wherever *FeynHiggs* is used to calculate quantities in the complex MSSM.

FeynHiggs also allows the resummation of some corrections to the b-quark mass. (we will discuss this topic further in Section 5.3).

It is useful to consider the contribution that different types of corrections make to the neutral Higgs masses in the CPX scenario. These have been calculated using the programs *FeynArts* [41–43], *FormCalc* [43, 45] and *LoopTools* [45] and then checked for consistency with the results from *FeynHiggs*. As many of the techniques used here will be used for the $h_a h_b h_c$ vertex later, this is a very useful check of our calculation. In addition, it provides a very useful idea of the sensitivity of the CPX scenario to the various loop corrections in the Higgs sector, which will prove very valuable when analysing the Higgs cascade decays. Figure 4.2 shows the lightest Higgs mass as a function of $\tan\beta$. We show results for the m_t^4 approximation, the full 1-loop terms where m_b is evaluated at the scale of m_b and the full 1-loop terms where m_b is evaluated at the scale of m_t. Unless otherwise stated, we use a running top mass $m_t(m_t)$. Also shown is the result obtained from using self-energies from *FeynHiggs*, which include the $\mathcal{O}(\alpha_t\alpha_s)$ contributions and resummation of corrections to the b-quark mass. As expected, the m_t^4 approximation includes the bulk of the 1-loop corrections at low $\tan\beta$ but fails at higher $\tan\beta$ where

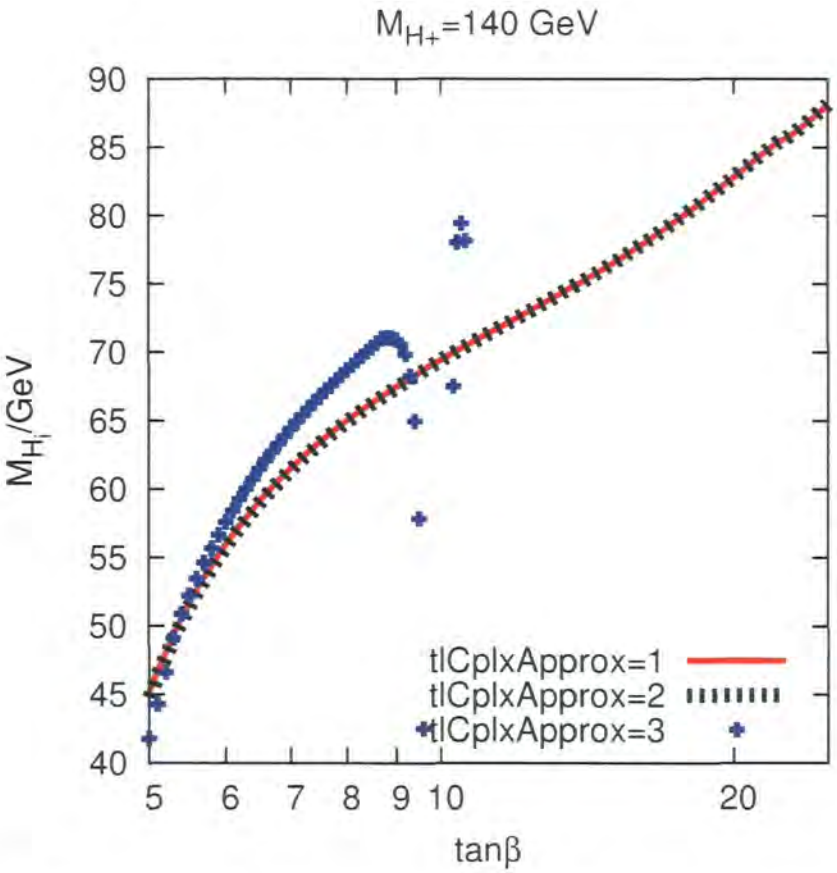

Figure 4.1: Comparison of different combinations of 2-loop corrections to the Higgs masses in the complex MSSM that are implemented in *FeynHiggs* [31, 56–58] through the flag `tlCplxApprox`. All of these options include the 2-loop corrections at $\mathcal{O}(\alpha_t\alpha_s)$. `tlCplxApprox`=1 uses no other 2-loop contributions. `tlCplxApprox`=2 also includes the sub-leading 2-loop corrections where the parameters that were assumed to be real during the derivation are now substituted with the real parts of the complex parameters. `tlCplxApprox`=3 calculates the sub-leading contributions at phase of π and $-\pi$ for each complex parameter and interpolates between these results.

terms from the sbottom sector are enhanced. If $m_b(m_b) = 4.20$ GeV is used, the scenario becomes unstable at around $\tan\beta = 20$. Some of the higher order QCD corrections can be taken into account through the use of $m_b(m_t)$. $m_b(m_t)$ is less than $m_b(m_b)$, so using $m_b(m_t)$ actually has the effect of reducing the impact of the bottom/sbottom sector at higher $\tan\beta$. Figure 4.2 also shows that the $\mathcal{O}(\alpha_t\alpha_s)$ corrections are very significant, which is well known also for the CP conserving case.

Figure 4.3 shows the effect of different approximations for the internal momentum p^2 on the lightest Higgs mass in the CPX scenario at $M_{H^-} = 140$ GeV, as described in Section 4.3. Here, for clarity, only 1-loop diagrams involving tops, stops, bottoms,

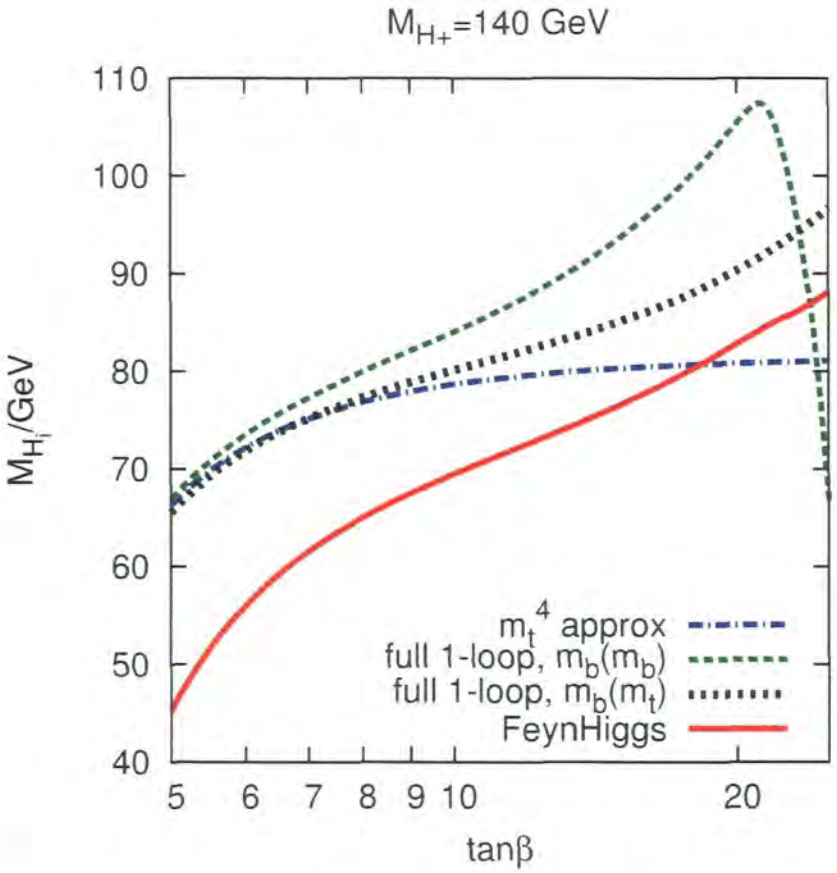

Figure 4.2: The lightest Higgs mass as a function of $\tan\beta$, in various approximations. 'm_t^4 approx' denotes the Higgs masses found if only the Yukawa term (which are proportional to m_t^4) are included in the neutral Higgs self-energies. We show the results of full 1-loop calculations in which m_b is either at the scale of m_b or m_t. Also shown are the full 1-loop terms where m_b is at the scale of m_b and m_t. Also shown is the full result from *FeynHiggs* [31, 56–58], which includes the leading $\mathcal{O}(\alpha_t\alpha_s)$ contributions and resummation of some corrections to the b-quark mass.

sbottoms are included. It can be seen that both approximations work fairly well but are still noticeably different to the full $t, \tilde{t}, b, \tilde{b}$ result.

4.4 Loop corrected propagators expressed in terms of self-energies

Although we have derived relations between the Higgs renormalised self-energies and Higgs propagators explicitly using equation (4.3), we will now introduce a pictorial

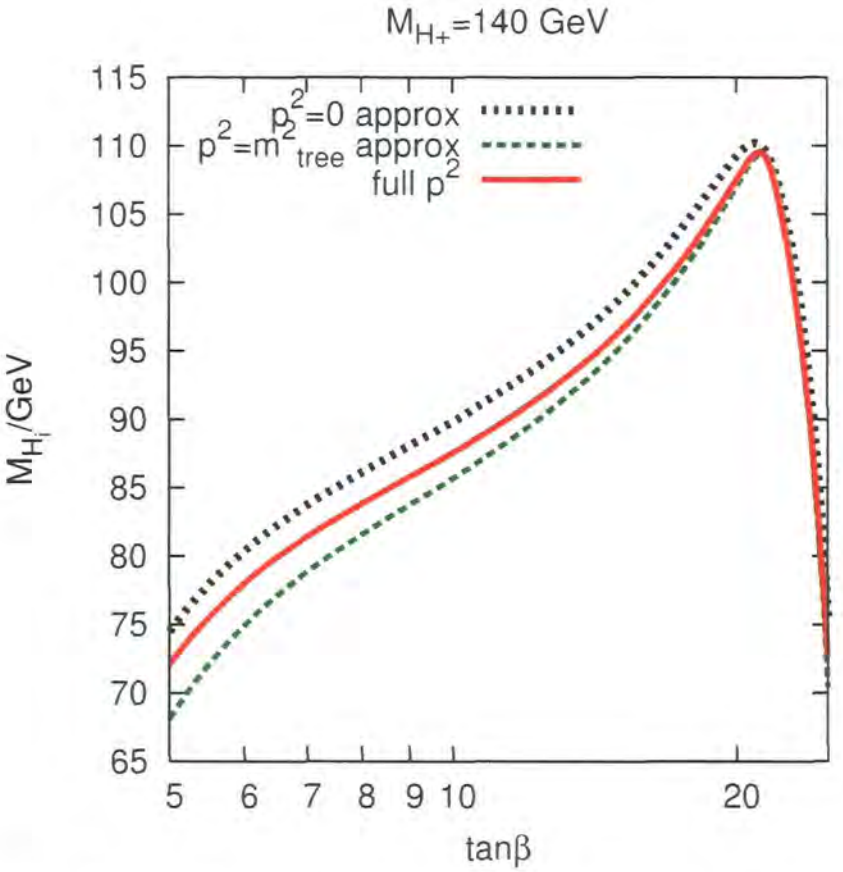

Figure 4.3: The effect of different approximations for the internal momentum p^2 on the lightest Higgs mass as a function of $\tan\beta$, using the 1-loop top, stop, bottom, sbottom contributions only. (see Section 4.3 for details of approximations)

notation which we feel gives a more intuitive understanding of the system. We start from the usual tree level h propagator.

tree level propagator

$$\underset{h}{\text{- - - - - - - - - - - - - - -}} = \frac{i}{p^2 - m_h^2}.$$

We combine this with the renormalised self-energy $\hat{\Sigma}_{hh}$ to get the

no-mixing loop-corrected propagator

$$\underset{\hat{\Sigma}_{hh}}{\bigcirc} \rightarrow \underset{\text{- - - - - - - - - - - - - - -}}{\overset{h \qquad\qquad h}{}} = \frac{i}{p^2 - m_h^2 + \hat{\Sigma}_{hh}(p^2)} =: \frac{i}{Y_h(p^2)}.$$

All the possible combinations of $\hat{\Sigma}_{hh}$ and tree level h propagators have been collectively rewritten by putting the piece $\hat{\Sigma}_{hh}$ in the denominator of the tree level propagator. In other words, we have resummed $\hat{\Sigma}_{hh}$ in the usual way in order to get the standard result for a loop-corrected propagator in the case of no Higgs mixing, which we represent in our pictorial notation with two dashed lines. We have also introduced the notation $Y_h(p^2) = p^2 - m_h^2 + \hat{\Sigma}_{hh}(p^2)$.

In order to include mixing between h and A, we require the

2-particle mixing loop-corrected propagator

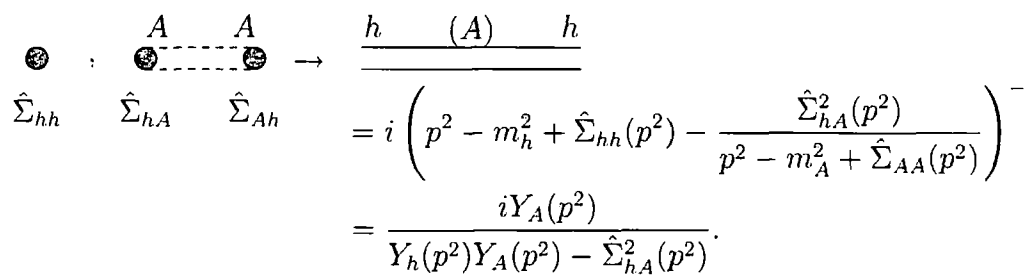

$$= i\left(p^2 - m_h^2 + \hat{\Sigma}_{hh}(p^2) - \frac{\hat{\Sigma}_{hA}^2(p^2)}{p^2 - m_A^2 + \hat{\Sigma}_{AA}(p^2)}\right)^{-1}$$

$$= \frac{iY_A(p^2)}{Y_h(p^2)Y_A(p^2) - \hat{\Sigma}_{hA}^2(p^2)}.$$

We have combined the tree level h propagator with a $\hat{\Sigma}_{hh}$ as before but also with a piece composed of a no-mixing loop-corrected A propagator with a $\hat{\Sigma}_{hA}$ on either end. Summing these pieces by putting them in the denominator as before has given us the 2-particle mixing loop-corrected propagator, which starts and ends on a tree level h propagator. We represent this using two solid lines, labelled at either end by h, and labelled in the centre by the other particle involved.

In order to extend this to a propagator involving mixing between 3 particles, we need to combine the tree level h propagator with pieces involving mixing between H and A, to get the

3-particle mixing loop-corrected propagator

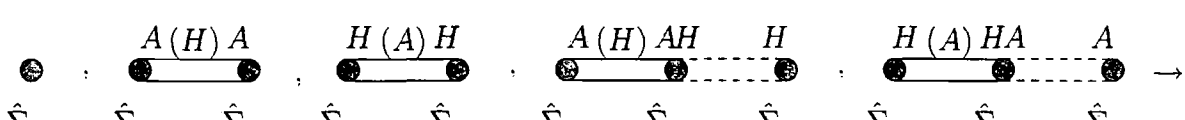

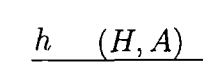

$$= i\left(Y_h + \frac{-\hat{\Sigma}_{hA}^2 Y_H - \hat{\Sigma}_{hH}^2 Y_A + 2\hat{\Sigma}_{hA}\hat{\Sigma}_{hH}\hat{\Sigma}_{HA}}{Y_H Y_A - \hat{\Sigma}_{HA}^2}\right)^{-1}. \qquad (4.27)$$

Here, each piece needs to begin and end on a renormalised self-energy involving a h. In order to make sure we have included all possible combinations, we require the five separate pieces, which, once again, we put in the denominator. Each self-energy and Y_i has the argument p^2, which has been omitted in this expression for brevity. We have denoted the 3-particle mixing loop-corrected propagator by three solid lines, labelled at either end with the tree level propagator which begins and ends the loop-corrected propagator and labelled in the centre with the other particles involved. We can write this 3-particle mixing loop-corrected propagator in terms of an effective self-energy $\hat{\Sigma}^{\text{eff}}_{hh}(p^2)$.

$$\Delta_{hh}(p^2) \;=\; \overset{h \quad (H,A) \quad h}{\Longrightarrow\!\!\Longrightarrow\!\!\Longrightarrow} \;= i\left(1+\hat{\Sigma}^{\text{eff}}_{hh}(p^2)\right)^{-1}. \tag{4.28}$$

This method can easily be extended to cases in which more than three particles mix.

We shall now investigate the combination $\Delta_{ij}(p^2)/\Delta_{ii}(p^2)$, in which an off-diagonal element of the propagator matrix is divided by a diagonal element. Using equation (4.3), we can expand this combination in terms of self-energies and tree level propagators to get

$$\begin{aligned}
\frac{\Delta_{hH}(p^2)}{\Delta_{hh}(p^2)} &= \frac{\hat{\Sigma}_{hA}(p^2)\hat{\Sigma}_{HA}(p^2) - \hat{\Sigma}_{hH}(p^2)Y_A(p^2)}{Y_H(p^2)Y_A(p^2) - \hat{\Sigma}^2_{HA}(p^2)} \\
&= i\hat{\Sigma}_{hH}(p^2)\frac{i}{p^2-m_H^2} \\
&+ i\hat{\Sigma}_{hH}(p^2)\frac{i}{p^2-m_H^2}i\hat{\Sigma}_{HH}(p^2)\frac{i}{p^2-m_H^2} \\
&+ i\hat{\Sigma}_{hA}(p^2)\frac{i}{p^2-m_A^2}i\hat{\Sigma}_{HA}(p^2)\frac{i}{p^2-m_H^2} \\
&+ \mathcal{O}(\text{3-loop}).
\end{aligned} \tag{4.29}$$

We can see that the combination $\Delta_{hH}(p^2)/\Delta_{hh}(p^2)$ represents terms which start on the self-energy $\hat{\Sigma}_{hH}(p^2)$ or $\hat{\Sigma}_{hA}(p^2)$ and end on the H tree level propagator. It contains no self-energy of the type $\hat{\Sigma}_{hh}(p^2)$ and contains no h tree level propagators.

Therefore, we can express $\Delta_{hH}(p^2)/\Delta_{hh}(p^2)$ in our pictorial notation as

$$\frac{\Delta_{hH}(p^2)}{\Delta_{hh}(p^2)} \;=\; \overset{A \qquad AH\,(A)\,H}{\bullet\!\!-\!\!-\!\!-\!\!-\!\!\bullet\!\!-\!\!-\!\!-\!\!-} \;+\; \overset{H\,(A)\,H}{\bullet\!\!-\!\!-\!\!-\!\!-} \tag{4.30}$$

$\hat{\Sigma}_{hA} \qquad \hat{\Sigma}_{AH} \qquad\qquad \hat{\Sigma}_{hH}$

If these diagrams were attached to a $\hat{\Sigma}_{hH}$, they would be identical to the third and fourth pieces which make up the 3-particle mixing loop-corrected propagator in equation (4.27).

This leads to a compact expression for the 3-particle mixing loop-corrected propagator $\Delta_{hh}(p^2)$, in terms of an effective self-energy $\hat{\Sigma}^{\text{eff}}_{hh}(p^2)$ as before.

$$\Delta_{hh}(p^2) = \frac{i}{p^2 - m_i^2 + \hat{\Sigma}^{\text{eff}}_{hh}(p^2)}, \tag{4.31}$$

$$\hat{\Sigma}^{\text{eff}}_{hh}(p^2) = \hat{\Sigma}_{hh}(p^2) + \frac{\Delta_{hH}(p^2)}{\Delta_{hh}(p^2)}\hat{\Sigma}_{hH}(p^2) + \frac{\Delta_{hA}(p^2)}{\Delta_{hh}(p^2)}\hat{\Sigma}_{hA}(p^2). \tag{4.32}$$

Using this relation (which can also be derived straight from equation (4.3)) we can rewrite equation (4.2) in the form

$$\mathcal{M}^2_{h_a} - m_i^2 + \hat{\Sigma}^{\text{eff}}_{ii}(\mathcal{M}^2_{h_a}) = 0, \tag{4.33}$$

where $i = h$, H or A and there is no sum over i. Note that for any particular i, this equation holds for $h_a = h_1, h_2$ or h_3. It is also worth noting that we should not expand the effective self-energy $\hat{\Sigma}^{\text{eff}}_{ii}$ about $p^2 = M^2_{h_a}$ directly, since the presence of Y_j, Y_k terms result in large higher order terms. Expanding the individual self-energies $\hat{\Sigma}$ contained within $\hat{\Sigma}^{\text{eff}}_{ii}$, according to equation (4.24) as before, avoids this problem.

4.5 Wave function normalisation factors

In order to ensure that the S-matrix is correctly normalised, we need to ensure that the residues of the propagators are set to one. We achieve this by including finite wave function normalisation factors which are composed of the renormalised self-energies. These 'Z-factors' can be collected in to a matrix $\hat{\mathbf{Z}}$ where

$$\lim_{p^2 \to \mathcal{M}^2_{h_a}} -\frac{i}{p^2 - \mathcal{M}^2_{h_a}} \left(\hat{\mathbf{Z}} \cdot \hat{\mathbf{\Gamma}}_2 \cdot \hat{\mathbf{Z}}^T\right)_{hh} = 1, \tag{4.34}$$

$$\lim_{p^2 \to \mathcal{M}^2_{h_b}} -\frac{i}{p^2 - \mathcal{M}^2_{h_b}} \left(\hat{\mathbf{Z}} \cdot \hat{\mathbf{\Gamma}}_2 \cdot \hat{\mathbf{Z}}^T\right)_{HH} = 1, \tag{4.35}$$

$$\lim_{p^2 \to \mathcal{M}^2_{h_c}} -\frac{i}{p^2 - \mathcal{M}^2_{h_c}} \left(\hat{\mathbf{Z}} \cdot \hat{\mathbf{\Gamma}}_2 \cdot \hat{\mathbf{Z}}^T\right)_{AA} = 1, \tag{4.36}$$

such that

$$\begin{pmatrix} \hat{\Gamma}_{h_a} \\ \hat{\Gamma}_{h_b} \\ \hat{\Gamma}_{h_c} \end{pmatrix} = \hat{\mathbf{Z}} \cdot \begin{pmatrix} \hat{\Gamma}_h \\ \hat{\Gamma}_H \\ \hat{\Gamma}_A \end{pmatrix} . \tag{4.37}$$

where $\hat{\Gamma}_{h_a}$ is a one-particle irreducible n-point vertex-function which involves a single external Higgs h_a and h_a, h_b, h_c = some combination of h_1, h_2, h_3.

The matrix $\hat{\mathbf{Z}}$ is non-unitary. We write it as

$$\hat{\mathbf{Z}} = \begin{pmatrix} \sqrt{Z_h} & \sqrt{Z_h} Z_{hH} & \sqrt{Z_h} Z_{hA} \\ \sqrt{Z_H} Z_{Hh} & \sqrt{Z_H} & \sqrt{Z_H} Z_{HA} \\ \sqrt{Z_A} Z_{Ah} & \sqrt{Z_A} Z_{AH} & \sqrt{Z_A} \end{pmatrix} . \tag{4.38}$$

We find the elements of $\hat{\mathbf{Z}}$ by solving equation (4.34), which gives

$$Z_h = \frac{1}{\frac{\partial}{\partial p^2}\left(\frac{i}{\Delta_{hh}(p^2)}\right)\Big|_{p^2=\mathcal{M}^2_{h_a}}} , \quad Z_H = \frac{1}{\frac{\partial}{\partial p^2}\left(\frac{i}{\Delta_{HH}(p^2)}\right)\Big|_{p^2=\mathcal{M}^2_{h_b}}} , \quad Z_A = \frac{1}{\frac{\partial}{\partial p^2}\left(\frac{i}{\Delta_{AA}(p^2)}\right)\Big|_{p^2=\mathcal{M}^2_{h_c}}} \tag{4.39}$$

$$Z_{hH} = \left.\frac{\Delta_{hH}}{\Delta_{hh}}\right|_{p^2=\mathcal{M}^2_{h_a}} , \quad Z_{Hh} = \left.\frac{\Delta_{hH}}{\Delta_{HH}}\right|_{p^2=\mathcal{M}^2_{h_b}} , \quad Z_{Ah} = \left.\frac{\Delta_{hA}}{\Delta_{AA}}\right|_{p^2=\mathcal{M}^2_{h_c}} , \tag{4.40}$$

$$Z_{hA} = \left.\frac{\Delta_{hA}}{\Delta_{hh}}\right|_{p^2=\mathcal{M}^2_{h_a}} , \quad Z_{HA} = \left.\frac{\Delta_{HA}}{\Delta_{HH}}\right|_{p^2=\mathcal{M}^2_{h_b}} , \quad Z_{AH} = \left.\frac{\Delta_{HA}}{\Delta_{AA}}\right|_{p^2=\mathcal{M}^2_{h_c}} . \tag{4.41}$$

We choose $h_a = h_1$, $h_b = h_2$ and $h_c = h_3$. The square root is taken such that $\sqrt{Z_i}\sqrt{Z_i} = Z_i$, where Z_i is, in general, complex. Other choices for the Z-factors are possible, such as that in [79], where we use the limit $p^2 = M^2_{h_{1,2,3}}$. However, this does not allow the same freedom for choosing a, b, c and also is less stable numerically.

The elements of $\hat{\mathbf{Z}}$ involve evaluating self-energies at complex momenta. The expansion in equation (4.24) is used. In order to make sure that the neglected higher order terms in equation (4.24) are small, we also calculate $\hat{\mathbf{Z}}$ using equation (4.26), and check that the results are not significantly different.

We include the matrix $\hat{\mathbf{Z}}$ once for each external Higgs boson involved in the process, such that

$$\begin{aligned}
\hat{\Gamma}_{h_a} &= \hat{\mathbf{Z}}_{ai}\hat{\Gamma}_i, \\
\hat{\Gamma}_{h_a h_b} &= \hat{\mathbf{Z}}_{bj}\hat{\mathbf{Z}}_{ai}\hat{\Gamma}_{ij}, \\
\hat{\Gamma}_{h_a h_b h_c} &= \hat{\mathbf{Z}}_{ck}\hat{\mathbf{Z}}_{bj}\hat{\mathbf{Z}}_{ai}\hat{\Gamma}_{ijk}.
\end{aligned}$$

Again, we can use our pictorial representation to get a more intuitive understanding of these contributions. For example, applying the Z-factors to a decay of a neutral Higgs in to a fermion, anti-fermion pair gives

$$\hat{\Gamma}_{h_1 f\bar{f}} = \hat{\mathbf{Z}}_{ai}\hat{\Gamma}_i = \sqrt{Z_h}\left(\hat{\Gamma}_{hf\bar{f}} + Z_{hH}\hat{\Gamma}_{Hf\bar{f}} + Z_{hA}\hat{\Gamma}_{Af\bar{f}}\right),$$

which can be represented as

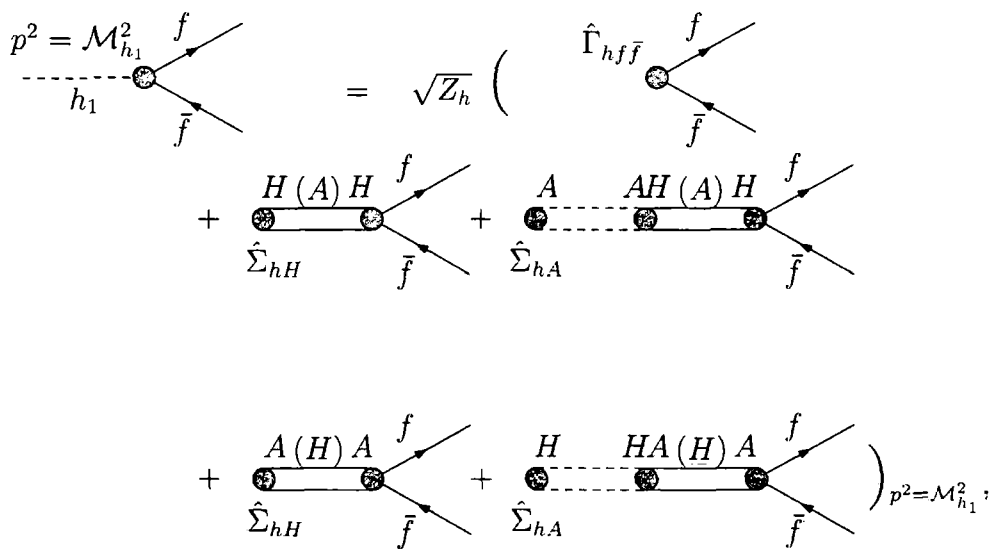

(4.42)

i.e. $\sqrt{Z_h}$ gives an overall normalisation factor which depends on the 3-particle mixing loop-corrected hh propagator, while Z_{ij} are composed of $\frac{\Delta_{ij}}{\Delta_{ii}}$ from equation (4.30), taken at incoming momentum $p^2 = \mathcal{M}^2_{h_1}$. The $\frac{\Delta_{ij}}{\Delta_{ii}}$ are present in order to take into account diagrams which have a H or A tree level Higgs propagator directly connecting to the fermions, as opposed to a h tree level propagator.

As we have discussed, the Z-factors are designed to ensure the correct normalisation of an S-matrix containing external Higgs bosons. However, they are an approximation

which attempts to compensate for the fact that we are treating an unstable particle as an external particle. Strictly, the entire decay and production process should be taken into account.

As an explicit example, we consider the case where two processes with external Higgs are combined to make one process with an internal Higgs, using the narrow width approximation (see Appendix B). We consider the case where two arbitrary scalar particles annihilate into a h_1 (at a vertex labelled by a) and the h_1 subsequently decays into two arbitrary scalar particles (at a vertex labelled by b). We use our pictorial notation to ensure that we consider every possible combination of self-energies and tree level propagators in the internal h_1 propagator:

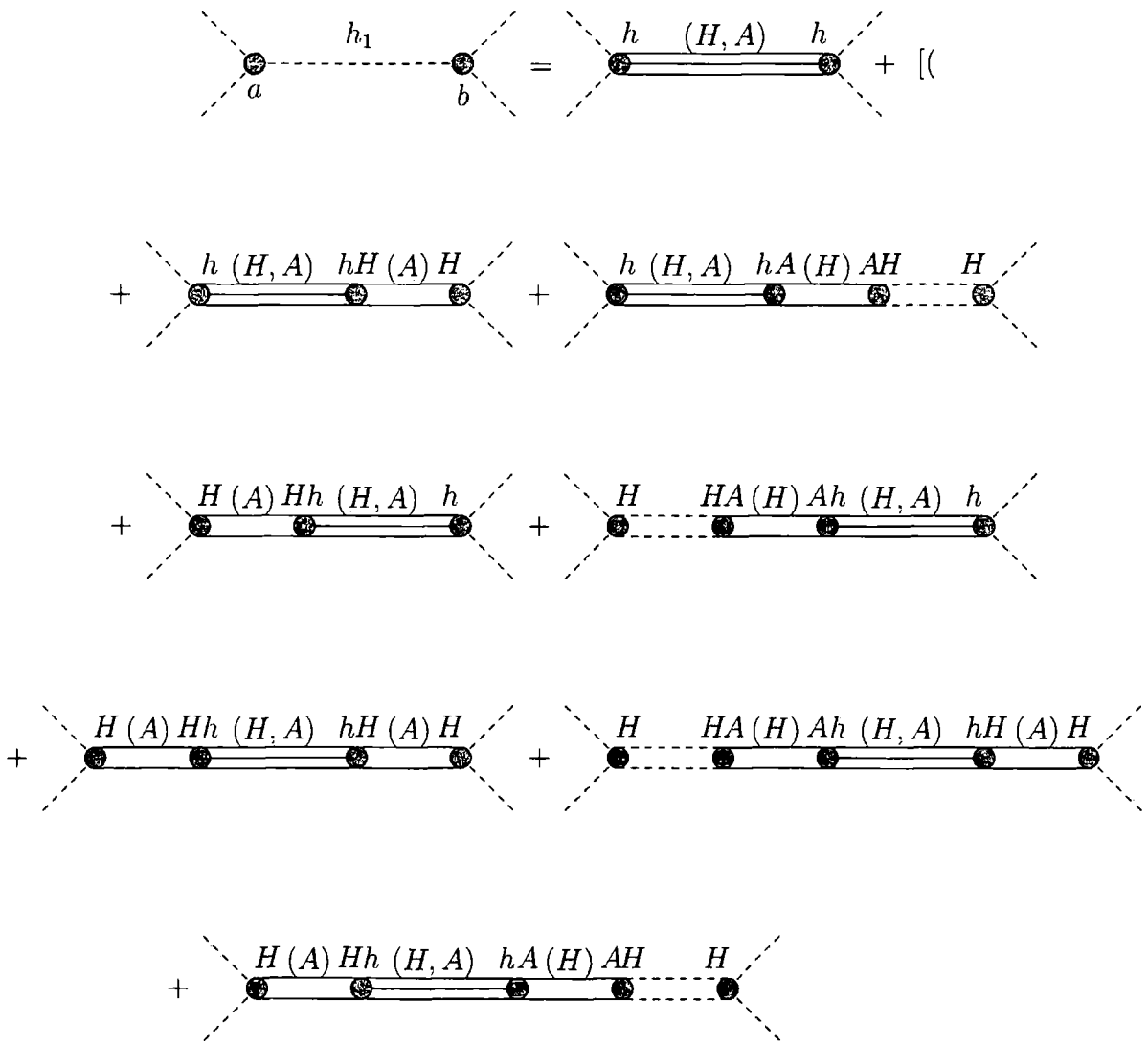

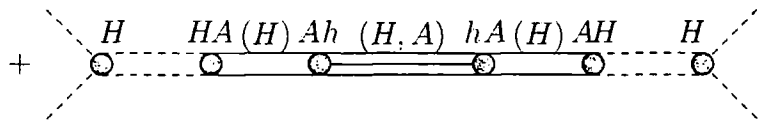

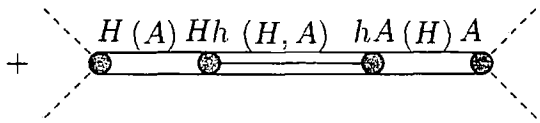

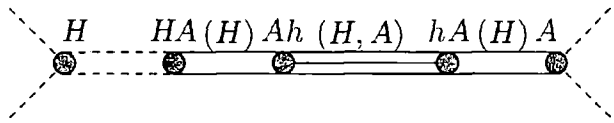

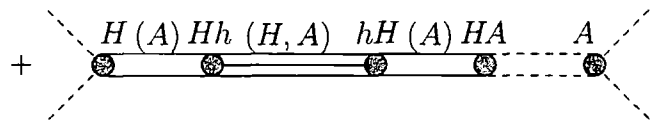

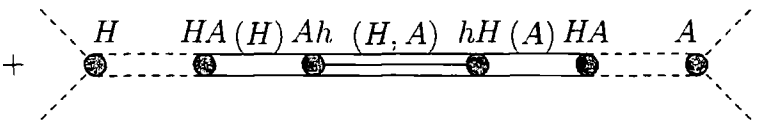

$$) + (H \leftrightarrow A)] \,. \tag{4.43}$$

As explained previously, the different types of propagators can be combined and written as

$$\left(\Gamma_h^a + \frac{\Delta_{hH}(p^2)}{\Delta_{hh}(p^2)}\Gamma_H^a + \frac{\Delta_{hA}(p^2)}{\Delta_{hh}(p^2)}\Gamma_A^a\right)\Delta_{hh}(p^2)\left(\Gamma_h^b + \frac{\Delta_{hH}(p^2)}{\Delta_{hh}(p^2)}\Gamma_H^b + \frac{\Delta_{hA}(p^2)}{\Delta_{hh}(p^2)}\Gamma_A^b\right). \tag{4.44}$$

In general, the $\Gamma_i^{a,b}$ also depend on p^2 but this is left out here for simplicity. Expanding the resummed propagator about $p^2 = \mathcal{M}_{h_1}^2$ gives

$$\begin{aligned} \frac{i}{p^2 + m_h^2 + \hat{\Sigma}_{hh}^{\text{eff}}(p^2)} &= \frac{i}{p^2 - \mathcal{M}_1^2} \left(\frac{1}{1 + \left(\hat{\Sigma}_{hh}^{\text{eff}}\right)'(\mathcal{M}_1^2) + \ldots} \right) \\ &= \frac{i}{p^2 - \mathcal{M}_1^2} Z_h. \end{aligned} \tag{4.45}$$

This $\frac{i}{p^2 - \mathcal{M}_1^2}$ becomes a δ-function in the limit of vanishing width. Therefore, in the narrow width approximation (see Appendix B), we get

$$\left| \sqrt{Z_h} \left(\Gamma_h^a + Z_{hH} \Gamma_H^a + Z_{hA} \Gamma_A^a \right) \right|^2 \left| \sqrt{Z_h} \left(\Gamma_h^b + Z_{hH} \Gamma_H^b + Z_{hA} \Gamma_A^b \right) \right|^2, \tag{4.46}$$

as we would expect from applying the Z-factors to the two processes a and b separately and combining them.

Therefore, we expect that using the Z-factors improves the treatment of imaginary parts in situations in which it is impractical to calculate the full production and decay process.

4.6 Normalised effective Higgs couplings to gauge bosons

Using the $p^2 = 0$ approximation for the renormalised self-energies results in real Z-factors and the matrix $\mathbf{Z}$ becomes a unitary rotation matrix $\hat{\mathbf{U}}$, such that

$$\begin{pmatrix} M_{h_a,U}^2 & 0 & 0 \\ 0 & M_{h_b,U}^2 & 0 \\ 0 & 0 & M_{h_c,U}^2 \end{pmatrix} = \hat{\mathbf{U}} \cdot \mathbf{M}_U \cdot \hat{\mathbf{U}}^\dagger, \tag{4.47}$$

i.e. $\hat{\mathbf{U}}$ diagonalises $\mathbf{M}_U$. This also leads to a simple expression for $Z_{i,U}$,

$$Z_{i,U} = \frac{1}{1 + Z_{ij,U}^2 + Z_{ik,U}^2}. \tag{4.48}$$

This rotation matrix can be used to create a normalised effective coupling between neutral Higgs bosons and Z bosons,

$$g_{h_aZZ,U} = \mathbf{U}_{ai} g^{\text{tree}}_{h_iZZ}. \tag{4.49}$$

where $g^{\text{tree}}_{h_iZZ}$ are derived from Section 2.5 and normalised to the SM coupling, such that $(g^{\text{tree}}_{hZZ})^2 = \sin^2(\beta-\alpha)$, $(g^{\text{tree}}_{HZZ})^2 = \cos^2(\beta-\alpha)$ and $(g^{\text{tree}}_{AZZ})^2 = 0$. This leads to the simple relations $g^2_{h_1ZZ,U} + g^2_{h_2ZZ,U} + g^2_{h_3ZZ,U} = 1$ and $g^2_{h_aZZ,U} = g^2_{h_bh_bZ,U}$, where h_a, h_b, h_c are all different.

However, the Higgs propagator corrections for external Higgs bosons are more fully taken into account if the effective couplings between Higgs and gauge bosons are obtained through the use of the full matrix $\mathbf{Z}$, such that

$$g^{\text{eff}}_{h_aZZ} = \mathbf{Z}_{ai} g^{\text{tree}}_{h_iZZ}, \tag{4.50}$$

$$g^{\text{eff}}_{h_ah_bZ} = \mathbf{Z}_{bj}\mathbf{Z}_{ai} g^{\text{tree}}_{h_ih_jZ}. \tag{4.51}$$

As before, we have normalised $g^{\text{tree}}_{h_iZZ}$ to the SM coupling. In addition, we normalise the $g^{\text{tree}}_{h_ih_jZ}$ such that $(g^{\text{tree}}_{hAZ})^2 = \cos^2(\beta-\alpha)$ and $(g^{\text{tree}}_{HAZ})^2 = \sin^2(\beta-\alpha)$ (all other $g^{\text{tree}}_{h_ih_jZ}$ are zero).

Since $\mathbf{Z}$ is not unitary, we now have the approximate relations $|g^{\text{eff}}_{h_1ZZ}|^2 + |g^{\text{eff}}_{h_2ZZ}|^2 + |g^{\text{eff}}_{h_3ZZ}|^2 \sim 1$ and $|g^{\text{eff}}_{h_aZZ}|^2 \sim |g^{\text{eff}}_{h_bh_bZ}|^2$, where h_a, h_b, h_c are all different.

We will make use of both types of effective couplings during the course of this thesis.

4.7 Goldstone or gauge bosons mixing contributions to the Higgs propagators

For any full 1-loop calculation involving a Higgs propagator, the self-energies $\hat{\Sigma}_{hG}$, $\hat{\Sigma}_{HG}$, $\hat{\Sigma}_{AG}$ and $\hat{\Sigma}_{hZ}$, $\hat{\Sigma}_{HZ}$, $\hat{\Sigma}_{AZ}$ also need to be included, such as in the example shown in Figure 4.4. Although their numerical contribution will turn out to be very small, these diagrams will have a gauge parameter dependence which cancels out the gauge parameter dependence in other parts in the 1-loop calculation.

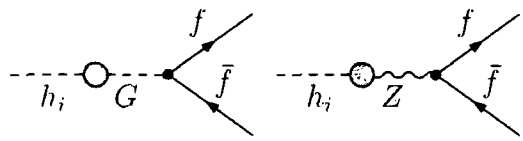

Figure 4.4: Goldstone and Z boson propagator corrections to the $h_i \to f\bar{f}$ decay, where $h_i = h, H$ or A

We will use the lowest order Z-boson propagator containing explicit gauge parameter dependence,

$$\frac{-ig_{\mu\nu}}{k^2 - M_Z^2} + i\frac{(1-\xi_Z)k_\mu k_\nu}{(k^2 - M_Z^2)(k^2 - \xi_Z M_Z^2)}. \tag{4.52}$$

This rearranges to

$$\frac{-ig_{\mu\nu}}{k^2 - M_Z^2} + \frac{k_\mu k_\nu}{k^2}\frac{i}{(k^2 - M_Z^2)} - \frac{k_\mu k_\nu}{k^2}\frac{i\xi_Z}{(k^2 - \xi_Z M_Z^2)}, \tag{4.53}$$

where all the gauge parameter dependence is conveniently contained in the last term. We use the G-boson propagator

$$\frac{i}{k^2 - \xi_Z M_Z^2}. \tag{4.54}$$

Since we will be attaching Z-factors to the Higgs propagators, our calculation will not be restricted solely to 1-loop pieces. Inevitably, our result will have a slight gauge parameter dependence that is formally of higher order. However, we need to make sure that the gauge parameter dependence completely cancels at the strict 1-loop level without introducing an unphysical pole (whose position is gauge-parameter dependent) in to the rest of the calculation. This requires a detailed understanding of the behaviour of the Goldstone and gauge bosons mixing contributions.

Using a Feynman-diagrammatic calculation, we find that the following relations hold:

$$\begin{aligned}
M_Z\Sigma_{\phi_2 G}(p^2) + ip^2\Sigma_{\phi_2 Z}(p^2) &= -\frac{e}{2c_W s_W}c_\beta t_A, \\
M_Z\Sigma_{\phi_1 G}(p^2) + ip^2\Sigma_{\phi_1 Z}(p^2) &= \frac{e}{2c_W s_W}s_\beta t_A, \\
M_Z\Sigma_{AG}(p^2) + ip^2\Sigma_{AZ}(p^2) + M_Z(p^2 - m_A^2)f_0(p^2) &= \frac{e}{2c_W s_W}\left(c_\beta t_{\phi_2} - s_\beta t_{\phi_1}\right), \\
M_Z\Sigma_{GG}(p^2) + 2ip^2\Sigma_{GZ}(p^2) - \frac{p^2}{M_Z}\Sigma_{ZZ}^L(p^2) &= \frac{e}{2c_W s_W}\left(s_\beta t_{\phi_2} + c_\beta t_{\phi_1}\right), \\
M_W\Sigma_{H\text{-}G^+}(p^2) - p^2\Sigma_{H\text{-}W^+}(p^2) + M_W(p^2 - m_{H^\pm}^2)f_\pm(p^2) &= \frac{e}{2s_W}\left(c_\beta t_{\phi_2} - s_\beta t_{\phi_1} + it_A\right), \\
M_W\Sigma_{G\text{-}G^+}(p^2) - 2p^2\Sigma_{G\text{-}W^+}(p^2) - \frac{p^2}{M_W}\Sigma_{WW}^L(p^2) &= \frac{e}{2s_W}\left(s_\beta t_{\phi_2} + c_\beta t_{\phi_1}\right),
\end{aligned} \tag{4.55}$$

where

$$\begin{aligned}
f_0(p^2) &= -\frac{\alpha}{16\pi s_W^2 M_W^2}s_{\beta-\alpha}c_{\beta-\alpha}M_Z^2\xi_Z\left[B_0\left(p^2, m_h^2, M_Z^2\xi_Z\right) - B_0\left(p^2, m_H^2, M_Z^2\xi_Z\right)\right], \\
f_\pm(p^2) &= -\frac{\alpha}{16\pi s_W^2 M_W^2}s_{\beta-\alpha}c_{\beta-\alpha}M_W^2\xi_W\left[B_0\left(p^2, m_h^2, M_W^2\xi_W\right) - B_0\left(p^2, m_H^2, M_W^2\xi_W\right)\right].
\end{aligned} \tag{4.56}$$

$f_0, f_\pm$ are finite and disappear if the particle is on-shell.

In terms of renormalised quantities defined in equation (3.3.2), these become

$$\hat{\Sigma}_{hG}(p^2) + \frac{ip^2}{M_Z}\hat{\Sigma}_{hZ}(p^2) = 0, \tag{4.57}$$

$$\hat{\Sigma}_{HG}(p^2) + \frac{ip^2}{M_Z}\hat{\Sigma}_{HZ}(p^2) = 0, \tag{4.58}$$

$$\hat{\Sigma}_{AG}(p^2) + \frac{ip^2}{M_Z}\hat{\Sigma}_{AZ}(p^2) + (p^2 - m_A^2)f_0(p^2) = 0, \tag{4.59}$$

$$\hat{\Sigma}_{GG}(p^2) + \frac{2ip^2}{M_Z}\hat{\Sigma}_{GZ}(p^2) - \frac{p^2}{M_Z^2}\hat{\Sigma}_{ZZ}^L(p^2) = 0, \tag{4.60}$$

$$\hat{\Sigma}_{H\text{-}G^+}(p^2) - \frac{p^2}{M_W}\hat{\Sigma}_{H\text{-}W^+}(p^2) + (p^2 - m_{H^\pm}^2)f_\pm(p^2) = 0. \tag{4.61}$$

$$\hat{\Sigma}_{G\text{-}G^+}(p^2) - \frac{2p^2}{M_W}\hat{\Sigma}_{G\text{-}W^+}(p^2) - \frac{p^2}{M_W^2}\hat{\Sigma}_{WW}^L(p^2) = 0. \tag{4.62}$$

These relations have been checked algebraically using the $t, \tilde{t}, b, \tilde{b}$ sector and the gauge and Higgs boson sector. These relations have also been checked numerically for the entire MSSM. These relations simplify in the CP-conserving case.

This means that diagrams involving mixing with Z can be expressed in terms of diagrams involving mixing with G.

As an example, we will look at diagrams involving a neutral Higgs decaying to two fermions via a self-energy, as in Figure 4.4. We can use the fact that, for a two body decay into on-shell particles with identical mass,

$$\begin{aligned} \mathcal{M}_1 &= \overline{u}_3 \left[A + B\gamma_5 + (C + D\gamma_5)\not{p}\right] v_2, \\ \mathcal{M}_2 &= \overline{u}_3 \left[A + (B - 2m_f D)\gamma_5\right] v_2, \\ \sum_{\text{all spins}} \mathcal{M}_1 \mathcal{M}_1^* &= \sum_{\text{all spins}} \mathcal{M}_2 \mathcal{M}_2^*. \end{aligned} \tag{4.63}$$

This means that, instead of using the usual $Zf\overline{f}$ coupling (involving $\not{p}$), we can use a coupling $p_\nu \Gamma^{\text{tree}}_{\text{Zff}}$ which is given in terms of $\Gamma^{\text{tree}}_{\text{Gff}}$, i.e.

$$p_\nu \Gamma^{\text{tree}}_{\text{Zff}} = -i \frac{M_Z}{p^2} p_\nu \Gamma^{\text{tree}}_{\text{Gff}}. \tag{4.64}$$

We can then directly compare the two contributions at the level of the matrix element.

For the $h \to f\bar{f}$ decay with incoming momentum p^2 (Figure 4.4 with $h_i = h$),

$$\begin{aligned} &i\hat{\Sigma}_{hG}(p^2) \frac{i}{p^2 - M_Z^2 \xi_Z} \Gamma^{\text{tree}}_{\text{Gff}} + ip^\nu \hat{\Sigma}_{hZ}(p^2) \frac{-i\xi_Z p_\mu p_\nu}{p^2(p^2 - M_Z^2 \xi_Z)} p^\mu \Gamma^{\text{tree}}_{\text{Zff}} \\ &= -\frac{\Gamma^{\text{tree}}_{\text{Gff}}}{p^2} \hat{\Sigma}_{hG}(p^2), \end{aligned} \tag{4.65}$$

which does not contain a pole at $p^2 = M_Z^2 \xi_Z$. However, for the decay $A \to f\bar{f}$ via a self-energy (Figure 4.4 with $h_i = A$),

$$\begin{aligned} &i\hat{\Sigma}_{AG}(p^2) \frac{i}{p^2 - M_Z^2 \xi_Z} \Gamma^{\text{tree}}_{\text{Gff}} + ip^\nu \hat{\Sigma}_{AZ}(p^2) \frac{-i\xi_Z p_\mu p_\nu}{p^2(p^2 - M_Z^2 \xi_Z)} p^\mu \Gamma^{\text{tree}}_{\text{Zff}} \\ &= -\frac{\Gamma^{\text{tree}}_{\text{Gff}}}{p^2} \left(\hat{\Sigma}_{AG}(p^2) - (p^2 - m_A^2) f_0(p^2) \frac{M_Z^2 \xi_Z}{p^2 - M_Z^2 \xi_Z} \right), \end{aligned} \tag{4.66}$$

which is problematic because the existence of the f_0 prevents the cancellation of the pole at $p^2 = M_Z^2 \xi_Z$. However, this term vanishes if the tree level mass is used for the

incoming momentum i.e. $p^2 = m_A^2$. This means that, in a strict 1-loop expansion (where the Z-factors are also expanded), the Higgs-fermion-fermion vertex is

$$h : -\frac{\hat{\Sigma}'_{hh}(m_h^2)}{2}\Gamma^{\text{tree}}_{\text{hff}} - \frac{\hat{\Sigma}_{hH}(m_h^2)}{m_h^2 - m_H^2}\Gamma^{\text{tree}}_{\text{Hff}} - \frac{\hat{\Sigma}_{hA}(m_h^2)}{m_h^2 - m_A^2}\Gamma^{\text{tree}}_{\text{Aff}} - \frac{\hat{\Sigma}_{hG}(m_h^2)}{m_h^2}\Gamma^{\text{tree}}_{\text{Gff}} + \Gamma^{\text{1-loop}}_{\text{hff}},$$

$$H : -\frac{\hat{\Sigma}'_{HH}(m_H^2)}{2}\Gamma^{\text{tree}}_{\text{Hff}} - \frac{\hat{\Sigma}_{hH}(m_H^2)}{m_H^2 - m_h^2}\Gamma^{\text{tree}}_{\text{hff}} - \frac{\hat{\Sigma}_{HA}(m_H^2)}{m_H^2 - m_A^2}\Gamma^{\text{tree}}_{\text{Aff}} - \frac{\hat{\Sigma}_{HG}(m_H^2)}{m_H^2}\Gamma^{\text{tree}}_{\text{Gff}} + \Gamma^{\text{1-loop}}_{\text{Hff}},$$

$$A : -\frac{\hat{\Sigma}'_{AA}(m_A^2)}{2}\Gamma^{\text{tree}}_{\text{Aff}} - \frac{\hat{\Sigma}_{HA}(m_A^2)}{m_A^2 - m_H^2}\Gamma^{\text{tree}}_{\text{Hff}} - \frac{\hat{\Sigma}_{hA}(m_A^2)}{m_A^2 - m_h^2}\Gamma^{\text{tree}}_{\text{hff}} - \frac{\hat{\Sigma}_{AG}(m_A^2)}{m_A^2}\Gamma^{\text{tree}}_{\text{Gff}} + \Gamma^{\text{1-loop}}_{\text{Aff}}.$$

where m_h^2, m_H^2, m_A^2 are tree level masses as before and there are no poles dependent on ξ_Z. In fact, we have checked that these expressions are independent of ξ_Z numerically using *FeynArts* [41–43] and *FormCalc* [43, 45].

For the full calculation, we need to incorporate higher order results without recreating the pole at $p^2 = M_Z^2\xi_Z$. Therefore, whenever contributions involving mixing between h_i and G, Z bosons are included, they should be calculated at incoming momentum corresponding to the tree level mass, rather than the loop corrected mass.

So, for the example used above of the $h_a \to f\bar{f}$ decay, we would combine 'Z-factors', vertex corrections and Goldstone/Z boson mixing contributions by

$$\Gamma^{\text{full}}_{h_a f\bar{f}} = \hat{\mathbf{Z}}_{ai}\left[\Gamma^{\text{1PI}}_{h_i f\bar{f}}\left(M_{h_a}^2\right) + \Gamma^{\text{G,Zse}}_{h_i f\bar{f}}\left(m_{h_i}^2\right)\right]. \tag{4.67}$$

We could have chosen to multiply the $\Gamma^{\text{G,Zse}}_{h_i f\bar{f}}\left(m_{h_i}^2\right)$ by tree level Z-factors rather than the full Z-factors. The advantage of our choice is simply that there is no need to calculate these tree level 'Z-factors' (the tree level $\hat{\mathbf{Z}}$ elements are all either 1 or 0. However, $\hat{\mathbf{Z}}$ might not correspond to $\mathbb{1}$).

Similarly, for the triple Higgs decay, there are similar cancellations between the G and Z self-energy contributions which cancel the unphysical pole. Therefore, we can use

$$\Gamma^{\text{full}}_{h_a h_b h_c} = \hat{\mathbf{Z}}_{ck}\hat{\mathbf{Z}}_{bj}\hat{\mathbf{Z}}_{ai}\left[\Gamma^{\text{1PI}}_{h_i h_j h_k}\left(M_{h_a}^2, M_{h_b}^2, M_{h_c}^2\right) + \Gamma^{\text{G,Zse}}_{h_i h_j h_k}\left(m_{h_i}^2, m_{h_j}^2, m_{h_k}^2\right)\right]. \tag{4.68}$$

Chapter 5

Resummation of Standard Model and SUSY QCD corrections

In this chapter, we provide a brief introduction to elements of Standard Model QCD which we will require later in the thesis. We also outline a method to resum the potentially large SUSY QCD loop corrections to the Higgs to b-quark coupling, which includes a consistent treatment of the complex phases.

5.1 SM QCD corrections

We will discuss the Standard Model QCD corrections to the running of the strong coupling constant and the b-quark mass, which will be particularly relevant when calculating the $h_a \to b\bar{b}$ decay. For a general introduction to this area of QCD, see [80, 81]. Our conventions closely follow those of [82]. However, since we will be combining these results with the 1-loop QCD corrections to the $h_a \to b\bar{b}$ decay, we restrict the discussion to 1-loop order, as advised by [83]. This will avoid the inclusion of unnecessary renormalisation scheme-dependent higher order terms in the decay width in Section 7.2.2.

5.1.1 The running of the strong coupling constant in the Standard Model

In the Standard Model, the $\overline{\rm MS}$ QCD coupling α_s depends on the renormalisation scale $\mu_{\rm ren}$ through the relation

$$\mu_{\rm ren}\frac{\partial\alpha_s}{\partial\mu_{\rm ren}} = 2\beta(\alpha_s), \tag{5.1}$$

where

$$\beta(\alpha_s) = -\frac{\beta_0}{(4\pi)}\alpha_s^2 - \frac{\beta_1}{(4\pi)^2}\alpha_s^3 + \mathcal{O}(\alpha_s^4), \tag{5.2}$$

$$\beta_0 = 11 - \frac{2}{3}N_f, \tag{5.3}$$

$$\beta_1 = 102 - \frac{38}{3}N_f. \tag{5.4}$$

N_f is the number of active quarks i.e. the number of quarks with mass less than or equal to $\mu_{\rm ren}$.

The solution can be written (see e.g. [80]) as an expansion in inverse L_q where $L_q = \log\left(\frac{\mu_{\rm ren}^2}{(\Lambda_{\rm QCD}^{(n_f)})^2}\right)$, such that

$$\alpha_s(\mu_{\rm ren}^2) = \frac{4\pi}{\beta_0 L_q}\left(1 - \frac{\beta_1\log(L_q)}{\beta_0^2 L_q}\right) + \mathcal{O}\left(\frac{1}{L_q}\right)^3, \tag{5.5}$$

where $\Lambda_{\rm QCD}^{(n_f)}$ is a constant of integration, representing the scale at which the strong coupling becomes strong. We find $\Lambda_{\rm QCD}^{(5)}$ by numerically solving equation (5.5) for $\alpha_s(M_Z^2) = 0.118$, giving the result $\Lambda_{\rm QCD}^{(5)} = 227.0 \times 10^{-3}$ GeV.

We calculate $\Lambda_{\rm QCD}^{(6)}$ using the relation

$$\Lambda_{\rm QCD}^{(6)} = \Lambda_{\rm QCD}^{(5)}\left(\frac{m_t}{\Lambda_{\rm QCD}^{(5)}}\right)^{-2/21}\left[2\log\frac{m_t}{\Lambda_{\rm QCD}^{(5)}}\right]^{-107/1127}. \tag{5.6}$$

which we derive from requiring that $\alpha_s(\mu_{\rm ren}^2)$ is continuous at $\mu_{\rm ren}^2 = m_t^2$ up to first order terms. We find $\Lambda_{\rm QCD}^{(6)} = 94.42 \times 10^{-3}$ GeV for $m_t = 172.6$ GeV. This method gives $\alpha_s(m_t^2 = 172.6^2\ {\rm GeV}^2) = 0.1077$. This can be compared to the value $\alpha_s(m_t^2 = 172.6^2\ {\rm GeV}^2) = 0.1070$ given by [84], which includes higher order terms.

5.1.2 The running of the b-quark mass in the Standard Model

Calculating the gluon 1-loop correction to the b-quark mass in the on-shell scheme and in the $\overline{\text{MS}}$ scheme gives a relation between the on-shell b-quark mass m_b^{pole} and the $\overline{\text{MS}}$ b-quark mass $m_b(\mu_{\text{ren}})$,

$$m_b^{2,pole} = m_b^2(\mu_{\text{ren}}) \left[1 + \frac{2\alpha_s(\mu_{\text{ren}}^2)}{3\pi}\left(4 + 3\log\left(\frac{\mu_{\text{ren}}^2}{m_b^2}\right)\right)\right], \tag{5.7}$$

which is valid if $\mu_{\text{ren}} \sim m_b$. Performing the calculation in the dimensional reduction scheme gives an expression for the $\overline{\text{DR}}$ b-quark mass which differs from equation (5.7) in that the factor '4' is replaced by a '5'.

However, we will need to calculate the running bottom quark mass at the scales m_t and M_{h_i}. This involves solving the renormalisation group equation for m_b in order to sum the terms $\log\left(\frac{\mu_{\text{ren}}^2}{m_b^2}\right)$ to all orders. For $m_b \leq \mu_{\text{ren}} \leq m_t$ this gives (see e.g. [80])

$$m_b(\mu_{\text{ren}}) = m_b(m_b) U_f^{(5)}(m_b^2, \mu_{\text{ren}}^2), \tag{5.8}$$

where

$$U_f^{(N_f)}(m^2, \mu_{\text{ren}}^2) = \left(\frac{\alpha_s(\mu_{\text{ren}}^2)}{\alpha_s(m^2)}\right)^{D_f} \left(1 + \frac{J_f}{4\pi}\left(\alpha_s(m^2) - \alpha_s(\mu_{\text{ren}}^2)\right)\right), \tag{5.9}$$

$$D_f = \frac{12}{33 - 2N_f}, \tag{5.10}$$

$$J_f = \frac{-\left(8982 - 504N_f + 40N_f^2\right)}{3\left(33 - 2N_f\right)^2}. \tag{5.11}$$

For $\mu_{\text{ren}} > m_t$, the result is (see e.g. [80])

$$m_b(\mu_{\text{ren}}) = m_b(m_b^2) U_f^{(5)}(m_b^2, m_t^2) U_f^{(6)}(m_t^2, q^2). \tag{5.12}$$

Figure 5.1 shows the dependence of the running b-quark mass on the energy scale. We can see a numerically insignificant discontinuity at $\mu_{\text{ren}} = m_t$, which is caused by the higher order terms which we have neglected in equation (5.6).

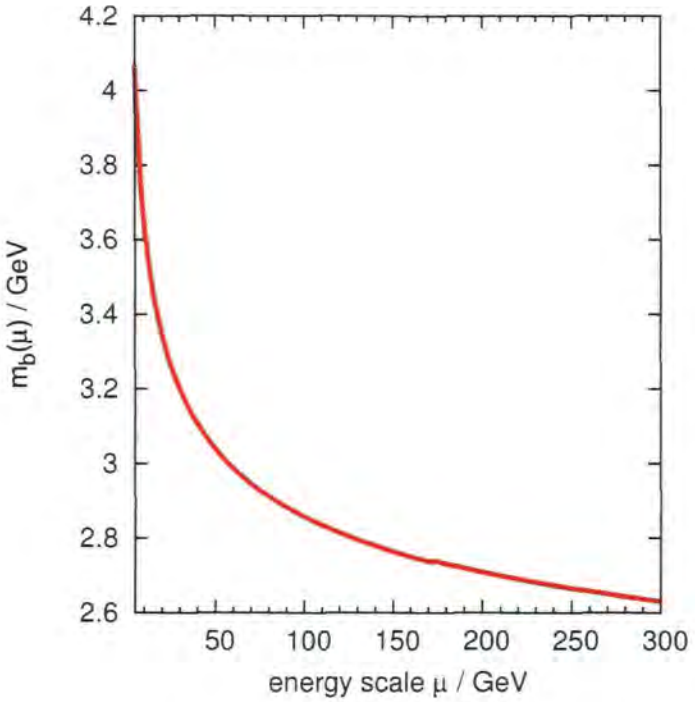

Figure 5.1: The running b-quark Standard Model $\overline{\text{MS}}$ mass as function of the energy scale m. Note the small discontinuity at $\mu_{\text{ren}} = m_t$

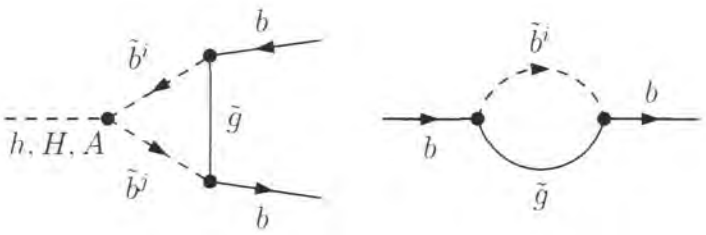

Figure 5.2: SUSY QCD corrections induced by gluino and sbottom quark loops which can be enhanced at large $\tan\beta$. $(i, j = 1, 2)$

5.2 Resummation of SUSY QCD contributions

5.3 The Δm_b correction

The renormalised $h_i \to b\bar{b}$ decay involves loops containing gluons and sbottoms, as in Figure 5.3. It is well known that, at large t_β, these SUSY QCD contributions can be enhanced (see [85] and references contained therein). This is due to the fact that the term $m_b\mu$, which is part of the off-diagonal component of the sbottom mass matrix, is proportional to t_β.

Since these effects are universal in that they affect neutral and charged Higgs equally and are independent of kinematic configuration, we can incorporate this effect by writing a effective Lagrangian which includes a non-zero coupling of b-quarks to the H_{22}^* component of the Higgs field, as in [86, 87],

$$\mathcal{L}_{\text{eff}} = -\lambda_b \bar{b}_R \left[H_{11} + \frac{\Delta m_b}{t_\beta} H_{22}^* \right] b_L + \text{h.c.} \tag{5.13}$$

This leads to a new relation between the Yukawa coupling and the b-quark mass,

$$m_b = \lambda_b v_1 \left(1 + \Delta m_b\right). \tag{5.14}$$

In previous studies, Δm_b was assumed to be real. However, our analysis will focus on the general case, in which Δm_b is allowed to be complex. $\mathcal{L}_{\text{eff}}$ can thus be rewritten as

$$\mathcal{L}_{\text{eff}} = -\frac{1}{(1+\Delta m_b)} \frac{m_b}{v_1} \bar{b}_R \left[H_{11} + \frac{\Delta m_b}{t_\beta} H_{22}^* \right] b_L + \text{h.c.} \tag{5.15}$$

$$= -\frac{(1-ix)}{(1+y)} \frac{m_b}{v_1} \bar{b}_R \left[H_{11} + \frac{\Delta m_b}{t_\beta} H_{22}^* \right] b_L + \text{h.c.}, \tag{5.16}$$

where x, y are real and given by

$$x = \frac{\text{Im}\Delta m_b}{1 + \text{Re}\Delta m_b}, \tag{5.17}$$

$$y = \text{Re}\Delta m_b + x\text{Im}\Delta m_b. \tag{5.18}$$

Neglecting the term involving the Goldstone boson, this leads to

$$\begin{aligned}\mathcal{L}_{\text{eff}} \in \bar{b}\frac{1}{1+y} \quad & \left(\left[1-\frac{1}{t_\alpha t_\beta}y+i\gamma_5 x\left(1+\frac{1}{t_\alpha t_\beta}\right)\right] v^{\text{tree}}_{\text{h}\bar{\text{b}}\text{b}} h\right. \\ & +\left[1+\frac{t_\alpha}{t_\beta}y+i\gamma_5 x\left(1-\frac{t_\alpha}{t_\beta}\right)\right] v^{\text{tree}}_{\text{H}\bar{\text{b}}\text{b}} H \\ & \left.+\left[1-\frac{1}{t_\beta^2}y+i\gamma_5 x\left(1+\frac{1}{t_\beta^2}\right)\right] v^{\text{tree}}_{\text{A}\bar{\text{b}}\text{b}} A\right) b, \end{aligned} \tag{5.19}$$

where $v^{\text{tree}}_{\text{h}\bar{\text{b}}\text{b}}$, $v^{\text{tree}}_{\text{H}\bar{\text{b}}\text{b}}$ and $v^{\text{tree}}_{\text{A}\bar{\text{b}}\text{b}}$ are defined by

$$\mathcal{L}^{\text{tree}} \in \bar{b}\left[v^{\text{tree}}_{\text{h}\bar{\text{b}}\text{b}} h + v^{\text{tree}}_{\text{H}\bar{\text{b}}\text{b}} H + v^{\text{tree}}_{\text{A}\bar{\text{b}}\text{b}} A\right] b. \tag{5.20}$$

Note that, in this convention, $v^{\text{tree}}_{\text{A}\bar{\text{b}}\text{b}}$ contains a γ_5 dependence.

In order to find Δm_b, we perform a Feynman-diagrammatic calculation of the leading 1-loop gluino contributions to the renormalised $h_i \to b\bar{b}$ decays, using the $p^2 = 0$ approximation and $i = h, H, A$. In this $p^2 = 0$ approximation, the b-quark self-energy reduces to

$$\Sigma^{p^2=0}(p) = \omega_-\Sigma^l(0) + \omega_+\Sigma^r(0), \tag{5.21}$$

which leads to the on-shell counter-terms

$$\delta m_{p^2=0} = \frac{1}{2}\left[\Sigma^l(0)+\Sigma^r(0)\right] = \text{Re}\Sigma^l(0), \tag{5.22}$$

$$\delta Z^L_{p^2=0} = \left[\frac{1}{2m}\left(\Sigma^l(0)-\Sigma^r(0)\right)\right] = \frac{i}{m}\text{Im}\Sigma^l(0), \tag{5.23}$$

$$\delta Z^R_{p^2=0} = \left[\frac{1}{2m}\left(\Sigma^r(0)-\Sigma^l(0)\right)\right] = \frac{-i}{m}\text{Im}\Sigma^l(0). \tag{5.24}$$

Recall that $\Sigma^l(p^2) = \Sigma_r(p^2)^*$ and that, in the $p^2 = 0$ approximation, the loop integrals can be reduced to A_0 integrals, which are real. Comparing this calculation to equation (5.19) gives the structure of Δm_b as

$$\Delta m_b^{\tilde{g}} = \frac{4}{3}\frac{1}{2}\frac{\alpha_s}{\pi}\mu^* M_3^* t_\beta I\left(m^2_{\tilde{b}_1}, m^2_{\tilde{b}_2}, m^2_{\tilde{g}}\right), \tag{5.25}$$

$$I(a,b,c) = -\frac{ab\text{Log}\left(\frac{b}{a}\right)+ac\text{Log}\left(\frac{a}{c}\right)+bc\text{Log}\left(\frac{c}{b}\right)}{(a-c)(c-b)(b-a)}. \tag{5.26}$$

We note, in passing, that the unrenormalised b-quark self-energy is finite and given by

$$\Sigma_{b,\tilde{g}}^{p^2=0}(p) = m_b\left(\mathrm{Re}\Delta_{\tilde{g}} - i\gamma_5 \mathrm{Im}\Delta_{\tilde{g}}\right), \tag{5.27}$$

$$\Delta_{\tilde{g}} = \frac{\Delta m_b^{\tilde{g}} X_b}{t_\beta \mu^*} \tag{5.28}$$

$$= \frac{4}{3}\frac{1}{2}\frac{\alpha_s}{\pi} X_b M_3^* I\left(m_{\tilde{b}_1}^2, m_{\tilde{b}_2}^2, m_{\tilde{g}}^2\right), \tag{5.29}$$

i.e. it is proportional to the entire off-diagonal element $m_b X_b = m_b(A_b - \mu^* t_\beta)$ of the sbottom matrix. [87] (which performs the calculation in the real MSSM) includes an additional correction Δ_1 which is proportional to A_b. [87] incorporates this into the calculation as a higher order contribution through the substitution $\Delta m_b^{\tilde{g}} \to \Delta m_b^{\tilde{g}}(1+\Delta_1)$. We do not consider corrections of this type in this thesis.

5.3.1 Incorporating Electroweak corrections due to higgsino loops

In the $h_i \to b\bar{b}$ decay, diagrams involving charged higgsinos also contain t_β enhanced contributions [85,86]. We treat these analogously to the $\Delta m_b^{\tilde{g}}$ corrections above. Comparison with the 1-loop Feynman-diagrammatic calculation in the complex MSSM gives

$$\Delta m_b^{\tilde{h}} = \frac{\alpha_t}{4\pi} A_t^* \mu^* t_\beta I\left(m_{\tilde{t}_1}^2, m_{\tilde{t}_2}^2, |\mu|^2\right), \tag{5.30}$$

where

$$\alpha_t = \frac{h_t^2}{4\pi}, \tag{5.31}$$

$$h_t = \frac{m_t}{v_2} = \frac{m_t e}{\sqrt{2} s_\beta s_W M_W}. \tag{5.32}$$

We note that the higgino contribution to the b-quark unrenormalised self-energy is

$$\Sigma_{b,\tilde{h}}^{p^2=0}(p) = m_b\left(\mathrm{Re}\Delta_{\tilde{h}} - i\gamma_5 \mathrm{Im}\Delta_{\tilde{h}}\right), \tag{5.33}$$

$$\Delta_{\tilde{h}} = -\frac{\Delta m_b^{\tilde{h}} X_t^*}{A_t^*} \tag{5.34}$$

$$= -\frac{\alpha_t}{4\pi} X_t^* \mu^* t_\beta I\left(m_{\tilde{t}_1}^2, m_{\tilde{t}_2}^2, |\mu|^2\right). \tag{5.35}$$

We therefore resum both the gluino and higgsino contributions by using a Δm_b correction of

$$\Delta m_b = \Delta m_b^{\tilde{g}} + \Delta m_b^{\tilde{h}} \tag{5.36}$$

$$= \frac{4}{3}\frac{1}{2}\frac{\alpha_s}{\pi}\mu^* M_3^* t_\beta I\left(m^2_{\tilde{b}_1}, m^2_{\tilde{b}_2}, m^2_{\tilde{g}}\right) + \frac{\alpha_t}{4\pi}A_t^*\mu^* t_\beta I\left(m^2_{\tilde{t}_1}, m^2_{\tilde{t}_2}, |\mu|^2\right). \tag{5.37}$$

In Section 7.2.7 we will demonstrate the numerical significance of $\Delta m_b^{\tilde{h}}$ in the CPX scenario.

It is also possible to incorporate effects from loops involving winos in to Δm_b as in [86] (or even winos and binos as in [85]). We do not choose to do this as they are numerically small compared to the higgsino component [86]. However, since we will explicitly calculate the 1-loop diagrams involving winos and binos when calculating the full 1-loop $h_a \to b\bar{b}$ decay width, the effect of leaving them out of the Δm_b is of sub-leading 2-loop order.

5.3.2 Δm_b corrections in the Higgs Cascade Decays

There are a number of ways in which Δm_b could be included in loop corrections involving m_b in the $h_a \to h_b h_c$ decay in the real MSSM. Care is needed to make sure that the UV divergences still cancel, which means that corrections also need to apply to the m_b appearing in the sbottom mass matrix.

The simplest method would be to replace m_b with $m_b/(1+\Delta m_b)$ in the entire calculation. This method does not distinguish between the different types of Higgs and would be incorrect in the decoupling limit $t_\alpha \to -1/t_\beta$, where the $hb\bar{b}$ coupling should be independent of Δm_b. This method would also give corrections to the b-quark masses and b-squark masses in the propagators.

Alternatively, in the real MSSM, the UV divergences cancel in the $h_i h_j h_k$ vertex for all $i,j = h, H$ if only the Yukawa terms proportional to m_b^4 are kept and vertices are given a factor $\frac{1}{1+\Delta m_b}\left(1 - \frac{\Delta m_b}{t_\alpha t_\beta}\right)$ or $\frac{1}{1+\Delta m_b}\left(1 + \frac{t_\alpha}{t_\beta}\Delta m_b\right)$ for each h or H they involve respectively.

Although the justification of this is not clear at present, this could be an interesting line of investigation for the complex MSSM.

We decide not to include Δm_b corrections to the Higgs Cascade Decay vertex in our numerical comparisons in the complex MSSM in this thesis.

5.3.3 Δm_b corrections in neutral Higgs self-energies

The program *FeynHiggs* [31, 56-58] allows the user the option of incorporating Δm_b in to the neutral Higgs self-energies and this is recommended by the *FeynHiggs* authors. Unless otherwise stated, we will use this option whenever we use *FeynHiggs* to obtain self-energies.

In *FeynHiggs*, in the 1-loop option or the option involving 1-loop terms plus only 2-loop terms of $\mathcal{O}(\alpha_s\alpha_s)$ [55], Δm_b is incorporated using an effective bottom mass of $m_b/|1+\Delta m_b|$ [88]. For the case where other 2-loop terms are included [74–78], the situation is more complicated as it is necessary to ensure that there is no double counting. In both cases, the Δm_b corrections have a large numerical effect on the neutral Higgs masses in the CPX scenario.

Chapter 6

Higgs cascade decay

6.1 Introduction

Higgs self-couplings (triple Higgs couplings $h_a h_b h_c$ and quartic Higgs couplings $h_a h_b h_c h_d$) are a crucial element of electroweak symmetry breaking via the Higgs mechanism. While the prospects for a direct experimental determination of the quartic Higgs coupling at present and future colliders is small (see, e.g., [89]), probing the triple-Higgs coupling will be one of the prime goals in the experimental programme for testing the Higgs mechanism. This coupling can be accessed via a precision measurement of the Higgs production process $e^+e^- \to Zh_ah_a$ at the ILC [90][1] or CLIC [91], and via Higgs cascade decays of the form $h_a \to h_b h_c$. While Higgs cascade decays are obviously impossible in the Standard Model, they can play an important role in models with extended Higgs sectors, such as the MSSM.

Besides the interest in Higgs cascade decays as a means to directly probe Higgs self-couplings, a precise prediction for decays of this kind is also important for phenomenological reasons. Where kinematically possible, these decays can even be dominant and thus affect Higgs phenomenology very significantly. For example, in the region of CPX parameter space 30 GeV $\lesssim M_{h_1} \lesssim$ 50 GeV (which could not be excluded by LEP Higgs searches [24], as discussed in Section 2.8), the $h_2 \to h_1 h_1$ channel is the dominant h_2 decay mode. Since the h_1 coupling to Z bosons is suppressed in this region of parameter space, the extent of the unexcluded region is heavily dependent on the $h_2 \to h_1 h_1$ decay width.

[1] At collider energies of $\sim$ 1 TeV, double Higgs production in WW fusion can also be important for investigating the triple Higgs coupling [90].

In order to reliably determine which parameter regions of the MSSM with a very light Higgs boson are unexcluded by the Higgs searches so far and which regions will be accessible by Higgs searches in the future, precise predictions for the Higgs cascade decays $h_a \to h_b h_c$ in the MSSM with complex parameters are indispensable.

As we discussed in detail in Chapter 4, loop corrections to the neutral Higgs mass matrix $\mathbf{M}$ are well known for the real and complex MSSM and have been used to find propagator corrections to processes involving external neutral Higgs particles, for example through the use of the matrix $\mathbf{Z}$ or the matrix which diagonalises the mass matrix.

However, the genuine vertex corrections to the triple Higgs decay can also be sizable. In the real MSSM, the leading Yukawa vertex corrections and the complete 1-loop vertex corrections have been calculated [92–98]. However, for the complex MSSM, previous to the results described in this thesis, only effective coupling approximations were available [99, 100].

In this chapter, we calculate the full 1-loop vertex corrections within the Feynman-diagrammatic approach, taking into account the full dependence on all complex phases of the supersymmetric parameters. We include the full propagator corrections, using neutral Higgs self-energies as provided by the program *FeynHiggs* [31, 56–58] and we consistently include 1-loop mixing with the Z boson and the unphysical Goldstone-boson degree of freedom. For the numerical examples, we will use the $h_2 \to h_1 h_1$ decay in the CPX scenario (as discussed in Section 2.8), since an understanding of the characteristics of this decay will be useful in order to understand the exclusion plots presented in Chapter 9, which are obtained by comparing the LEP cross-section limits with our improved theoretical predictions.

6.2 Investigating the kinematic behaviour of the $h_2 \to h_1 h_1$ decay width

In order to understand the behaviour of the $h_2 \to h_1 h_1$ decay width, it is necessary to be familiar with its kinematic dependence. We use the general expression for 2-body decays,

$$\Gamma(h_a \to h_b h_c) = \frac{S\rho|\mathcal{M}|^2}{8\pi M_{h_a}^2}, \tag{6.1}$$

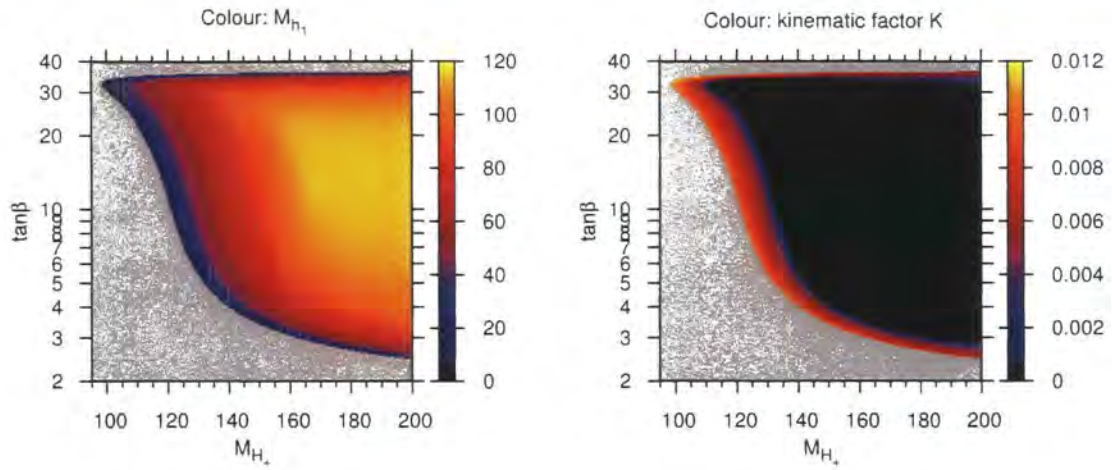

(a) (b)

Figure 6.1: Plot of $\tan\beta$ against the charged Higgs mass M_{H^-} in the CPX scenario. (a) colour bar shows the value of the lightest neutral Higgs mass M_{h_1} (b) colour bar shows the value of the kinematic factor K for the decay $h_2 \to h_1 h_1$

where $\mathcal{M}$ is the matrix element. For identical final state particles, $h_b = h_c$,

$$\rho = \frac{M_{h_a}}{2}\sqrt{1 - \frac{4M_{h_b}^2}{M_{h_a}^2}}, \tag{6.2}$$

and the symmetry factor $\mathcal{S}$ is $\frac{1}{2}$. For the case $h_b \neq h_c$,

$$\rho = \frac{1}{2M_{h_a}}\sqrt{M_{h_a}^4 + M_{h_b}^4 + M_{h_c}^4 - 2\left(M_{h_a}^2 M_{h_b}^2 + M_{h_b}^2 M_{h_c}^2 + M_{h_c}^2 M_{h_a}^2\right)}, \tag{6.3}$$

and the symmetry factor is 1. We define a factor K, which will be useful for studying the kinematic dependence of $\Gamma(h_2 \to h_1 h_1)$.

$$K = \frac{2}{M_{h_2}^2}\rho = \frac{1}{M_{h_2}}\sqrt{1 - \frac{4M_{h_1}^2}{M_{h_2}^2}}. \tag{6.4}$$

Figure 6.1 (a) shows the lightest neutral Higgs mass M_{h_1} (colour) in the CPX scenario, as a function of $\tan\beta$ and charged Higgs mass M_{H_+}. There is a sizable region of unphysical parameter space (grey), in which a positive M_{h_1} can not be calculated in this scenario. As this region is approached, M_{h_1} tends to zero. Figure 6.1 (b) shows the kinematic factor K (colour) over this region. We can see that the $h_2 \to h_1 h_1$ decay

is only kinematically allowed in a narrow region of the CPX parameter space shown in this plot. We can see this region more clearly if we plot K as a function of $\tan\beta$ against M_{h_1}, as in Figure 6.2. Since we use $\tan\beta$ and $M_{H^\pm}$ as input parameters, we vary $M_{H^\pm}$ iteratively to obtain the required M_{h_1} for each parameter point. We begin the x-axis at $M_{h_1} = 15$ GeV as calculations in the region $M_{h_1} < 15$ GeV are problematic, since quantities such as the Higgs masses vary strongly with slight changes in other parameters (it is unstable). Other experimental constraints (such as meson decays) also need to be considered[2]. The very low M_{h_1} region will not be relevant to our discussions in Chapter 9, where we will be particularly interested in the effect of the new $h_2 \to h_1 h_1$ vertex corrections on the unexcluded region found at $30 \text{ GeV} \lesssim M_{h_1} \lesssim 50$ GeV.

In Figure 6.2, the edge of unphysical parameter space (grey) occurs at $M_{H^\pm} = M_{H^\pm}^{\max,\text{CPX}} = 1000$ GeV. However, the position of this edge on the $M_{h_1} - \tan\beta$ plane is relatively insensitive to slight variations in $M_{H^\pm}^{\max,\text{CPX}}$.

Figure 6.3 (a) and (b) show some of the features of Figure 6.2 in more detail. Figure 6.3 shows that the kinematic factor K (colour) decreases as M_{h_1} approaches the kinematic limit for the $h_2 \to h_1 h_1$ decay. In Figure 6.3 (b), we see that the kinematic factor K (colour) is roughly independent of $\tan\beta$ in the range $3 \lesssim \tan\beta \lesssim 25$. This relative independence of kinematics will be extremely useful when investigating the effect of loop corrections. Outside this region, K falls off dramatically. In the unstable regions $\tan\beta \lesssim 2$ and $\tan\beta \gtrsim 34$, very small variations in $\tan\beta$ have a huge effect on the value of the $M_{H^\pm}$ required to keep M_{h_1} constant.

It is worth noting that the region $M_{H^\pm} \lesssim 200$ GeV is not the only region of CPX parameter space with a significant $h_2 \to h_1 h_1$ decay width. In Figure 6.4, we can see that this decay is kinematically allowed for all values of $\tan\beta$ above $M_{H^\pm} \sim 220$ GeV.

6.3 Calculation of the genuine $h_i \to h_j h_k$ vertex contributions

We calculate the full 1PI (one-particle irreducible) 1-loop vertex corrections to the $h_i \to h_j h_k$ decay width within the Feynman-diagrammatic approach, taking into account the phases of all supersymmetric parameters. h_i, h_j, h_k are some combination of the tree

[2]For a recent analysis of experimental exclusions in the very low M_{h_1} region of the CPX scenario, see [101]

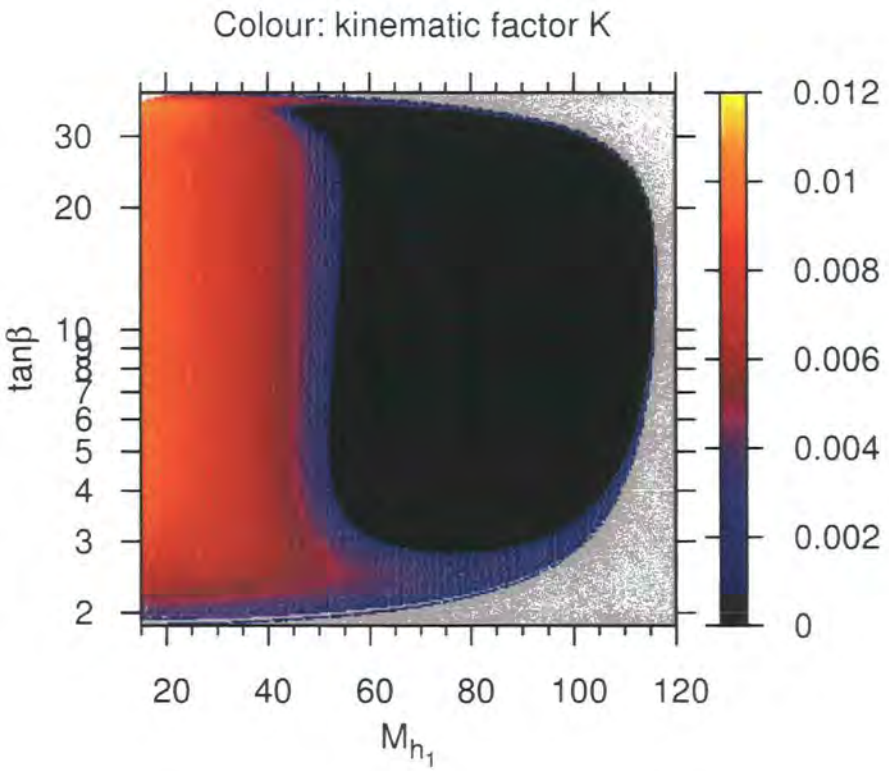

Figure 6.2: Plot of $\tan\beta$ against the lightest Higgs mass M_{h_1} in the CPX scenario. $M_{H^\pm}$ is adjusted to give each M_{h_1} as required. The colour bar shows the value of the kinematic factor K for the decay $h_2 \to h_1 h_1$.

level Higgs propagators h, H, A. The programs *FeynArts* [41–43] and *FormCalc* [43, 45] are used to draw and evaluate the Feynman diagrams using dimensional reduction and *LoopTools* [45] is used to evaluate the majority of the integrals. We use $m_b = m_b(m_t^{\text{on-shell}})$ in the vertex corrections and when calculating sbottom masses and a top mass of $m_t = m_t(m_t) = m_t^{\text{on-shell}} / \left(1 + \frac{4}{3\pi}\alpha_s(m_t^{\text{on-shell}})\right)$ in order to absorb some of the higher order SM QCD corrections (see discussion in Section 5.1.2). We use a unit CKM matrix and assume no squark generation mixing.

6.3.1 Leading corrections (Yukawa terms)

At low to moderate values of $\tan\beta$, the leading corrections to the $h_i \to h_j h_k$ vertex are the Yukawa terms from the $t, \tilde{t}$ sector. These arise from the diagrams shown in Figure 6.5.

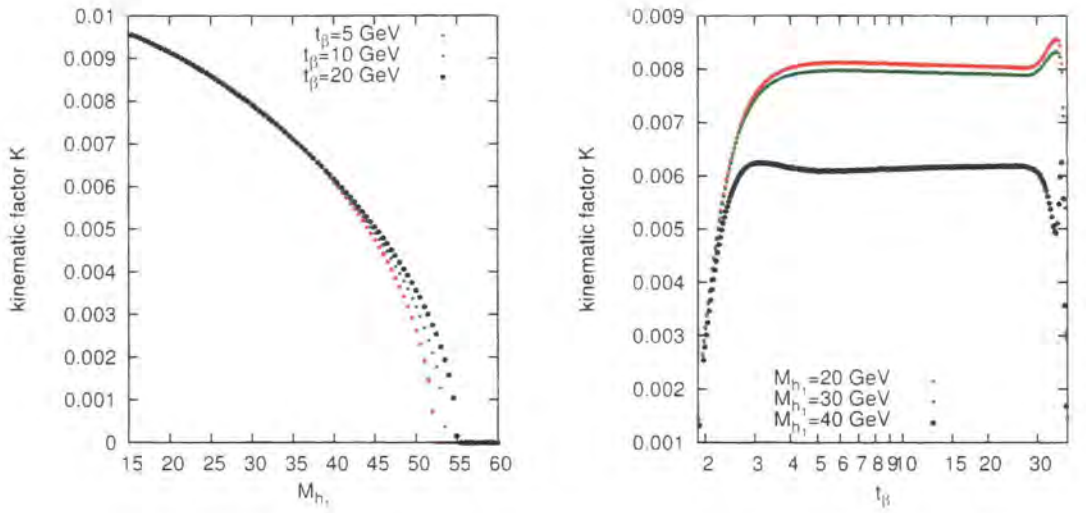

(a) (b)

Figure 6.3: The kinematic factor K for the decay $h_2 \to h_1 h_1$ in the CPX scenario (a) as a function of the lightest Higgs mass M_{h_1} for various values of $\tan\beta$ and (b) as a function of $\tan\beta$ for various values of the lightest Higgs mass M_{h_1}.

We calculate these contributions using the Yukawa approximation (as defined in Section 6.3.1), in order to obtain compact analytical expressions for the leading corrections to the $h_i h_j h_k$ vertex. To evaluate these corrections, we require 3-point scalar integrals C_0 at zero momentum, as given in Appendix A. We find that there are no counter-term contributing to the $h_i h_j h_k$ vertex in this approximation.

We therefore arrive at the following expressions for the leading Yukawa corrections in the $t/\bar{t}$ sector, for vertices involving the CP-even tree-level Higgs bosons:

$$\Delta\iota^{\rm Yuk}_{\phi_1\phi_1\phi_1} = -\frac{3e^3 m_t^4}{32\pi^2 M_{\rm W}^3 \cdot s_{\rm W}^3 \cdot s_\beta^3} \frac{{\rm Re}\,[\mu X_t]}{m^2_{\tilde{t}_1} - m^2_{\tilde{t}_2}} \left\{ 4m_t^2 {\rm Re}^2[\mu X_t] \mathcal{E}_{11122-11222} + 3\mu\mu^* \mathcal{C}_{112-122} \right\}. \tag{6.5}$$

$$\begin{aligned}\Delta\iota^{\rm Yuk}_{\phi_1\phi_1\phi_2} = & -\frac{3e^3 m_t^4}{32\pi^2 M_{\rm W}^3 \cdot s_{\rm W}^3 \cdot s_\beta^3} \frac{1}{m^2_{\tilde{t}_1} - m^2_{\tilde{t}_2}} \left\{ \mu\mu^* \left(2\log\left(\frac{m_{\tilde{t}_1}}{m_{\tilde{t}_2}}\right) - 3{\rm Re}\,[A_t^* X_t] \mathcal{C}_{112-122} \right) \right. \\ & -4m_t^2 {\rm Re}^2[\mu X_t] \left(\mathcal{D}_{1112-1222} + {\rm Re}\,[A_t^* X_t] \mathcal{E}_{11122-11222} \right) \\ & \left. +2{\rm Im}^2[\mu X_t] \mathcal{C}_{112-122} \right\}. \end{aligned} \tag{6.6}$$

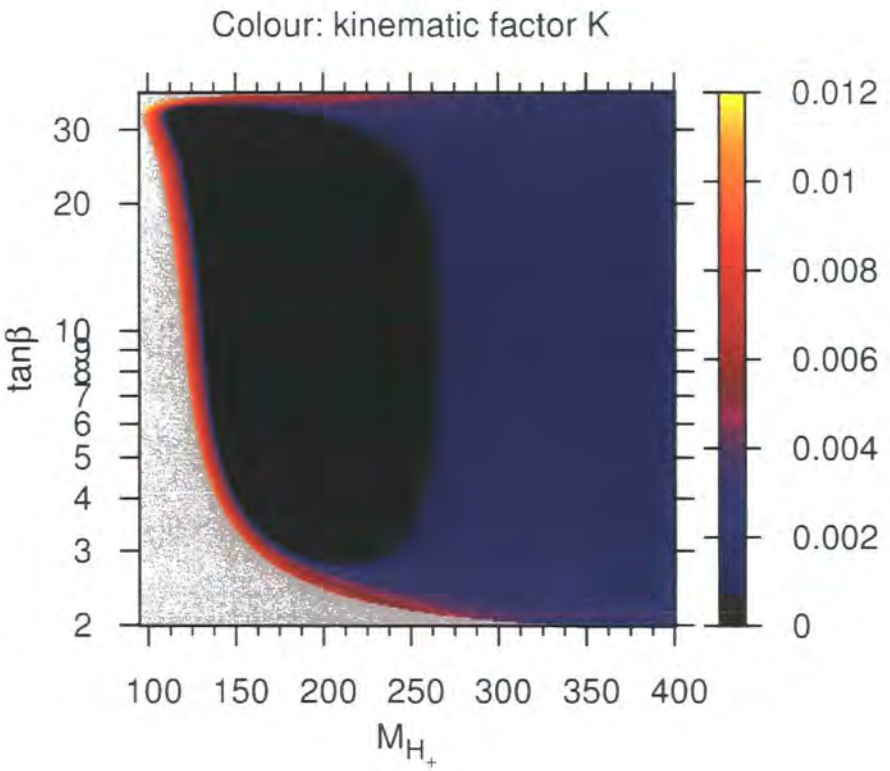

Figure 6.4: Plot of $\tan\beta$ against the charged Higgs mass M_{H^-} in the CPX scenario. The colour bar shows the value of the kinematic factor K in the decay $h_2 \to h_1 h_1$

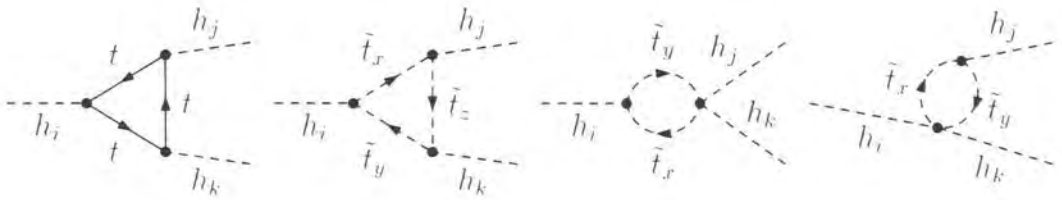

Figure 6.5: Leading vertex corrections to the decay $h_i \to h_j h_k$, involving $t/\tilde{t}$ loops. (x,y,z = 1,2)

$$
\begin{aligned}
\Delta c^{\mathrm{Yuk}}_{\phi_1\phi_2\phi_2} = \; & \frac{3e^3 m_t^4}{16\pi^2 M_W^3 \cdot s_W^3 \cdot s_\beta^5} \frac{1}{m^2_{\tilde{t}_1} - m^2_{\tilde{t}_2}} \left\{ 2\mu\mu^* s_\beta c_\beta \log\left(\frac{m_{\tilde{t}_1}}{m_{\tilde{t}_2}}\right) \right. \\
& - s_\beta^2 \mathrm{Re}\left[\mu X_t\right] \left(\frac{m_t^2}{m^2_{\tilde{t}_1} m^2_{\tilde{t}_2}} \left(m^2_{\tilde{t}_1} - m^2_{\tilde{t}_2}\right) - 3\log\left(\frac{m_{\tilde{t}_1}}{m_{\tilde{t}_2}}\right) + \frac{3}{2}\mathcal{C}_{112-122} A_t A_t^* \right. \\
& \left. + 2m_t^2 \mathrm{Re}\left[A_t^* X_t\right] \left(2\mathcal{D}_{1112-1222} + \mathcal{E}_{11122-11222} \mathrm{Re}\left[A_t^* X_t\right]\right)\right) \\
& \left. - c_\beta s_\beta \mathrm{Im}^2[\mu X_t] \mathcal{C}_{112-122} \right\} . \qquad (6.7)
\end{aligned}
$$

$$\begin{aligned}
\Delta v^{\text{Yuk}}_{\phi_2\phi_2\phi_2} &= \frac{3e^3 m_t^4}{16\pi^2 M_W^3 \cdot s_W^3 \cdot s_\beta^3} \frac{1}{m_{\tilde{t}_1}^2 - m_{\tilde{t}_2}^2} \left\{ \left(m_{\tilde{t}_1}^2 - m_{\tilde{t}_2}^2\right) \left(2 - 3\log\left(\frac{m_{\tilde{t}_1} m_{\tilde{t}_2}}{m_t^2}\right)\right) \right. \\
&\quad -3\log\left(\frac{m_{\tilde{t}_1}}{m_{\tilde{t}_2}}\right) \left(A_t A_t^* + \text{Re}\left[A_t^* X_t\right]\right) - \frac{m_t^2}{m_{\tilde{t}_1}^2 m_{\tilde{t}_2}^2} \left(m_{\tilde{t}_1}^4 - m_{\tilde{t}_2}^4\right) \\
&\quad +3\text{Re}\left[A_t^* X_t\right] \left(\frac{m_t^2}{m_{\tilde{t}_1}^2 m_{\tilde{t}_2}^2} \left(m_{\tilde{t}_1}^2 - m_{\tilde{t}_2}^2\right) + \frac{1}{2} \mathcal{C}_{112-122} A_t A_t^* \right. \\
&\quad \left. \left. + \frac{2}{3} m_t^2 \text{Re}\left[A_t^* X_t\right] \left(3\mathcal{D}_{1112-1222} + \mathcal{E}_{11122-11222} \text{Re}\left[A_t^* X_t\right]\right) \right) \right\}, \qquad (6.8)
\end{aligned}$$

where

$$\begin{aligned}
Y_t &= A_t + t_\beta \mu^* \qquad (6.9) \\
\mathcal{D}_{1112-1222} &= \text{D}_0\left(0,0,0,0,m_{\tilde{t}_1}^2, m_{\tilde{t}_1}^2, m_{\tilde{t}_1}^2, m_{\tilde{t}_2}^2\right) - \text{D}_0\left(0,0,0,0,m_{\tilde{t}_1}^2, m_{\tilde{t}_2}^2, m_{\tilde{t}_2}^2, m_{\tilde{t}_2}^2\right) \\
&= -\frac{1}{2\left(m_{\tilde{t}_1}^2 - m_{\tilde{t}_2}^2\right)} \left(\frac{m_{\tilde{t}_1}^2 + m_{\tilde{t}_2}^2}{m_{\tilde{t}_1}^2 m_{\tilde{t}_2}^2} - \frac{4}{m_{\tilde{t}_1}^2 - m_{\tilde{t}_2}^2} \log\left(\frac{m_{\tilde{t}_1}}{m_{\tilde{t}_2}}\right) \right), \qquad (6.10) \\
\mathcal{E}_{11122-11222} &= \text{E}_0\left(0,0,0,0,0,m_{\tilde{t}_1}^2, m_{\tilde{t}_1}^2, m_{\tilde{t}_1}^2, m_{\tilde{t}_2}^2, m_{\tilde{t}_2}^2\right) \\
&\quad - \text{E}_0\left(0,0,0,0,0,m_{\tilde{t}_1}^2, m_{\tilde{t}_1}^2, m_{\tilde{t}_2}^2, m_{\tilde{t}_2}^2, m_{\tilde{t}_2}^2\right) \\
&= \frac{1}{2} \left(\frac{1}{m_{\tilde{t}_1}^2 m_{\tilde{t}_2}^2 \left(m_{\tilde{t}_1}^2 - m_{\tilde{t}_2}^2\right)} \right. \\
&\quad + \left. \frac{12}{\left(m_{\tilde{t}_1}^2 - m_{\tilde{t}_2}^2\right)^3} \left(1 - \frac{\left(m_{\tilde{t}_1}^2 + m_{\tilde{t}_2}^2\right)}{\left(m_{\tilde{t}_1}^2 - m_{\tilde{t}_2}^2\right)} \log\left(\frac{m_{\tilde{t}_1}}{m_{\tilde{t}_2}}\right)\right) \right), \qquad (6.11)
\end{aligned}$$

and $m_{\tilde{q}_{1,2}}^2$ are the stop masses under the Yukawa approximation, as given by equation (4.7). $\mathcal{C}_{112-122}$ is defined in equation (4.8). $\mathcal{D}_{1112-1222}$ and $\mathcal{E}_{11122-11222}$ are functions of D_0 and E_0 scalar integrals, which are defined in Appendix A and solved for zero external momentum. Since we are describing a process with 3 external legs, D_0 and E_0 do not appear explicitly in the Feynman diagrams. However, these functions are very useful for simplifying the vertex expressions.

The 1-loop corrections to a $h_i h_j h_k$ vertex involving at least one CP-odd eigenstate are given by

$$\begin{aligned}
\Delta v^{\text{Yuk}}_{\phi_1\phi_1 A} &= \frac{3e^3 m_t^4}{32\pi^2 M_W^3 s_W^3 s_\beta^4} \frac{\text{Im}\left[\mu X_t\right]}{m_{\tilde{t}_1}^2 - m_{\tilde{t}_2}^2} \left\{ \right. \\
&\quad \left. \left(\mu\mu^* - 2c_\beta s_\beta \text{Re}\left[\mu X_t\right]\right) \mathcal{C}_{112-122} + 4m_t^2 \text{Re}^2[\mu X_t] \mathcal{E}_{11122-11222} \right\}, \qquad (6.12)
\end{aligned}$$

$$\Delta v^{\rm Yuk}_{\phi_1\phi_2 A} = -\frac{3e^3 m_t^4}{32\pi^2 M_W^3 s_W^3 s_\beta^4}\frac{{\rm Im}\left[\mu X_t\right]}{m_{\tilde{t}_1}^2 - m_{\tilde{t}_2}^2}\left\{+2c_\beta s_\beta \log\left(\frac{m_{\tilde{t}_1}}{m_{\tilde{t}_2}}\right)\right.$$
$$+\left(2{\rm Re}\left[\mu A_t\right] - c_\beta s_\beta\left(\mu\mu^* + A_t A_t^*\right)\right)\mathcal{C}_{112-122}$$
$$\left.+4m_t^2{\rm Re}\left[\mu X_t\right]\left(\mathcal{D}_{1112-1222} + {\rm Re}\left[A_t^* X_t\right]\mathcal{E}_{11122-11222}\right)\right\}. \qquad (6.13)$$

$$\Delta v^{\rm Yuk}_{\phi_2\phi_2 A} = -\frac{3e^3 m_t^4}{32\pi^2 M_W^3 s_W^3 s_\beta^4}\frac{{\rm Im}\left[\mu X_t\right]}{m_{\tilde{t}_1}^2 - m_{\tilde{t}_2}^2}\left\{-2\frac{m_t^2}{m_{\tilde{t}_1}^2 m_{\tilde{t}_2}^2}\left(m_{\tilde{t}_1}^2 - m_{\tilde{t}_2}^2\right)\right.$$
$$+2\left(2s_\beta^2+1\right)\log\left(\frac{m_{\tilde{t}_1}}{m_{\tilde{t}_2}}\right) - \left(2s_\beta^2{\rm Re}\left[A_t^* X_t\right] + A_t A_t^*\right)\mathcal{C}_{112-122}$$
$$\left.-4m_t^2{\rm Re}\left[A_t^* X_t\right]\left(2\mathcal{D}_{1112-1222} + {\rm Re}\left[A_t^* X_t\right]\mathcal{E}_{11122-11222}\right)\right\}, \qquad (6.14)$$

$$\Delta v^{\rm Yuk}_{\phi_1 AA} = \frac{3e^3 m_t^4}{32\pi^2 M_W^3 s_W^3 s_\beta^5}\frac{1}{m_{\tilde{t}_1}^2 - m_{\tilde{t}_2}^2}\left\{c_\beta^2 s_\beta^2{\rm Re}\left[\mu X_t\right]\left(2\log\left(\frac{m_{\tilde{t}_1}}{m_{\tilde{t}_2}}\right) - Y_t Y_t^* \mathcal{C}_{112-122}\right)\right.$$
$$\left.+2{\rm Im}^2\left[\mu X_t\right]\left(c_\beta s_\beta \mathcal{C}_{112-122} - 2m_t^2{\rm Re}\left[\mu X_t\right]\mathcal{E}_{11122-11222}\right)\right\}, \qquad (6.15)$$

$$\Delta v^{\rm Yuk}_{\phi_2 AA} = \frac{3e^3 m_t^4}{32\pi^2 M_W^3 s_W^3 s_\beta^5}\frac{1}{m_{\tilde{t}_1}^2 - m_{\tilde{t}_2}^2}\left\{s_\beta^2 c_\beta^2\left(-2\left(m_{\tilde{t}_1}^2 - m_{\tilde{t}_2}^2\right)\log\left(\frac{m_{\tilde{t}_1} m_{\tilde{t}_2}}{m_t^2}\right)\right.\right.$$
$$-2\left({\rm Re}\left[A_t^* X_t\right] + Y_t Y_t^*\right)\log\left(\frac{m_{\tilde{t}_1}}{m_{\tilde{t}_2}}\right) + Y_t Y_t^*{\rm Re}\left[A_t^* X_t\right]\mathcal{C}_{112-122}\Big)$$
$$\left.+2{\rm Im}^2\left[\mu X_t\right]\left(s_\beta^2\mathcal{C}_{112-122} + 2m_t^2\left(\mathcal{D}_{1112-1222} + {\rm Re}\left[A_t^* X_t\right]\mathcal{E}_{11122-11222}\right)\right)\right\}, \qquad (6.16)$$

$$\Delta v^{\rm Yuk}_{AAA} = -\frac{3e^3 m_t^4}{32\pi^2 M_W^3 s_W^3 s_\beta^6}\frac{{\rm Im}^2\left[\mu X_t\right]}{m_{\tilde{t}_1}^2 - m_{\tilde{t}_2}^2}\left\{3c_\beta^2 s_\beta^2\left(2\log\left(\frac{m_{\tilde{t}_1}}{m_{\tilde{t}_2}}\right) - Y_t Y_t^*\mathcal{C}_{112-122}\right)\right.$$
$$\left.-4m_t^2{\rm Im}^2\left[\mu X_t\right]\mathcal{E}_{11122-11222}\right\}. \qquad (6.17)$$

These compact, momentum independent expressions have the advantage that they are extremely easy to implement into a computer code and therefore make very convenient 'effective' vertices. In this form, we are also able to see that, despite including the effect of complex phases, these corrections are themselves entirely real. These vertex corrections simplify considerably in the real MSSM.

6.3.2 Full 1-loop 1PI vertex corrections

For the full 1PI 1-loop corrections to the $h_i h_j h_k$ vertex, we need the counter-terms shown in Table 3.2 which were derived from the Lagrangian in Section 2.2. Note that, for triple Higgs vertices with an external Higgs boson A, the field renormalisation constant δZ_{AG} is required in order to ensure that the vertex is UV-finite. We have extended the *FeynArts* [41–43] model files in order to include these counter-terms.

Examples of Feynman diagrams contributing to these vertex corrections are shown in Figure 6.6.

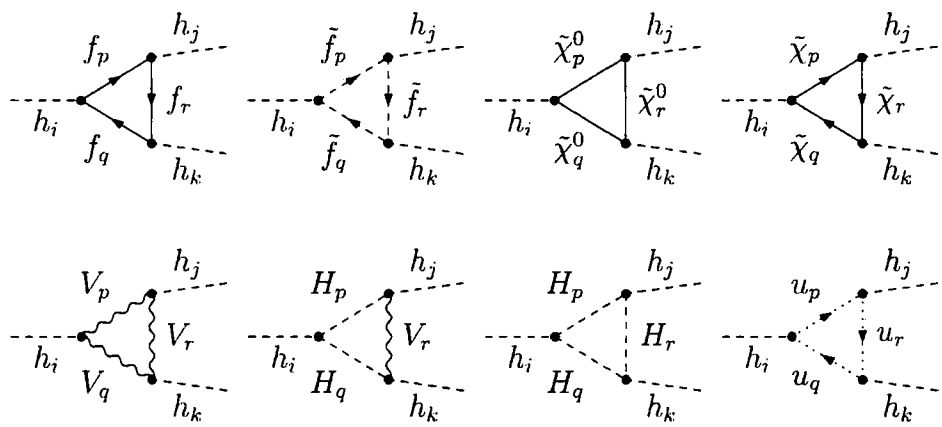

Figure 6.6: Examples of generic diagrams (showing only one of the topologies) contributing to the processes $h_i \to h_j h_k$. h_i, h_j, h_k are the physical Higgs fields at tree level (h, H, A), f are SM fermions, $\tilde{f}$ are their superparters, $\tilde{\chi}^0, \tilde{\chi}$ are neutralinos and charginos, V are vector bosons, H denote the neutral and charged Higgs bosons and the Goldstone bosons, u are Faddeev–Popov ghost fields.

We also investigated the effect of including loop-corrected Higgs bosons in the loop corrections to the $h_i h_j h_k$ vertex, instead of the tree level Higgs masses. In order to ensure the UV divergences cancelled, we transformed the couplings of the internal Higgs to the other particles using the unitary matrix $\hat{\mathbf{U}}$ from Section 4.6, through an appropriately adapted *FeynArts* [41–43] model file. For consistency, the loop corrected Higgs masses used for these internal Higgs bosons were calculated using the mass matrix in equation (4.47). These corrections were numerically insignificant in the examples investigated.

6.4 Combining the 1PI vertex corrections with propagator corrections to obtain the full $h_a \to h_b h_c$ decay width

We can combine vertices involving the tree level Higgs bosons h_i, h_j, h_k with the wave-function normalisation factors contained in the matrix $\mathbf{Z}$, which contain self-energies from the program *FeynHiggs*, in order to obtain processes involving the loop-corrected states h_a, h_b, h_c as the external particles (as discussed in Section 4.5).

These 'Z-factors' can be used in conjunction with tree level vertices $\Gamma^{\text{tree}}_{h_i h_j h_k}$ (given in Table 3.2) using (sum over i, j, k)

$$\Gamma^{\text{tree}}_{h_a h_b h_c} = \hat{\mathbf{Z}}_{ck} \hat{\mathbf{Z}}_{bj} \hat{\mathbf{Z}}_{ai} \Gamma^{\text{tree}}_{h_i h_j h_k}. \tag{6.18}$$

We obtain our full result by combining the genuine 1-loop vertex corrections $\Gamma^{\text{1PI}}_{h_i h_j h_k}$ and the vertex involving 1-loop Goldstone and Z boson self-energy contributions $\Gamma^{\text{G,Zse}}_{h_i h_j h_k}$ with the Z-factors, such that (sum over i, j, k)

$$\Gamma^{\text{full}}_{h_a h_b h_c} = \hat{\mathbf{Z}}_{ck} \hat{\mathbf{Z}}_{bj} \hat{\mathbf{Z}}_{ai} \left[\Gamma^{\text{1PI}}_{h_i h_j h_k} \left(M^2_{h_a}, M^2_{h_b}, M^2_{h_c} \right) + \Gamma^{\text{G,Zse}}_{h_i h_j h_k} \left(m^2_{h_i}, m^2_{h_j}, m^2_{h_k} \right) \right]. \tag{6.19}$$

The genuine 1-loop vertex corrections $\Gamma^{\text{1PI}}_{h_i h_j h_k}$ contain full momentum dependence and therefore depend on the loop-corrected masses $M^2_{h_a}, M^2_{h_b}, M^2_{h_c}$. However, as discussed in detail in Section 4.7, $\Gamma^{\text{G,Zse}}_{h_i h_j h_k}$ are calculated by approximating the external momenta to the tree level values $m^2_{h_i}, m^2_{h_j}, m^2_{h_k}$.

6.5 Numerical Results

We will now investigate the importance of the full 1-loop genuine corrections through their numerical impact on the $h_2 \to h_1 h_1$ decay width. All the results plotted in this section include the wave-function normalisation factors, through the matrix $\mathbf{Z}$. The case where only wave-function normalisation factors but no genuine one-loop vertex contributions are included will be denoted 'tree'.

Figure 6.7 compares the 'tree' result with the result which includes the genuine vertex correction and all propagator corrections, as described by equation (6.19). In Figure 6.7

(a), we can see that both the full and 'tree' $h_2 \to h_1 h_1$ decay widths have a strong dependence on $\tan\beta$ and both have a similar pattern of peaks and minima. However, the behaviour of the 'tree' result is shifted with respect to the full result. For example, the decay widths drop to zero in the low $\tan\beta$ region of the graph at $\tan\beta = 2.7$ and $\tan\beta = 4.3$ respectively. Quantitatively, the results are also very different. For example, the peak in the 'tree' decay width at medium values of $\tan\beta$ is approximately 13% of the corresponding peak in the full decay width. We disregard the behaviour at $\tan\beta \lesssim 2$ and $\tan\beta \gtrsim 34$, since we concluded from Figure 6.3 that these regions of parameter space are unstable.

In Figure 6.7 (b), we can see that both the 'tree' and full decay widths decrease as the lightest Higgs mass M_{h_1} increases, governed by the kinematic dependence we saw in Figure 6.3 (b). Again, the 'tree' level result is heavily suppressed compared to the full result. We can conclude from Figure 6.7 that calculations which just combine the propagator corrections with the tree level vertex are an extremely poor approximation to the full result.

In Figure 6.8, we focus on the peak in the full $h_2 \to h_1 h_1$ decay width at $\tan\beta \sim 8$, which has a significant effect on the LEP exclusions in the CPX scenario, as we will see in Chapter 9. We can see that the Yukawa corrections (labelled 'Yukawa') provide the

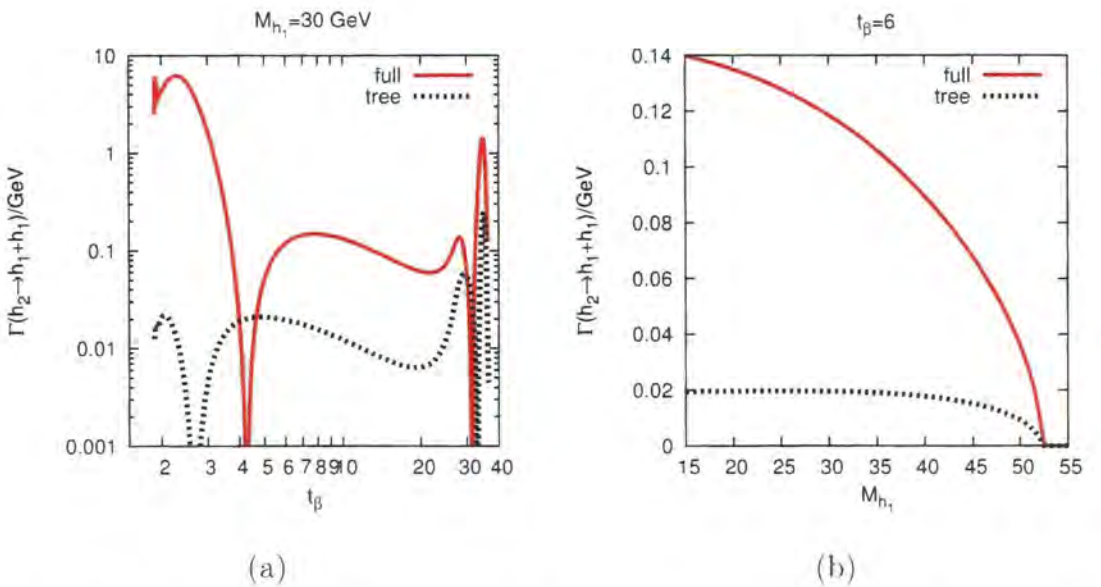

Figure 6.7: The decay width $\Gamma(h_2 \to h_1 h_1)$ in the CPX scenario (a) as a function of $\tan\beta$ at $M_{h_1} = 30$ GeV and (b) as a function of M_{h_1} at $t_\beta = 6$. $M_{H^\pm}$ is adjusted to give each M_{h_1} as required. 'tree' indicates that the tree level vertex corrections have been combined with the propagator corrections while 'full' includes full vertex corrections and propagator corrections.

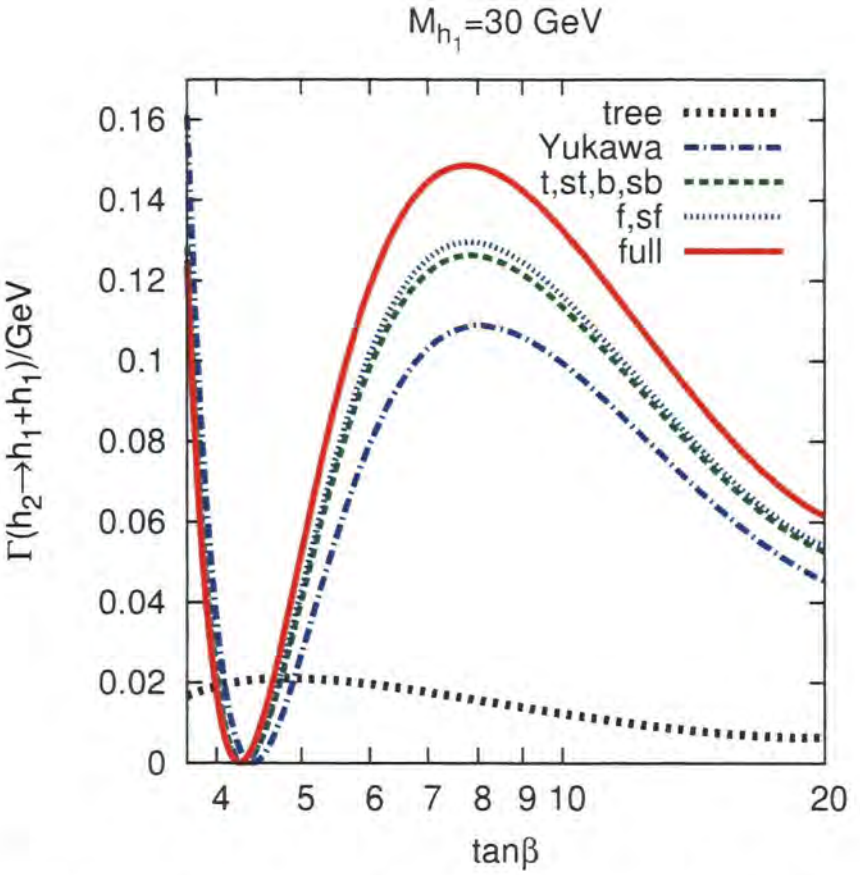

Figure 6.8: $\Gamma(h_2 \to h_1 h_1)$ as function of $\tan\beta$ for $M_{h_1} = 30$ GeV in the CPX scenario. Result including the full vertex corrections is compared to the result including just the leading vertex corrections, which are calculated using the Yukawa approximation ('Yukawa'), the vertex corrections from loops involving top, stop, bottom, sbottoms ('t,st,b,sb') and the vertex corrections from loops involving all Standard Model fermions and their superpartners ('f,sf'). All results included propagator corrections.

leading contributions to the full $h_2 \to h_1 h_1$ decay width, as expected. However, the peak in the decay width calculated using Yukawa approximation is only $\sim 73\%$ of the peak in the full decay width. Including all vertex contributions for $t, \tilde{t}, b, \tilde{b}$ loops ('t,st,b,sb') gives a better approximation, predicting a peak in the decay width which is $\sim 84\%$ of the full result. We can see that, numerically, there is relatively little difference between including all Standard Model fermions and their superpartners in the loop corrections ('f,sf') and just the $t, \tilde{t}, b, \tilde{b}$ contributions.

In Figure 6.9, we investigate the significance of some of the choices we made when performing the $h_a \to h_b h_c$ decay width calculation. As discussed in Section 3.3.3, for the full result, we parametrise our result in terms of an electric charge calculated from $\alpha(M_Z)$, whereas for calculations involving only Standard Model fermions and their superpart-

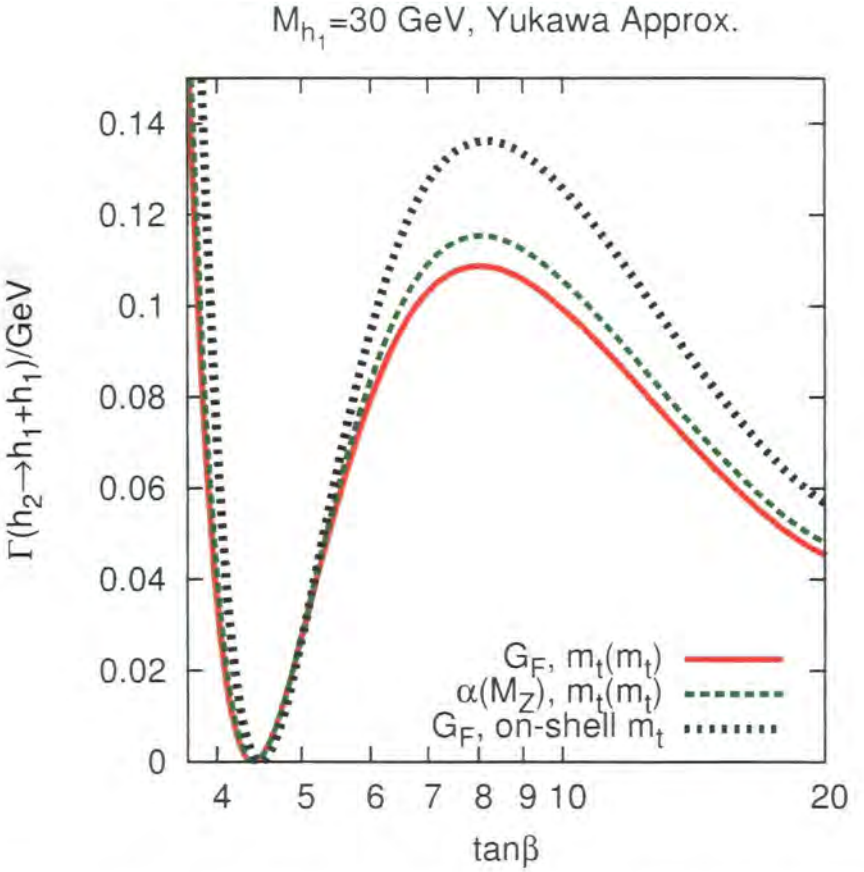

Figure 6.9: $\Gamma(h_2 \to h_1 h_1)$ as function of $\tan\beta$ for $M_{h_1} = 30$ GeV, using vertex corrections calculated in the Yukawa approximation. All results include propagator corrections. '$G_F, m_t(m_t)$' indicates that the vertex corrections have been parameterised in terms of an electric charge calculated from the experimental value of G_F and a running top quark mass evaluated at the scale m_t. '$\alpha(M_Z), m_t(m_t)$' indicates that the vertex corrections have been parametrised in terms of an electric charge calculated from $\alpha(M_Z)$ and $m_t(m_t)$ as before and 'G_F, on-shell m_t' indicates that the calculation has been parametrised in terms of an electric charge calculated from G_F and an on-shell top quark mass.

ners (such as calculations performed with the Yukawa approximation), we parametrise our result in terms of an electric charge obtained from the experimental value of the Fermi constant G_F. In Figure 6.9, we can see that this has a numerical effect of $\sim 7\%$ at the peak in the $h_2 \to h_1 h_1$ decay width. As we have discussed, we also chose to use a running top mass of $m_t = m_t(m_t)$ in the calculation, in order to absorb some of the higher order SM QCD corrections. Since the Yukawa corrections are proportional to m_t^4 or m_t^6, it is unsurprising that using a top mass of $m_t = m_t^{\text{on-shell}}$ has a large numerical effect, as we can see from Figure 6.9.

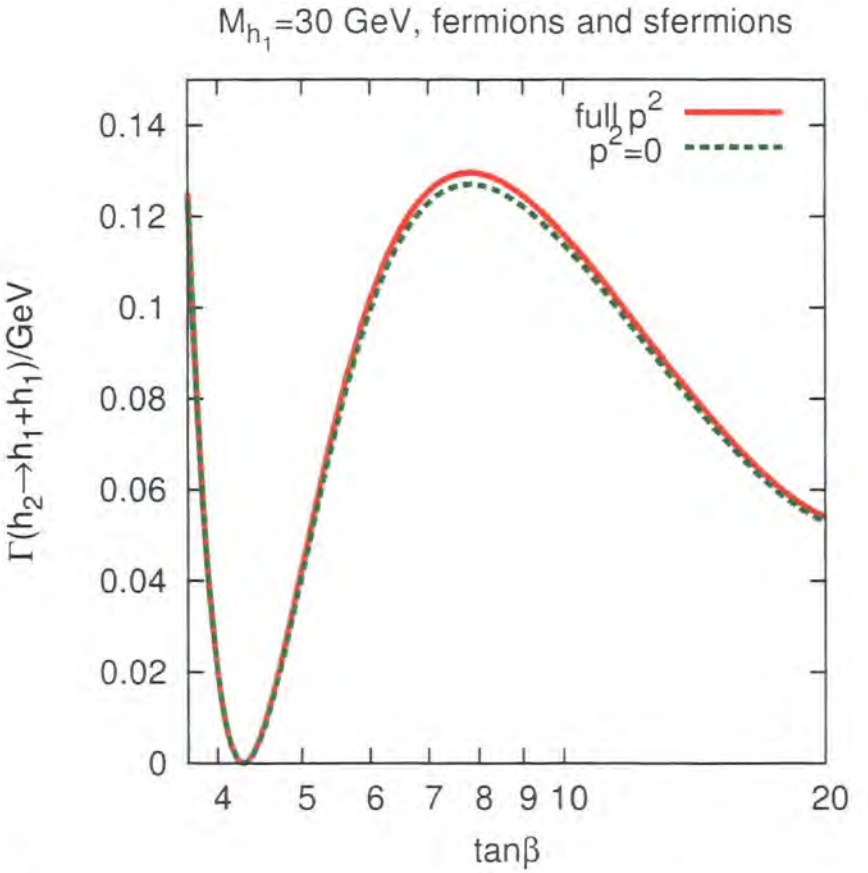

Figure 6.10: $\Gamma(h_2 \to h_1 h_1)$ as function of $\tan\beta$ for $M_{h_1} = 30$ GeV in the CPX scenario, using propagator corrections and fermion/sfermion contributions to the vertex corrections. 'full p^2' indicates that the full momentum dependence was taken into account while '$p^2 = 0$' indicates that the external momentum was approximated to zero in the vertex corrections.

In Figure 6.10, we compare the contribution from fermion and sfermion loops with the full momentum dependence to the result under the approximation of zero external momentum. At the peak in the $h_2 \to h_2 h_1$ decay width, the $p^2 = 0$ approximates the full $f, \tilde{f}$ result to an accuracy of 2%. This approximation could be very useful in making an effective triple Higgs coupling, which would approximate the full result significantly better than an effective coupling made using the Yukawa approximation.

In Figure 6.11 and Figure 6.12 we investigate the dependence of the $h_2 \to h_1 h_1$ decay width on other SUSY parameters. We choose the parameters A_t, μ and $M_{\rm SUSY}$, since these all appear in the leading corrections, as we can see from equation (6.5)–(6.17). Figure 6.11 (a) shows that varying $\arg A_t$ by 10% has a highly significant effect on the $h_2 \to h_1 h_1$ decay width, through shifting the minimum and the peak at moderate $\tan\beta$ to higher values of $\tan\beta$ as $\arg A_t$ increases. The magnitude of the peak at moderate $\tan\beta$

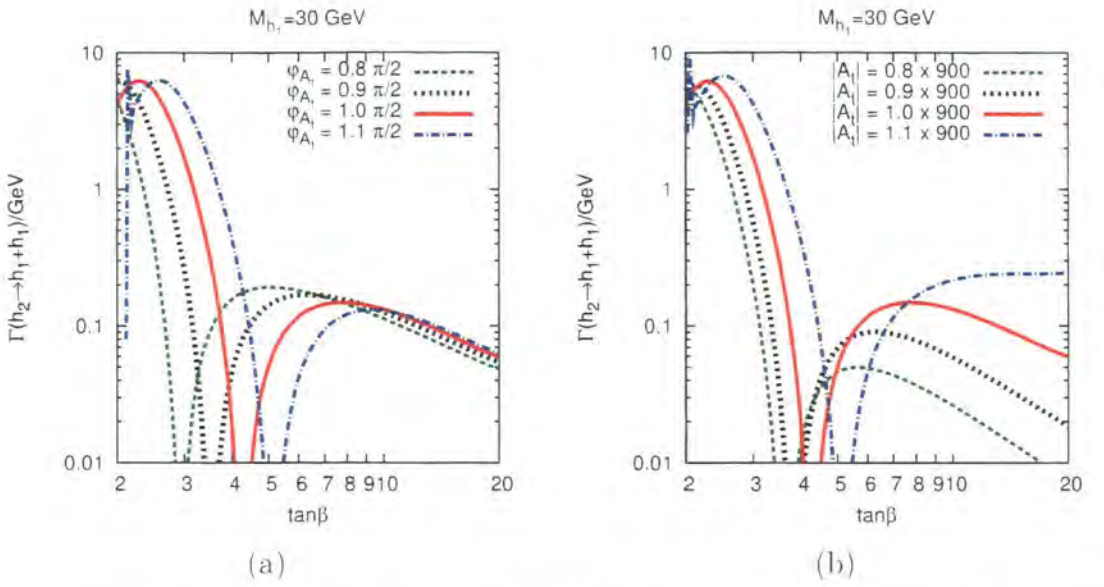

Figure 6.11: $\Gamma(h_2 \to h_1 h_1)$ as function of $\tan\beta$ for $M_{h_1} = 30$ GeV and various values of (a) the phase of the trilinear coupling φ_{A_t} and (b) the absolute value of the trilinear coupling $|A_t|$. (All trilinear couplings are set to these values, other parameters are as for the CPX scenario)

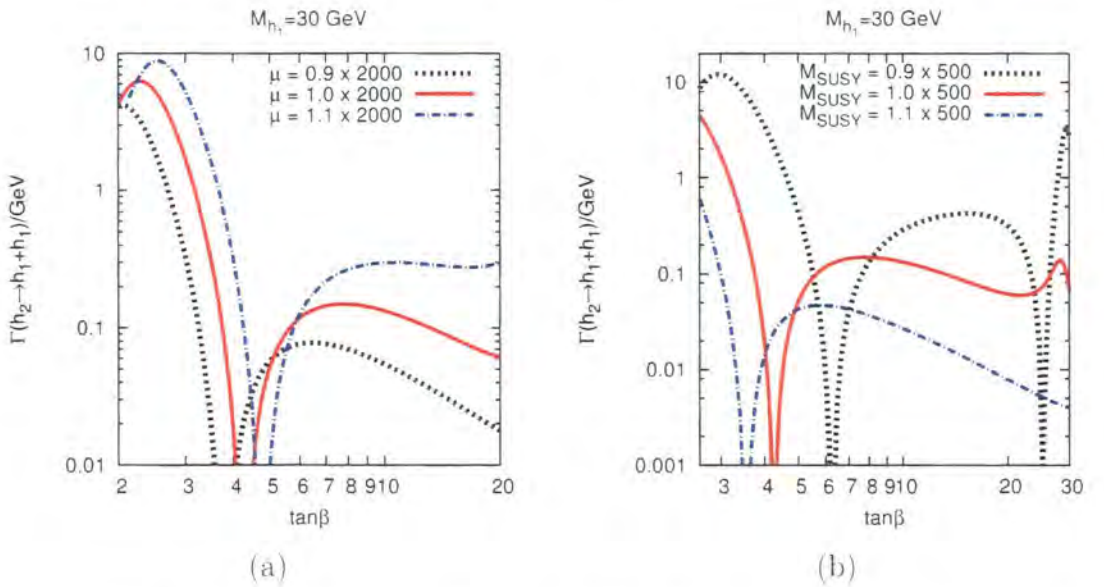

Figure 6.12: $\Gamma(h_2 \to h_1 h_1)$ as function of $\tan\beta$ for $M_{h_1} = 30$ GeV and various values of (a) the higgsino mass parameter μ and (b) the soft SUSY breaking parameter $M_{\rm SUSY}$. (Other parameters are as for the CPX scenario.)

decreases as $\arg A_t$ increases. This dramatic dependence on a complex phase emphasises the importance of including complex phases in the calculation. In Figure 6.11 (b), we see that increasing $|A_t|$ also shifts the minimum and the peak at moderate $\tan\beta$ to

higher values of $\tan\beta$. However, in this case, the magnitude of the peak at moderate $\tan\beta$ increases as $\arg A_t$ increases and the gradient of the decay width at higher values of $\tan\beta$ varies significantly. Varying μ has a similar qualitative effect to varying $|A_t|$, as we can see in Figure 6.12 (a). In Figure 6.12 (b), we can see that increasing $M_{\rm SUSY}$ by 10% dramatically increases the $h_2 \to h_1 h_1$ decay width and moves the two points at which the decay width falls to zero to closer values of $\tan\beta$. We will return to these plots in Chapter 9 in order to explain the variation in the size and shape of the region of CPX parameter space at $\tan\beta \sim 8$ which the LEP results are unable to exclude.

As discussed in Section 6.3, we also investigated the effect of including loop-corrected Higgs bosons as internal particles. In the range $2 < \tan\beta < 30$, for $M_{h_1} = 30$ GeV, we found that this changed the $h_2 \to h_1 h_1$ decay width by less than 0.3%, apart from in the immediate vicinity of the point at which the full decay width drops to zero.

6.6 Conclusion

In this section, we have calculated the full 1-loop vertex corrections within the Feynman-diagrammatic approach for the process $h_a \to h_b h_c$, taking into account the full phase dependence of the supersymmetric parameters. These vertex corrections incorporate the full momentum dependence. We have included the full propagator corrections, using neutral Higgs self-energies as provided by the program *FeynHiggs* [31,56–58] and we have consistently included 1-loop mixing with the Z boson and the unphysical Goldstone-boson degree of freedom. Our results are currently the most precise predictions for the $h_a \to h_b h_c$ decay width. These results will be included in the program *FeynHiggs* [31,56–58].

We have found that the genuine vertex corrections to the triple Higgs vertex are numerically very important. Their inclusion changes the predictions for the decay widths very drastically, compared to an approximation which is based solely on propagator-type corrections and tree level vertex corrections. Using the corrections obtained in the Yukawa approximation yields a prediction for the decay width which is closer to the full result, but we still find deviations of $\sim 27\%$ in the example of the CPX parameter space at $\tan\beta \sim 8$, $M_{h_1} \sim 30$ GeV, which will be particularly relevant to LEP exclusions discussed in Chapter 9.

We have also presented two effective coupling approximations in the complex MSSM. The Yukawa approximation includes all leading corrections and can be expressed in a very compact form, thus providing a very convenient way to go beyond the tree level vertex contributions. The effective coupling created from the full fermion/sfermion vertex corrections at zero incoming momentum is a more sophisticated effective coupling approximation. These effective couplings can be used for determining accurate cross-sections for processes such as $e^+e^- \to h_1 Z \to h_1 h_1 Z$ at the ILC, which provide a way to directly access the Higgs self-couplings and thus investigate a crucial element of the Higgs mechanism.

Chapter 7

Higgs decay to SM fermions

7.1 Introduction

The fermionic decay modes of the neutral Higgs bosons are crucially important to collider phenomenology. These modes have been used when obtaining a lower bound on the Standard Model Higgs mass [17] and to exclude large regions of MSSM parameter space [24, 102, 103]. In particular, an accurate prediction for the Higgs decay to b-quarks has been vital for these analyses, since, for Standard Model Higgs bosons with mass less than about 130 GeV and for a variety of SUSY scenarios, $h_a \to b\bar{b}$ is the dominant decay mode, and the resulting b-jets can be tagged in the detector. The decay to τ-leptons can also be useful for providing exclusions, such as those found recently for various benchmark MSSM scenarios in the high $\tan\beta$ region at the Tevatron [104, 105].

In the Standard Model, the fermionic decay width is extremely well known (for a review, see [106] and references therein) and much of the analysis for the photon and gluon contributions to the process involving the Standard Model Higgs also apply in the MSSM. As we discussed in Section 5.3, the SUSY QCD corrections can be sizable for the $h_a \to b\bar{b}$ decay and should be resummed (see, for example, [87], for an investigation into these effects). Results supplemented with leading 2-loop propagator corrections [82] and full electroweak contributions [107] are also available in the real MSSM.

The program *HDecay* [108] provides $h_a \to f\bar{f}$ decay widths for the Standard Model and the real MSSM. For the complex MSSM, the program *CPsuperH* [59], is available. This calculation involves effective $h_a f\bar{f}$ couplings, as described in [100].

The program *FeynHiggs* [31, 56–58] calculates the $h_a \to f\bar{f}$ decay width using the Feynman-diagrammatic approach, including the most significant QCD corrections, resummed SUSY QCD corrections and propagator corrections incorporating the full neutral Higgs self-energies. This calculation is valid in the real and complex MSSM. However, it does not currently include the full 1-loop electroweak vertex corrections.

Therefore, in this chapter, we calculate the full 1-loop electroweak vertex corrections to the $h_a \to f\bar{f}$ decay width in the complex MSSM, including full phase and momentum dependence, for eventual inclusion in *FeynHiggs*. We supplement these new corrections with 1-loop QED, SM QCD corrections, propagator corrections calculated using neutral Higgs self-energies from *FeynHiggs* and 1-loop propagator mixing with unphysical Goldstone bosons and Z bosons. We include resummed SUSY QCD corrections with full phase dependence.

7.2 Calculation of the $h_a \to b\bar{b}$ decay width

7.2.1 Tree level

At tree level, the $h_i \to b\bar{b}$ decay width is given by

$$\Gamma^{\text{tree}}(h_i \to b\bar{b}) = \frac{N_c}{8\pi M_{h_a}^2} \frac{M_{h_a}}{2} \sqrt{1 - \frac{4m_b^2}{M_{h_a}^2}} \left|\mathcal{M}^{\text{tree}}\right|^2 . \tag{7.1}$$

The mass dependence of the squared matrix element $|\mathcal{M}^{\text{tree}}|^2$ will be affected by the CP properties of the Higgs boson.

7.2.2 Standard Model QED corrections

The real and virtual QED contributions to the Standard Model $H \to b\bar{b}$ decay width lead to the 1-loop correction

$$\delta\Gamma_{\text{QED}}(H \to b\bar{b}) = \Gamma_{\text{tree}}(H \to b\bar{b}) \frac{\alpha}{\pi} Q_b^2 \left(-3\log(\frac{M_H}{m_b(m_b)}) + \frac{9}{4} \right), \tag{7.2}$$

for $M_H^2 >> m_f$, as derived by [109]. In this limit, this equation holds for both scalar and pseudoscalar Higgs [107]. We will therefore use the correction term

$$\delta_{\rm QED} := \frac{\alpha}{\pi} Q_b^2 \left(-3 \log(\frac{M_{h_a}}{m_b(m_b)}) + \frac{9}{4} \right) \tag{7.3}$$

in our MSSM calculation.

7.2.3 Standard Model QCD corrections

If the factor $Q_b^2 \alpha$ in equation (7.2) is replaced by the factor $C_f \alpha_s(M_H)$, the expression for the 1-loop QCD correction to the $H \to b\bar{b}$ decay in the Standard Model is obtained, as shown by [109]. $C_f = \frac{4}{3}$ is a colour factor and the running coupling $\alpha_s(M_H^2)$ is given by equation (5.5). Including the tree level result gives

$$\Gamma_{\rm QCD}(H \to b\bar{b}) = \left[\frac{\Gamma^{\rm tree}(h_a \to b\bar{b})}{m_b^{2,\rm tree}} \right] m_b^{2,\rm tree} \left[1 + \frac{\alpha_s(\mu_{\rm ren}^2)}{\pi} C_f \left(-3 \log(\frac{M_H}{m_b}) + \frac{9}{4} \right) \right], \tag{7.4}$$

where we have removed the dependence on the tree level Yukawa coupling from the term in the square bracket.

This equation is not valid in the mass range we are interested in, $M_H >> m_b$. However, substituting equation (5.7) into equation (7.4) gives

$$\Gamma_{\rm QCD}(H \to b\bar{b}) = \left[\frac{\Gamma^{\rm tree}(h_a \to b\bar{b})}{m_b^{2,\rm tree}} \right] m_b^2(\mu_{\rm ren}) \left[1 + \frac{\alpha_s(\mu_{\rm ren}^2)}{4\pi} \left(-16 \log(\frac{M_H}{\mu_{\rm ren}}) + \frac{68}{3} \right) \right], \tag{7.5}$$

and we can choose $\mu_{\rm ren} = M_H$ in order to cancel the logarithmic terms.

In practice, we parametrise our calculation in terms of $m_b = m_b(M_{h_a})$, where $m_b(M_{h_a})$ is found using equation (5.8) or equation (5.12). Therefore, in order to encompass the full 1-loop Standard Model-like QCD corrections in our calculation, we will need to add a correction

$$\delta_{\rm QCD} := \frac{17}{3} \frac{\alpha_s(M_{h_a}^2)}{\pi} \tag{7.6}$$

to the $h_a \to b\bar{b}$ decay width.

Our method differs from that of [82], which includes some higher order terms in $\alpha_s(\mu^2_{\rm ren})$ and $m_b(\mu_{\rm ren})$ and an extra term proportional to $\frac{\alpha_s(m_b^2)}{\alpha_s(M^2_{h_a})}$. Our method also differs from [87], which includes terms proportional to α_s^2. However, some of these terms depend on the CP properties of the Higgs, and thus are not trivially extendable to the complex MSSM. Both [82] and [87] restrict their analyses to the real MSSM.

7.2.4 Full 1-loop 1PI $h_i \to b\bar{b}$ vertex corrections

In order to calculate the 1 particle irreducible vertex corrections at 1-loop, $\Gamma^{\rm 1PI,1-loop}_{h_i b\bar{b}}$, we use the counter-terms shown in Table 3.3 and Table 3.4. Note that the counter term δZ_{AG} is required. We include the full MSSM, apart from 1-loop diagrams involving gluons or photons since we have treated these contributions separately. We include all complex phases. As discussed above, we use $m_b(M_{h_a})$ in these corrections in order to absorb some of the higher order terms. As before, we use a unit CKM matrix and include no squark generation mixing.

7.2.5 Resummed Δm_b corrections to $h_i \to b\bar{b}$

In order to resum the leading SUSY QCD (and higgsino) corrections for the limit of large $\tan\beta$ in the limit of heavy SUSY particles, we use the effective couplings which we derived in Section 5.3. However, as we are combining with the full genuine vertex corrections, we need to make sure we are not counting the 1-loop corrections involving gluinos or higgsinos twice. Therefore, we use effective couplings

$$\begin{aligned}
v^{\Delta m_b}_{\rm h\bar{b}b} &= \frac{1}{1+y}\left[1 - \frac{1}{t_\alpha t_\beta}y + i\gamma_5 x\left(1+\frac{1}{t_\alpha t_\beta}\right)\right] v^{\rm tree}_{\rm h\bar{b}b} \\
&- \left[{\rm Re}\Delta m_b\left(-1-\frac{1}{t_\alpha t_\beta}\right) + i\gamma_5 {\rm Im}\Delta m_b\left(1+\frac{1}{t_\alpha t_\beta}\right)\right] v^{\rm tree}_{\rm h\bar{b}b}, \qquad (7.7)\\
v^{\Delta m_b}_{\rm H\bar{b}b} &= \frac{1}{1+y}\left[1 + \frac{t_\alpha}{t_\beta}y + i\gamma_5 x\left(1-\frac{t_\alpha}{t_\beta}\right)\right] v^{\rm tree}_{\rm H\bar{b}b} \\
&- \left[{\rm Re}\Delta m_b\left(-1+\frac{t_\alpha}{t_\beta}\right) + i\gamma_5 {\rm Im}\Delta m_b\left(1-\frac{t_\alpha}{t_\beta}\right)\right] v^{\rm tree}_{\rm H\bar{b}b}, \qquad (7.8)\\
v^{\Delta m_b}_{\rm A\bar{b}b} &= \frac{1}{1+y}\left[1 - \frac{1}{t_\beta^2}y + i\gamma_5 x\left(1+\frac{1}{t_\beta^2}\right)\right] v^{\rm tree}_{\rm A\bar{b}b} \\
&- \left[{\rm Re}\Delta m_b\left(-1+\frac{1}{t_\beta^2}\right) + i\gamma_5 {\rm Im}\Delta m_b\left(1+\frac{1}{t_\beta^2}\right)\right] v^{\rm tree}_{\rm A\bar{b}b}, \qquad (7.9)
\end{aligned}$$

where the second line in each equation cancels the 1-loop terms. Recall that x, y are real and given by

$$x = \frac{\mathrm{Im}\Delta m_b}{1+\mathrm{Re}\Delta m_b}, \tag{7.10}$$

$$y = \mathrm{Re}\Delta m_b + x\mathrm{Im}\Delta m_b, \tag{7.11}$$

$$\Delta m_b = \frac{4}{3}\frac{1}{2}\frac{\alpha_s}{\pi}\mu^* M_3^* t_\beta I\left(m^2_{\tilde{b}_1}, m^2_{\tilde{b}_2}, m^2_{\tilde{g}}\right) + \frac{\alpha_t}{4\pi}A_t^*\mu^* t_\beta I\left(m^2_{\tilde{t}_1}, m^2_{\tilde{t}_2}, |\mu|^2\right). \tag{7.12}$$

(See Section 5.3 for full description of notation.) Following the procedure in the program *FeynHiggs* [31, 56–58], we will use $\alpha_s(m_t^2)$ in Δm_b.

7.2.6 Combining these contributions with propagators to obtain the full $h_a \to b\bar{b}$ decay width

The amplitude $A_{h_a b\bar{b}}$ is found by adding the Δm_b corrected coupling $v^{\Delta m_b}_{\mathrm{h_i\bar{b}b}}$ (which includes the tree level result) to the 1 particle irreducible 1-loop vertex corrections $\Gamma^{\mathrm{1PI,1-loop}}_{h_i b\bar{b}}$ and the 1-loop corrections $\Gamma^{\mathrm{G,Zse}}_{h_i b\bar{b}}$, which are due to $h_i Z$ or $h_i G$ mixing. This is combined with propagator corrections dependent on neutral Higgs self-energies, which we obtain from *FeynHiggs* and incorporate through the matrix $\mathbf{Z}$, such that

$$A_{h_a b\bar{b}} = \hat{\mathbf{Z}}_{ai}\left[v^{\Delta m_b}_{h_i b\bar{b}} + \Gamma^{\mathrm{1PI,1-loop}}_{h_i b\bar{b}}\left(M^2_{h_a}\right) + \Gamma^{\mathrm{G,Zse}}_{h_i b\bar{b}}\left(m^2_{h_i}\right)\right]. \tag{7.13}$$

The arguments to $\Gamma^{\mathrm{1PI,1-loop}}_{h_i b\bar{b}}$ and $\Gamma^{\mathrm{G,Zse}}_{h_i b\bar{b}}$ denote the external momenta used. $A_{h_a b\bar{b}}$ is combined with the external fermion wavefunctions. then we take the squared modulus and sum over external spins in the conventional way to get $|\mathcal{M}_{h_a b\bar{b}}|^2$.

The full $h_a \to b\bar{b}$ decay width is thus found using

$$\Gamma^{\mathrm{full}}(h_i \to b\bar{b}) = [1+\delta_{\mathrm{QCD}}+\delta_{\mathrm{QED}}]\frac{N_c}{8\pi M^2_{h_a}}\frac{M_{h_a}}{2}\sqrt{1-\frac{4m_b^2}{M^2_{h_a}}}\,|\mathcal{M}_{h_a b\bar{b}}|^2, \tag{7.14}$$

which is an extension of the method used to combine QED, QCD and Z-factor corrections in [82].

7.2.7 Numerical Results

We shall first investigate the effect of the SM QCD and QED corrections. Figure 7.1 shows the $H \to b\bar{b}$ decay width in the Standard Model as a function of Higgs mass, using the SM QED and QCD corrections described in equation (7.2) and equation (7.5) respectively ('QED, QCD'). This is compared to the tree level result ('tree') and result if only SM QCD corrections are included ('QCD'). For the purposes of this comparison, we parametrise the calculation in terms of $\alpha(M_Z^2)$ [1]. We find that the inclusion of the SM QCD effects reduces the decay width considerably, whereas the QED contributions are comparatively insignificant. We compare these results to those obtained from the publicly available program *HDecay* [108]. *HDecay* includes SM QCD corrections at order α_s^2 and α_s^3, and thus gives a more sophisticated treatment of the SM QCD corrections. [2] We should consider the difference between the *HDecay* SM $H \to b\bar{b}$ decay width and the decay width we obtain using equation (7.2) and equation (7.5) as a possible theoretical uncertainty and bear in mind that the $H \to b\bar{b}$ decay width could be increased by about 10% due to these additional QCD corrections (the difference is 12% at $M_H = 100$ GeV and 9.1% at $M_H = 300$ GeV).

We now consider the full MSSM $h_a \to b\bar{b}$ decay widths in the CPX scenario. Figure 7.2 illustrates the $h_1 \to b\bar{b}$ (upper), $h_2 \to b\bar{b}$ (middle) and $h_3 \to b\bar{b}$ (lower) decay widths as a function of charged Higgs mass for $\tan\beta = 10$ (left) and $\tan\beta = 30$ (right). All results include the propagator corrections, incorporated via the matrix $\mathbf{Z}$. The decay widths calculated by combining tree level vertices with propagator corrections are denoted 'tree'. We note that the h_1 and h_2 decay widths have steep gradients at $\tan\beta = 10$, $M_{H^\pm} \sim 167$ GeV due to a 'cross-over' effect in the masses (i.e. M_{h_1} and M_{h_2} approach each other). At $\tan\beta = 10$, $M_H^+ \sim 160$ GeV, h_1 is mostly A, h_2 is mostly h and h_3 is mostly H whereas at $\tan\beta = 10$, $M_H^+ \sim 180$ GeV, h_1 is mostly h, h_2 is mostly A and h_3 is mostly H.

Figure 7.2 also illustrates that including the QED and SM QCD corrections ('tree, QED, QCD'), causes a suppression in the $h_a \to b\bar{b}$ decay widths, as expected from our discussion of Figure 7.1.

[1] We compared this to the result from parameterising the calculation in terms of G_F and found an insignificant numerical effect compared to other uncertainties in the calculation.

[2] The $H \to b\bar{b}$ calculated in *HDecay* also includes leading SM electroweak contributions. However, the effect of these terms is numerically insignificant [108].

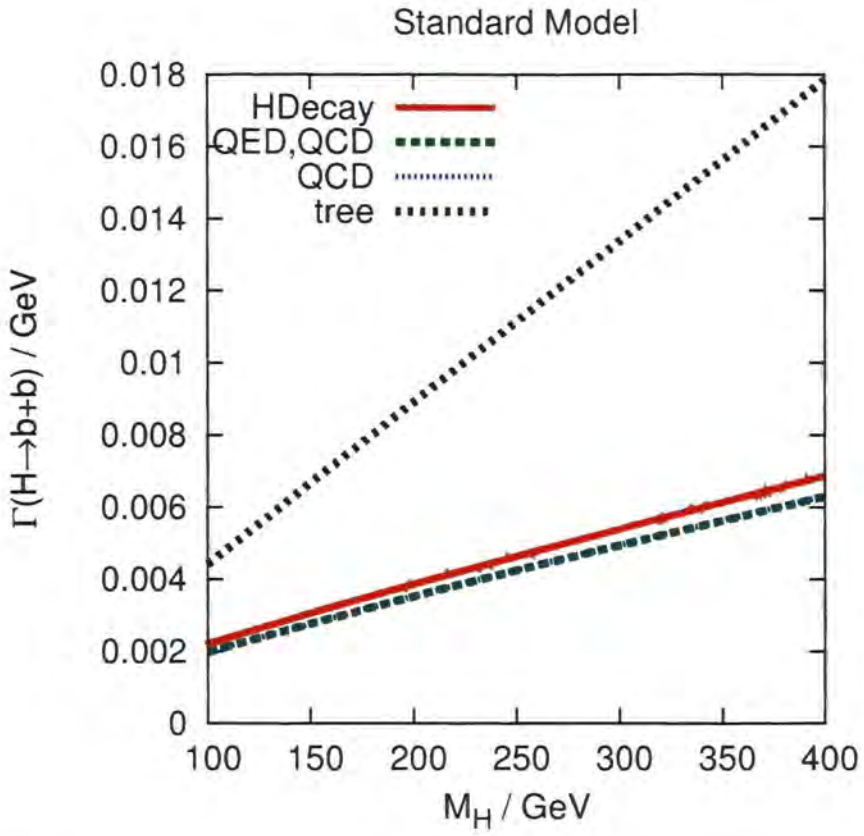

Figure 7.1: The $H \to b\bar{b}$ decay width in the Standard Model. The lines labelled 'QED,QCD' and 'QCD' include only the corrections described in equation (7.2) and equation (7.5). The line labelled 'tree' does not include these terms. The line labelled 'HDecay' has been obtained using the program HDecay [108].

Including the resummed Δm_b contributions ('tree, QED, QCD, Δm_b') has a very significant impact, as shown in Figure 7.2. These contributions have the greatest effect on the $h_1 \to b\bar{b}$ decay width at $\tan\beta = 30$, $M_{H^-} \sim 200$ GeV, where the suppression reaches an order of magnitude. We would expect the Δm_b contributions to be more significant at $\tan\beta = 30$ than at $\tan\beta = 10$, since Δm_b is proportional to $\tan\beta$, and this is reflected in the results. Note that, for different SUSY parameters, it would be possible for the resummed Δm_b corrections to cause an enhancement in the $h_a \to b\bar{b}$ decay width, rather than a suppression.

Figure 7.2 also includes the full decay widths ('full'), which combine the propagator, QED, SM QCD, SUSY QCD corrections with the full electroweak genuine vertex corrections, as described by equation (7.14). This is almost indistinguishable from the 'tree,QED,QCD,Δm_b' result, apart from in the $h_1 \to b\bar{b}$ decay width at $\tan\beta = 30$,

$M_{H^\pm} \sim 200$ GeV, where the full decay width is just 57% of the size of the 'tree, QED, QCD, Δm_b' result. The full result also includes propagator-type mixing with the Goldstone and Z boson. However, we have confirmed that this effect is numerically insignificant in all the examples plotted here.

In Figure 7.3, we consider the Δm_b corrections to the $h_2 \to b\bar{b}$ decay width in more detail, at $\tan\beta = 10$ (a) and $\tan\beta = 30$ (b). All results shown in this plot include propagator, QED, SM QCD and resummed Δm_b corrections. However, the composition of Δm_b is varied. In Figure 7.3 (upper graphs), we can see that the result obtained when including just gluino corrections to Δm_b is a good approximation to the result obtained if both gluino and higgsino corrections are included, but the difference is non-negligible. The lower graphs in Figure 7.3 include just the gluino contribution to Δm_b and vary the scale at which the strong coupling constant is evaluated, from m_t (default) to $\alpha_s(M^2_{h_i})$, which is the value of α_s used in the SM-like QCD corrections and $\alpha_s(\frac{1}{9}\left(m_{\tilde{b}_1} + m_{\tilde{b}_2} + m_{\tilde{g}}\right)^2)$, which is used in [87]. The plots show that the choice of scale in Δm_b can have a sizable impact. Changing the scale from m_t to $\frac{1}{3}\left(m_{\tilde{b}_1} + m_{\tilde{b}_2} + m_{\tilde{g}}\right)$ increases the $h_2 \to b\bar{b}$ decay width by 8% for $\tan\beta = 10$ and up to 35% for $\tan\beta = 30$ (for $M_{H^\pm} < 135$ GeV). We should consider this as an uncertainty in our calculation.

Figure 7.4 shows that using the full $h_a \to b\bar{b}$ calculation, as described in equation (7.14), differs from the result obtained if only propagator, QED, SM QCD and Δm_b corrections are included by less than 6.5% in all the numerical examples discussed above apart from the case $h_a = h_1, \tan\beta = 30$. In this latter case, the difference can be over 70%. This occurs at a very low decay width of $\Gamma(h_1 \to b\bar{b}) = 0.00066$ GeV.

Figure 7.5 demonstrates the dependence of the $h_1 \to b\bar{b}$ decay width on the phase of the trilinear coupling A_t, focusing on the minimum in the decay width at $\Gamma(h_1 \to b\bar{b}) = 0.00066$ GeV, where the full result (full lines) differs significantly from the result which includes just propagator, QED, SM QCD and Δm_b corrections (dashed lines). The dependence on the phase A_t is pronounced, which is due in particular to the propagator corrections.

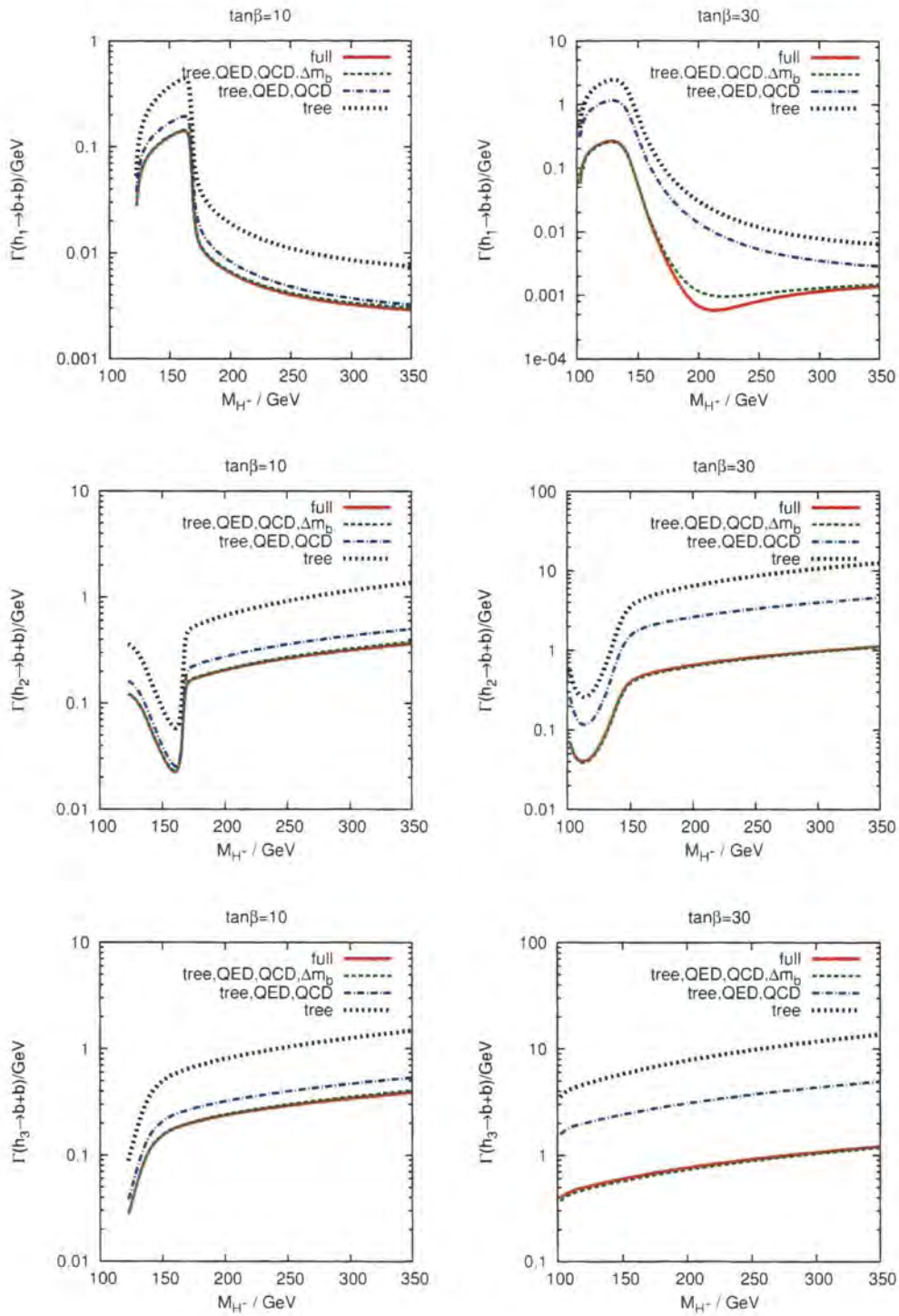

Figure 7.2: The $h_a \to b\bar{b}$ decay width in the CPX scenario as a function of the charged Higgs mass. 'tree' denotes the tree level result corrected by Z-factors. 'tree,QED,QCD' also includes the SM-like QED and QCD corrections and 'tree,QED,QCD,Δm_b' additionally includes the resummed Δm_b contribution. 'full' denotes the full result, as described by equation (7.14).

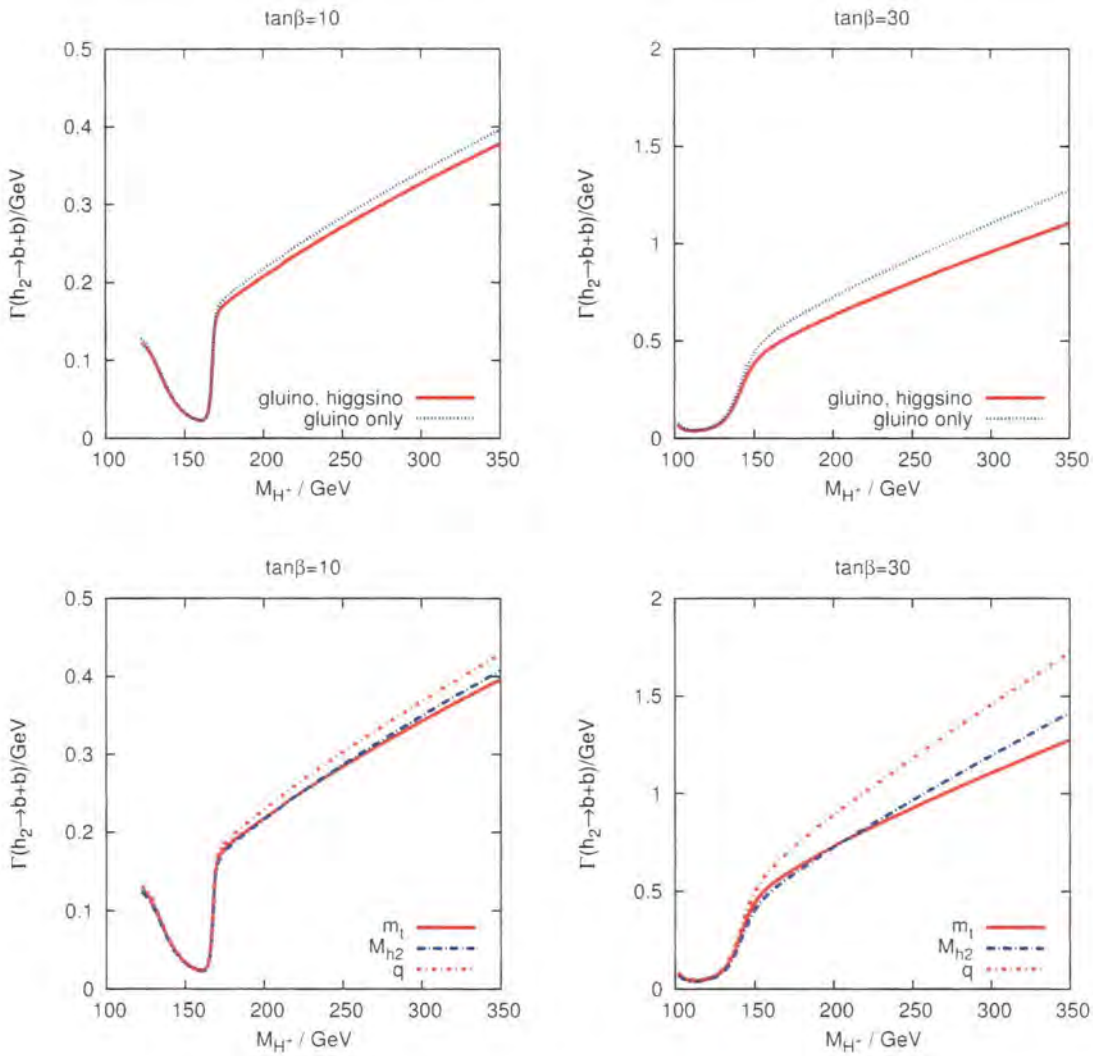

Figure 7.3: The $h_2 \to b\bar{b}$ decay width at $\tan\beta = 10$ (a) and $\tan\beta = 30$ (b), including propagator, QED, SM QCD and resummed Δm_b corrections. In the upper graphs, 'gluino and higgsino' indicates that both the gluino and higgsino contributions are included in Δm_b, whereas, in the 'gluino only' result, only gluino contributions have been included in Δm_b. In the lower graphs, only gluino contributions are included in Δm_b and the scale at which the α_s is calculated within Δm_b is varied. We show results obtained using $\alpha_s(m_t^2)$ (as used in the upper graphs), $\alpha_s(M_{h_2}^2)$ and $\alpha_s(q^2)$ where $q = \frac{1}{3}\left(m_{\tilde{b}_1} + m_{\tilde{b}_2} + m_{\tilde{g}}\right)$. (CPX scenario)

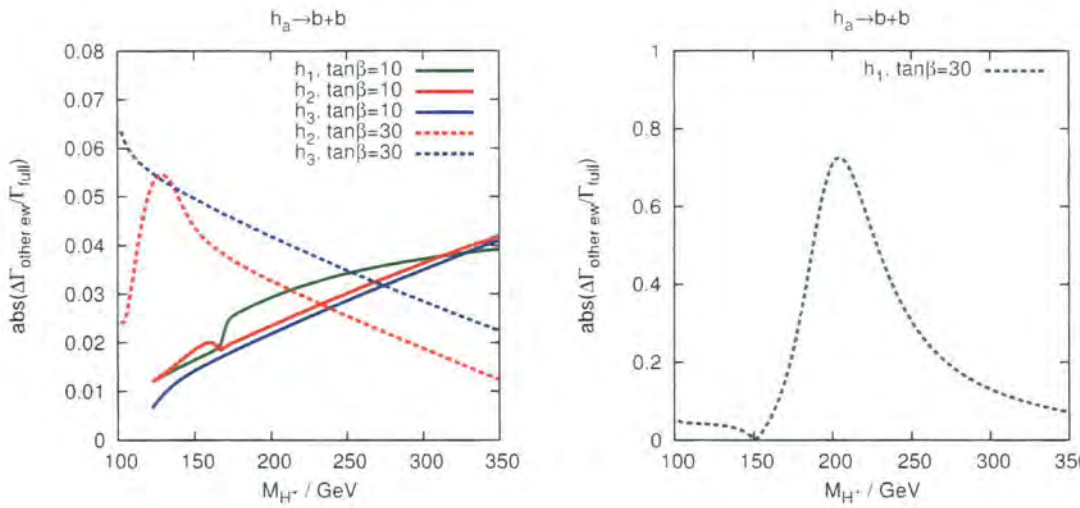

Figure 7.4: The difference ($\Delta\Gamma_{\text{other ew}}$) between the full $h_a \to b\bar{b}$ decay width (Γ_{full}) and the decay width including Z-factors, QED, SM QCD and Δm_b corrections only, as a fraction of the full decay width. Results are shown for $\tan\beta = 10$ and $\tan\beta = 30$. (CPX scenario)

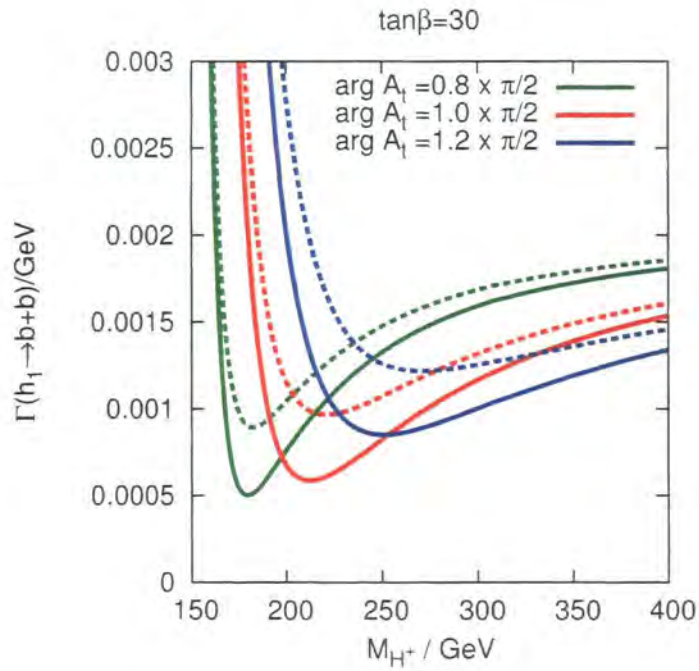

Figure 7.5: The $h_1 \to b\bar{b}$ decay width in the CPX scenario as a function of the charged Higgs mass, for various values of the phase of the trilinear coupling A_t. The full decay widths (as described by equation (7.14)) are shown with solid lines and the decay width including Z-factors, QED, SM QCD and Δm_b corrections only are shown with dashed lines.

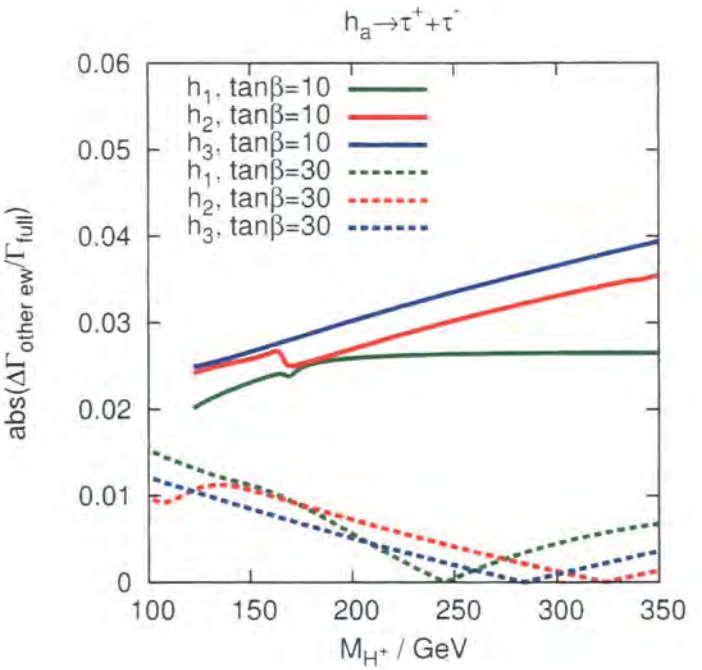

Figure 7.6: The difference ($\Delta\Gamma_{\text{other ew}}$) between the full $h_a \to \tau^+\tau^-$ decay width (Γ_{full}) and the decay width including Z-factors and QED corrections only, as a fraction of the full decay width. Results are shown for $\tan\beta = 10$ and $\tan\beta = 30$. (CPX scenario)

7.3 Calculation of the $h_a \to \tau^+\tau^-$ decay width

The calculation of the $h_a \to \tau^+\tau^-$ decay width is similar to that of the $h_a \to b\bar{b}$ decay width, with the simplification that no QCD corrections are required. We calculate the full 1-loop genuine vertex corrections and supplement these with propagator corrections (including 1-loop mixing with Goldstone and Z bosons) and QED corrections. As before, we have included all complex phases.

7.3.1 Numerical Results

Figure 7.6 compares the $h_a \to \tau^+\tau^-$ decay width from the full calculation with the result obtained if only propagator and QED corrections are included. As before, we use the example of the CPX scenario, with $\tan\beta = 10$ and $\tan\beta = 30$ and 100 GeV $< M_{H^+} <$ 350 GeV. For $\tan\beta = 10$, neglecting the extra electroweak 1-loop vertex corrections and 1-loop propagator mixing with G, Z bosons changes the result by less than 4%, whereas for $\tan\beta = 30$, the result changes by less than 1.5%.

7.4 Conclusion

We have presented the full 1-loop electroweak vertex corrections to the $h_a \to f\bar{f}$ decay width in the complex MSSM, including full phase dependence. Although we have found that these corrections are small in the numerical examples we have considered, these contributions will be incorporated in to the program *FeynHiggs*. We have supplemented these new corrections with 1-loop QED, SM QCD corrections, propagator corrections calculated using neutral Higgs self-energies from *FeynHiggs* and 1-loop propagator mixing with unphysical Goldstone bosons and Z bosons.

We also included resummed SUSY QCD corrections with full phase dependence. We note here that this method could also be used to preserve the phase dependence of the resummed SUSY QCD contributions in Higgs radiation off b-quarks, which is the dominant production mechanism for supersymmetric Higgs bosons in hadron colliders at large values of $\tan\beta$ (see [85] for a recent analysis in the real MSSM).

These $h_a \to b\bar{b}$ and $h_a \to \tau^+\tau^-$ decay widths will be combined with the $h_a \to h_b h_c$ decay widths as calculated in Chapter 6 and used in conjunction with the LEP topological cross-section limits in Chapter 9 in order to investigate the experimentally excluded regions of parameter space in the CPX scenario.

Chapter 8

Higgs branching ratios

8.1 Introduction

Accurate predictions for Higgs branching ratios are vital for Higgs phenomenology. In particular, they are frequently required as part of calculations of cross sections of collider processes involving the production and decay of an on-shell Higgs boson, which are often performed using the narrow width approximation (this is described in more detail in Appendix B). In Chapter 9, we will use Higgs branching ratios for the CPX scenario in conjunction with the LEP topological cross section limits. In order to understand the resulting exclusions, it will be necessary to refer to the behaviour of the contributing branching ratios.

We combine the $h_a \to h_b h_c$ decay widths calculated in Chapter 6[1] with the $h_a \to b\bar{b}$ and $h_a \to \tau^-\tau^+$ decay widths calculated in Chapter 7. As we have discussed, these decay widths include the full 1-loop genuine vertex corrections and are combined with propagator corrections obtained using neutral Higgs self-energies from the program *FeynHiggs* [31, 56–58], which include the leading 2-loop contributions. The 1-loop propagator mixing with Goldstone and Z bosons is also consistently incorporated. These results take into account the full phase dependence of the supersymmetric parameters. For the $h_a \to b\bar{b}$ decay width, the Δm_b corrections are resummed in a way that preserves the phase dependence. We take all other decay widths from the program *FeynHiggs* [31, 56–58].

[1] Note that, although we have calculated $\Gamma(h_3 \to h_2 h_1)$ explicitly here, unless otherwise stated, we do not calculate it explicitly in the parameter scans in Chapter 9, as it will rarely be relevant.

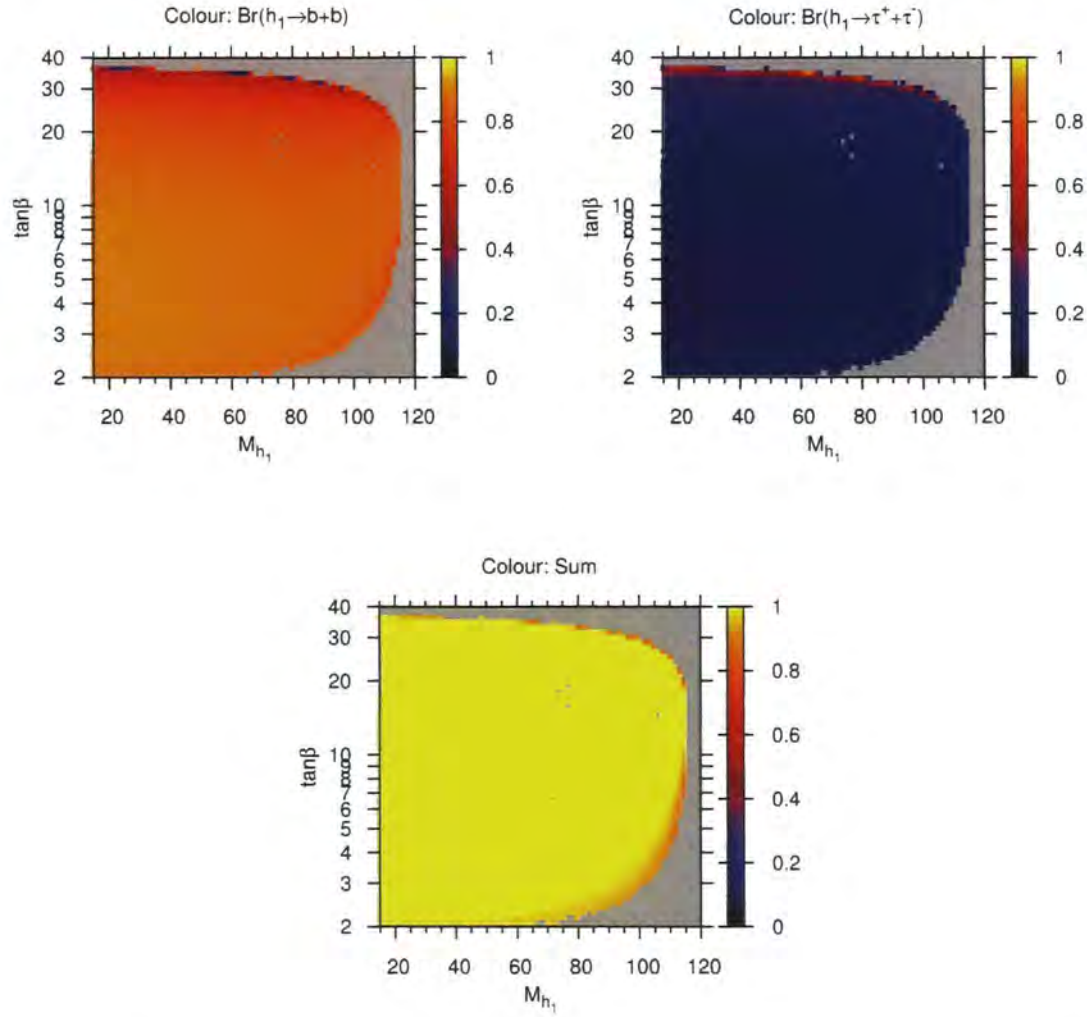

Figure 8.1: Branching ratios of the lightest neutral Higgs boson in the CPX scenario. Top left: $\mathrm{Br}(h_1 \to b\bar{b})$, top right: $\mathrm{Br}(h_1 \to \tau^+\tau^-)$, lower center: sum of $\mathrm{Br}(h_1 \to b\bar{b})$ and $\mathrm{Br}(h_1 \to \tau^+\tau^-)$.

8.2 Numerical results

Figure 8.1 (a) and (b) show the $h_1 \to b\bar{b}$ and $h_1 \to \tau^+\tau^-$ branching ratios respectively, plotted on the $M_{h_1} - \tan\beta$ plane in the CPX scenario. As expected, the $h_1 \to b\bar{b}$ decay process is dominant, although the contribution from the $h_1 \to \tau^+\tau^-$ decay is non-negligible. These are the significant decay modes for the lightest Higgs boson in the CPX scenario, as can be seen Figure 8.1, which shows that the sum of these two branching ratios is close to one across the whole of the $M_{h_1} - \tan\beta$ plane. Notice also that there are some points within the CPX parameter space that are shown here without

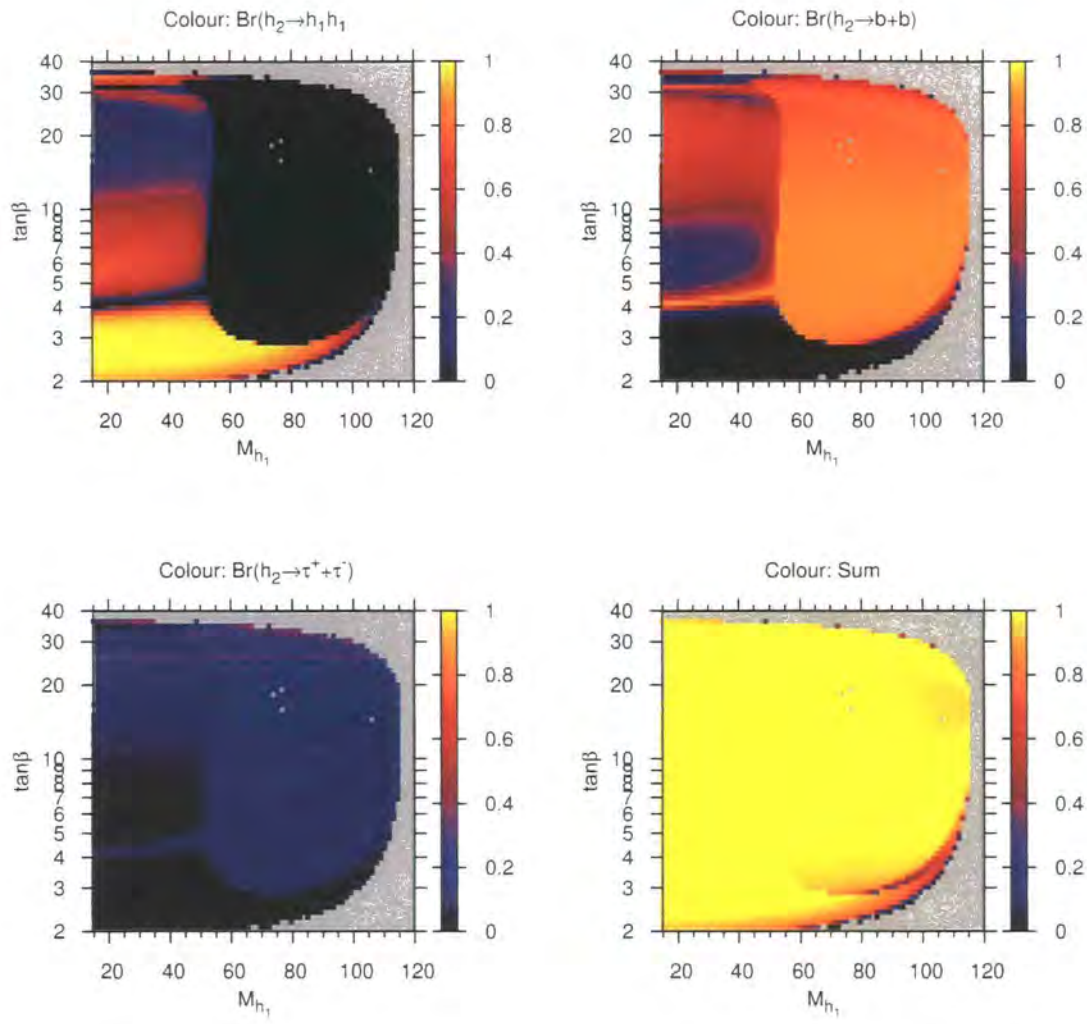

Figure 8.2: Branching ratios of the second lightest neutral Higgs boson in the CPX scenario. Top left: $\mathrm{Br}(h_2 \to h_1 h_1)$, top right: $\mathrm{Br}(h_2 \to b\bar{b})$, lower left: $\mathrm{Br}(h_2 \to \tau^+\tau^-)$, lower right: sum of $\mathrm{Br}(h_2 \to h_1 h_1)$, $\mathrm{Br}(h_2 \to b\bar{b})$ and $\mathrm{Br}(h_2 \to \tau^+\tau^-)$ branching ratios

a branching ratio value and that the edge of the allowed parameter region is uneven. These are points where either the mass calculation or the Z-factor calculation failed because the terms involving double derivatives of self-energies were non-negligible, as described in equation (4.26). Since this is only relevant for a very small number of parameter points and conveys interesting information about the stability of the Higgs sector in these places, we leave these features in in the majority of our scans.

Figure 8.2 illustrates the pronounced dependence of the $h_2 \to h_1 h_1$ branching ratio on $\tan\beta$ and M_{h_1}. Comparison with Figure 6.2 shows that this decay mode is significant

and often dominant in almost all of the regions where it is kinematically allowed. In this region, we can see that the characteristics of the $h_2 \to h_1 h_1$ branching ratio are determined by the behaviour of the $h_2 \to h_1 h_1$ decay widths, which were illustrated in Figure 6.7. Note, in particular, the two narrow regions of very low $h_2 \to h_1 h_1$ branching ratio, which occur at $\tan\beta \sim 4.3$ and $\tan\beta \sim 31$, where the $h_2 \to h_1 h_1$ decay width tends to zero. Figure 8.2 also demonstrates that the behaviour of the $h_2 \to b\bar{b}$ branching ratio is, to a very good approximation, determined entirely by the $h_2 \to h_1 h_1$ decay width where it is allowed kinematically. The $h_2 \to \tau^+\tau^-$ branching ratio is small, but non-negligible in regions where the $h_2 \to h_1 h_1$ decay width is suppressed. Figure 8.2 also shows that the $h_2 \to b\bar{b}$, $h_2 \to h_1 h_1$ and $h_2 \to \tau^+\tau^-$ decay modes dominate the total h_2 width across the majority of the CPX parameter space.

Figure 8.3 shows the branching ratios for the $h_3 \to h_1 h_1$, $h_3 \to h_2 h_1$, $h_3 \to b\bar{b}$ and $h_3 \to \tau^+\tau^-$ decay modes. Note that the Higgs cascade decays dominate in the majority of the region where they are kinematically allowed. The $h_3 \to h_1 h_1$ branching ratio has a narrow region at $\tan\beta \sim 4.5$ in which the $h_3 \to h_1 h_1$ decay is kinematically allowed, but the decay width is suppressed, characteristically similar to the suppressed regions we observed in the $h_2 \to h_1 h_1$ branching ratio. Once again, the behaviour of the $h_3 \to b\bar{b}$ decay width is governed by the behaviour of the Higgs cascade decays where they are kinematically allowed. In particular, h_3 can be relevant to the LEP exclusions in the region $10 \lesssim \tan\beta \lesssim 30$, $M_{h_1} \lesssim 60$ for variations on the CPX scenario. In this region of parameter space, the $h_3 \to h_1 h_1$ decay width is crucially important to the $h_3 \to h_1 h_1$ and $h_3 \to b\bar{b}$ branching ratios. Figure 8.3 also confirms that, once again, the Higgs decay to tau-leptons is non-negligible in regions of parameter space where the Higgs cascade decay are suppressed. We can see that there is also a region $\tan\beta \lesssim 5$ at moderate to high values of M_{h_1} in which other decays begin to contribute significantly to the h_3 total decay width, such as the $h_3 \to h_1 Z$ decay mode. As mentioned previously, we take these decay widths from *FeynHiggs*. However, the majority of this region is already excluded by the LEP Higgs searches.

8.3 Conclusion

We have investigated the behaviour of $h_a \to h_b h_c$, $h_a \to b\bar{b}$ and $h_a \to \tau^+\tau^-$ branching ratios and confirmed that these decay modes are the most significant decay modes in the areas of parameter space which will be most relevant to the discussion of the LEP

Higgs searches in the next chapter. In particular, in the region of parameter space $M_{h_1} \lesssim 60$ GeV, we have found that the dominant branching ratios are heavily dependent on the Higgs cascade decay widths. Therefore an accurate determination of these decay widths, as performed in Chapter 6, will be crucially important to the behaviour of the unexcluded regions in this part of CPX parameter space.

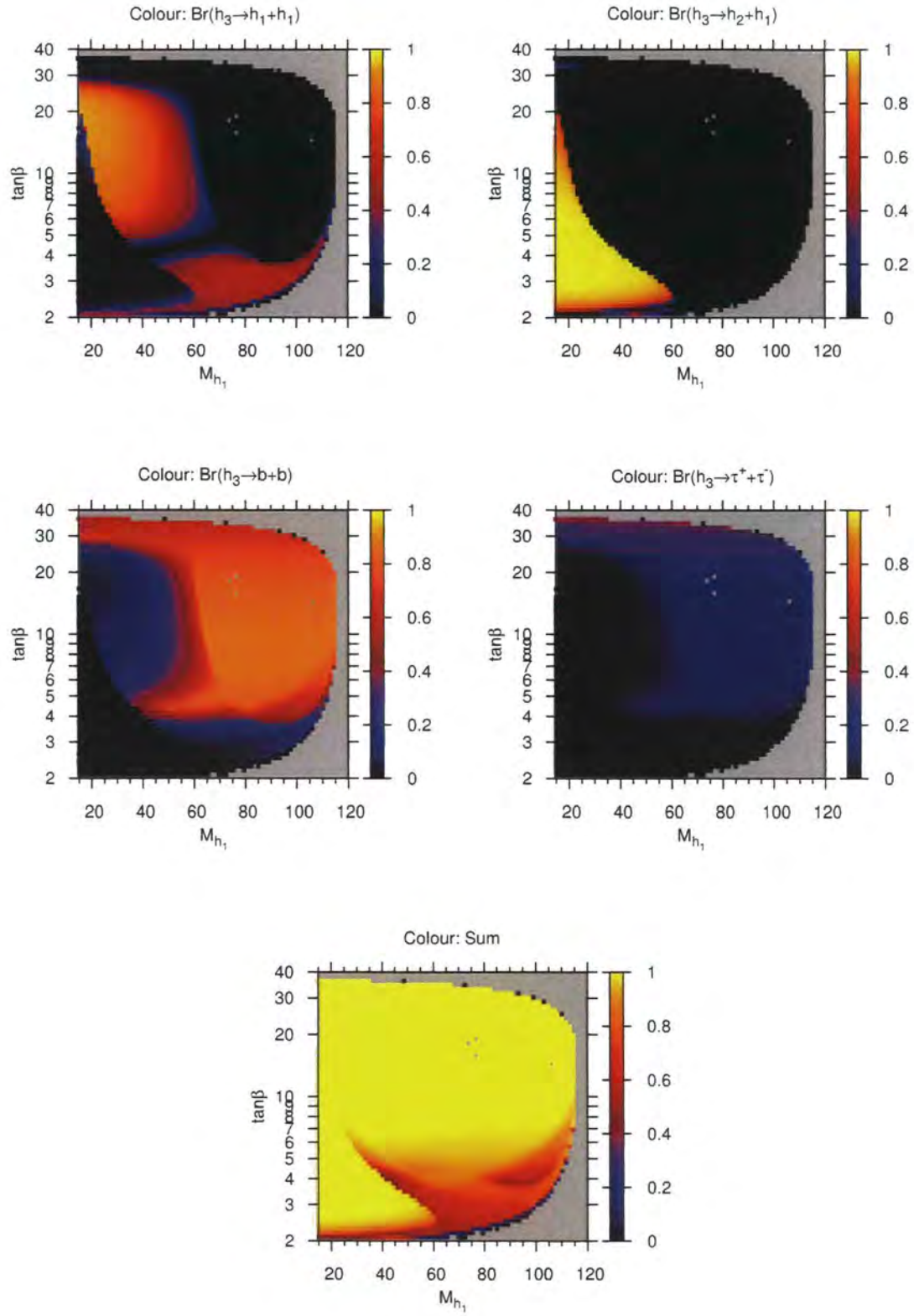

Figure 8.3: Branching ratios of the second lightest neutral Higgs boson in the CPX scenario. Clockwise from top left: $\mathrm{Br}(h_3 \to h_1 h_1)$, $\mathrm{Br}(h_3 \to h_2 h_1)$, $\mathrm{Br}(h_3 \to b\bar{b})$ and $\mathrm{Br}(h_3 \to \tau^+\tau^-)$. 'Sum' indicates the sum of $\mathrm{Br}(h_3 \to h_1 h_1)$, $\mathrm{Br}(h_3 \to h_2 h_1)$, $\mathrm{Br}(h_3 \to b\bar{b})$ and $\mathrm{Br}(h_3 \to \tau^+\tau^-)$.

Chapter 9

Limits on the MSSM parameter space from the Higgs searches at LEP

In this chapter, we will review the results from the Higgs searches at LEP, as presented by the LEP Higgs Working Group and the LEP Collaborations. We will then discuss the way in which the topological cross-section limits can be used in conjunction with new Higgs sector theoretical results, in order to provide a new analysis of the available MSSM parameter space. Using this method, we will investigate the impact of our new genuine vertex corrections to the $h_2 \to h_1 h_1$ decay on the LEP exclusions for the CPX scenario. We will also examine the effects of recent improvements in the program *FeynHiggs* [31, 56–58], which are not yet publicly available. We will conclude with a preliminary comparison between our results and those obtained with the program *CPsuperH* [59].

9.1 Results as presented by the LEP Higgs Working Group and LEP Collaborations

After the LEP programme finished in 2000, the final results from the four LEP collaborations (ALEPH [17, 110, 111], DELPHI [112, 113], L3 [114] and OPAL [115, 116]) were combined and examined for consistency with a background hypothesis and a signal plus background hypothesis in a coordinated effort between the LEP Higgs Working Group for Higgs Searches and the LEP collaborations. The results showed no significant excess

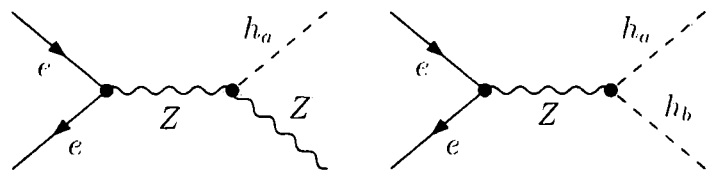

Figure 9.1: The most important Higgs production processes used in the LEP Higgs searches: Higgsstrahlung (left) and pair production (right).

of events which would indicate the discovery of a Higgs. In the Standard Model, a lower bound on the Higgs mass of 114.4 GeV at the 95% confidence level was established [17] while restrictions were placed on the available parameter space of a variety of MSSM benchmark scenarios [24]. The results were also provided in the form of upper limits on cross-sections for a selection of topologies.

In this section we will describe these search topologies, paying particular attention to the $e^+e^- \rightarrow (h_a)Z \rightarrow (b\bar{b})Z$ channel, which has been particularly powerful for excluding large regions of Standard Model and MSSM parameter space. We will then describe the results of the dedicated CPX scenario analysis.

9.1.1 Topological cross-section bounds

In order to allow the LEP results to be applied to a wide variety of theoretical models, they have been made publicly available in the form of upper limits on cross-sections of the neutral Higgs search topologies [24]. In each topology considered here, the Higgs is produced either through Higgsstrahlung or pair production (Figure 9.1) and decays either to b-quarks, tau-leptons or via the Higgs cascade decay. To a very good approximation, the kinematic distributions of these processes are independent of the CP properties of the Higgs bosons involved, as discussed in [24]. Therefore, the same topological bounds can be used for CP-even, CP-odd or mixed CP Higgs bosons.

The neutral Higgs search topologies are

1. $e^+e^- \rightarrow (h_a)Z \rightarrow (b\bar{b})Z$

2. $e^+e^- \rightarrow (h_a)Z \rightarrow (\tau^+\tau^-)Z$
3. $e^+e^- \rightarrow (h_a \rightarrow h_b h_b)Z \rightarrow (b\bar{b}b\bar{b})Z$
4. $e^+e^- \rightarrow (h_a \rightarrow h_b h_b)Z \rightarrow (\tau^+\tau^-\tau^+\tau^-)Z$
5. $e^+e^- \rightarrow (h_a h_b) \rightarrow (b\bar{b}b\bar{b})$
6. $e^+e^- \rightarrow (h_a h_b) \rightarrow (\tau^+\tau^-\tau^+\tau^-)$
7. $e^+e^- \rightarrow (h_a \rightarrow h_b h_b)h_b \rightarrow (b\bar{b}b\bar{b})b\bar{b}$
8. $e^+e^- \rightarrow (h_a \rightarrow h_b h_b)h_b \rightarrow (\tau^+\tau^-\tau^+\tau^-)\tau^+\tau^-$
9. $e^+e^- \rightarrow (h_a \rightarrow h_b h_b)Z \rightarrow (b\bar{b})(\tau^+\tau^-)Z$
10. $e^+e^- \rightarrow (h_a \rightarrow b\bar{b})(h_b \rightarrow \tau^+\tau^-)$
11. $e^+e^- \rightarrow (h_a \rightarrow \tau^+\tau^-)(h_b \rightarrow b\bar{b})$

Here, a and b label individual neutral Higgs bosons in a theory. For example, in the MSSM, $a, b = 1, 2, 3$. In topologies involving more than one Higgs, the masses are ordered such that $M_{h_a} > M_{h_b}$.

Figure 9.2 shows the topological cross-section limits for the topology $e^+e^- \rightarrow (h_a)Z \rightarrow (b\bar{b})Z$, as published in [17, 24], as a function of the mass of the Higgs involved. This topology was the most important for the purposes of deriving the lower bound on the Standard Model Higgs mass [17]. S_{95} is the ratio of the maximum cross-section compatible with data at the 95% confidence level to the theoretical Standard Model Higgsstrahlung cross-section $e^+e^- \rightarrow h_a Z$ (we will discuss this quantity in more detail in the next section). There is a good agreement between the observed limit (solid line) and the median expected limit based on Monte Carlo simulations with no signal (dashed line). The observed limit reaches more than one sigma above the expected result for Higgs masses of 89.6 GeV $< M_H <$ 107 GeV and fluctuates downwards by more than one sigma at $M_H \sim 65$ GeV. Over extended searches, such as this, a local excess in one particular mass region should be interpreted with care. The mass resolution for this process is typically $2-3$ GeV [17], giving parameter space 'bins' of approximately $4-6$ GeV. Therefore, in extended searches which cover a mass range of ~ 120 GeV, we would expect to find regions containing local excesses of $1-2$ sigma [24].

However, the excess at 89.6 GeV $< M_H <$ 107 GeV will turn out to have a large influence on our results. We will denote this region as the 'slight excess' region (to avoid confusion with the excess at 115 GeV which was observed by ALEPH [110]).

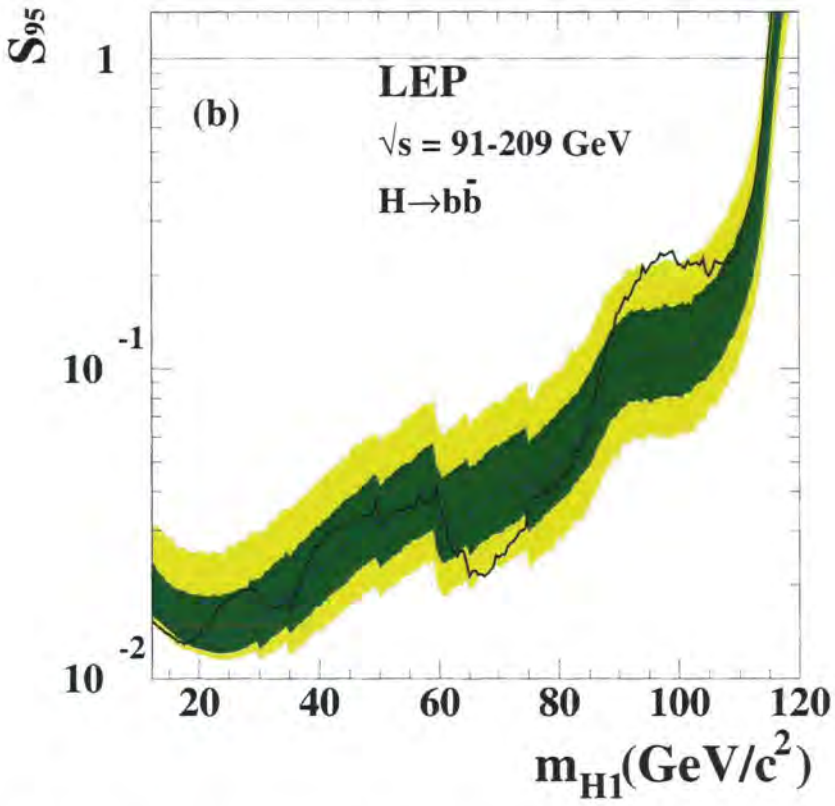

Figure 9.2: The topological cross-section limits for the topology $e^+e^- \to (h_a)Z \to (b\bar{b})Z$, as a function of the Higgs mass M_{h_a} [17, 24] (labelled 'm_{H1}'). S_{95} is the ratio of the maximum cross-section compatible with data at the 95% confidence level to the theoretical Standard model Higgsstrahlung cross-section $e^+e^- \to h_aZ$. The solid line is the observed limit, the dashed line is the median expected result (based on Monte Carlo simulations with no signal) and the green and yellow areas correspond to the 68% and 95% probability bands respectively. *This figure has been reproduced from* [24].

9.1.2 Results of the dedicated analysis in the CPX scenario

The LEP Higgs Working Group and LEP collaborations also published combined analyses [24] of MSSM benchmark scenarios [117, 118], including the CPX scenario [39]. Note that the definition of the CPX scenario used in [24, 39] differs slightly from the definition used in this thesis, as discussed in Section 2.8.

Figure 9.3 shows the regions of CPX parameter space which could be excluded by this analysis at 95% CL (light green) and 99.7% CL (dark green). Also shown are the domains which were expected to be excluded at the 95% CL on the basis of Monte Carlo simulations with no signal (dotted lines).

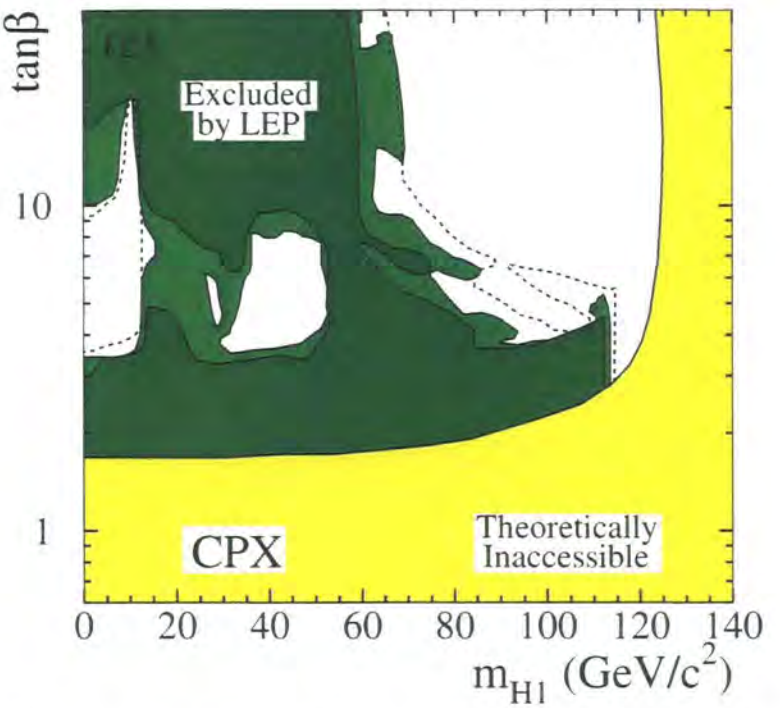

Figure 9.3: LEP Exclusions in the dedicated analysis of the CPX benchmark scenario of [24], as a function of the mass of the lightest Higgs (labelled 'm_{H1}') and $\tan\beta$. Domains excluded at 95% CL are light green: those excluded at 99.7% CL are dark green. The yellow region, which has been labelled 'theoretically inaccessible', is not part of the CPX parameter space. The dashed lines indicate the regions expected to be excluded at the 95% CL on the basis of Monte Carlo simulations with no signal. *This figure has been reproduced from* [24].

The dashed lines indicate the regions expected to be excluded at the 95% CL on the basis of Monte Carlo simulations with no signal. There are three particularly large unexcluded regions:

- (A) 60 GeV $\lesssim M_{h_1}$ and $3 \lesssim \tan\beta$
- (B) 30 GeV $\lesssim M_{h_1} \lesssim$ 50 GeV and $3 \lesssim \tan\beta \lesssim 10$
- (C) 0 GeV $\lesssim M_{h_1} \lesssim$ 10 GeV and $3 \lesssim \tan\beta \lesssim 20$

For the purposes of the analysis in [24], two different programs were used to calculate Higgs masses and branching ratios in the complex MSSM: *FeynHiggs* version 2.0 [58] and *CPH* [39], which was predecessor of the program *CPsuperH* [59]. *FeynHiggs* uses a Feynman-diagrammatic approach and on-shell mass renormalisation whereas *CPH* is based on a renormalisation group improved effective potential calculation and $\overline{\text{DR}}$

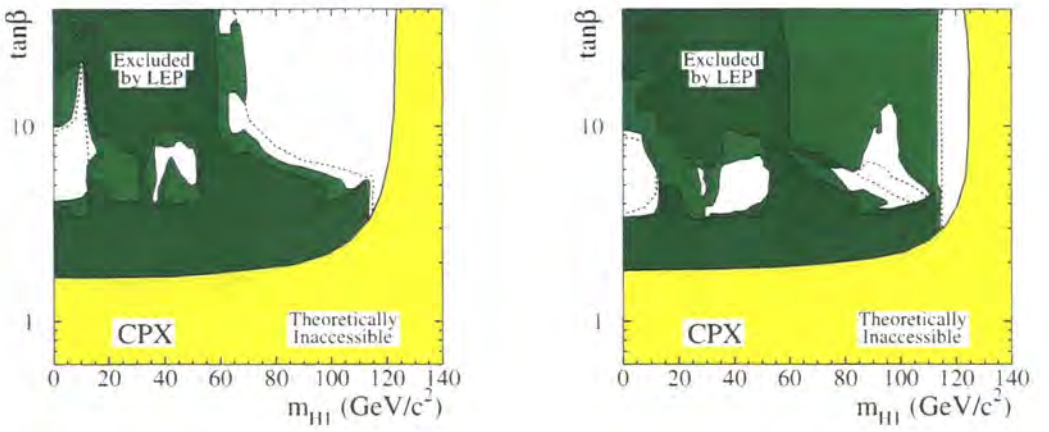

Figure 9.4: LEP Exclusions in the dedicated analysis of the CPX benchmark scenario of [24] using the program *CPH* [39] (left) and the program *FeynHiggs* [31, 56–58] version 2.0 (right). The results shown here were combined to get Figure 9.3. by deciding that a point in parameter space is excluded only if both the *CPH* and *FeynHiggs* analyses found it to be excluded. See caption to Figure 9.3 for the legend. *This figure has been reproduced from* [24].

renormalisation. As discussed in Section 3.1. some care is necessary when comparing results from these codes, since they use different renormalisation schemes. In [24], the relation

$$\tilde{X}_t^{\mathrm{CPH}} = \tilde{X}_t^{\mathrm{FH}} + \frac{\alpha_s}{3\pi} M_{\mathrm{SUSY}} \left[8 + \frac{4\tilde{X}_t^{\mathrm{FH}}}{M_{\mathrm{SUSY}}} - \frac{\pi \tilde{X}_t^{\mathrm{FH}}}{M_{\mathrm{SUSY}}} \log \left(\frac{m_t^{\mathrm{OS.2}}}{M_{\mathrm{SUSY}}^2} \right) \right] \tag{9.1}$$

was used [119] to convert between different definitions for $|A_t|$, with $\alpha_s = 0.108$ and $\tilde{X}_t = |A_t| - \mu/\tan\beta$. This is analogous to the expression for on-shell to $\overline{\mathrm{MS}}$ conversion in the real MSSM given by [60][1].

$$X_t^{\overline{\mathrm{MS}}} = X_t^{\mathrm{OS}} + \frac{\alpha_s}{3\pi} M_S \left[8 + \frac{4X_t}{M_S} - \frac{X_t^2}{M_S^2} - \frac{3X_t}{M_S} \log \left(\frac{m_t^2}{M_S^2} \right) \right]. \tag{9.2}$$

where $M_S = \sqrt{M_{\mathrm{SUSY}}^2 + m_t^2}$.

For the analysis in [24], there was no conversion between different definitions of $\arg(A_t)$ or $M_{\mathrm{SUSY}} (= M_L = M_{\tilde{t}_R})$ and A_b was set to be the same as A_t.

In addition to the issue of parameter conversion, the two codes also have significant differences in the incorporated higher order corrections. Therefore, separate analyses

[1] This expression was obtained using $m_{\tilde{g}} = M_{\mathrm{SUSY}}$, $\mu_{\mathrm{ren}} = M_S$ and the assumptions $m_t/M_S << 1$ and $m_t X_t/M_S^2 << 1$ [60]

were performed using *FeynHiggs* and *CPH*. In order to combine these results to create Figure 9.3, a point in parameter space was said to be excluded if it was excluded by each program separately. This method is conservative, in that it minimises the exclusion region.

There was an additional complication, since *FeynHiggs* did not have a reliable calculation for the loop corrections to the triple Higgs couplings in the CP-violating MSSM. For the purposes of the '*FeynHiggs*' analysis, this coupling was therefore obtained from *CPH*, and then combined with Higgs masses and other Higgs sector quantities as calculated by *FeynHiggs* in the standard way [24, 88]. This will be particularly relevant to the discussion of LEP exclusions in the region of CPX parameter space $M_{h_1} \lesssim 50$ GeV, where the $h_2 \to h_1 h_1$ decay width has a large influence on the h_2 branching ratios (as we saw in Section 8).

The results from the separate *FeynHiggs* and *CPH* analyses are shown in Figure 9.4, (with colours defined as for Figure 9.3). It is notable that both analyses have unexcluded regions of type B and C, although the shapes of these regions vary. In particular, the *FeynHiggs* analysis has a larger unexcluded region of type B. The unexcluded regions of type A at 99.7 % CL are very similar in shape and size. However, in the *FeynHiggs* analysis, much of this region is excluded at 95% CL, whereas the *CPH* analysis has the majority of this region unexcluded. Both analyses show unexcluded regions at $M_{h_1} \gtrsim 114.4$ GeV, where the lightest Higgs boson is Standard Model-like.

9.2 Using the LEP topological cross-section limits

Topological cross-section limits are given by [24] in the form of scaling factors S_{95}, defined as

$$S_{95} = \sigma_{\rm max}/\sigma_{\rm ref}, \tag{9.3}$$

where $\sigma_{\rm max}$ is the largest cross-section compatible with the data at 95 % CL and $\sigma_{\rm ref}$ is a reference cross-section for the Higgs production.

For the Higgsstrahlung topologies, the reference cross-section $\sigma_{\rm ref}$ is the SM cross-section for the Higgs production $\sigma^{\rm SM}(e^+e^- \to HZ)$, for a SM-like Higgs of mass $M_H = M_{h_a}$.

For the pair production topologies, the reference cross-section $\sigma_{\rm ref}$ is the MSSM cross-section for the Higgs production $e^+e^- \to h_a h_b$, where the MSSM suppression factor $|g^{\rm eff}_{h_a h_b Z}|^2$ has been set to 1. This suppression factor can be approximated by the normalised effective coupling of the Higgs bosons h_a and h_b to the Z boson squared, as defined in equation (4.51) (hence the notation). We can also relate the reference cross-section for pair production processes to the Standard Model Higgsstrahlung production cross-section

$$\sigma_{\rm ref} = \bar{\lambda}\sigma^{\rm SM}(e^+e^- \to HZ). \tag{9.4}$$

$\bar{\lambda}$ is a kinematic factor which takes into account the different kinematic dependences of the SM Higgsstrahlung and the pair production process, i.e.

$$\bar{\lambda} = \lambda^{3/2}_{h_a h_b} / \left(12M_Z^2/s + \lambda_{ZH}\right) / \lambda^{1/2}_{ZH}, \tag{9.5}$$

$$\lambda_{xy} = \left[1 - (M_x + M_y)^2/s\right]\left[1 - (M_x - M_y)^2/s\right], \tag{9.6}$$

where H is a SM-like Higgs with mass M_H.

In order to use the S_{95} values, we need to compare them to the scaling factors $S_{\rm theo}$, where

$$S_{\rm theo} = \sigma_{\rm theo}/\sigma_{\rm ref}, \tag{9.7}$$

and $\sigma_{\rm theo}$ is the theoretically predicted cross-section.

In the MSSM, it is convenient to calculate the $S_{\rm theo}$ values using the narrow width approximation (see Appendix B) and neglecting any production diagrams that do not appear in Figure 9.1. We approximate the h_a-Z-Z and h_a-h_b-Z vertices by the normalised effective couplings defined in equation (4.51), which take into account Higgs propagator corrections.

For example, in this approximation,

$$\begin{aligned}
S_{\rm theo}\left[(h_1)Z \to (b\bar{b})Z\right] &= |g^{\rm eff}_{h_1 ZZ}|^2 {\rm Br}(h_1 \to b\bar{b}), \\
S_{\rm theo}\left[(h_2 \to h_1h_1)Z \to (b\bar{b}b\bar{b})Z\right] &= |g^{\rm eff}_{h_2 ZZ}|^2 {\rm Br}(h_2 \to h_1h_1){\rm Br}(h_1 \to b\bar{b})^2, \\
S_{\rm theo}\left[e^+e^- \to (h_2 \to h_1h_1)h_1 \to (b\bar{b}b\bar{b})b\bar{b}\right] &= |g^{\rm eff}_{h_2 h_1 Z}|^2 {\rm Br}(h_2 \to h_1h_1){\rm Br}(h_1 \to b\bar{b})^3.
\end{aligned}$$

Therefore, for each point in parameter space, we first calculate an $S_{\rm theo}$ value for every combination of neutral Higgs possible in each search topology. Since $|g^{\rm eff}_{h_a h_a Z}|^2 \simeq 0$ and, where two Higgs bosons are involved, we have specified the mass ordering $M_{h_a} > M_{h_b}$, this results in a total of 33 channels.

In each channel, we then calculate the ratio $R^{\rm expected} = S_{\rm theo}/S_{95}^{\rm expected}$, where $S_{95}^{\rm expected}$ is the median expected S_{95} value, based on Monte Carlo simulations with no signal. The channel with the highest value of $R^{\rm expected}$ is the channel with the highest statistical sensitivity. For this particular channel (and this channel only), we then calculate the ratio $R^{\rm obs} = S_{\rm theo}/S_{95}^{\rm obs}$, where $S_{95}^{\rm obs}$ is based on the actual results observed at LEP. If $R^{\rm obs} > 1$, we say that this parameter point is excluded at 95% confidence level.

This method has been suggested by [119] in order to ensure that we can correctly interpret exclusions obtained in this way as having a confidence level of 95%. If, for one parameter point, we had made use of more than one observed limit, we would have increased the probability of a false exclusion above 5%.

The tables of S_{95} values which we use in our analysis have been obtained from [120]. These are more detailed than those published in [24] and include the numerical values of $S_{95}^{\rm expected}$. We linearly interpolate between points in these tables.

It should be noted that the dedicated analyses carried out in [24] for specific MSSM benchmark scenarios have a higher exclusion power than the method outlined above. This is particularly true near to borders between regions of parameter space where different channels are expected to have the highest statistical sensitivity. In addition, our analysis will not take into account the uncertainty in the Higgs mass, coupling and branching ratio calculations due to unknown higher order corrections.

9.3 Using the LEP topological cross-section limits in conjunction with our Higgs sector results

In this section, we will use the topological cross-section limits from LEP in conjunction with more recent results for the Higgs masses, couplings and branching ratios. In particular, we shall be using our full 1-loop diagrammatic calculation for the $h_i \to h_j h_k$ decay with full phase dependence as described in Chapter 6 and we will be using renormalised

neutral Higgs self-energies obtained from the current version of *FeynHiggs* [31, 56, 58] (which includes corrections at $\mathcal{O}(\alpha_s\alpha_t)$ with full phase dependence).

We calculate the Higgs masses and couplings to gauge bosons as described in Chapter 4 and the Higgs branching ratios as described in Chapter 6. Unless otherwise stated, we will use the CPX scenario, as defined in Section 2.8.

Using the Higgs masses, we can investigate the regions in which the Higgsstrahlung topology $e^+e^- \to (h_a)Z \to (b\bar{b})Z$ might struggle to provide exclusions. Figure 9.5 shows the regions $M_{h_1} \geq 114.4$ GeV (red) and $M_{h_2} \geq 114.4$ GeV (cyan) within the CPX parameter space, as plotted on the $M_{h_1} - \tan\beta$ plane. We would not expect the Higgsstrahlung channel $e^+e^- \to (h_1)Z \to (b\bar{b})Z$ or $e^+e^- \to (h_1)Z \to (b\bar{b})Z$ to be able to provide exclusions in these areas, respectively.

In Figure 9.5, we can see that there is a sizable region in which 89.6 GeV $< M_{h_2} <$ 107 GeV (dark blue). Recall that, in this mass range, the observed limit was more than one sigma above the expected limit (based on no signal) in the $e^+e^- \to (h_2)Z \to (b\bar{b})Z$ channel. Note that this region covers the area in which the analysis of [24] found an unexcluded region of type B.

Figure 9.6 illustrates the normalised squared effective Higgs couplings to gauge bosons $|g^{\text{eff}}_{h_aZZ}|^2$ in the CPX scenario. Recall that $\sum_{a=1}^{3} |g^{\text{eff}}_{h_aZZ}|^2 \sim 1$. We can see that the h_1-Z-Z coupling dominates around the edge of the available parameter space, the h_3-Z-Z coupling dominates in a region $M_{h_1} < 60$ GeV and $7 \lesssim \tan\beta \lesssim 25$ and the h_2-Z-Z coupling dominates the region in between. We can immediately see that the Higgsstrahlung topology $e^+e^- \to (h_a)Z \to (b\bar{b})Z$ will be very effective at providing exclusions in regions where $|g^{\text{eff}}_{h_aZZ}|^2 \sim 1$, for $a = 1, 2$. In these areas, we expect SM-like exclusions, following similar boundaries predicted to those in Figure 9.5, where the decay mode to b-quarks is dominant. However, over a large part of parameter space, $|g^{\text{eff}}_{h_1ZZ}|^2$ and $|g^{\text{eff}}_{h_2ZZ}|^2$ are suppressed and other search topologies may have higher statistical sensitivities. Since $|g^{\text{eff}}_{h_2h_1Z}|^2 \sim |g^{\text{eff}}_{h_3ZZ}|^2$, we can also predict that channels involving the pair production process $e^+e^- \to h_1h_2$ may be useful in providing exclusions in the region where $|g^{\text{eff}}_{h_3ZZ}|^2$ is high.

The $h_2 \to h_1h_1$ branching ratio for the CPX parameter space which was presented in Figure 8.2 has been reproduced in Figure 9.7 for ease of comparison.

Figure 9.8 indicates which channel has the highest sensitivity and therefore which channel will be used to set an exclusion limit at each point in CPX parameter space.

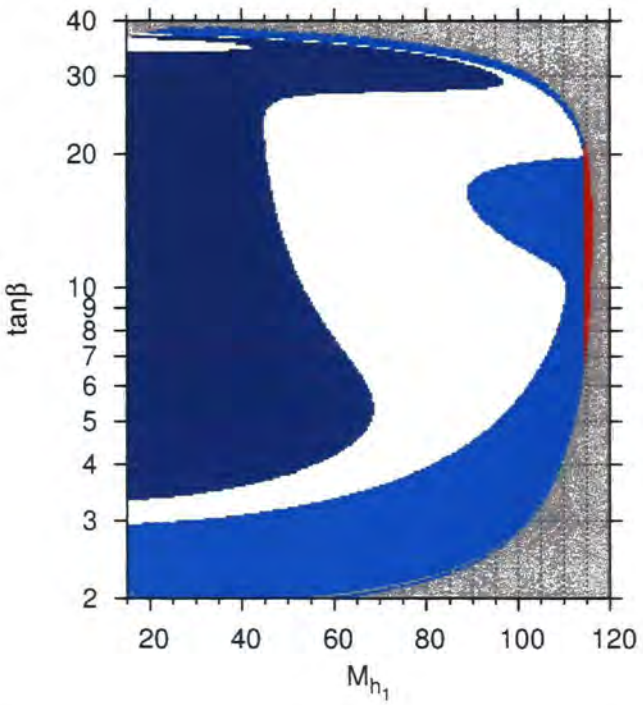

Figure 9.5: Regions of CPX parameter space which could be especially challenging when attempting to use the topology $e^+e^- \to (h_a)Z \to (b\bar{b})Z$ to provide exclusions. The red region indicates where $M_{h_1} \geq M_H^{\text{SM limit}}$ and the cyan region indicates where $M_{h_2} \geq M_H^{\text{SM limit}}$, where $M_H^{\text{SM limit}} = 114.4$ GeV. We also indicate the 'slight excess' region 89.6 GeV $< M_{h_2} <$ 107 GeV by dark blue. In this region, the observed S_{95} was more than one sigma above the expected S_{95}, based on Monte Carlo results with no signal, as shown in Figure 9.2. The grey area is theoretically inaccessible.

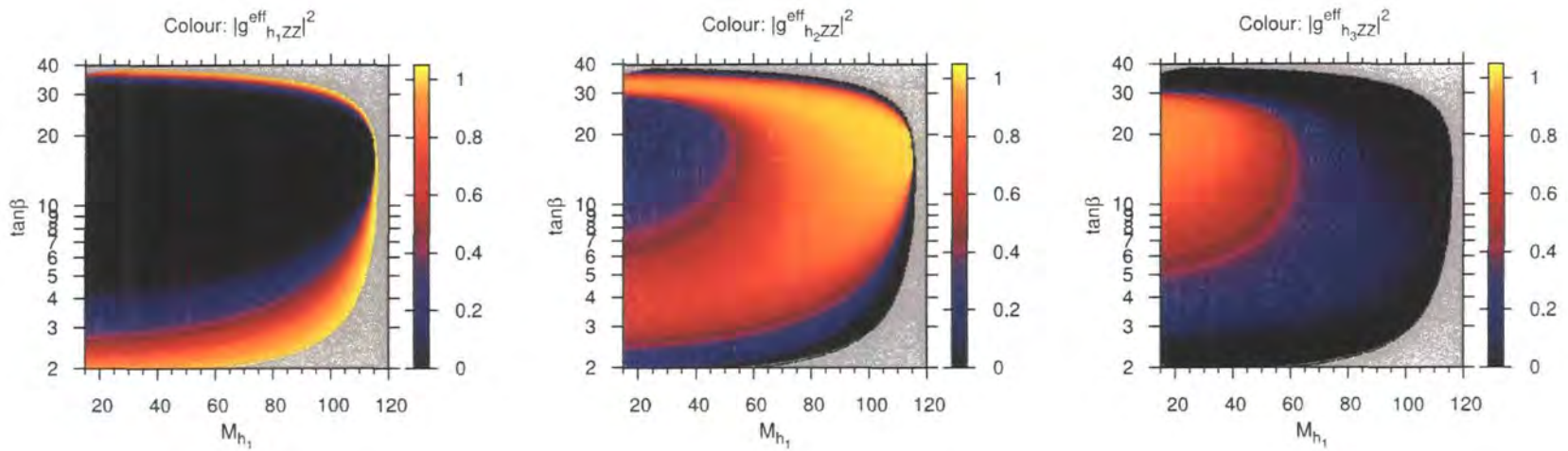

Figure 9.6: The effective coupling of the neutral Higgs to two Z bosons $|g^{\rm eff}_{h_1ZZ}|^2$,$|g^{\rm eff}_{h_2ZZ}|^2$ and $|g^{\rm eff}_{h_3ZZ}|^2$, which include the Higgs propagator corrections (see Section 4.6 for definitions).

In most of the CPX parameter space, the channels $h_1 Z \to b\bar{b}Z$ (■) and $h_2 Z \to b\bar{b}Z$ (■) have the highest statistical sensitivity. Through comparison with Figure 9.6, we can see that this occurs in the areas where h_1 and h_2 have significant couplings to Z bosons, as expected.

In the region of CPX parameter space with high values of $|g^{\text{eff}}_{h_3ZZ}|^2$, the channels with the highest statistical sensitivity are $h_2h_1 \to b\bar{b}b\bar{b}$ (■) and $h_2h_1 \to h_1h_1h_1 \to b\bar{b}b\bar{b}b\bar{b}$ ( ), which both involve $g^{\text{eff},2}_{h_1h_2Z}$, as expected. The position of the boundary between these two regions is governed by the Higgs branching ratio $h_2 \to h_1h_1$, which, as we can see from Figure 9.7, is the dominant branching ratio in this part of parameter space but is decreasing as $\tan\beta$ increases[2]. We can see that the $h_2h_1 \to h_1h_1h_1 \to b\bar{b}b\bar{b}b\bar{b}$ ( ) region appears at a peak in this branching ratio at $\tan\beta \sim 7$, which is due to a peak in the $h_2 \to h_1h_1$ decay width as we saw in Figure 6.7 in Chapter 6.

There is a sizable region in Figure 9.8 at 15 GeV $\lesssim M_{h_1} \lesssim$ 40 GeV , $\tan\beta \sim 6$ in which the channel $h_2Z \to h_1h_1Z \to b\bar{b}b\bar{b}Z$ (□) has the highest statistical sensitivity. This is also due to the peak in the $h_2 \to h_1h_1$ decay width at moderate $\tan\beta$ (Figure 9.7), combined with the fact that the coupling $g^2_{h_2ZZ}$ is relatively unsuppressed in this area (Figure 9.6).

In Figure 9.9, we have compared our new theoretical cross-section predictions for each parameter point in the CPX scenario with the observed topological cross-section limits obtained at LEP for the channel with the highest statistical sensitivity at that point. As expected, $M_{h_1} \gtrsim 114.4$ GeV is not excluded. This unexcluded region extends to $M_{h_1} \sim 85$ GeV at $\tan\beta \sim 16$, since, in this area, the second lightest Higgs is SM-like and therefore follows the contour plotted at $M_{h_2} = 114.4$ GeV in Figure 9.5. As before, we call this region 'unexcluded region A'. It has a narrow 'tail', which extends to lower $\tan\beta$, one side of which is bounded by the limit for a SM-like M_{h_2} and one side of which is bounded by the edge of the region where the channel $h_1Z \to b\bar{b}Z$ (■) has the highest statistical significance, as shown in Figure 9.8.

Figure 9.9 also has an unexcluded region of type B at $M_{h_1} \sim 40$ GeV and $\tan\beta \sim 8$, similar to that shown in Figure 9.3 (we leave a more detailed comparison between our new results and those shown in Figure 9.3 until Section 9.4). The $h_2 \to h_1h_1$ branching ratio for the CPX parameter space which was presented in Chapter 8 has been reproduced in Figure 9.7 for ease of comparison. We can see that the entire unexcluded region B in

[2]For cosmetic reasons, in the high resolution scans of the CPX parameter space, such as Figure 9.7, we plot all points, including those which were deemed to be less stable because of non-neglible second order terms in the mass or Z-factor calculation. For this stability information, refer to Figure 8.2.

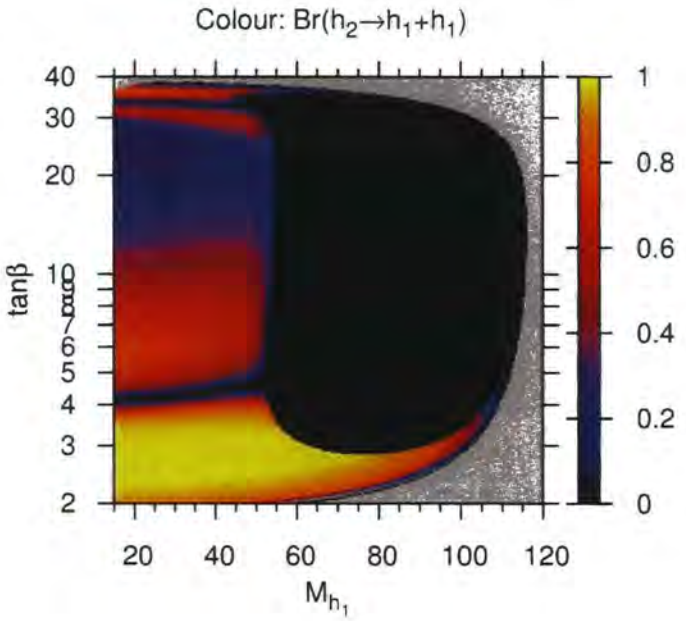

Figure 9.7: The $h_2 \to h_1 h_1$ branching ratio for the M_{h_1}–$\tan\beta$ plane of the CPX scenario (as seen in Figure 8.2)

Figure 9.9 lies in an area where the $h_2 \to h_1 h_1$ branching ratio is sizable. We examine this unexcluded region B in more detail in Figure 9.10, where we show an enlarged version of the relevant part of parameter space from Figure 9.8 and Figure 9.9. As we can see, the three thin extensions of the unexcluded region all lie along boundaries between areas where different processes have the highest statistical significance. As we have discussed, we would expect our method of combining channels (which only makes use of one observed limit for each parameter point) to be less effective at such boundaries. Thus, a dedicated analysis which included the combination of different channels may well be able to exclude such areas.

Figure 9.10 also shows that the bulk of the unexcluded region B lies in an area in which the channel $h_2 Z \to b\bar{b}Z$ (■) has the highest statistical sensitivity. The extent of the unexcluded region B on the higher $\tan\beta$ side is very sensitive to the $h_2 \to b\bar{b}$ branching ratio, which, as can be seen from Figure 9.7, is also heavily dependent on the $h_2 \to h_1 h_1$ branching ratio in this region of CPX parameter space.

The extent of the unexcluded region B towards lower values of M_{h_1} is determined by the edge of the region in which the channel $h_2 Z \to b\bar{b}Z$ (■) has the highest statistical sensitivity. This boundary is also very sensitive to the $h_2 \to h_1 h_1$ branching ratio, which

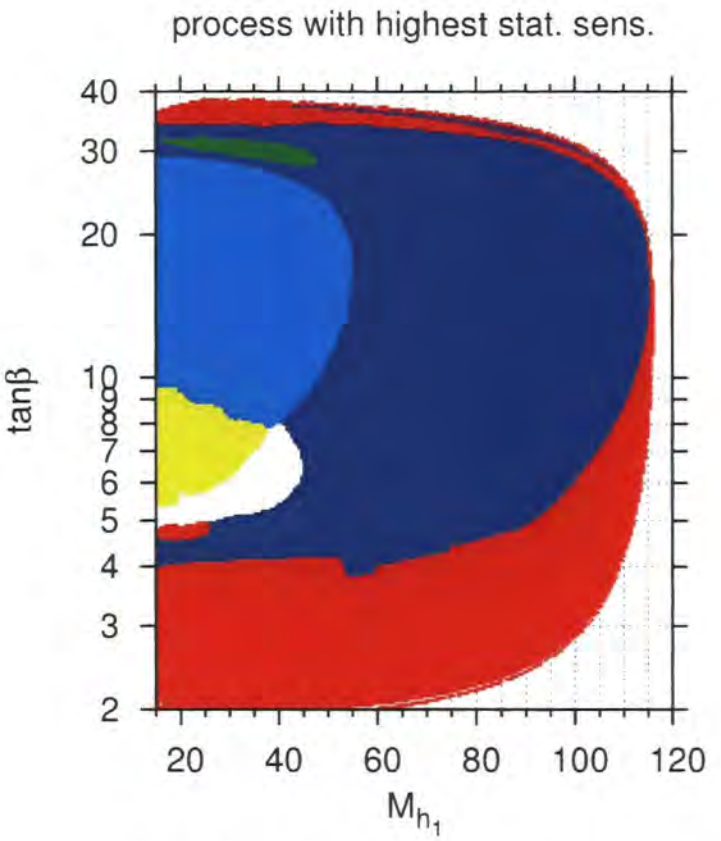

Figure 9.8: Coverage of the LEP Higgs searches in the M_{h_1}–$\tan\beta$ plane of the CPX scenario, showing the channels that are predicted to have the highest statistical sensitivity for setting an exclusion limit. The colour codings are: red = $h_1 Z \to b\bar{b}Z$ (■), blue = $h_2 Z \to b\bar{b}Z$ (■), white = $h_2 Z \to h_1 h_1 Z \to b\bar{b}b\bar{b}Z$ (□), cyan = $h_2 h_1 \to b\bar{b}b\bar{b}$ (■), yellow = $h_2 h_1 \to h_1 h_1 h_1 \to b\bar{b}b\bar{b}b\bar{b}$ (■), green = $h_3 h_1 \to b\bar{b}b\bar{b}$ (■), purple = other channels (■).

has a large influence on the theoretical predictions S_{95}^{theo} of the relevant channels $h_2 Z \to b\bar{b}Z$ (■), $h_2 h_1 \to b\bar{b}b\bar{b}$ (■), $h_2 h_1 \to h_1 h_1 h_1 \to b\bar{b}b\bar{b}b\bar{b}$ (■) and $h_2 Z \to h_1 h_1 Z \to b\bar{b}b\bar{b}Z$ (□).

Comparison of Figure 9.9 with Figure 9.5 also shows that the unexcluded region B occurs in the region affected by the 'slight excess' observed at LEP for the $h_a \to b\bar{b}$ topology. It is interesting to investigate the effect of the 'slight excess' on the extent of the unexcluded region B. Figure 9.11 shows what the exclusion would have been in the hypothetical situation in which the observed S_{95} value was exactly the same as the expected S_{95} value (left) or exactly 1σ above the predicted value (centre). For the case in which we set the 'observed' S95 value to be exactly the same as the expected S_{95} value, we see that the entire CPX parameter space is excluded, apart from thin unexcluded regions along boundary lines and apart from the region $M_{h_1} \gtrsim 114.4$ GeV (the limit for

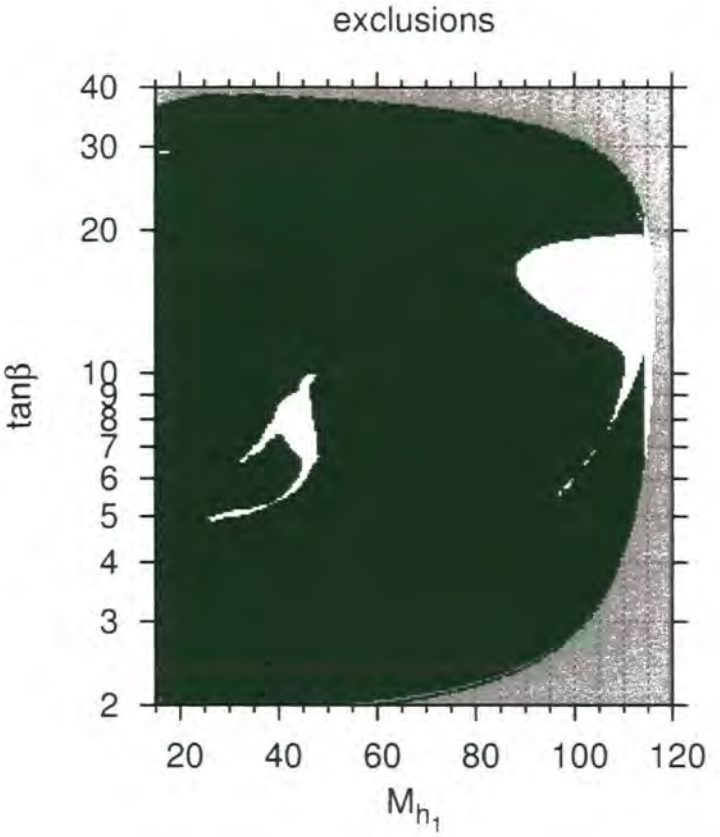

Figure 9.9: Coverage of the LEP Higgs searches in the M_{h_1}-$\tan\beta$ plane of the CPX scenario, showing the parameter regions excluded at the 95% C.L. by the topological cross-section limits obtained at LEP. The colour codings are: green = LEP excluded, white = LEP allowed.

a SM-like Higgs). For the case in which we set the 'observed' S_{95} value to 1σ above the expected S_{95} value, we see that unexcluded regions of type A and B are both present, although both are smaller than the unexcluded regions in Figure 9.9. We conclude that the presence of the 'slight excess' in the LEP results for the $(h_a)Z \to (b\bar{b})Z$ topology is crucial to the existence of substantial unexcluded regions in the CPX scenario. We also conclude that the extent of the unexcluded regions is very sensitive to the size of the excess.

In order to further investigate the effects of our new genuine vertex corrections to the $h_2 \to h_1 h_1$ decay, we now compare the LEP exclusion regions based on the full result with the case where we have used the Yukawa approximation to calculate the genuine vertex corrections to the $h_2 \to h_1 h_1$ decay. This approximation was investigated in Chapter 6. Recall that the Yukawa corrections comprised the leading genuine vertex corrections and that, in the region $\tan\beta \sim 8$, the $h_2 \to h_1 h_1$ decay width calculated

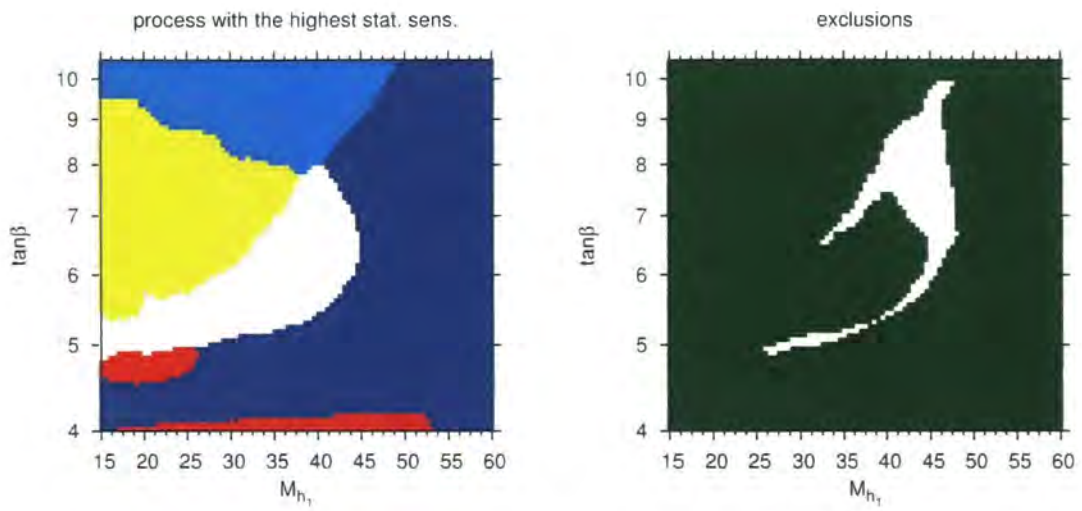

(a) (b)

Figure 9.10: (a) Channels with the highest statistical sensitivity for the CPX scenario, showing a section of Figure 9.8 in more detail. (b) LEP exclusion regions for the CPX scenario, showing a section of Figure 9.9 in more detail. See the captions of Figure 9.8 and Figure 9.9 for the legend.

using the Yukawa approximation for the vertex corrections was $\sim 25\%$ lower than the full $h_2 \to h_1 h_1$ decay width. Figure 9.12 illustrates the effect of using this approximation on the determination of which channel has the highest statistical sensitivity (left) and the effect on the exclusions (right) in the region of the CPX parameter space containing the unexcluded region of type B. The boundary between channels related to $|g^{\text{eff}}_{h_2 ZZ}|^2$ (i.e. $h_2 Z \to h_1 h_1 Z \to b\bar{b}b\bar{b}Z$ (□) and $h_2 Z \to b\bar{b}Z$ (■)) and those related to $|g^{\text{eff}}_{h_2 h_1 Z}|^2$ (i.e. $h_2 h_1 \to b\bar{b}b\bar{b}$ (■) and $h_2 h_1 \to h_1 h_1 h_1 \to b\bar{b}b\bar{b}b\bar{b}$ (■)) are in approximately the same position as in Figure 9.10. However, the boundaries between channels directly involving the $h_2 \to h_1 h_1$ decay and those that do not involve this decay have shifted. In particular, the region where the channel $h_2 Z \to h_1 h_1 Z \to b\bar{b}b\bar{b}Z$ (□) has the highest statistical sensitivity has been substantially reduced. This has a considerable impact on the shape of the unexcluded region B in Figure 9.12 as compared to Figure 9.10. We conclude that including the full genuine vertex corrections to the $h_2 \to h_1 h_1$ decay, rather than just the leading vertex corrections, is vital in order to accurately determine the shape of the unexcluded region B. However, we note that the calculation which used the Yukawa vertex corrections was able to confirm the existence of the excluded region B and give an approximate idea of its position in the M_{h_1}-tan β plane of CPX parameter space. Therefore, it could be a useful approximation in situations where the inclusion of the full vertex corrections is impractical.

It is interesting to consider the effect of the mass of the top quark. Since the leading corrections to the $h_2 \to h_1 h_1$ vertex are Yukawa corrections proportional to m_t^6 or m_t^4, we would expect the unexcluded region B to exhibit a strong dependence on m_t. The neutral Higgs masses are also very sensitive to m_t, since they also depend on Yukawa corrections (as demonstrated in Chapter 4). We consider $m_t = 170.9$ GeV, which was the world average [121] at the time we first published these results in [122], and $m_t = 174.3$ GeV, which was the central value used in the LEP Higgs Working Group and LEP collaborations' dedicated analysis of the CPX scenario [24].[3] Figure 9.13 contains plots of the $h_2 \to h_1 h_1$ branching ratio (left), the regions excluded by the LEP topological cross-section limits (center) and the channels with the highest statistical sensitivity (right) for $m_t = 170.9$ GeV (top) and $m_t = 174.3$ GeV (bottom).

It is immediately apparent that the size of the unexcluded region A dramatically increases as m_t increases, which is due to the effect of m_t on the neutral Higgs self-energies. We can also see that the area in which $h_2 Z \to h_1 h_1 Z \to b\bar{b}b\bar{b}Z$ ($\Box$) has the highest statistical sensitivity increases as m_t increases, as we would expect, since the Yukawa corrections to the $h_2 \to h_1 h_1$ vertex are proportional to m_t^6 or m_t^4. The increase in the $h_2 \to h_1 h_1$ vertex corrections (and therefore the decrease in the $h_2 \to b\bar{b}$ branching ratio) has resulted in a larger unexcluded region B.

The variation of $\arg A_t$ also has a very interesting impact on the unexcluded regions. We saw in Figure 6.11 (a) that varying $\arg A_t$ by 10% has a dramatic effect on the $h_2 \to h_1 h_1$ decay width, through changing the magnitude and position of the peak at moderate $\tan\beta$ and changing the position of the minimum of $\mathrm{Br}(h_2 \to h_1 h_1)$. In Figure 9.14, which uses $\arg A_t = 0.9 \times \pi/2$ GeV and $\arg A_t = 1.1 \times \pi/2$ GeV, we can see these effects reflected in the $h_2 \to h_1 h_1$ branching ratio. In particular, we see that the thin horizontal minimum in $\mathrm{Br}(h_2 \to h_1 h_1)$ shifts to higher $\tan\beta$ as $\arg A_t$ increases. We can also see a change in the shape of the region in which the $h_2 \to h_1 h_1$ decay is kinematically allowed and a reduction of the size of CPX parameter space as plotted on the $M_{h_1} - \tan\beta$ plane.

As we would expect, this affects the balance of processes with the highest statistical sensitivity. The boundary between processes involving $|g^{\mathrm{eff}}_{h_2 ZZ}|^2$ and those involving $|g^{\mathrm{eff}}_{h_2 h_1 Z}|^2$ also shifts to higher $\tan\beta$. As a result, the unexcluded region B occurs at higher $\tan\beta$ as $\arg A_t$ increases and its shape changes significantly. The unexcluded region A increases in size as $\arg A_t$ increases. At $\arg A_t = 0.9 \times \pi/2$, this region is

[3] We note here that a new preliminary world average top quark mass of $m_t = 172.4 \pm 1.2$ GeV has recently become available [123]

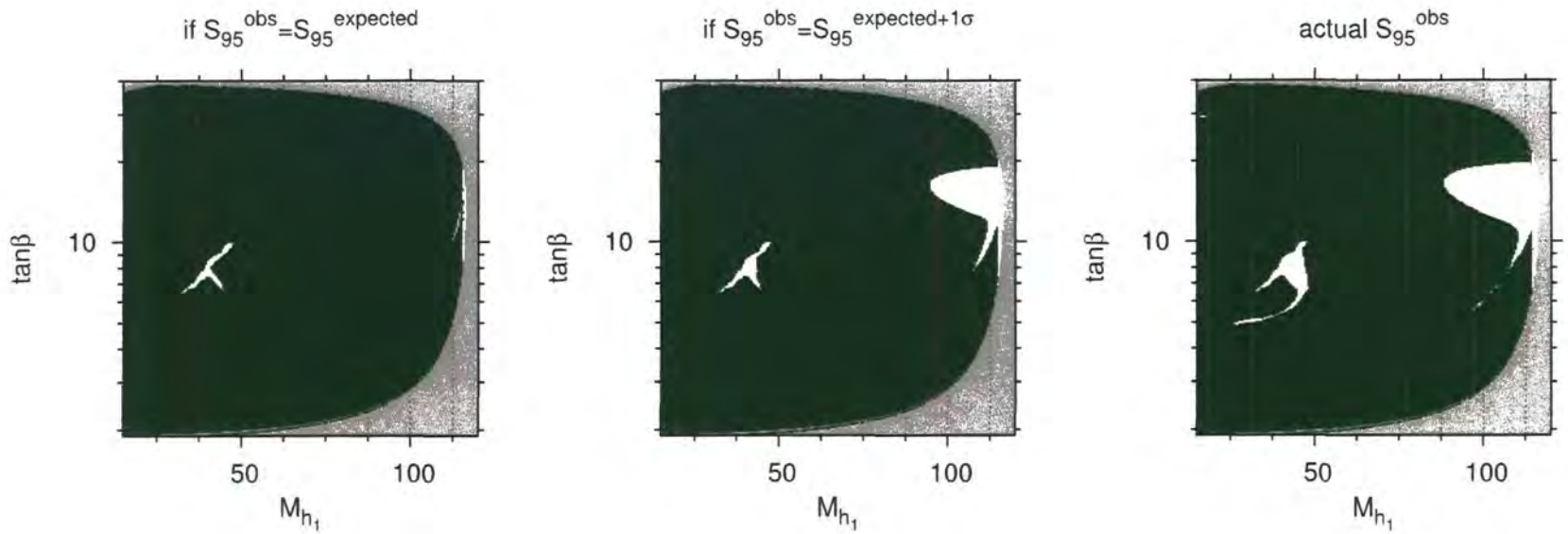

Figure 9.11: LEP exclusion regions for the hypothetical cases where the observed S95 value had been either the same as (a) the predicted value or (b) 1 sigma above the predicted value. We include the actual observed result (c) for comparison. The colour codings are: green = LEP excluded, white = LEP allowed.

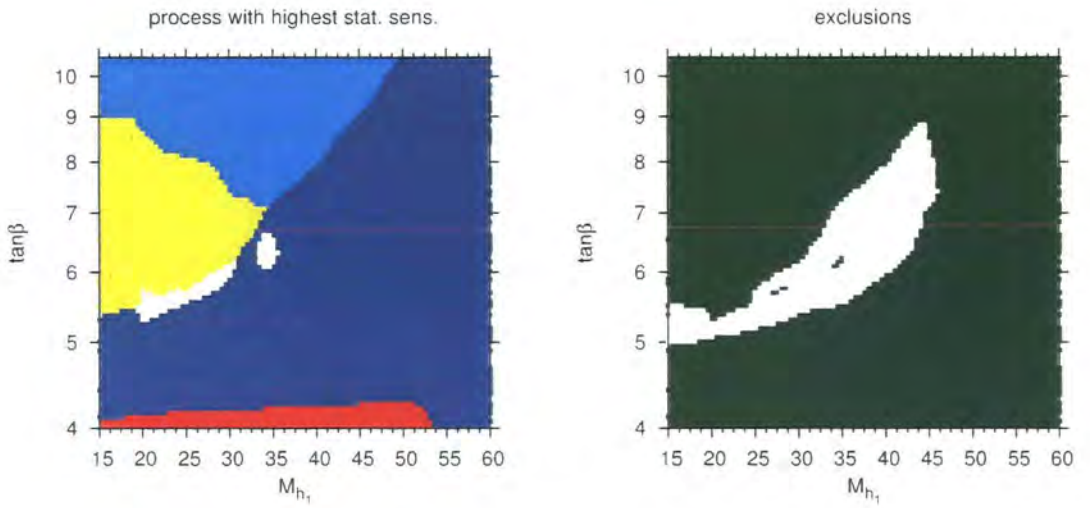

(a) (b)

Figure 9.12: Channels with the highest statistical sensitivity (a) and LEP exclusion regions (b) for the CPX scenario at low values of M_{h_1} and moderate values of $\tan\beta$. The vertex corrections to the $h_2 \to h_1 h_1$ branching ratio have been calculated using the Yukawa approximation and combined with the full propagator corrections. See the captions of Figure 9.8 and Figure 9.9 for the legend.

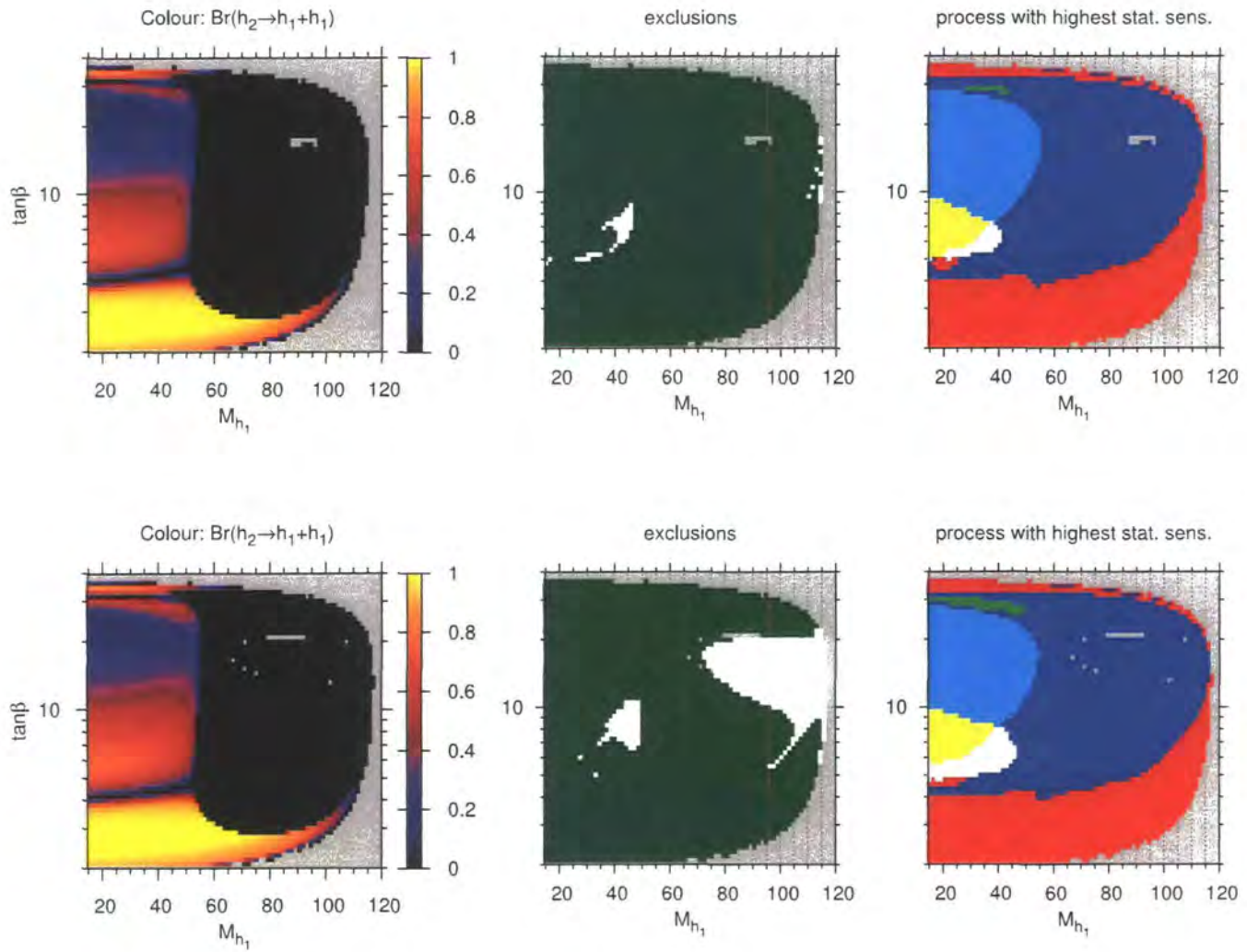

Figure 9.13: $h_2 \to h_1 h_1$ branching ratio, LEP exclusions and channels with the highest statistical sensitivity plotted on the $M_{h_1} - \tan\beta$ plane. Upper graphs show $m_t = 170.9$ GeV, lower graphs show $m_t = 174.3$ GeV, other parameters taken from CPX scenario. See the captions of Figure 9.8 and Figure 9.9 for the legend.

bisected by a thin vertical excluded region, due to the fact that the process with the highest statistical sensitivity in this part of parameter space is $h_1 Z \to b\bar{b}Z$ (■) rather than $h_2 Z \to b\bar{b}Z$ (■). For the case with $\arg A_t = 1.1 \times \pi/2$, the unexcluded region A also extends to significantly lower values of $\tan\beta$.

Figure 9.15 illustrates the substantial effect that varying $|A_t|$ by 10% has on the LEP exclusions in the CPX parameter space. Recall that Figure 6.11 (b) demonstrated that increasing $|A_t|$ increased the size of the peak in the $h_2 \to h_1 h_1$ decay width at moderate $\tan\beta$ and shifted the position of the minimum and the peak to higher values of $\tan\beta$. It also significantly changed the gradient of the $h_2 \to h_1 h_1$ decay width above $\tan\beta \sim 7$. We see these effects reflected in the $h_2 \to h_1 h_1$ branching ratio in Figure 9.15. We also see a significant increase in the area of parameter space in which the $h_2 \to h_1 h_1$ decay is kinematically allowed. At $|A_t| = 0.9 \times 900$ GeV, the unexcluded region B has almost disappeared and the unexcluded region A has also reduced in size.

For the case in which $|A_t| = 1.1 \times 900$ GeV, the plot illustrating the channels with the highest statistical sensitivity in Figure 9.15 is dramatically different from those we have seen so far. This is partly because $|g^{\text{eff}}_{h_1 h_2 Z}|^2$ is reduced, which drastically reduces the area where $h_2 h_1 \to b\bar{b}b\bar{b}$ (■) has the highest statistical sensitivity. The area where the channel $h_2 h_1 \to h_1 h_1 h_1 \to b\bar{b}b\bar{b}b\bar{b}$ (■) has the highest statistical sensitivity occurs at higher $\tan\beta$ than previously and is now unexcluded. Also, the suppression of $|g^{\text{eff}}_{h_1 h_2 Z}|^2$ also means that the channel $h_3 h_1 \to b\bar{b}b\bar{b}$ has the highest statistical sensitivity over a much larger region than we have seen in our previous examples, and this region can only be partially excluded by this LEP limit. Therefore, the excluded LEP regions are dramatically different for the CPX scenario with $|A_t| = 1.1 \times 900$ GeV. It is worth noting, however, that this value of $|A_t|$ tends towards an unstable region of parameter space.

The gluino mass parameter M_3 does not feature in the 1-loop corrections to the $h_2 \to h_1 h_1$ decay or the 1-loop corrections to the Higgs masses. However, the Higgs self-energies from *FeynHiggs* depend on M_3 through the $\mathcal{O}\alpha_s\alpha_t$ corrections and the Δm_b corrections. Therefore, it is interesting to see if varying this parameter has a significant effect on the LEP exclusions.

In Figure 9.16, we vary $\arg M_3$ by 20%. We can see that this has a dramatic effect on the shape of the CPX parameter space, as plotted on the $M_{h_1} - \tan\beta$ plane. If $\arg M_3 = 0.8 \times \pi/2$, the parameter space is stretched to higher $\tan\beta$ values, whereas, if $\arg M_3 = 1.2 \times \pi/2$, the CPX parameter space does not extend above $\tan\beta \sim 14$. Since

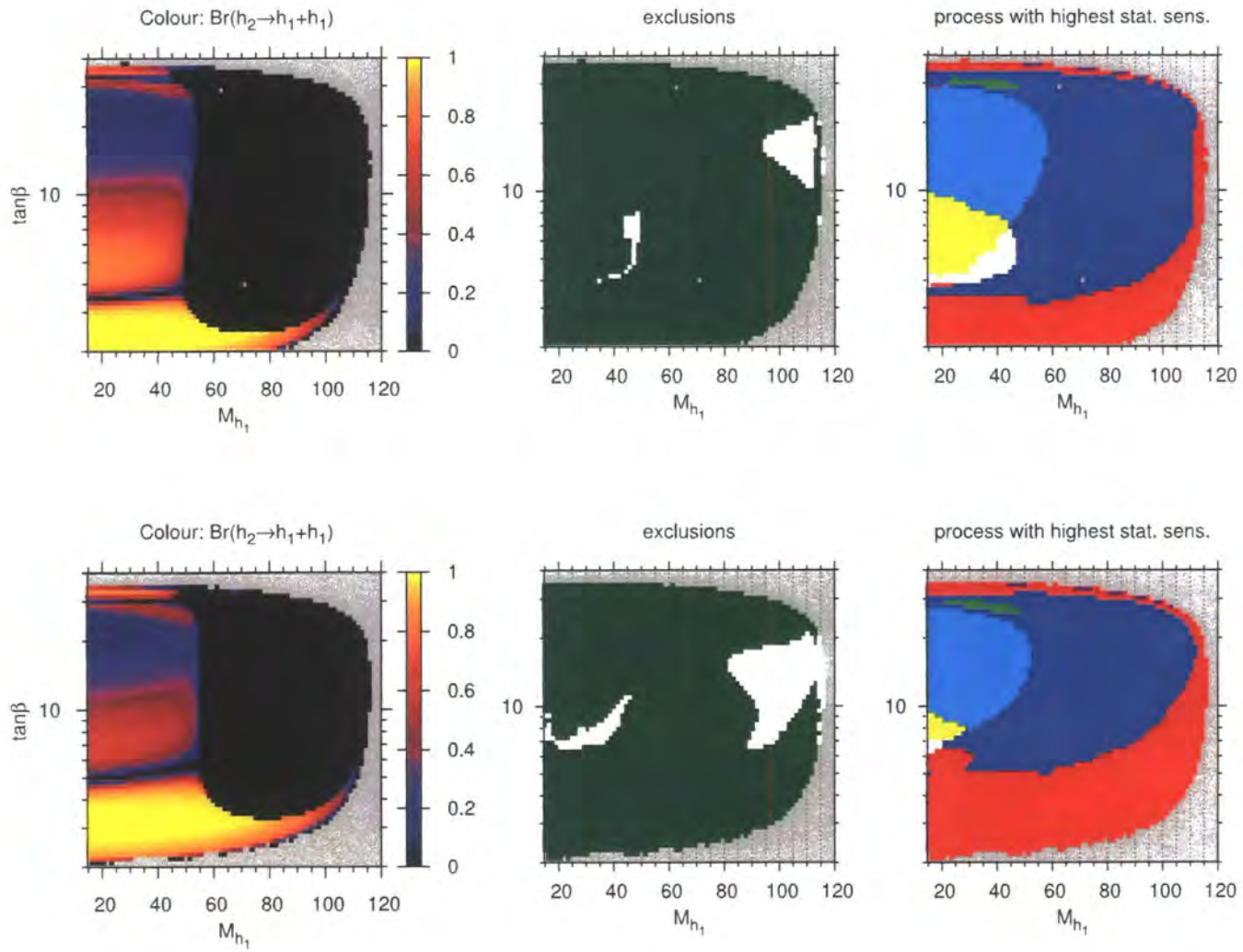

Figure 9.14: $h_2 \to h_1 h_1$ branching ratio, LEP exclusions and channels with the highest statistical sensitivity plotted on the $M_{h_1} - \tan\beta$ plane. Upper graphs show $\arg A_t = 0.9 \times \pi/2$, lower graphs show $\arg A_t = 1.1 \times \pi/2$, other parameters taken from CPX scenario. See the captions of Figure 9.8 and Figure 9.9 for the legend.

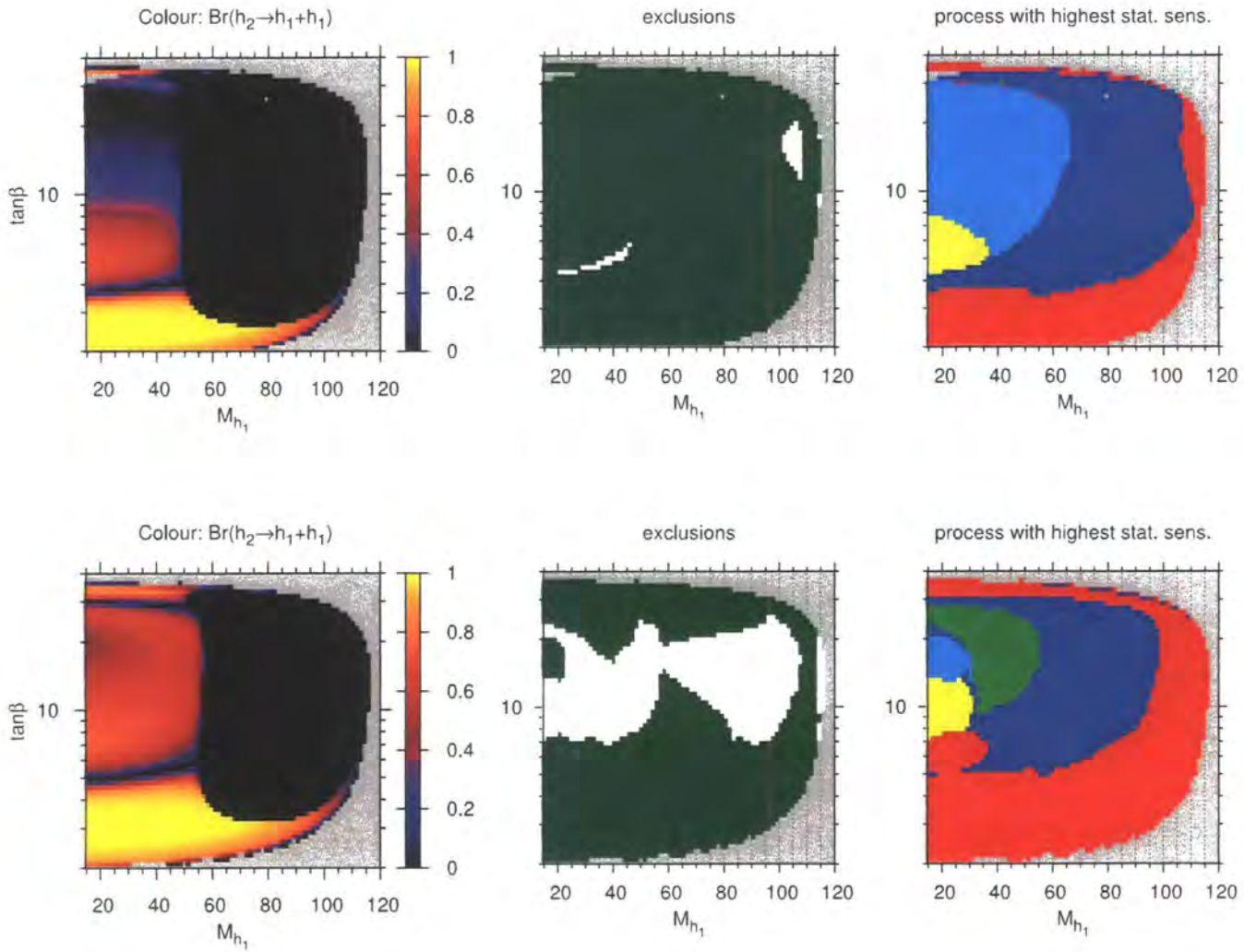

Figure 9.15: $h_2 \to h_1 h_1$ branching ratio, LEP exclusions and channels with the highest statistical sensitivity plotted on the $M_{h_1} - \tan\beta$ plane. Upper graphs show $|A_t| = 0.9 \times 900$ GeV, lower graphs show $|A_t| = 1.1 \times 900$ GeV. other parameters taken from CPX scenario. See the captions of Figure 9.8 and Figure 9.9 for the legend.

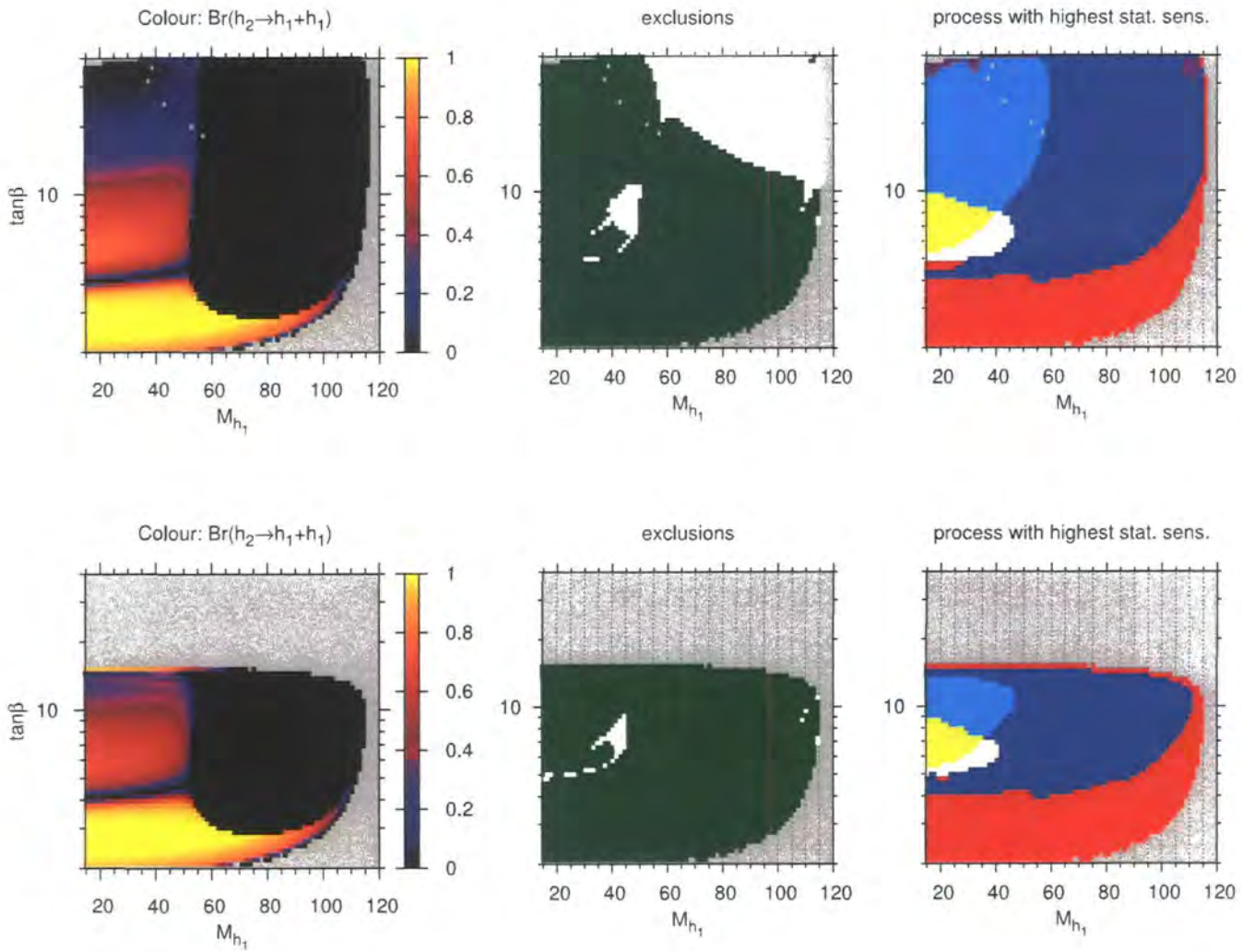

Figure 9.16: $h_2 \to h_1 h_1$ branching ratio, LEP exclusions and channels with the highest statistical sensitivity plotted on the $M_{h_1} - \tan\beta$ plane. Upper graphs show $\arg M_3 = 0.8 \times \pi/2$, lower graphs show $\arg M_3 = 1.2 \times \pi/2$, other parameters taken from CPX scenario. See the captions of Figure 9.8 and Figure 9.9 for the legend.

there is such a pronounced dependence on $\tan\beta$, we conclude that this behaviour is a result of the Δm_h corrections, which are enhanced at large $\tan\beta$. At $\arg M_3 = 0.8 \times \pi/2$, the area of the unexcluded region A increases considerably, such that it extends to $M_{h_1} \sim 50$ GeV. The size of the unexcluded region B also increases slightly.

Figure 9.17 illustrates the effect of increasing and decreasing $|M_3|$ by 20%. This has negligible effect on the size of the CPX parameter space, as plotted on the $M_{h_1} - \tan\beta$ plane, and very little effect on the distribution of channels with the highest statistical sensitivity. Therefore, the shape and position of the unexcluded region B shows little variation. However, the size of unexcluded region A decreases as $|M_3|$ increases, due to differences in M_{h_2} in this part of the plots.

It is also interesting to consider the effect of varying the Higgsino mass parameter μ. For example, it has been suggested that a scenario similar to the CPX but with a lower value of μ would be easier to reconcile with the relic abundance [101]. Recall from Figure 6.12 (a) that the effect of varying μ by 10% was similar to the effect of varying $|A_t|$ by 10% in Figure 6.11 (b). Therefore, the branching ratios shown in Figure 9.18 are qualitatively very similar to those in Figure 9.15. As μ increases, $|g^{\text{eff}}_{h_2ZZ}|^2$ is enhanced at the expense of $|g^{\text{eff}}_{h_2h_1Z}|^2$ and this determines the relative sizes of the regions involving these couplings. The plot with $\mu = 1.1 \times 2000$ GeV in Figure 9.18 has a large region in which the channel $h_2Z \to h_1h_1Z \to b\bar{b}b\bar{b}Z$ (□) has the highest statistical sensitivity. The size of the unexcluded regions of type B increase substantially as μ increases and largely consist of areas in which the channels $h_2Z \to h_1h_1Z \to b\bar{b}b\bar{b}Z$ (□), $h_2h_1 \to h_1h_1h_1 \to b\bar{b}b\bar{b}b\bar{b}$ ( ) and $h_3h_1 \to b\bar{b}b\bar{b}$ (■) have the highest statistical sensitivity. In contrast to Figure 9.15, the size of unexcluded region A remains relatively unchanged as μ increases.

Similarly, the effect of varying the soft-breaking term M_{SUSY} by 10%, as shown in Figure 9.19, can be explained by an enhancement of $|g^{\text{eff}}_{h_2ZZ}|^2$ at the expense of $|g^{\text{eff}}_{h_2h_1Z}|^2$ and a suppression of $\text{Br}(h_2 \to b\bar{b})$ as M_{SUSY} decreases (c.f. Figure 6.12 (b)). Again, the size of the CPX parameter space in the $M_{h_1} - \tan\beta$ plane also changes - it decreases as M_{SUSY} decreases. Note that we incorporated our full calculation of the $h_3 \to h_2h_1$ decay width into the parameter scan for $M_{\text{SUSY}} = 0.9 \times 500$ GeV, since we could not tell *a priori* that it would not be relevant. However, the difference this made was negligible.

As we saw in Figure 6.4, above $M_{H^\pm} \sim 260$ GeV the decay $h_2 \to h_1h_1$ is allowed throughout the CPX parameter space. Figure 9.20 shows the $h_2 \to h_1h_1$ branching ratio in this region, LEP exclusions and channels with the highest statistical sensitivity. It illustrates that over a significant region of parameter space, at low $\tan\beta$ and

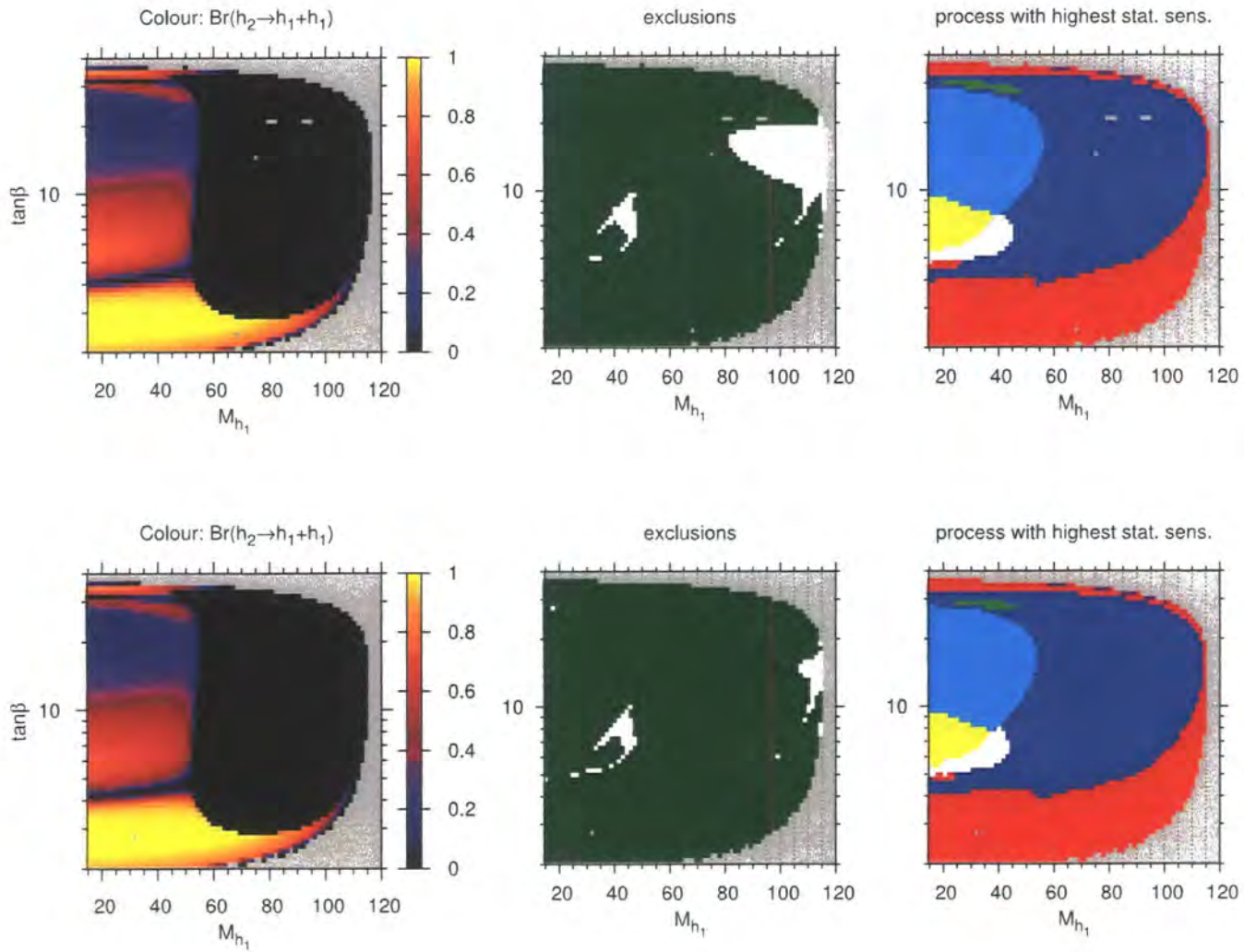

Figure 9.17: $h_2 \to h_1 h_1$ branching ratio, LEP exclusions and channels with the highest statistical sensitivity plotted on the $M_{h_1} - \tan\beta$ plane. Upper graphs show $|M_3| = 0.8 \times 1000$ GeV, lower graphs show $|M_3| = 1.2 \times 1000$ GeV, other parameters taken from CPX scenario. See the captions of Figure 9.8 and Figure 9.9 for the legend.

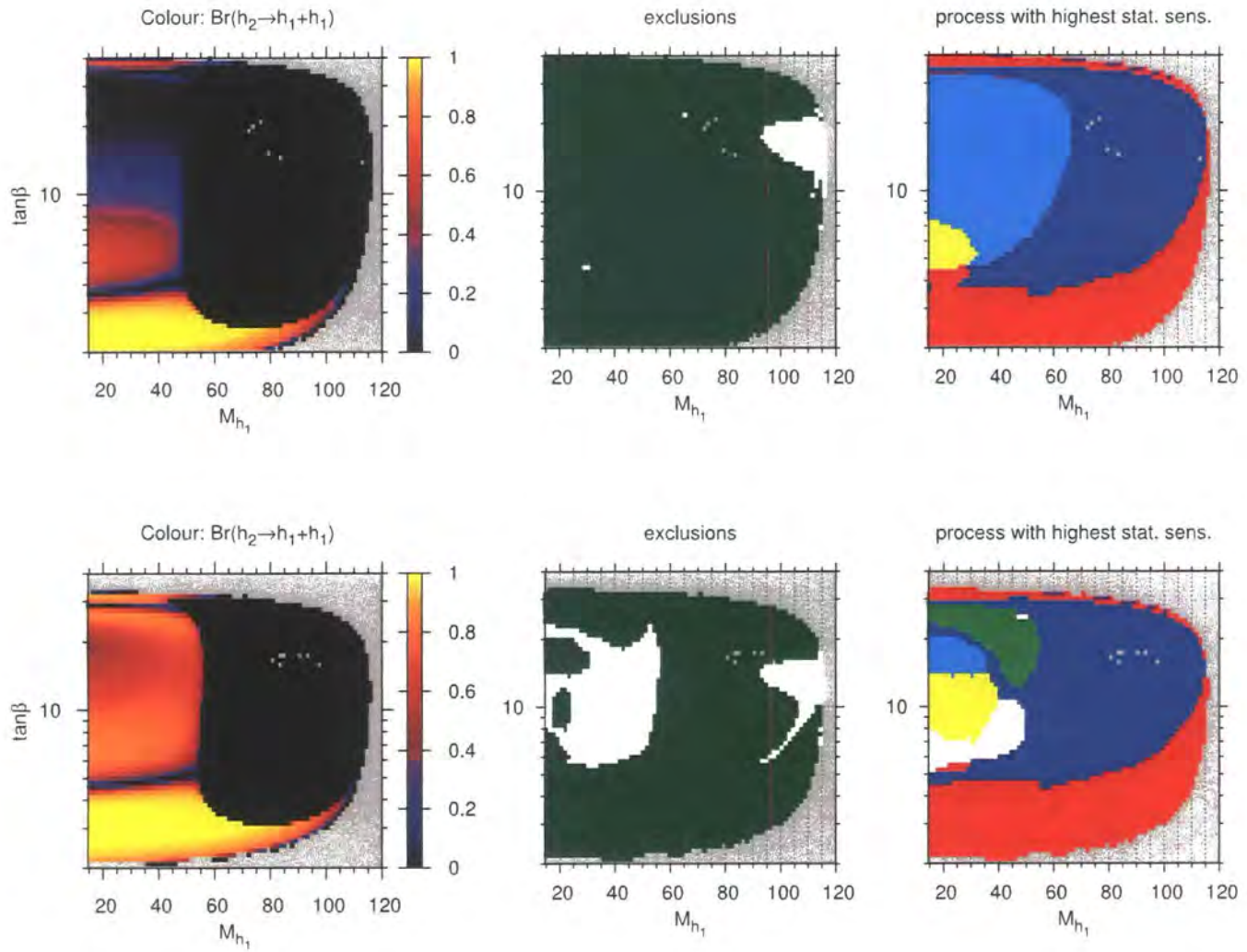

Figure 9.18: $h_2 \to h_1 h_1$ branching ratio, LEP exclusions and channels with the highest statistical sensitivity plotted on the $M_{h_1} - \tan\beta$ plane. Upper graphs show $\mu = 0.9 \times 2000$ GeV, lower graphs show $\mu = 1.1 \times 2000$ GeV, other parameters taken from CPX scenario. See the captions of Figure 9.8 and Figure 9.9 for the legend.

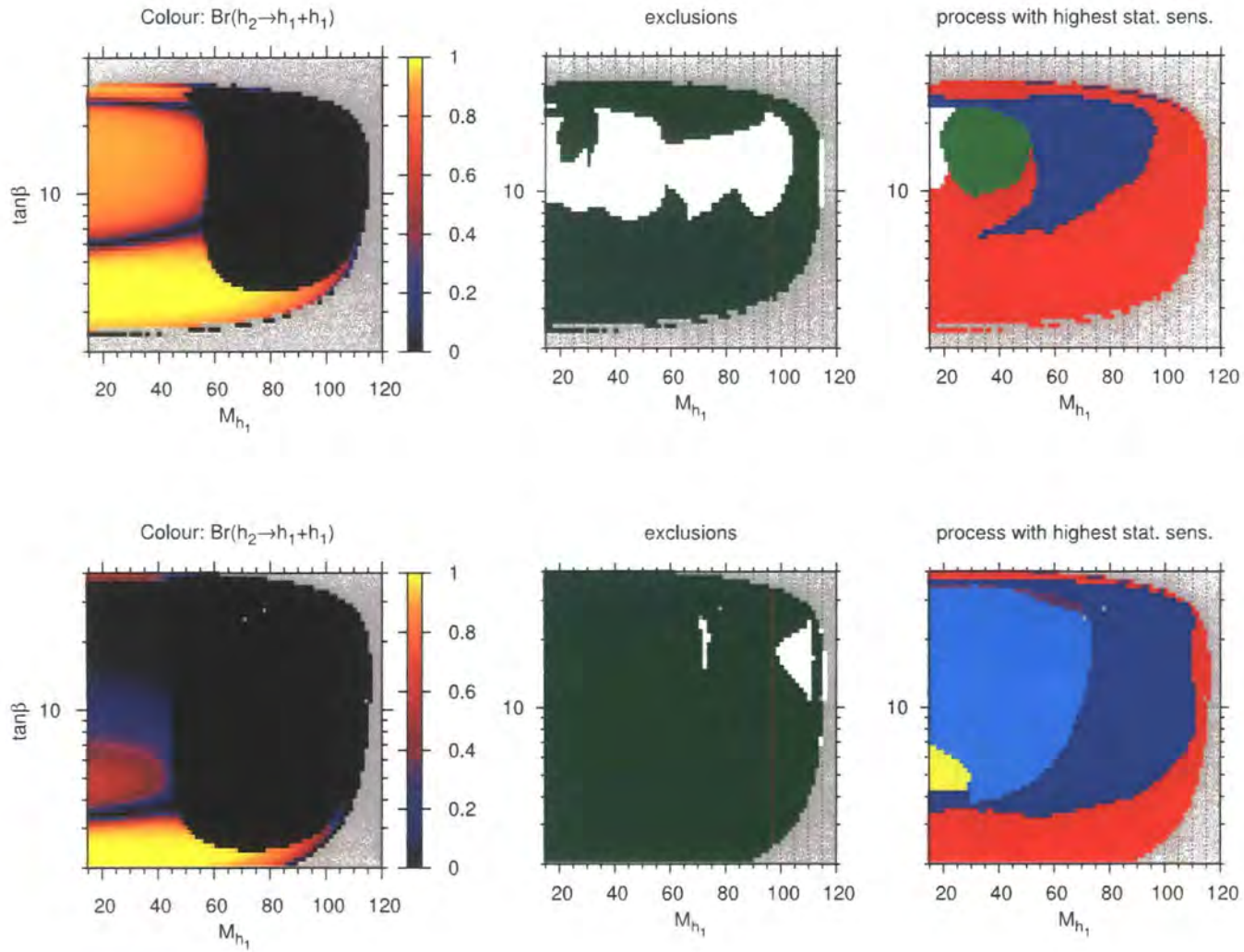

Figure 9.19: $h_2 \to h_1 h_1$ branching ratio, LEP exclusions and channels with the highest statistical sensitivity plotted on the $M_{h_1} - \tan\beta$ plane. Upper graphs show $M_{\rm SUSY} = 0.9 \times 500$ GeV, lower graphs show $M_{\rm SUSY} = 1.1 \times 500$ GeV. other parameters taken from CPX scenario. See the captions of Figure 9.8 and Figure 9.9 for the legend.

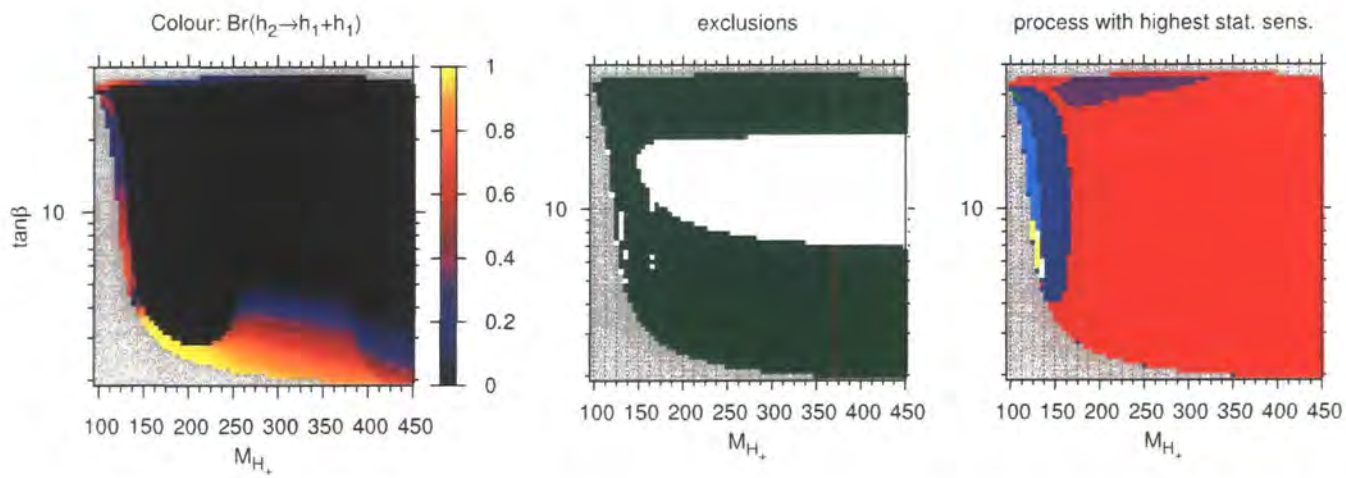

Figure 9.20: $h_2 \to h_1 h_1$ branching ratio, LEP exclusions and channels with the highest statistical sensitivity for the CPX scenario, plotted on the $M_{H^+} - \log\tan\beta$ plane. See the captions of Figure 9.8 and Figure 9.9 for the legend.

$M_{H^\pm} \gtrsim 250$ GeV, the $h_2 \to h_1 h_1$ branching ratio is sizable. This reduces the $h_2 \to b\bar{b}$ branching ratio, which could have had implications for the LEP coverage, since exclusions in this region relies on the cross-section limits for the topology $h_a Z \to b\bar{b}Z$. However, we can see that, despite the lower $\mathrm{Br}(h_2 \to b\bar{b})$, LEP can still exclude this region. This is because there is no suppression of $|g^{\mathrm{eff}}_{h_1 ZZ}|^2$.

9.4 Results using a preliminary new version of the program *FeynHiggs* (FH 2.6.5beta)

We also investigate the LEP exclusions using a preliminary new version of *FeynHiggs*, FH2.6.5beta [124], which has not yet been made publicly available. This version has two main improvements compared to the current version under public release, FH2.6.4, which we have used in this thesis up to this point.

Recall from Section 4.3.6 that *FeynHiggs* allows the user to specify the 2-loop corrections included in the calculation of the neutral Higgs self-energies via the flag `tlCplxApprox`. If `tlCplxApprox=1`, the 2-loop contributions at $\mathcal{O}(\alpha_s \alpha_t)$, which have full phase dependence, are included [55]. If `tlCplxApprox=2`, additional 2-loop corrections are also included. However, since these additional corrections were calculated for the real MSSM, they use only the real parts of complex parameters as input. Since we carry out much of our analysis in the CPX scenario, where the trilinear couplings and the gluino mass parameter are entirely imaginary, we made the decision to use the setting `tlCplxApprox=1`.

Recall also from Section 5.3.3 that *FeynHiggs* recommends the option which uses an effective value of m_b in the 1-loop contributions to the self-energies in order to absorb Δm_b corrections. For the option `tlCplxApprox=2`, the renormalisation is chosen such that the majority of the corrections at $\mathcal{O}(\alpha_s \alpha_b)$ and $\mathcal{O}(\alpha_b \alpha_t)$ can be absorbed into m_b in this way [75].

In the new *FeynHiggs* version FH2.6.5beta, the treatment of m_b for the option `tlCplxApprox=1`, has been significantly improved to use the complex Δm_b everywhere, while in the previous version the effective bottom mass obtained from the corrections valid for the MSSM with real parameters had been used [88]. This means that an effective b-quark mass of $m_b^{\mathrm{eff}} = m_b(m_b)/|1 + \Delta m_b|$ is now used, and no contributions involving the approximation $A_t = \mathrm{Re}A_t$, $M_3 = \mathrm{Re}M_3$ are included. In addition, in FH2.6.5beta, Δm_b is calculated using $\alpha_s(\sqrt{m_{\tilde{b}_1} m_{\tilde{b}_2}})$, rather than $\alpha_s(m_t)$ as in FH2.6.4.

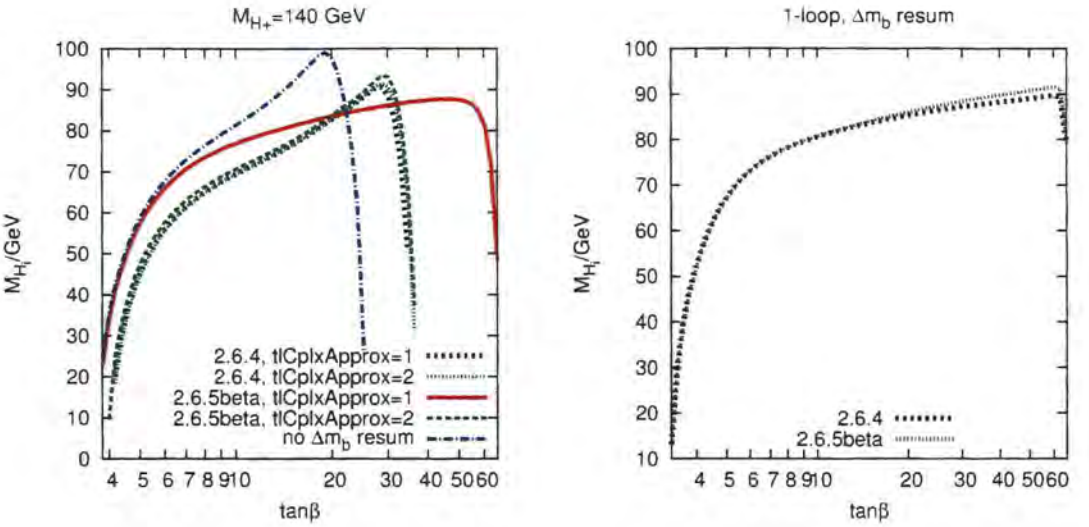

Figure 9.21: Lightest Higgs mass as calculated by *FeynHiggs* [31, 56–58] version 2.6.4 or 2.6.5beta, as a function of $\tan\beta$. (a) '`tlCplxApprox`' is a input flag for the 2-loop contributions in *FeynHiggs* (see text for description). All lines include resummation of corrections to m_b, apart from the option 'no Δm_b resum' (this option was calculated using FH2.6.5beta with the flag `tlCplxApprox`=1). (b) Only 1-loop contributions and Δm_b resummation is included.

In Figure 9.21 (a), we compare the lightest Higgs mass, as calculated using `tlCplxApprox`=1 and `tlCplxApprox`=2, using versions FH2.6.4 and FH2.6.5beta, as a function of $\tan\beta$, using an effective m_b in the 1-loop calculation. We can see that this leads to a substantial difference between the results of FH2.6.4 and FH2.6.5beta for `tlCplxApprox`=1. Figure 9.21 (a) also includes the results from FH2.6.5beta for `tlCplxApprox`=1 and no Δm_b correction in order to further emphasise that this category of correction can have a high numerical impact in the CPX scenario. Figure 9.21 (b) compares the results of versions FH2.6.4 and FH2.6.5beta for the lightest Higgs mass at 1-loop level with the addition of Δm_b resummation, in order to show that the effect of altering the scale of α_s in the Δm_b correction is relatively minor.

Figure 9.22 has been calculated using neutral Higgs self-energies from *FeynHiggs* version FH2.6.5beta, using the CPX scenario with $m_t = 172.6$ GeV (top) and $m_t = 174.3$ GeV (bottom). Comparison with Figure 9.7 and Figure 9.13 shows that the effect of using FH2.6.5beta on the CPX parameter space on the $M_{h_1} - \tan\beta$ plane is to stretch it to higher values of $\tan\beta$. This has dramatically increased the unexcluded region A. in comparison to Figure 9.9 and Figure 9.13. The unexcluded region B is in a similar position in parameter space and extends to slightly higher values of M_{h_1}. It increases as

m_t increases, as we observed with *FeynHiggs* version FH2.6.4. Therefore, the appearance of the unexcluded region B is robust with respect to the variations in *FeynHiggs*.

In the rest of this chapter, unless otherwise stated, we will use *FeynHiggs* version FH2.6.5beta.

9.5 Using parameters defined in a different renormalisation scheme

As described in Section 2.8, our usual definition of the CPX scenario defines the parameters according to the on-shell renormalisation scheme. In this section, however, we investigate the impact of using $A_t^{\overline{\rm DR}} = 1000$ GeV and $M_L^{2,\overline{\rm DR}} = M_{\tilde{t}_R}^{2,\overline{\rm DR}} = 500$ GeV in conjunction with the parameter conversion described in Section 3.4 in order to find values of $A_t^{\rm on-shell}$, $M_L^{2,\rm on-shell}$, $M_{\tilde{t}_R}^{2,\rm on-shell}$, which we then use as input in our Feynman-diagrammatic calculation.

Figure 9.23 illustrates the effect which changing these parameters has on the $h_2 \to h_1 h_1$ branching ratio, the LEP exclusions and the channels with the highest statistical sensitivity. Comparison with Figure 9.22 shows that the unexcluded region B has greatly increased in size and extends to higher $\tan\beta$, such that it joins the unexcluded region A. This is due to the fact that, even after the shifts, the values of $|A_t|$ used as input in Figure 9.23 are higher than those used in Figure 9.22. (Recall that we saw in Figure 9.15 that larger values of $|A_t|$ resulted in plots with a larger unexcluded region)

However, if we would like to see the effect of the new $h_2 \to h_1 h_1$ vertex corrections and the effect of improvements in *FeynHiggs* (such as the phase dependence of the Higgs self-energies at $\mathcal{O}(\alpha_s \alpha_t)$), it is instructive to do an analysis using exactly the same parameter conversion as [24], which is given in equation (9.1). The results from using this parameter conversion in conjunction with the new Higgs sector results are shown in Figure 9.24 for $m_t = 172.6$ GeV (upper) and $m_t = 174.3$ GeV (lower). We compare the plots for $m_t = 174.3$ GeV in Figure 9.24 to the *FeynHiggs* analysis in Figure 9.4 (b). We can see that the unexcluded region B has decreased in size slightly and occurs at marginally higher values of $\tan\beta$. The unexcluded region A has increased in size substantially, although some of the lower values of $\tan\beta$, which were previously unexcluded, are excluded in the new analysis.

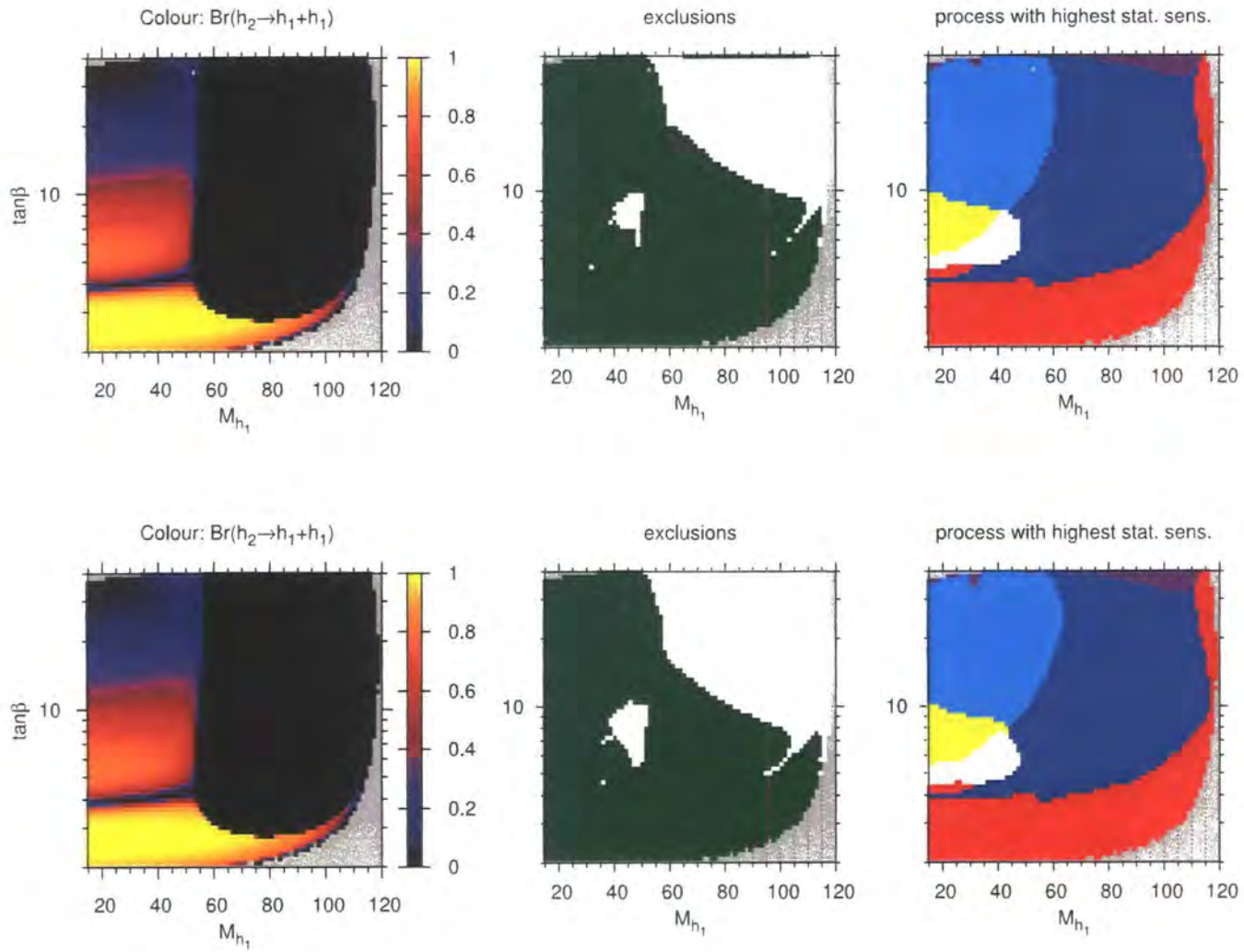

Figure 9.22: $h_2 \to h_1 h_1$ branching ratio, LEP exclusions and channels with the highest statistical sensitivity plotted on the $M_{h_1} - \tan\beta$ plane, using neutral Higgs self-energies from *FeynHiggs* version 2.6.5beta. The CPX scenario has been used. Upper graphs show $m_t = 172.6$ GeV, lower graphs show $m_t = 174.3$ GeV. See the captions of Figure 9.8 and Figure 9.9 for the legend.

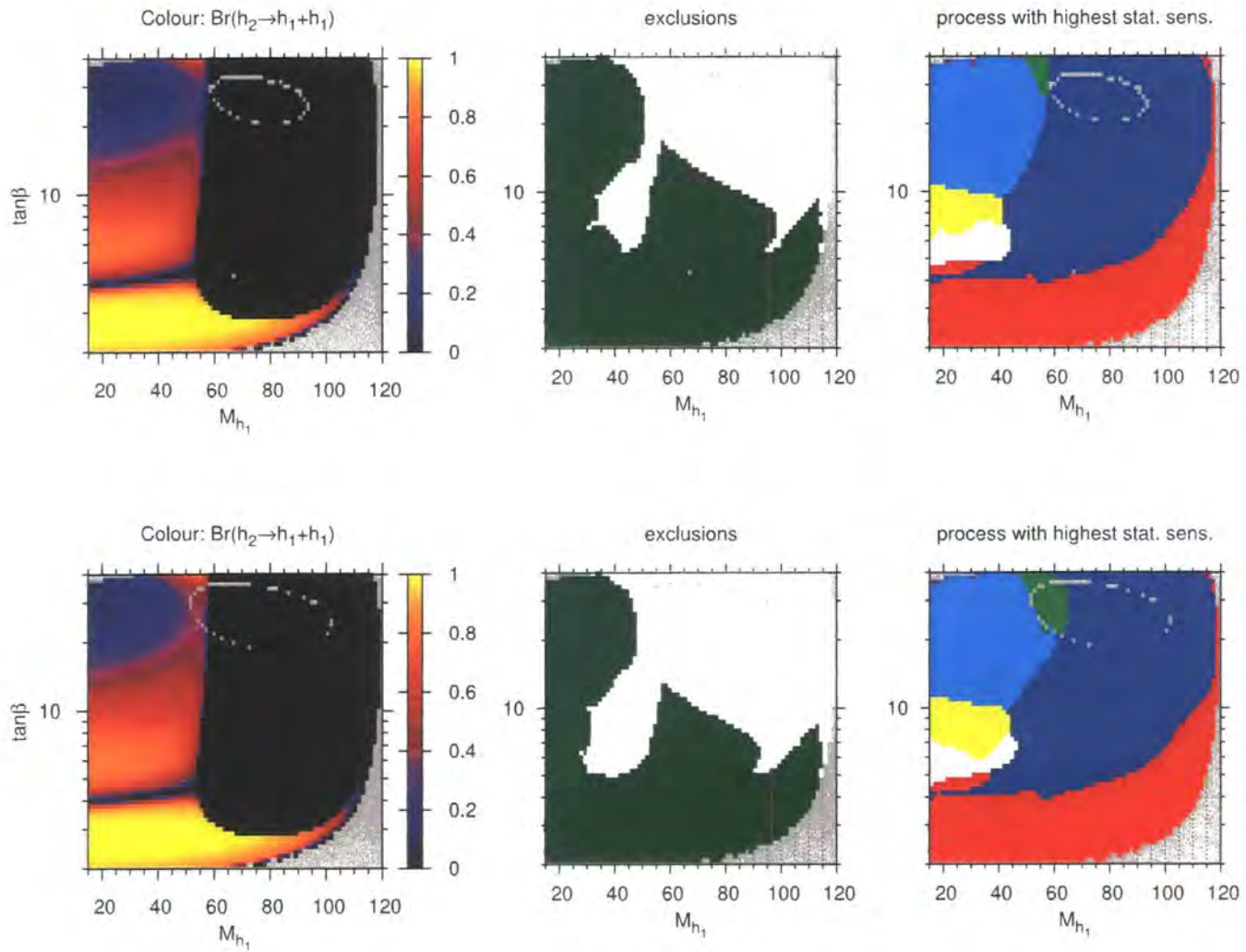

Figure 9.23: $h_2 \to h_1 h_1$ branching ratio, LEP exclusions and channels with the highest statistical sensitivity plotted on the $M_{h_1} - \tan\beta$ plane, using neutral Higgs self-energies from *FeynHiggs* version 2.6.5beta. The CPX scenario has been used, except with $A_t^{\overline{\rm DR}} = 1000i$ GeV and $M_L^{2,\overline{\rm DR}} = M_{\tilde{t}_R}^{2,\overline{\rm DR}} = 500$ GeV. Upper graphs show $m_t = 172.6$ GeV, lower graphs show $m_t = 174.3$ GeV (conversion is given in Section 3.4). See the captions of Figure 9.8 and Figure 9.9 for the legend.

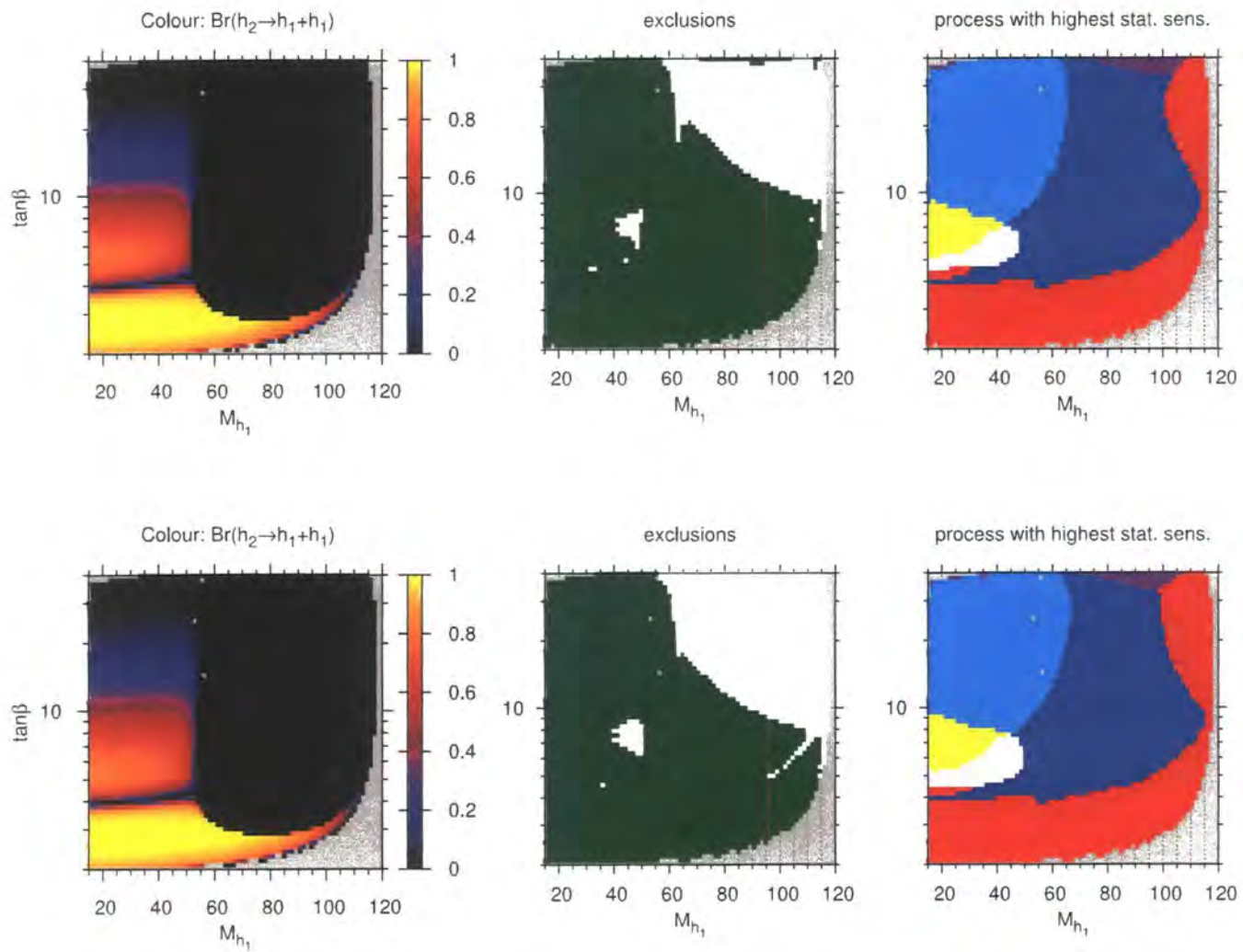

Figure 9.24: $h_2 \to h_1 h_1$ branching ratio, LEP exclusions and channels with the highest statistical sensitivity plotted on the $M_{h_1} - \tan\beta$ plane, using neutral Higgs self-energies from *FeynHiggs* version 2.6.5beta. The CPX scenario has been used, except with $|A_t^{\overline{\rm DR}}| = 1000$ GeV. Upper graphs show $m_t = 172.6$ GeV, lower graphs show $m_t = 174.3$ GeV (conversion of $|A_t|$ given in equation (9.1)). See the captions of Figure 9.8 and Figure 9.9 for the legend.

9.6 Using *CPsuperH* with the topological cross-section bounds

We would expect our analysis to provide less exclusion than a dedicated CPX analysis of the type used in [24], since, as we have discussed, we can only use one observed topological cross-section limit for each point in parameter space.

We can investigate this effect further by applying the topological cross-section limits to Higgs masses, couplings and branching ratios as calculated with *CPsuperH* [59], which we show in Figure 9.25. As input, we use the CPX scenario with $A_t^{\overline{\rm DR}} = 1000$ GeV and $M_L^{2,\overline{\rm DR}} = M_{\tilde{t}_R}^{2,\overline{\rm DR}} = 500$ GeV. We use values for the on-shell top mass of $m_t = 172.6$ GeV (top) and $m_t = 174.3$ GeV (bottom).

We compare the result for $m_t = 174.3$ GeV with the *CPH* analysis in Figure 9.4. The excluded regions A and B appear in similar areas of parameter space, although the shape of the unexcluded region B differs. It should be noted that we are comparing the results from two different codes and therefore would expect some differences, although, since *CPH* is an earlier version of *CPsuperH*, we would expect these differences to be relatively minor. We therefore concur with the results from previous investigations [119], which concluded that using the topological cross-section bounds is a useful way to confirm the existence and approximate positions of unexcluded regions. However, in situations where the shape of these regions is important, a dedicated analysis may be required.

It is also interesting to see that, for both values of m_t shown in Figure 9.25, there is a large region $M_{h_1} \gtrsim 70$ GeV and $\tan\beta \gtrsim 10$ GeV in which the channel $h_1 Z \rightarrow b\bar{b}Z$ (■) has the highest statistical sensitivity. This did not appear in any of the plots in the previous section and is due to higher values of M_{h_2} at these particular $M_{h_1}, \tan\beta$ coordinates.

9.7 Combining the results

Figure 9.26 illustrates the resulting excluded regions if Figure 9.23 and Figure 9.25 are combined such that a point in the CPX parameter space is only excluded in Figure 9.26 if it is excluded in both Figure 9.23 and Figure 9.25, in analogy to the method used

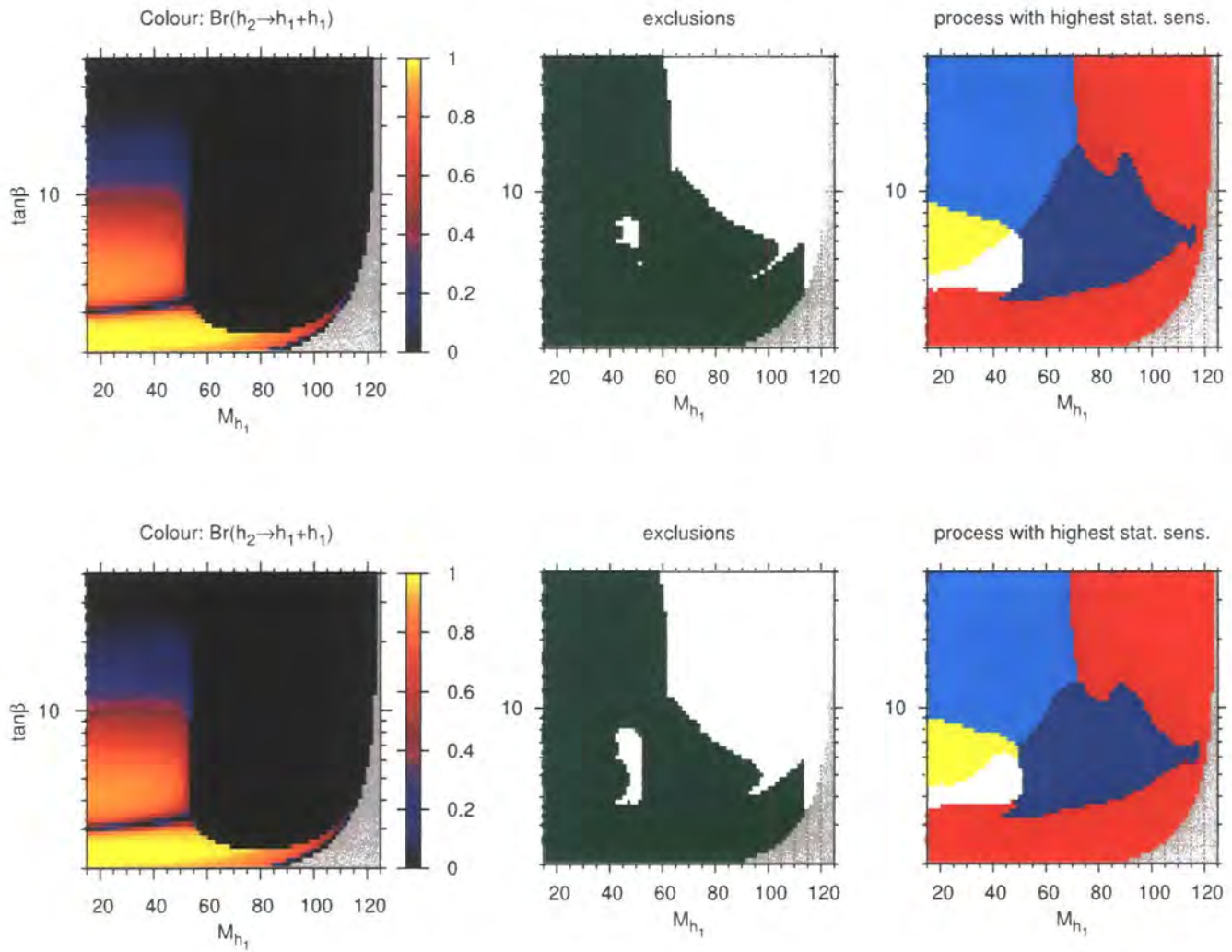

Figure 9.25: $h_2 \to h_1 h_1$ branching ratio, LEP exclusions and channels with the highest statistical sensitivity plotted on the $M_{h_1} - \tan\beta$ plane, using *CPsuperH* [59] and $A_t^{\overline{\rm DR}} = 1000$ GeV, other parameters taken from CPX scenario. Upper graphs show $m_t = 172.6$ GeV. lower graphs show $m_t = 174.3$ GeV. See the captions of Figure 9.8 and Figure 9.9 for the legend.

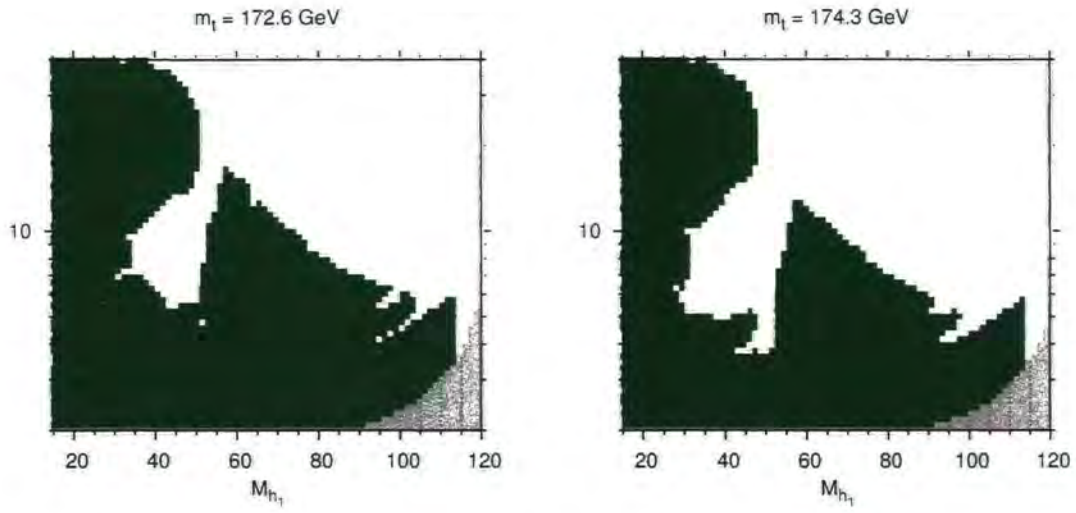

Figure 9.26: LEP exclusions plotted on the $M_{h_1} - \tan\beta$ plane, for the CPX scenario. We have combined the results from Figure 9.23 (which used *FeynHiggs* [31,56–58] version 2.6.5beta with a $\overline{\text{DR}}$ to on-shell conversion) and Figure 9.25 (which used *CPsuperH*) such that a point in parameter space is only excluded if both of these analyses found it to be excluded. Green areas indicate excluded regions, white regions indicate unexcluded regions.

to combine results from *FeynHiggs* and *CPH* in [24]. It is interesting to see that the unexcluded regions increase substantially compared to Figure 9.3.

However, these results should be treated with caution. A thorough comparison between results obtained using *FeynHiggs* and *CPsuperH* would require a detailed knowledge of both *FeynHiggs* and *CPsuperH* and take into account differences in higher order contributions and parameter definitions. This is beyond the scope of the thesis. It is also notable that the results using the approximate parameter conversion given by equation (9.1) (Figure 9.24) are more similar to the *CPsuperH* results (Figure 9.25) than the results from using the more rigorous $\overline{\text{DR}}$ to on-shell conversion derived in Section 3.4 (Figure 9.23).

9.8 Conclusion

The topological cross-section limits provided by [24] can be used to calculate regions of parameter space which have been excluded by LEP for models and scenarios that differ from those investigated in dedicated analyses [24]. We have used these limits to investigate the impact that our new branching ratio results have on the LEP exclusions

in the CPX scenario. We have found that unexcluded regions remain and we have investigated the dependence of these regions on various MSSM parameters. We have discussed the impact of a new version of the program *FeynHiggs*, which has not yet been made publicly available. In order to compare to the results of the dedicated analysis of the CPX scenario in [24], we performed an on-shell to $\overline{\text{DR}}$ parameter conversion, using the 'full' conversion outlined in Section 3.4 and the conversion originally used in [24]. We have performed a preliminary combination of the results using the 'full' conversion and the results from the program *CPsuperH*, and the resultant plots show enlarged unexcluded regions in comparison to [24]. We have discussed the limitations of this comparison, which stem particularly from difficulties in performing the conversion between parameters used in *CPsuperH* and those used in *FeynHiggs*.

Chapter 10

The program *HiggsBounds*: Comparing theoretical predictions with limits from Higgs searches at LEP and the Tevatron

In order to perform the analysis in the previous chapter, we implemented the expected and experimentally measured topological cross-section limits from the LEP Higgs searches [24] into the fortran program *HiggsBounds* [29][1]. This program takes theoretical Higgs sector predictions as input, determines which channel has the highest exclusion power at each parameter point and then compares the theoretical prediction in that channel with the experimentally measured limit.

We have extended *HiggsBounds* to be applicable to models with an arbitrary number of neutral Higgs bosons and we are including the new results from the Higgs searches at the Tevatron collider as they are released. We currently have an online version of the program available at the address

`http://www.ippp.dur.ac.uk/HiggsBounds`

and we will shortly be releasing a downloadable version of the code.

In this chapter, we discuss the additional features which we implemented in order to take advantage of the limits provided by the Tevatron experiments. We will then discuss a numerical example, using one of the MSSM benchmark scenarios.

[1] For other applications of preliminary versions of *HiggsBounds*, see [125, 126].

and the total SM Higgs decay width, as provided by the program *HDecay* [108]. *HiggsBounds* also contains functions fitted to the SM Higgs hadronic production cross-sections[3]

- associated production $p\bar{p} \to q\bar{q} \to HW^{\pm}$ and $p\bar{p} \to q\bar{q} \to HZ$
- gluon fusion $p\bar{p} \to gg \to H$
- vector boson fusion $p\bar{p} \to q\bar{q} \to q\bar{q}H$
- b-quark fusion $p\bar{p} \to b\bar{b} \to H$

HiggsBounds also requires SM Higgs hadronic cross-sections[4] for

- $p\bar{p} \to (b/\bar{b})g \to H(b/\bar{b})$

without cuts and with cuts which mimic those used in the analysis [141].

In addition, *HiggsBounds* contains internal functions which are fitted to the SM ratios[5]

- $R^{q_i\bar{q}_j}_{HW^+} = \sigma^{\rm SM}(p\bar{p} \to q_i\bar{q}_j \to HW^+)/\sigma^{\rm SM}(p\bar{p} \to HW^{\pm})$
- $R^{q_i\bar{q}_j}_{HW^-} = \sigma^{\rm SM}(p\bar{p} \to q_i\bar{q}_j \to HW^-)/\sigma^{\rm SM}(p\bar{p} \to HW^{\pm})$
- $R^{q_i\bar{q}_i}_{HZ} = \sigma^{\rm SM}(p\bar{p} \to q_i\bar{q}_i \to HZ)/\sigma^{\rm SM}(p\bar{p} \to HZ)$
- $R^{gg}_{H} = \sigma^{\rm SM}(p\bar{p} \to gg \to H)/\sigma^{\rm SM}(p\bar{p} \to H)$
- $R^{b\bar{b}}_{H} = \sigma^{\rm SM}(p\bar{p} \to b\bar{b} \to H)/\sigma^{\rm SM}(p\bar{p} \to H)$

where q_i, q_j denote the allowed combinations of quarks u, d, s, c, b.

These internal functions are used in conjunction with Higgs sector input from the user. This input will contain the Higgs masses and some combination of normalised effective Higgs couplings squared, Higgs branching ratios, normalised hadronic Higgs production cross-sections and normalised partonic Higgs production cross-sections (see *HiggsBounds* documentation for allowed combinations). We use 'normalised' here to denote division by the equivalent SM result. The multiple input options are designed to allow the program to be applied to a wide variety of models while still maintaining convenient input modes for the most frequently used applications. However, note

[3]Obtained from the TeV4LHC Higgs Working Group compilation, maintained by F. Maltoni, at `http://maltoni.home.cern.ch/maltoni/TeV4LHC/`

[4]We use calculations by O. Brein, which are in agreement with [148, 149]

[5]See previous footnote.

that *HiggsBounds* can only be used if the narrow width approximation is applicable to the Higgs production and decay process (see Appendix B) and the model under study predicts SM-like rates for the background processes.

Limits which have been obtained by combining different search channels under the assumption of SM-like Higgs are only applied to a particular parameter point if all the relevant production cross-sections and branching ratios for that point are related to the SM predictions by the same factor. However, we treat combined D0 and CDF limits on a SM-like Higgs [146,147] as single $p\bar{p} \to h_a \to W^-W^+$ channels above $M_{h_a} = 150$ GeV, since, to a good approximation, this is the only process which contributes to the limit in this mass range.

If two Higgs particles are nearly degenerate, we add up their cross-sections in each relevant Tevatron channel. By default, we combine the theoretical prediction for two channels of the same type if the Higgs masses have a mass difference of less than $\Delta m_H = 10$ GeV (although this quantity can be varied). This is particularly relevant for obtaining exclusions in the MSSM parameter space at large $\tan\beta$.

We combine the LEP and Tevatron limits by searching for the LEP or Tevatron channel which is predicted to have the highest statistical sensitivity. The theoretical prediction is then compared to the experimentally measured cross-section limit for this channel only, as before. In this way we maintain the correct statistical interpretation of the limits at the 95% CL. At present, *HiggsBounds* considers $(n_H \times 2 + n_H^2 \times 9)$ LEP channels (although not all of these channels will be kinematically allowed) and $(n_H \times 23)$ Tevatron channels, where n_H is the number of neutral Higgs bosons in the model under study.

10.2 Numerical results

In this section, we demonstrate the use of *HiggsBounds* in conjunction with theoretical Higgs sector predictions from the program *FeynHiggs* [31,56–58] (version FH2.6.4).

We use the option in which the user provides the Higgs masses, branching ratios and normalised effective couplings squared as input. We perform the calculation in the $m_h^{\text{max+}}$ benchmark scenario [117], which we define as

$m_h^{\max+}$ benchmark scenario

$$M_{SUSY} = 1000 \text{ GeV}, \ \mu = 200 \text{ GeV}, \ M_1 = M_2 = 200 \text{ GeV}, \ M_3 = 800 \text{ GeV}$$
$$X_t = 2M_{SUSY}, \ A_t = X_t + \mu/\tan\beta, \ m_t = 172.6 \text{ GeV}$$

HiggsBounds uses the normalised effective couplings squared to find Higgs hadronic production cross-sections via the relations:

$$\begin{aligned}
\sigma(p\bar{p} \to h_a W^\pm) &= \sigma^{\rm SM}(p\bar{p} \to HW^\pm)|g^{\rm eff}_{h_a WW}|^2 \left(R^{u\bar{d}}_{HW^+} + R^{c\bar{s}}_{HW^+} + R^{d\bar{u}}_{HW^-} + R^{s\bar{c}}_{HW^-}\right) \\
&= \sigma^{\rm SM}(p\bar{p} \to HW^\pm)|g^{\rm eff}_{h_a WW}|^2, \qquad (10.1) \\
\sigma(p\bar{p} \to h_a Z) &= \sigma^{\rm SM}(p\bar{p} \to HZ)|g^{\rm eff}_{h_a ZZ}|^2 \left(R^{u\bar{u}}_{HZ} + R^{d\bar{d}}_{HZ} + R^{c\bar{c}}_{HZ} + R^{s\bar{s}}_{HZ} + R^{b\bar{b}}_{HZ}\right) \\
&= \sigma^{\rm SM}(p\bar{p} \to HZ)|g^{\rm eff}_{h_a ZZ}|^2, \qquad (10.2) \\
\sigma(p\bar{p} \to h_a) &= \sigma^{\rm SM}(p\bar{p} \to H)\left(|g^{\rm eff}_{h_a gg}|^2 R^{gg}_H + |g^{\rm eff}_{h_a bb}|^2 R^{b\bar{b}}_H\right), \qquad (10.3) \\
\sigma(h_a \text{ via VBF}) &= \sigma^{\rm SM}(h_a \text{ via VBF})|g^{\rm eff}_{h_a WW}|^2, \qquad (10.4)
\end{aligned}$$

$$\begin{aligned}
\sigma(p\bar{p} \to h_a(b/\bar{b})) &= \sigma^{\rm SM}(p\bar{p} \to H(b/\bar{b}))|g^{\rm eff}_{h_a bb}|^2. \qquad (10.5) \\
\sigma_{\text{with cuts}}(p\bar{p} \to h_a(b/\bar{b})) &= \sigma^{\rm SM}_{\text{with cuts}}(p\bar{p} \to H(b/\bar{b}))|g^{\rm eff}_{h_a bb}|^2. \qquad (10.6)
\end{aligned}$$

Figure 10.1 (a) illustrates the processes with the highest statistical sensitivity in the $m_h^{\max+}$ benchmark scenario. There is a significant region where the LEP process $e^+e^- \to h^0 Z \to b\bar{b}Z$ (■) has the highest statistical sensitivity at low-to-moderate values of $\tan\beta$ and a narrow region at $M_A \sim 90$ GeV where the LEP process $e^+e^- \to h_a h_b \to b\bar{b}b\bar{b}$ (■) has the highest statistical sensitivity. However, at high values of $\tan\beta$, the plot is dominated by the Tevatron process $p\bar{p} \to h_a \to \tau^+\tau^-(\ )$ [104, 105]. Above $M_A = 140$ GeV, there is a large region in which the process $p\bar{p} \to h_a \to W^+W^-$(□) has the highest statistical sensitivity at moderate $\tan\beta$. The process $p\bar{p} \to h_a V \to b\bar{b}V$ with missing E_T (■) features in a thin region at $\tan\beta \sim 7$, $M_A > 130$ GeV.

The regions of $m_h^{\max+}$ parameter space which can be excluded by current limits from Higgs searches at LEP and the Tevatron are shown in Figure 10.1 (b). Much of the area below $M_A \sim 90$ GeV and the area below $\tan\beta \sim 5 - 10$ can be excluded by LEP results. There is also a substantial excluded region due to Tevatron limits on the process $p\bar{p} \to h_a \to \tau^+\tau^-(\ )$ at large $\tan\beta$, which extends to $\tan\beta \sim 40$ at $M_A = 140$ GeV. In

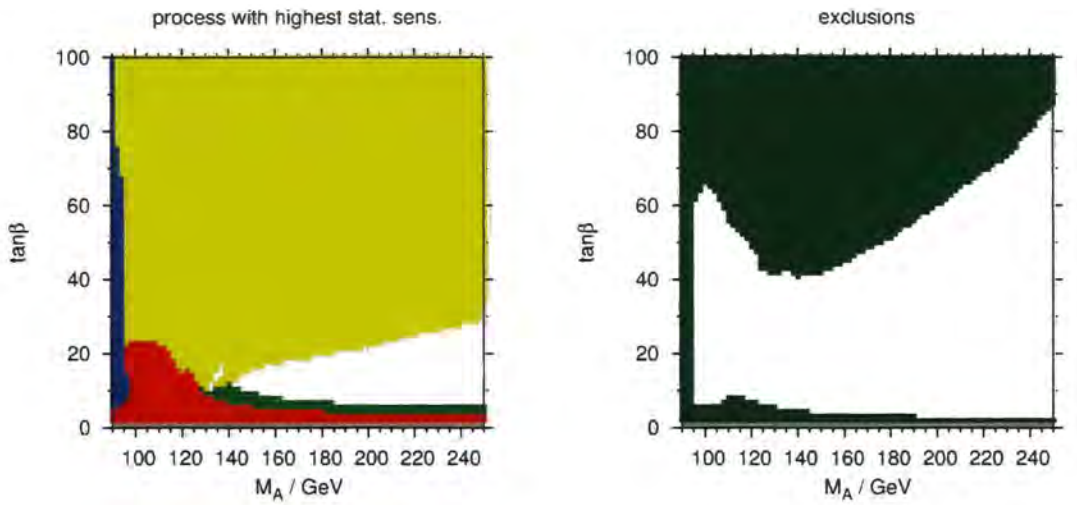

(a) (b)

Figure 10.1: Processes with the highest statistical sensitivity and regions excluded at 95% CL in the $m_h^{\max+}$ benchmark scenario by the program *HiggsBounds* [29]. If the separation in Higgs masses is less than $\Delta M_H = 10$ GeV, the Tevatron cross-sections involving these Higgs bosons are added. (a) The colour codings are: red = $e^+e^- \to h^0 Z \to b\bar{b}Z$ (■), blue = $e^+e^- \to h_a h_b \to b\bar{b}b\bar{b}$ (■), green = $p\bar{p} \to h_a V \to b\bar{b}V$ with missing E_T (■), white = $p\bar{p} \to h_a \to W^+W^-$(□), yellow = $p\bar{p} \to h_a \to \tau^+\tau^-$(■) (b)green = excluded, white = unexcluded

this part of parameter space, at least two neutral Higgs bosons have a mass difference $\Delta m_H < 10$ GeV and therefore the theoretical predictions for these cross-sections are combined.

Figure 10.2 demonstrates the excluded regions in the $m_h^{\max+}$ benchmark scenario for the case where Tevatron cross-sections are not combined for similar masses. As we would expect, the excluded region has reduced in size significantly.

10.3 Conclusion

We have described a new program *HiggsBounds*, which uses cross-section limits from Higgs searches at both LEP and the Tevatron to determine which regions of parameter space of a model with an arbitrary number of neutral Higgs bosons have already been excluded at the 95% CL. As input, it requires theoretical predictions for the Higgs sector. We have demonstrated some of the key features of *HiggsBounds* using the $m_h^{\max+}$ benchmark scenario and illustrated how a combination of LEP and Tevatron results can be used to place substantial constraints on the available parameter space in this scenario.

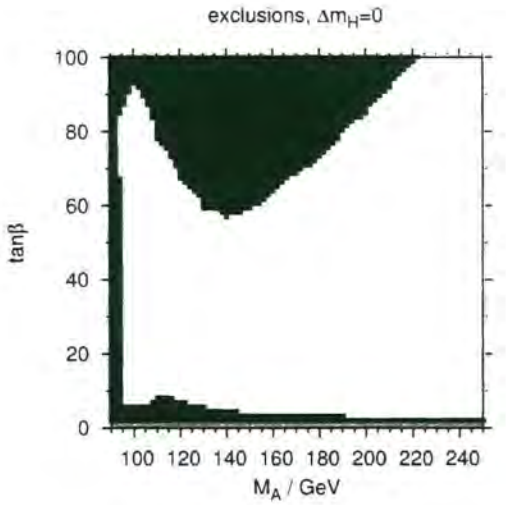

Figure 10.2: Regions of the $m_h^{\max+}$ benchmark scenario which are excluded at 95 % CL by the program *HiggsBounds* [29] Cross-sections in channels with similar values of the Higgs mass are not combined. (green = excluded, white = unexcluded)

Our code provides a quick and convenient way for phenomenologists and model-builders to check whether a particular model or scenario has already been excluded by the Higgs searches.

An online version of *HiggsBounds* has been made publicly available and a downloadable version will be released shortly. We intend to update the program frequently in order to ensure that it continues to use the most up-to-date Tevatron limits.

The authors of the publicly available programs *FeynHiggs* [31, 56–58] and *DarkSUSY* [150] (which performs calculations of relic density and various signals for direct and indirect searches, especially for supersymmetric dark matter) have expressed an interest in using *HiggsBounds* in conjunction with their respective programs. We will also provide an interface to the code *CPsuperH* [59].

HiggsBounds will be extended to include limits from Higgs searches at the LHC as they become available.

Chapter 11

Conclusion

"Theory is a good thing but a good experiment lasts forever."
-- Peter Leonidovich Kapitsa 1894–1984

The two theories of Supersymmetry and the Higgs mechanism have widespread popularity throughout the particle physics community. So far, these theories have not been confirmed by experiment, but neither has it been possible to rule them out. Over the next few decades, we will be able to rigorously test these models at the Large Hadron Collider and the International Linear Collider. This thesis deals with some of the phenomenological issues associated with investigating an example involving aspects of both theories - the Higgs sector of the complex Minimal Supersymmetric Standard Model.

After discussing the composition and renormalisation of the complex MSSM, we derived the counter-terms necessary for the calculations in this thesis. We then reviewed the status of the Higgs mass predictions and repeated the calculation of the neutral Higgs self-energies at 1-loop order for the complex MSSM. We have derived a way to incorporate these self-energies into propagator corrections to processes with external Higgs bosons, which is an extension of previously published results for the real MSSM. We have developed a method which allows the inclusion of Higgs mixing with Goldstone bosons and Z bosons into processes involving an external Higgs bosons, without inadvertently introducing a gauge parameter dependence at the 1-loop level.

We have discussed some of the issues surrounding Standard Model and SUSY QCD contributions to processes and explicitly checked that the way in which the resummation

of the SUSY QCD corrections is performed is fully consistent with the inclusion of complex phases.

We have calculated the full 1-loop vertex corrections within the Feynman-diagrammatic approach for the process $h_a \to h_b h_c$, taking into account the dependence on all complex phases of the supersymmetric parameters and the full momentum dependence. These results will be included in the publicly available program *FeynHiggs* [31, 56–58]. We have included the full propagator corrections, using neutral Higgs self-energies as provided by *FeynHiggs*, and we have consistently included 1-loop mixing with the Z boson and the unphysical Goldstone-boson degree of freedom. Our results are currently the most precise predictions for the $h_a \to h_b h_c$ decay width.

We have found that the genuine vertex corrections to the triple Higgs vertex are numerically very important. Their inclusion changes the predictions for the decay widths drastically as compared to an approximation based solely on propagator-type corrections. Using the leading Yukawa contributions yields a prediction for the decay width which is closer to the full result, but we still find deviations of $\sim 27\%$ in the example of the CPX parameter space at $\tan\beta \sim 8$, $M_{h_1} \sim 30$ GeV.

We have also presented two effective coupling approximations in the complex MSSM. The Yukawa approximation includes all leading corrections and can be expressed in a very compact form, thus providing a convenient way to go beyond the tree level vertex contributions. The effective coupling created from the full fermion/sfermion vertex corrections at zero incoming momentum is a more sophisticated effective coupling approximation. These effective couplings can be used for determining accurate cross-sections for processes such as $e^+e^- \to h_1 Z \to h_1 h_1 Z$ at the ILC, which provide a way to directly access the Higgs self-couplings and thus investigate a crucial element of the Higgs mechanism.

We also have presented the full 1-loop electroweak vertex corrections to the $h_a \to f\bar{f}$ decay width in the complex MSSM, including full phase dependence, a result which has not been previously available in the literature. These contributions will be incorporated into the program *FeynHiggs*. We have supplemented these new corrections with 1-loop QED and SM QCD corrections, resummed SUSY QCD contributions, propagator corrections calculated using neutral Higgs self-energies from *FeynHiggs*, and 1-loop propagator mixing with Goldstone bosons and Z bosons.

Using these decay widths in conjunction with the topological cross section limits from the LEP Higgs searches, we were able to investigate the effect of the new vertex

contributions on the exclusions in the CPX benchmark scenario. Of particular interest was the region 30 GeV $\lesssim M_{h_1} \lesssim$ 50 GeV, $3 \lesssim \tan\beta \lesssim 10$, which previous analyses had not been able to exclude, despite the relatively low values of M_{h_1} involved. Since the coupling of the lightest Higgs to the Z bosons is suppressed in much of this region, processes involving the second heaviest Higgs or the heaviest Higgs are important. Across the majority of this region, the $h_2 \to h_1 h_1$ decay is dominant and therefore a precise theory prediction for this decay width is crucial for confirming the existence of the unexcluded area and mapping out its extent.

We have also investigated the dependence of these regions on various MSSM parameters and investigated the impact of a new version of the program *FeynHiggs*, which has not yet been made publicly available. We performed on-shell to $\overline{\text{DR}}$ parameter conversions in order to carry out a preliminary comparison with exclusions obtained using the publicly available program *CPsuperH* [59]. Although both analyses confirmed the existence of unexcluded regions in similar parts of CPX parameter space, the extent of these regions varied. The unexcluded parameter region with a very light Higgs bosons will be difficult to cover with the Higgs searches at the LHC [89, 151, 152] (see also [153] for a recent study) but can be thoroughly investigated at the ILC [90].

In order to facilitate the use of LEP results in conjunction with new Higgs sector results, we created a new fortran program, *HiggsBounds* [29]. We have extended it to apply to models containing an arbitrary number of neutral Higgs bosons and we have incorporated the preliminary results from the Tevatron Higgs searches. This program allows the easy comparison of models outside the usual benchmark scenarios with current Higgs search data. We will continue to update *HiggsBounds* to include the most recent Tevatron results and we will include limits from the LHC as they become available.

Appendix A

Scalar Integrals

Although we will use the program *LoopTools* [45] in general to perform the loop integrals, some situations will require explicit expressions in special limits, such as the case where the external momenta is put to zero. Also, simplified expressions for the loop integrals can be very useful when manipulating algebraic expressions obtained from Feynman-diagrammatic calculations or isolating leading terms, such as when investigating the structure of Δm_b.

If the external momenta are put to zero, scalar integrals can be decomposed into A_0 integrals. The solution to A_0 is found (using the procedure outlined in detail in [46]) to be

$$\begin{aligned} A_0(m^2) &= \frac{(2\pi\mu)^{4-D}}{i\pi^2}\int d^Dq \frac{1}{q^2-m^2+i\epsilon} \\ &= -m^2\left(\frac{m^2}{4\pi\mu^2}\right)^{\frac{D-4}{2}}\Gamma\left(\frac{2-D}{2}\right) \\ &= m^2\left(\Delta - \log\left(\frac{m^2}{\mu^2}\right)+1\right)+\mathcal{O}(D-4) \end{aligned} \tag{A.1}$$

where $\Delta = \frac{2}{4-D} = \gamma_E + \log(4\pi)$, $\gamma_E = 0.57721...$ is the Euler-Mascheroni constant and $\Gamma(x)$ is the gamma function.

We will require the 2-point, 3-point, 4-point and 5-point integrals, which are defined as

$$B_0(0, m_0^2, m_1^2) \tag{A.2}$$
$$= \frac{(2\pi\mu)^{4-D}}{i\pi^2} \int d^D q \frac{1}{(q^2 - m_0^2 + i\epsilon)(q^2 - m_1^2 + i\epsilon)}$$
$$C_0(0, 0, 0, m_0^2, m_1^2, m_2^2) \tag{A.3}$$
$$= \frac{1}{i\pi^2} \int d^D q \frac{1}{(q^2 - m_0^2 + i\epsilon)(q^2 - m_1^2 + i\epsilon)(q^2 - m_2^2 + i\epsilon)}$$
$$D_0(0, 0, 0, 0, m_0^2, m_1^2, m_2^2, m_3^2) \tag{A.4}$$
$$= \frac{1}{i\pi^2} \int d^D q \frac{1}{(q^2 - m_0^2 + i\epsilon)(q^2 - m_1^2 + i\epsilon)(q^2 - m_2^2 + i\epsilon)(q^2 - m_3^2 + i\epsilon)}$$
$$E_0(0, 0, 0, 0, 0, m_0^2, m_1^2, m_2^2, m_3^2, m_4^2) \tag{A.5}$$
$$= \frac{1}{i\pi^2} \int d^D q \frac{1}{(q^2 - m_0^2 + i\epsilon)(q^2 - m_1^2 + i\epsilon)(q^2 - m_2^2 + i\epsilon)(q^2 - m_3^2 + i\epsilon)(q^2 - m_4^2 + i\epsilon)}$$

where the momenta of the external particles are zero and m_0, m_1, m_2, m_3, m_4 are masses of internal particles. Note that since all the momenta are the same, the order of the masses is irrelevant. Explicit solutions for the 2-point and 3-point functions for the case with general momenta dependence can be found in [46].

For the case where all the internal particles have the same mass, we use partial differentiation in order to arrive at the expressions

$$B_0(0, a, a) = \frac{\partial A_0(a)}{\partial a} = \frac{A_0(a)}{a} - 1 \tag{A.6}$$
$$C_0(0, 0, 0, a, a, a) = \frac{1}{2}\frac{\partial^2 A_0(a)}{\partial a^2} = \frac{-1}{2a} \tag{A.7}$$
$$D_0(0, 0, 0, 0, a, a, a, a) = \frac{1}{6}\frac{\partial^3 A_0(a)}{\partial a^3} = \frac{1}{6a^2} \tag{A.8}$$
$$E_0(0, 0, 0, 0, 0, a, a, a, a, a) = \frac{1}{24}\frac{\partial^4 A_0(a)}{\partial a^4} = \frac{1}{48a^3} \tag{A.9}$$

We can find the other B_0, C_0, D_0 integrals by using partial fraction decomposition into integrals of type $A_0, B_0(0, a, a), C_0(0, 0, 0, a, a, a)$. For the 2-point function, this gives

$$B_0(0, a, b) = \frac{1}{a - b}(A_0(a) - A_0(b)) \tag{A.10}$$

For the 3-point function, we find

$$C_0(0,0,0,a,a,b) = \frac{1}{b-a} - \frac{bA_0(a) - aA_0(b)}{a(b-a)^2} \quad \text{(A.11)}$$

$$C_0(0,0,0,a,b,c) = \frac{(b-c)A_0(a) + (c-a)A_0(b) + (a-b)A_0(c)}{(a-b)(a-c)(b-c)} \quad \text{(A.12)}$$

These 3-point expressions are particularly important for our purposes as this limit is not covered by *LoopTools* [45] and they will be required in order to get numerical results when calculating momentum independent approximations to the triple Higgs vertex. They will also be used to simplify the algebraic expressions for the Higgs self-energies in the Yukawa approximation and the triple Higgs vertex in the Yukawa approximation.

This method can be easily extended to calculate all the D_0, E_0 integrals at zero incoming momenta. However, for the purposes of this thesis, we will only require

$$D_0(0,0,0,0,a,a,a,b) = \frac{a^2 - 2\mathrm{A0}(b)a - b^2 + 2b\mathrm{A0}(a)}{2a(a-b)^3} \quad \text{(A.13)}$$

$$E_0(0,0,0,0,0,a,a,a,b,b) = -\frac{b(-5a^2+4ba+b^2) - 2b(a+2b)\mathrm{A0}(a) + 2a(a+2b)\mathrm{A0}(b)}{2a(a-b)^4 b} \quad \text{(A.14)}$$

as these will be used when simplifying the algebraic expressions for the triple Higgs vertex in the Yukawa approximation.

We will also use

$$B_0(a,0,a) = B_0(0,a,a) + 2 \quad \text{(A.15)}$$

$$B_1(a,0,a) = \frac{-\mathrm{A0}(a)}{2a} \quad \text{(A.16)}$$

where B_1 is defined through

$$B_\mu(p, m_0^2, m_1^2) = \frac{(2\pi\mu)^{4-D}}{i\pi^2} \int d^D q \frac{q_\mu}{(q^2 - m_0^2 + i\epsilon)((q+p)^2 - m_1^2 + i\epsilon)} \quad \text{(A.17)}$$

$$= p_\mu B_1(p^2, m_0^2, m_1^2) \quad \text{(A.18)}$$

These were found using the procedure outlined in [46]. They will be used to calculate diagrams involving gluons in Section 3.3.1 and Section 3.4.

Other expressions for tensor integrals which were used when, for example, checking relations between $\Sigma_{h_i G}, \Sigma_{h_i Z}$, can be found in [46] and in the Mathematica file btensor.m, which is supplied with the program *FormCalc* [43, 45].

Appendix B

Narrow-width approximation

The narrow width approximation is commonly used to separate a process involving an internal propagator with a pole at $q^2 = M^2 - iM\Gamma$ into two parts- one involving the production of the internal particle and one involving its decay. These parts can then be calculated independently.

The approximation requires that $\Gamma \ll M$, that the centre-of-mass energy s of the full process is above the on-shell threshold for all particles involved in the 'production' part of the process and that the mass of the internal particle is sufficiently above the sum of the mass of its decay products. There should be no significant interference with non-resonant processes (as discussed in [154, 155]).

In these circumstances and using an arbitrary scalar process involving an internal propagator as an example, the cross section for the full process σ can be written as [156]

$$\sigma = \frac{1}{\pi}\int_{q^2_{\min}}^{q^2_{\max}} dq^2 \sigma_p(q^2) \frac{1}{(q^2 - M^2)^2 + (M\Gamma)^2} \left(\sqrt{q^2}\sigma_d(q^2)\right) \tag{B.1}$$

where $\sigma_p(q^2)$ refers to the part of the process which produces the internal particle at momentum q^2 and $\sigma_d(q^2)$ refers to the part of the process in which the internal particle at momentum q^2 decays i.e. $\sigma_d(q^2)$ is the off-shell decay width. The Breit-Wigner shape. $\frac{1}{(q^2-M^2)^2+(M\Gamma)^2}$ is the modulus squared of the internal propagator. For the narrow width approximation to hold, $q^2_{\min}$ should be less than the centre-of-mass energy that would be required to produce all the final state particles on-shell $q^2_{\text{f,threshold}}$ minus a few decay widths and $q^2_{\max}$ should be greater than the actual centre-of-mass energy of the process plus a few decay widths.

As $\Gamma \to 0$.

$$\frac{1}{(q^2 - M^2)^2 + (M\Gamma)^2} \sim \frac{\pi}{M\Gamma}\delta(q^2 - M^2) \tag{B.2}$$

Therefore, in this limit, the σ_p and σ_d can be calculated entirely on-shell, i.e. at $q^2 = M^2$, such that that the full cross section under the narrow-width approximation becomes

$$\sigma_{\rm NW} = \sigma_p^{\rm on-shell}\frac{\sigma_d^{\rm on-shell}}{\Gamma} = \sigma_p^{\rm on-shell}{\rm Br} \tag{B.3}$$

For example, an important process at LEP was $e^+e^- \to HZ \to b\bar{b}Z$. Under the narrow-width approximation, the full cross section could be approximated by

$$\sigma_{\rm NW}\left(e^+e^- \to b\bar{b}Z\right) = \sigma_{e^-e^- - HZ}^{\rm on-shell}{\rm Br}(H \to b\bar{b}) \tag{B.4}$$

which is much simpler to calculate than the full 2-to-3 process.

If the conditions for the narrow width approximation are not met, it may still be possible to find an approximation that avoids calculating the entire production and decay process simultaneously. Examples of finite-width approximations can be found in [155] and [51].

Acknowledgements

Firstly, I would like to thank my supervisor, Georg Weiglein, for his guidance and patience throughout this Ph.D.

I would like to thank everyone in the IPPP for providing such a friendly and warm environment and I am especially grateful to Sophy Palmer, Alison Fowler, Jamie Tattersall and Oliver Brein for generously reading through parts of the draft.

Special mention must go to my office mates: Martyn Gigg, Kemal Ozeren, Stefan Hoeche, Gareth Jones, Ciaran Williams, Nikos Fanidakis, Elise Jennings, Ben Lowing and Han Sik Kim, all of whom have been great company and a pleasure to work alongside.

I would like to thank the other people whose friendship has made my time in Durham so special and, in particular, Becca White, Tim Butterley, Tom Bradley and Helen Vaughan for their support in the last few months while I've been writing up. And, of course, I'd like to thank Phil Bett for his inspiration, strength and light entertainment.

Last, but certainly not least, I would like to mention my family: Mum, Dad, Heidi and Mat - this thesis is dedicated to you.

This thesis was made in LaTeX 2_ε using the "hepthesis" class [157].

Bibliography

[1] S. L. Glashow, *Partial Symmetries of Weak Interactions*, *Nucl. Phys.* **22** (1961) 579–588.

[2] S. Weinberg, *A Model of Leptons*, *Phys. Rev. Lett.* **19** (1967) 1264–1266.

[3] A. Salam, *Weak and Electromagnetic Interactions*, Originally printed in *Svartholm: Elementary Particle Theory, Proceedings Of The Nobel Symposium Held 1968 At Lerum, Sweden*, Stockholm 1968, 367-377.

[4] M. Gell-Mann, *A Schematic Model of Baryons and Mesons*, *Phys. Lett.* **8** (1964) 214–215.

[5] G. Zweig, *An SU(3) model for strong interaction symmetry and its breaking*, CERN-TH-401.

[6] H. Fritzsch, M. Gell-Mann, and H. Leutwyler, *Advantages of the Color Octet Gluon Picture*, *Phys. Lett.* **B47** (1973) 365–368.

[7] D. J. Gross and F. Wilczek, *Ultraviolet behavior of non-abelian gauge theories*, *Phys. Rev. Lett.* **30** (1973) 1343–1346.

[8] H. D. Politzer, *Reliable perturbative results for strong interactions?*, *Phys. Rev. Lett.* **30** (1973) 1346–1349.

[9] G. 't Hooft and M. J. G. Veltman, *Regularization and Renormalization of Gauge Fields*, *Nucl. Phys.* **B44** (1972) 189–213.

[10] P. W. Higgs, *Broken symmetries and the masses of gauge bosons*, *Phys. Rev. Lett.* **13** (1964) 508–509.

[11] P. W. Higgs, *Spontaneous Symmetry Breakdown Without Massless Bosons*, *Phys. Rev.* **145** (1966) 1156–1163.

[12] F. Englert and R. Brout, *Broken symmetry and the mass of gauge vector mesons*, *Phys. Rev. Lett.* **13** (1964) 321–322.

[13] G. S. Guralnik, C. R. Hagen, and T. W. B. Kibble, *Global conservation laws and massless particles*, *Phys. Rev. Lett.* **13** (1964) 585–587.

[14] T. W. B. Kibble, *Symmetry breaking in non-Abelian gauge theories*, *Phys. Rev.* **155** (1967) 1554–1561.

[15] **LEP** Collaboration, *A combination of preliminary electroweak measurements and constraints on the standard model*, hep-ex/0412015.

[16] **Particle Data Group** Collaboration, C. Amsler *et. al.*, *Review of particle physics*, *Phys. Lett.* **B667** (2008) 1.

[17] **LEP Working Group for Higgs boson searches** Collaboration, R. Barate *et. al.*, *Search for the standard model Higgs boson at LEP*, *Phys. Lett.* **B565** (2003) 61–75, [hep-ex/0306033].

[18] **CDF** Collaboration, T. T. W. Group, *Combined CDF and D0 Upper Limits on Standard Model Higgs- Boson Production with up to 2.4 fb-1 of data*, arXiv:0804.3423.

[19] S. Haywood *et. al.*, *Electroweak physics*, hep-ph/0003275.

[20] G. Bertone, D. Hooper, and J. Silk, *Particle dark matter: Evidence, candidates and constraints*, *Phys. Rept.* **405** (2005) 279–390, [hep-ph/0404175].

[21] M. Drees, *An introduction to supersymmetry*, hep-ph/9611409.

[22] M. Drees, R. H. Godbole, and P. Roy, *Theory and Phenomenology of Sparticles*, World Scientific, 2004.

[23] R. Haag, J. T. Lopuszanski, and M. Sohnius, *All Possible Generators of Supersymmetries of the s Matrix*, *Nucl. Phys.* **B88** (1975) 257.

[24] **ALEPH** Collaboration, S. Schael *et. al.*, *Search for neutral MSSM Higgs bosons at LEP*, *Eur. Phys. J.* **C47** (2006) 547–587, [hep-ex/0602042].

[25] J. H. Christenson, J. W. Cronin, V. L. Fitch, and R. Turlay, *Evidence for the 2 pi Decay of the k(2)0 Meson*, *Phys. Rev. Lett.* **13** (1964) 138–140.

[26] B. Aubert, D. Boutigny, J.-M. Gaillard, A. Hicheur, Y. Karyotakis, J. P. Lees, P. Robbe, V. Tisserand, A. Palano, G. P. Chen, J. C. Chen, N. D. Qi, G. Rong, P. Wang, Y. S. Zhu, G. Eigen, P. L. Reinertsen, B. Stugu, B. Abbott, G. S. Abrams, A. W. Borgland, A. B. Breon, D. N. Brown, J. Button-Shafer, R. N. Cahn, A. R. Clark, and M. S. Gill, *Observation of cp violation in the b meson system*, *Phys. Rev. Lett.* **87** (Aug, 2001) 091801.

[27] **Belle** Collaboration, K. Abe *et. al.*, *Observation of large CP violation in the neutral B meson system*, *Phys. Rev. Lett.* **87** (2001) 091802, [hep-ex/0107061].

[28] J. A. Peacock, *Cosmological Physics*, Cambridge University Press, 2005.

[29] P. Bechtle, O. Brein, S. Heinemeyer, G. Weiglein, and K. Williams, *Higgsbounds: a program for checking bounds from higgs searches at lep and tevatron for models with an arbitrary number of neutral higgs bosons*, *in prep.* **0** (2008).

[30] U. Amaldi, W. de Boer, and H. Furstenau, *Comparison of grand unified theories with electroweak and strong coupling constants measured at LEP*, *Phys. Lett.* **B260** (1991) 447–455.

[31] M. Frank *et. al.*, *The Higgs boson masses and mixings of the complex MSSM in the Feynman-diagrammatic approach*, *JHEP* **02** (2007) 047, [hep-ph/0611326].

[32] H. Rzehak, *Zwei-Schleifen-Beiträge im supersymmetrischen Higgs-Sektor*, PhD thesis, Technische Universität München, 2005.

[33] T.-F. Feng, *The two-loop gluino's corrections on the inclusive $B \to X/s$ gamma decay in the CP violation MSSM with large tan(beta)*, *Phys. Rev.* **D70** (2004) 096012, [hep-ph/0405192].

[34] S. Y. Choi, M. Drees, and J. S. Lee, *Loop corrections to the neutral Higgs boson sector of the MSSM with explicit CP violation*, *Phys. Lett.* **B481** (2000) 57–66, [hep-ph/0002287].

[35] A. Pilaftsis, *Higgs scalar-pseudoscalar mixing in the minimal supersymmetric standard model*, *Phys. Lett.* **B435** (1998) 88–100, [hep-ph/9805373].

[36] A. Pilaftsis and C. E. M. Wagner, *Higgs bosons in the minimal supersymmetric standard model with explicit CP violation*, *Nucl. Phys.* **B553** (1999) 3–42, [hep-ph/9902371].

[37] M. S. Carena, J. R. Ellis, A. Pilaftsis, and C. E. M. Wagner, *Renormalization-group-improved effective potential for the MSSM Higgs sector with explicit CP violation*, *Nucl. Phys.* **B586** (2000) 92–140, [hep-ph/0003180].

[38] J. F. Gunion, H. H. E., G. Kane, and S. Dawson, *The Higgs Hunter's Guide*, Addison Wesley Publishing Company, 1990.

[39] M. S. Carena, J. R. Ellis, A. Pilaftsis, and C. E. M. Wagner, *CP-violating MSSM Higgs bosons in the light of LEP 2*, *Phys. Lett.* **B495** (2000) 155–163, [hep-ph/0009212].

[40] **CDF** Collaboration, *A Combination of CDF and D0 Results on the Mass of the Top Quark*, arXiv:0803.1683.

[41] J. Kublbeck, M. Bohm, and A. Denner, *Feyn arts: computer algebraic generation of feynman graphs and amplitudes*, *Comput. Phys. Commun.* **60** (1990) 165–180.

[42] T. Hahn, *Generating Feynman diagrams and amplitudes with FeynArts 3*, *Comput. Phys. Commun.* **140** (2001) 418–431, [hep-ph/0012260].

[43] T. Hahn and C. Schappacher, *The implementation of the minimal supersymmetric standard model in FeynArts and FormCalc*, *Comput. Phys. Commun.* **143** (2002) 54–68, [hep-ph/0105349].

[44] G. 't Hooft and M. J. G. Veltman, *Scalar One Loop Integrals*, *Nucl. Phys.* **B153** (1979) 365–401.

[45] T. Hahn and M. Perez-Victoria, *Automatized one-loop calculations in four and D dimensions*, *Comput. Phys. Commun.* **118** (1999) 153–165, [hep-ph/9807565].

[46] H. Anlauf, "Radiative corrections in gauge theories." Adriatic School on Particle Physics and Physics Informatics. September 11th-21st. Split 2001.

[47] D. Bohm, M., A., and H. Joos, *Gauge Theories of Strong and Electroweak Interactions*. B. G. Teubner, 2001.

[48] A. Brignole, *Radiative corrections to the supersymmetric neutral Higgs boson masses*, *Phys. Lett.* **B281** (1992) 284.

[49] M. Frank, S. Heinemeyer, W. Hollik, and G. Weiglein, *The Higgs boson masses of the complex MSSM: A complete one-loop calculation*, hep-ph/0212037.

[50] A. Freitas and D. Stockinger, *Gauge dependence and renormalization of tan(beta) in the MSSM*, *Phys. Rev.* **D66** (2002) 095014, [hep-ph/0205281].

[51] A. Denner, *Techniques for calculation of electroweak radiative corrections at the one loop level and results for W physics at LEP-200*, *Fortschr. Phys.* **41** (1993) 307–420, [arXiv:0709.1075].

[52] M. Steinhauser, *Leptonic contribution to the effective electromagnetic coupling constant up to three loops*, *Phys. Lett.* **B429** (1998) 158–161, [hep-ph/9803313].

[53] K. Hagiwara, A. D. Martin, D. Nomura, and T. Teubner, *Predictions for g-2 of the muon and $\alpha_{\rm QED}(M_Z^2)$*, *Phys. Rev.* **D69** (2004) 093003, [hep-ph/0312250].

[54] T. Hahn, S. Heinemeyer, and G. Weiglein, *MSSM Higgs-boson production at the linear collider: Dominant corrections to the W W fusion channel*, *Nucl. Phys.* **B652** (2003) 229–258, [hep-ph/0211204].

[55] S. Heinemeyer, W. Hollik, H. Rzehak, and G. Weiglein, *The Higgs sector of the complex MSSM at two-loop order: QCD contributions*, *Phys. Lett.* **B652** (2007) 300–309, [arXiv:0705.0746].

[56] G. Degrassi, S. Heinemeyer, W. Hollik, P. Slavich, and G. Weiglein, *Towards high-precision predictions for the MSSM Higgs sector*, *Eur. Phys. J.* **C28** (2003) 133–143, [hep-ph/0212020].

[57] S. Heinemeyer, W. Hollik, and G. Weiglein, *The masses of the neutral CP-even Higgs bosons in the MSSM: Accurate analysis at the two-loop level*, *Eur. Phys. J.* **C9** (1999) 343–366, [hep-ph/9812472].

[58] S. Heinemeyer, W. Hollik, and G. Weiglein, *FeynHiggs: A program for the calculation of the masses of the neutral CP-even Higgs bosons in the MSSM*, *Comput. Phys. Commun.* **124** (2000) 76–89, [hep-ph/9812320].

[59] J. S. Lee *et. al.*, *CPsuperH: A computational tool for Higgs phenomenology in the minimal supersymmetric standard model with explicit CP violation*, *Comput. Phys. Commun.* **156** (2004) 283–317, [hep-ph/0307377].

[60] M. S. Carena *et. al.*, *Reconciling the two-loop diagrammatic and effective field theory computations of the mass of the lightest CP-even Higgs boson in the MSSM*, *Nucl. Phys.* **B580** (2000) 29–57, [hep-ph/0001002].

[61] A. Djouadi, *The anatomy of electro-weak symmetry breaking. II: The Higgs bosons in the minimal supersymmetric model*, *Phys. Rept.* **459** (2008) 1–241, [hep-ph/0503173].

[62] D. A. Demir, *Effects of the supersymmetric phases on the neutral Higgs sector*, *Phys. Rev.* **D60** (1999) 055006, [hep-ph/9901389].

[63] T. Ibrahim and P. Nath, *Corrections to the Higgs boson masses and mixings from chargino, W and charged Higgs exchange loops and large CP phases*, *Phys. Rev.* **D63** (2001) 035009, [hep-ph/0008237].

[64] T. Ibrahim and P. Nath, *Neutralino exchange corrections to the Higgs boson mixings with explicit CP violation*, *Phys. Rev.* **D66** (2002) 015005, [hep-ph/0204092].

[65] S. P. Martin, *Complete two-loop effective potential approximation to the lightest Higgs scalar boson mass in supersymmetry*, *Phys. Rev.* **D67** (2003) 095012, [hep-ph/0211366].

[66] S. P. Martin, *Strong and Yukawa two-loop contributions to Higgs scalar boson self-energies and pole masses in supersymmetry*, *Phys. Rev.* **D71** (2005) 016012, [hep-ph/0405022].

[67] S. P. Martin, *Three-loop corrections to the lightest Higgs scalar boson mass in supersymmetry*, *Phys. Rev.* **D75** (2007) 055005, [hep-ph/0701051].

[68] S. Heinemeyer, *The Higgs boson sector of the complex MSSM in the Feynman-diagrammatic approach*, *Eur. Phys. J.* **C22** (2001) 521–534, [hep-ph/0108059].

[69] S. Heinemeyer, W. Hollik, and G. Weiglein, *QCD corrections to the masses of the neutral CP-even Higgs bosons in the MSSM*, *Phys. Rev.* **D58** (1998) 091701, [hep-ph/9803277].

[70] S. Heinemeyer, W. Hollik, and G. Weiglein, *Precise prediction for the mass of the lightest Higgs boson in the MSSM*, *Phys. Lett.* **B440** (1998) 296–304, [hep-ph/9807423].

[71] J. S. Lee, M. Carena, J. Ellis, A. Pilaftsis, and C. E. M. Wagner, *CPsuperH2.0: an Improved Computational Tool for Higgs Phenomenology in the MSSM with Explicit CP Violation*, arXiv:0712.2360.

[72] S. Heinemeyer, *Zwei-Schleifen-Rechnungen im Minimalen Supersymmetrischen Standardmodell*, PhD thesis, Universität Karlsruhe, 1998.

[73] S. Heinemeyer, *MSSM Higgs physics at higher orders*, *Int. J. Mod. Phys.* **A21** (2006) 2659–2772, [hep-ph/0407244].

[74] A. Brignole, G. Degrassi, P. Slavich, and F. Zwirner, *On the $\mathcal{O}(\alpha_t^2)$ two-loop corrections to the neutral Higgs boson masses in the MSSM*, *Nucl. Phys.* **B631** (2002) 195–218, [hep-ph/0112177].

[75] A. Brignole, G. Degrassi, P. Slavich, and F. Zwirner, *On the two-loop sbottom corrections to the neutral Higgs boson masses in the MSSM*, *Nucl. Phys.* **B643** (2002) 79–92, [hep-ph/0206101].

[76] J. R. Espinosa and R.-J. Zhang, *Complete two-loop dominant corrections to the mass of the lightest CP-even Higgs boson in the minimal supersymmetric standard model*, *Nucl. Phys.* **B586** (2000) 3–38, [hep-ph/0003246].

[77] A. Dedes, G. Degrassi, and P. Slavich, *On the two-loop Yukawa corrections to the MSSM Higgs boson masses at large tan(beta)*, *Nucl. Phys.* **B672** (2003) 144–162, [hep-ph/0305127].

[78] S. Heinemeyer, W. Hollik, H. Rzehak, and G. Weiglein, *High-precision predictions for the MSSM Higgs sector at O(alpha(b) alpha(s))*, *Eur. Phys. J.* **C39** (2005) 465–481, [hep-ph/0411114].

[79] T. Hahn, S. Heinemeyer, W. Hollik, H. Rzehak, G. Weiglein, and K. Williams, *Higher-order corrected Higgs bosons in FeynHiggs 2.5*, *Pramana* **69** (2007) 861–870, [hep-ph/0611373].

[80] C. Caso, G. Conforto, A. Gurtu, M. Aguilar-Benitez, C. Amsler, R. Barnett, P. Burchat, C. Carone, O. Dahl, M. Doser, S. Eidelman, J. Feng, M. Goodman, C. Grab, D. Groom, K. Hagiwara, K. Hayes, J. Hernndez, K. Hikasa, K. Honscheid, F. James, M. Mangano, A. Manohar, K. Mnig, H. Murayama, K. Nakamura, K. Olive, A. Piepke, M. Roos, R. Schindler, R. Shrock, M. Tanabashi, N. Trnqvist, T. Trippe, P. Vogel, C. Wohl, R. Workman, and W.-M. Yao. *1998 review of particle physics. The European Physical Journal* **C3** (1998) 1.

[81] R. K. Ellis, W. J. Stirling, and B. R. Webber, *QCD and Collider Physics (Cambridge Monographs on Particle Physics, Nuclear Physics and Cosmology)*. Cambridge University Press, December, 2003.

[82] S. Heinemeyer, W. Hollik, and G. Weiglein, *Decay widths of the neutral cp-even mssm higgs bosons in the feynman-diagrammatic approach. Eur. Phys. J.* **C16** (2000) 139–153, [hep-ph/0003022].

[83] U. Nierste, "QCD Corrections to $H \to b\bar{b}$ for Sven." Private communication in response to hep-ph/0003022, May, 2004.

[84] I. Hinchliffe, *Alpha Strong (*`http://www-theory.lbl.gov/~ianh/alpha/alpha.html`*)*, 2008.

[85] S. Dittmaier, M. Kramer, A. Muck, and T. Schluter, *MSSM Higgs-boson production in bottom-quark fusion: Electroweak radiative corrections, JHEP* **03** (2007) 114, [hep-ph/0611353].

[86] M. S. Carena, D. Garcia, U. Nierste, and C. E. M. Wagner, *Effective Lagrangian for the anti-t b H+ interaction in the MSSM and charged Higgs phenomenology. Nucl. Phys.* **B577** (2000) 88–120, [hep-ph/9912516].

[87] J. Guasch, P. Hafliger, and M. Spira, *MSSM Higgs decays to bottom quark pairs revisited, Phys. Rev.* **D68** (2003) 115001, [hep-ph/0305101].

[88] G. Weiglein. Private communication.

[89] V. Buescher and K. Jakobs, *Higgs boson searches at hadron colliders, Int. J. Mod. Phys.* **A20** (2005) 2523–2602, [hep-ph/0504099].

[90] A. Djouadi *et. al.*, *International Linear Collider Reference Design Report Volume 2: PHYSICS AT THE ILC*, arXiv:0709.1893.

[91] **CLIC Physics Working Group** Collaboration, E. Accomando *et. al.*, *Physics at the CLIC multi-TeV linear collider*, hep-ph/0412251.

[92] V. D. Barger, M. S. Berger, A. L. Stange, and R. J. N. Phillips. *Supersymmetric Higgs boson hadroproduction and decays including radiative corrections. Phys. Rev.* **D45** (1992) 4128–4147.

[93] P. H. Chankowski, S. Pokorski, and J. Rosiek. *Supersymmetric Higgs boson decays with radiative corrections. Nucl. Phys.* **B423** (1994) 497–531.

[94] S. Heinemeyer and W. Hollik. *The decay $h_0 \to a_0 a_0$: a complete 1-loop calculation in the mssm. Nucl. Phys.* **B474** (1996) 32–56. [hep-ph/9602318].

[95] P. Osland and P. N. Pandita, *Measuring the trilinear couplings of MSSM neutral Higgs bosons at high-energy e+ e- colliders. Phys. Rev.* **D59** (1999) 055013. [hep-ph/9806351].

[96] W. Hollik and S. Penaranda. *Yukawa coupling quantum corrections to the self couplings of the lightest mssm higgs boson. Eur. Phys. J.* **C23** (2002) 163–172. [hep-ph/0108245].

[97] M. V. Dolgopolov and Y. P. Philippov, *The trilinear neutral Higgs self-couplings in the MSSM. Complete one-loop analysis*, hep-ph/0310018.

[98] Y. P. Philippov, *Yukawa radiative corrections to the trilinear self- couplings of neutral CP-even Higgs bosons and decay width Gamma(H ¿ h h) in the MSSM, Phys. Atom. Nucl.* **70** (2007) 1288–1293, [hep-ph/0611260].

[99] S. Y. Choi and J. S. Lee, *Decays of the MSSM Higgs bosons with explicit CP violation, Phys. Rev.* **D61** (1999) 015003, [hep-ph/9907496].

[100] M. S. Carena, J. R. Ellis, S. Mrenna, A. Pilaftsis, and C. E. M. Wagner, *Collider probes of the MSSM Higgs sector with explicit CP violation, Nucl. Phys.* **B659** (2003) 145–178, [hep-ph/0211467].

[101] J. S. Lee and S. Scopel, *Lightest Higgs boson and relic neutralino in the MSSM with CP violation, Phys. Rev.* **D75** (2007) 075001, [hep-ph/0701221].

[102] U. Aglietti *et. al.*, *Tevatron-for-LHC Report: Higgs*, hep-ph/0612172.

[103] A. Duperrin, *Review of searches for Higgs bosons and beyond the standard model physics at the Tevatron*, arXiv:0805.3624.

[104] **D0** Collaboration, *Search for Higgs bosons decaying to tau pairs in ppbar collisions with the D0 detector*, arXiv:0805.2491.

[105] **CDF** Collaboration, *Search for neutral MSSM Higgs bosons decaying to tau pairs with 1.8* fb^{-1} *of data*, CDF note 9071.

[106] A. Djouadi, *The anatomy of electro-weak symmetry breaking. I: The Higgs boson in the standard model. Phys. Rept.* **457** (2008) 1 216, [hep-ph/0503172].

[107] A. Dabelstein, *Fermionic decays of neutral MSSM Higgs bosons at the one loop level. Nucl. Phys.* **B456** (1995) 25-56, [hep-ph/9503443].

[108] A. Djouadi, J. Kalinowski, and M. Spira, *HDECAY: A program for Higgs boson decays in the standard model and its supersymmetric extension. Comput. Phys. Commun.* **108** (1998) 56–74, [hep-ph/9704448].

[109] E. Braaten and J. P. Leveille, *Higgs Boson Decay and the Running Mass, Phys. Rev.* **D22** (1980) 715.

[110] **ALEPH** Collaboration, R. Barate *et. al.*, *Observation of an excess in the search for the standard model Higgs boson at ALEPH, Phys. Lett.* **B495** (2000) 1–17, [hep-ex/0011045].

[111] **ALEPH** Collaboration, A. Heister *et. al.*, *Final results of the searches for neutral Higgs bosons in e+ e- collisions at $\sqrt{s}$ up to 209-GeV, Phys. Lett.* **B526** (2002) 191–205, [hep-ex/0201014].

[112] **DELPHI** Collaboration, P. Abreu *et. al.*, *Search for the standard model Higgs boson at LEP in the year 2000, Phys. Lett.* **B499** (2001) 23–37, [hep-ex/0102036].

[113] **DELPHI** Collaboration, J. Abdallah *et. al.*, *Final results from DELPHI on the searches for SM and MSSM neutral Higgs bosons, Eur. Phys. J.* **C32** (2004) 145–183, [hep-ex/0303013].

[114] **L3** Collaboration, M. Acciarri *et. al.*, *Higgs candidates in e^+e^- interactions at $\sqrt{s}$ = 206.6-GeV, Phys. Lett.* **B495** (2000) 18–25, [hep-ex/0011043].

[115] **OPAL** Collaboration, G. Abbiendi *et. al.*, *Search for the standard model Higgs boson in e+ e- collisions at $\sqrt{s}$ = 192 GeV - 209 GeV. Phys. Lett.* **B499** (2001) 38–52, [hep-ex/0101014].

[116] **OPAL** Collaboration, G. Abbiendi *et. al.*, *Search for the standard model Higgs boson with the OPAL detector at LEP, Eur. Phys. J.* **C26** (2003) 479–503, [hep-ex/0209078].

[117] M. S. Carena, S. Heinemeyer, C. E. M. Wagner, and G. Weiglein, *Suggestions for improved benchmark scenarios for Higgs- boson searches at LEP2*, hep-ph/9912223.

[118] M. S. Carena, S. Heinemeyer, C. E. M. Wagner, and G. Weiglein, *Suggestions for benchmark scenarios for MSSM Higgs boson searches at hadron colliders*, *Eur. Phys. J.* **C26** (2003) 601–607, [hep-ph/0202167].

[119] P. Bechtle, Private communication.

[120] P. Bechtle and A. Read, "Detailed tables of lep topological cross section limits." Private communication, 2007.

[121] **CDF** Collaboration, *A Combination of CDF and D0 results on the mass of the top quark*, hep-ex/0703034.

[122] K. E. Williams and G. Weiglein, *Precise predictions for $h_a \to h_b h_c$ decays in the complex MSSM*, *Phys. Lett.* **B660** (2008) 217–227, [arXiv:0710.5320].

[123] **The Tevatron Electroweak Working Group for CDF and D0** Collaboration, *Combination of CDF and D0 Results on the Mass of the Top Quark*, arXiv:0808.1089.

[124] T. Hahn, "Feynhiggs 2.6.5beta." Private communication, August, 2008.

[125] O. Brein and T. Hahn, *On MSSM charged Higgs boson production in association with an electroweak W boson at electron positron colliders*, *Eur. Phys. J.* **52** (2007) 397–411, [hep-ph/0610079].

[126] O. Brein and W. Hollik, *Distributions for MSSM Higgs boson + jet production at hadron colliders*, *Phys. Rev.* **D76** (2007) 035002, [arXiv:0705.2744].

[127] **CDF** Collaboration, *Search for Standard Model Higgs boson production in association with $W^{\pm}$ boson at CDF with 1.7 fb^{-1} data*, CDF note 8957.

[128] **D0** Collaboration, *Search for WH production using a neural network approach in $p\bar{p}$ collisions at $\sqrt{s} = 1.96$ TeV with 1.7 fb^{-1} of data*, D0note 5472-CONF.

[129] **CDF** Collaboration, *Search for Standard Model Higgs boson production in association with $W^{\pm}$ at CDF with 1.9 fb^{-1}*, CDF note 9219.

[130] J. Efron, B. Kilminster, R. Hughes, B. Parks, and B. Winer, *Search for $ZH \to l^+l^-b\bar{b}$ in 1 fb^{-1} of CDF Run 2 Data*, CDF note 8742.

[131] **D0** Collaboration, *Search for the standard model Higgs boson in $HZ \to b\bar{b}\nu\bar{\nu}$ channel in 2.1 fb^{-1} of $p\bar{p}$ collisions at $\sqrt{s} = 1.96$ TeV*, D0note 5586-CONF.

[132] **D0** Collaboration, *Search for the standard model Higgs boson in $HZ(\to l^+l^-b\bar{b})$ in $p\bar{p}$ collisions at $\sqrt{s} = 1960$ GeV*, D0note 5482-CONF.

[133] **CDF** Collaboration, *Search for $H \to WW^*$ production with matrix element methods at Tevatron using 1.9 fb^{-1} data*, CDF note 8958.

[134] **D0** Collaboration. *Search for the Higgs boson in* $H \to W^+W^- \to e\mu$ *decays at D0 in Run IIb.* D0note 5489-CONF.

[135] **D0** Collaboration. *Search for the Higgs boson in* $H \to W^+W^{-(*)} \to ll'(l, l' = e, \mu)$ *decays with 1.2* fb^{-1} *at D0 in Run IIb.* D0note 5624-CONF.

[136] **CDF** Collaboration. *Search for* $H \to W^+W^-$ *production with a combined matrix element method and neiral network technique at Tevatron using 2.4* fb^{-1} *data.* CDF note 9236.

[137] **D0** Collaboration. *Search for the associated Higgs boson production* $p\bar{p} \to WH \to WWW^* \to l^{\pm}\nu l'^{\pm}\nu' + X$ *at* $\sqrt{s} = 1.96$ *TeV*, D0note 5485-CONF.

[138] **CDF** Collaboration, *Search for the* Wh *production using high-*p_T *isolated like-sign dilepton events in Run II with 1.9* fb^{-1} *data.* CDF note 7307.

[139] **D0** Collaboration, *Search for neutral Higgs bosons at high* $\tan\beta$ *in multi-jet events.* D0note 5503-CONF.

[140] **CDF** Collaboration. *Search for Higgs bosons producted in association with b-quarks*, CDF note 9284.

[141] **D0** Collaboration, V. M. Abazov *et. al.*, *Search for neutral Higgs bosons in multi-b-jet events in* $p\bar{p}$ *collisions at* $\sqrt{s} = 1.96$ *TeV*, `arXiv:0805.3556`.

[142] **D0** Collaboration, *Search for a light Higgs boson in* $\gamma\gamma$ *final states at D0*, D0note 5601-CONF.

[143] **D0** Collaboration, V. M. Abazov *et. al.*, *Search for* $h_f \to \gamma\gamma$ *with the D0 detector at* $\sqrt{s} = 1.96$ *TeV*, `arXiv:0803.1514`.

[144] **CDF** Collaboration, *Neural network search for Standard Model Higgs boson in missing transverse energy plus jets channel with 1.7* fb^{-1}, CDF note 9166.

[145] **CDF** Collaboration. *Search for the Standard Model Higgs boson in* $H \to \tau\tau$ *channel at CDF Run II - Simultaneous search for WH/ZH/VBF/H processes.* CDF note 9248.

[146] **TEVHPH Working Group for CDF and D0** Collaboration, *Combined CDF and D0 upper limits on Standard Model Higgs boson producitons with up to 2.4* fb^{-1}, FERMILAB-PUB-08-069-E, CDF note 9290, D0 note 5645.

[147] **TEVHPH Working Group for CDF and D0** Collaboration, *Combined CDF and D0 upper limits on Standard Model Higgs boson produciton*, FERMILAB-PUB-07-656-E, CDF note 8961, D0 note 5536.

[148] T. Hahn, S. Heinemeyer, F. Maltoni, G. Weiglein, and S. Willenbrock, *SM and MSSM Higgs boson production cross sections at the Tevatron and the LHC*, hep-ph/0607308.

[149] J. Campbell, R. K. Ellis, F. Maltoni, and S. Willenbrock, *Higgs boson production in association with a single bottom quark*, *Phys. Rev.* **D67** (2003) 095002, [hep-ph/0204093].

[150] P. Gondolo *et. al.*, *DarkSUSY: Computing supersymmetric dark matter properties numerically*, *JCAP* **0407** (2004) 008, [astro-ph/0406204].

[151] M. Schumacher, *Investigation of the discovery potential for Higgs bosons of the minimal supersymmetric extension of the standard model (MSSM) with ATLAS*, hep-ph/0410112.

[152] E. Accomando *et. al.*, *Workshop on CP studies and non-standard Higgs physics*, hep-ph/0608079.

[153] P. Bandyopadhyay, A. Datta, A. Datta, and B. Mukhopadhyaya, *Associated Higgs Production in CP-violating supersymmetry: probing the 'open hole' at the Large Hadron Collider*, *Phys. Rev.* **D78** (2008) 015017, [arXiv:0710.3016].

[154] D. Berdine, N. Kauer, and D. Rainwater, *Breakdown of the Narrow Width Approximation for New Physics*, *Phys. Rev. Lett.* **99** (2007) 111601, [hep-ph/0703058].

[155] M. A. Gigg and P. Richardson, *Simulation of Finite Width Effects in Physics Beyond the Standard Model*, arXiv:0805.3037.

[156] N. Kauer, *Narrow-width approximation limitations*, *Phys. Lett.* **B649** (2007) 413–416, [hep-ph/0703077].

[157] A. Buckley, "The hepthesis LaTeX class."

List of figures

List of tables